The oxidation photochemistry and transport of hydrogen peroxide and formaldehyde at three sites in Europe: trends, budgets and 3-D model simulations

Dissertation
zur Erlangung des Grades
"Doktor der Naturwissenschaften"
im Promotionsfach Chemie
am Fachbereich Chemie, Pharmazie und Geowissenschaften
der Johannes Gutenberg-Universität
in Mainz

Raoul Daniel Axinte
geb. in Arad/Rumänien

Mainz, 2016

D77

Dekan: [redacted]

1. Berichterstatter: [redacted]
2. Berichterstatter: [redacted]

Tag der mündlichen Prüfung:

I hereby declare that I wrote the dissertation submitted without any unauthorized external assistance and used only sources acknowledged in the work. All textual passages, which are appropriated verbatim or paraphrased from published and unpublished texts as well as all information obtained from oral sources are duly indicated and listed in accordance with bibliographical rules. In carrying out this research, I complied with the rules of standard scientific practice as formulated in the statutes of Johannes Gutenberg-University Mainz to insure standard scientific practice.

Mainz, December 2016

Zusammenfassung

[1] Die Photochemie von Wasserstoffperoxid (H_2O_2) und Formaldehyd (HCHO) beeinflusst das Budget von HO_x (= OH + HO_2) und hat damit einen starken Einfluss auf Ozon (O_3) und NO_x (= NO + NO_2) in der Troposphäre. Umfangreiche Feldmesskampagnen wurden in Europa durchgeführt: DOMINO vom 20. Nov. – 9. Dez. 2008 (El Arenosillo, Südspanien), HUMPPA vom 12. Jul. - 12. Aug. 2010 (Hyytiälä, Südfinnland) und PARADE vom 15. Aug. – 10. Sep. 2011 (Kleiner Feldberg, Deutschland). Mischungsverhältnisse in der Gasphase wurden in-situ mittels zweier angepasster Instrumente auf einer Höhe zwischen 8 und 21 m vom Boden aufgezeichnet (Modell AL2021 bzw. AL4021, Aero-Laser GmbH, Garmisch-Partenkirchen, Deutschland).

[2] Die mittleren Tageswerte für H_2O_2 waren 82 pptv, 639 pptv, bzw. 323 pptv für DOMINO, HUMPPA und PARADE. In der Nacht erreichten die Mischungsverhältnisse 59 pptv (DOMINO), 99 pptv (HUMPPA) und 486 pptv (PARADE). Die mittleren Tagesgänge von H_2O_2 waren während DOMINO und HUMPPA stark ausgeprägt mit Höchstwerten am Nachmittag, wobei PARADE ein inverses Profil zeigte. Für HCHO erreichten die Durchschnittswerte 569 pptv, 465 pptv und 1.9 ppbv für DOMINO, HUMPPA und PARADE. Die Werte in der Nacht erreichten 505 pptv (DOMINO), 383 pptv (HUMPPA) und 1.9 ppbv (PARADE) mit jeweils wenig Variation. Die mittlere Abweichung vom photostationären Zustand (PSS) lag bei allen Feldmesskampagnen zwischen 1.2 und 1.5. Einfachen kinetischen Betrachtungen für den Gleichgewichtszustand nach wurde der Hauptanteil von H_2O_2 am Tag durch Photochemie erzeugt, wobei die Werte für HUMPPA um den Faktor 6 überschätzt wurden. Bei den Kampagnen DOMINO und HUMPPA stammte atmosphärisches HCHO aus photochemischen Quellen. Die Produktion ließ sich auf folgende Hintergrundreaktionen zurückführen: die Oxidation von Methan, Isopren und Methanol durch OH-Radikale. Im Gegensatz hierzu wurden bei PARADE über 80 % des Formaldehyds aus anthropogenen Quellen emittiert und abtransportiert.

[3] Ziel der HUMPPA Kampagne war die Überprüfung des derzeitigen Kenntnisstandes über die Quellen und Senken von H_2O_2 und HCHO im borealen Wald. Die Studie befasst sich hauptsächlich mit Berechnungen des PSS, von [RO_x], [OH] und der Budgets von H_2O_2 und HCHO. Vier chemische Regimes konnten identifizert und diskutiert werden: gestresst boreal (R1, 12. - 22. Jul. 2010), kalt & rein (R2, 23. - 25. Jul.), verschmutzt (R3, 26. - 29. Jul.) und normal boreal, letzters mit einigen kurzen Perioden verschmutzter Luft (R4, 1.-12. Aug.). Das berechnete [HO_2] stimmt mit den Beobachtungen überein (r^2 = 0.71), die OH-Zeitreihe ergibt eine qualitativ richtige Widergabe. Die Budgetberechnungen ohne trockene Deposition und Transport zeigen eine Überschätzung von H_2O_2 von Faktor 5 bis 10 (r^2 = 0.24), bzw. Faktor 3.6 im Falle von HCHO (r^2 = 0.26). Eine einfache Methode, basierend auf linearer Regression, ergibt im Median Depositionsgeschwindigkeiten von 3.03 cm s^{-1} für H_2O_2 und 1.08 cm s^{-1} für HCHO. Transport spielt eine wichtige Rolle im Verlauf eines borealen Sommertages: Entrainment H_2O_2-reicher Luft von oben erhöht die Mischungsverhältnisse, wobei HCHO-arme Luft diese im Fall von HCHO erniedrigt. Das Einbeziehen von trockener Deposition und Transport in die Budgetberechnungen führt zu einer guten Reproduktion von H_2O_2 (Steigung: 0.9520 ± 0.0834, Ordinate: 0.2330 ± 0.0543 ppbv, r^2 = 0.30) und HCHO (Steigung: 0.2320 ± 0.0258, Ordinate: 0.2980 ± 0.0224 ppbv, r^2 = 0.35). Die Klassifizierung der NO_x-Sensitivität im Bezug auf die Nettoproduktion von H_2O_2 zeigt Hinweise auf ein Maximum in dem NO_x-Intervall von 0.24 to 0.41 ppbv. Hingegen verlief die Nettoproduktion von HCHO linear bis zum NO-Intervall von 0.05 bis 0.07 ppbv. Höhere NO-Mischungsverhältnisse (70 bis 140 pptv) führten zur Bildung eines Plateaus.

[4] Drei Modellsimulationen (Referenz R; zwei Sensitivitätsstudien S1 und S2) wurden mit dem 3-D-Modell EMAC für HUMPPA unter Ausschluss von Terpenchemie durchgeführt. Die Parameter für S1 waren 50 % NO_x-Emissionen, für S2 50 % NO_x-Emissionen sowie doppelte Depositionsgeschwindigkeiten für H_2O_2 und HCHO. Die Evaluation von NO_x führte zur Untersuchung einer benachbarten Modell-Box aufgrund des Transports verschmutzter Luft aus einer nahegelegenen Stadt. Die resultierenden Tagesmittelwerte um 350 pptv sind im Einklang mit den Beobach-

tungen. Die synoptische Meteorologie, langlebige Spurengase (Kohlenstoffmonoxid und Methan) sowie der Transport von Biomasseverbrennungs-Plumes aus Russland wurden qualitativ wiedergegeben. Das Modell simulierte sogar den observierten Abwärtstransport von sekundärem HCHO aus den Plumes am frühen Morgen. Wie erwartet zeigte bereits R Defizite in der Radikalchemie aufgrund der fehlenden Terpenchemie. Die mittleren H_2O_2- und HCHO-Levels am Tag übertrafen die Messdaten um den Faktor 4, bzw. 3.4. Niedrigeres NO_x (S1 und S2) zeigte keinen signifikanten Einfluss auf die Mischungsverhältnisse der modellierten Spurengase inklusive H_2O_2 und HCHO. Höhere Depositionsgeschwindigkeiten (S2) ergaben immer noch eine 2.2fache (H_2O_2), bzw. 3fache (HCHO) Überschätzung der Levels. Sensitivitätsstudien mit höheren Depositionsgeschwindigkeiten und grundlegender Terpenchemie bleiben Ziel zukünftiger Forschung.

Abstract

[1] The photochemistry of hydrogen peroxide (H_2O_2) and formaldehyde (HCHO) mediates the budget of HO_x (= OH + HO_2) and thus has a strong impact on ozone (O_3) and NO_x (= NO + NO_2) in the troposphere. Comprehensive ground-based field measurements at three different sites in Europe were performed: DOMINO from Nov 20–Dec 9 2008 (El Arenosillo, Southern Spain), HUMPPA from Jul 12–Aug 12 2010 (Hyytiälä, Southern Finland) and PARADE from Aug 15–Sep 10 2011 (Kleiner Feldberg, Germany). Mixing ratios of gas-phase H_2O_2 and HCHO were measured in-situ between 8 and 21 m above ground level via two customized instruments (Model AL2021 respectively AL4021, Aero-Laser GmbH, Garmisch-Partenkirchen, Germany).

[2] Average daytime levels of H_2O_2 for DOMINO, HUMPPA and PARADE were 82 pptv, 639 pptv, and 323 pptv, respectively. Night-time mixing ratios reached 59 pptv (DOMINO), 99 pptv (HUMPPA) and 486 pptv (PARADE). Mean diurnal profiles of H_2O_2 showed a strong diurnal pronunciation for DOMINO and HUMPPA with maximum values in the afternoon, while an inverse profile was observed during PARADE. In case of HCHO, daytime HCHO averages of 569 pptv, 465 pptv and 1.9 ppbv were measured for DOMINO, HUMPPA and PARADE, respectively. Night-time mixing ratios were 505 pptv (DOMINO), 383 pptv (HUMPPA) and 1.9 ppbv (PARADE) and showed smooth diurnal variations. The average deviation from photostationary state (PSS) for all campaigns range from 1.2 to 1.5 . Simple steady-state calculations reveal that the major amount of daytime H_2O_2 during DOMINO and PARADE can be explained by photochemistry, while for HUMPPA the levels are overestimated by a factor of 6. Further, ambient HCHO was under photochemical control during DOMINO and HUMPPA. The production can be expressed by background chemical pathways, namely, the oxidation of methane, isoprene and methanol by OH radicals. During PARADE, over 80 % of ambient HCHO were primarily emitted from anthropogenic sources and transported.

[3] HUMPPA allows challenging the current understanding of sources and sinks of H_2O_2 and HCHO in the boreal forest. The study focuses on calculations of the PSS, [RO_x], [OH] and of the H_2O_2 and HCHO budgets. Four regimes can be identified and used for discussion: stressed boreal (R1, Jul 12-22 2010), cold & clean (R2, Jul 23-25), transported pollution (R3, Jul 26-29) and normal boreal with some short pollution events (R4, Aug 1-12). The calculated [HO_2] agrees with the observations (r^2 = 0.71), while the OH time series are reproduced reasonably well. The budget calculations excluding dry deposition show an average overestimation of H_2O_2 by a factor of 5 up to an order of magnitude (r^2 = 0.24), while HCHO exceed the measurement by 3.6 times (r^2 = 0.26). A simple linear regression method yield median values of deposition velocities of 3.03 cm s^{-1} for H_2O_2 and 1.08 cm s^{-1} for HCHO. Daytime transport plays a major role in boreal summer: entrainment of H_2O_2-rich air significantly enriches the ambient mixing ratios, while HCHO-poor air decreases the HCHO levels. Including deposition and transport, the budget of H_2O_2 is reproduced rather well (slope: 0.9520 ± 0.0834, intercept: 0.2330 ± 0.0543 ppbv, r^2 = 0.30), while that for HCHO was reasonable (slope: 0.2320 ± 0.0258, intercept: 0.2980 ± 0.0224 ppbv, r^2 = 0.35). The classification of the NO_x sensitivity concerning the net H_2O_2 production rate showed evidence for a maximum in the NO_x interval ranging from 0.24 to 0.41 ppbv. The net HCHO production, followed a linear trend until the NO interval from 0.05 to 0.07 ppbv. Higher NO mixing ratios (70 to 140 pptv) resulted in the formation of a plateau.

[4] Three model simulations (reference R; two sensitivity studies S1 and S2) were performed with the 3-D model EMAC for HUMPPA excluding terpene chemistry. The parameters for S1 were 50 % NO_x emissions and for S2 50 % NO_x emissions and double deposition velocities for H_2O_2 and HCHO). Evaluation of NO_x led to using a vicinal box due to pollutant transport from a nearby town. The resulting average daytime levels about 350 pptv agreed with the observations. Large-scale meteorology, long-lived trace chemical species (carbon monoxide and methane) and the transport of biomass burning plumes from Russia were reproduced reasonably well. The model reproduced the observed downward transport of secondary HCHO from biomass burning plumes in the morn-

ing hours. As expected, R showed deficits in radical chemistry due to lacking terpene chemistry. H_2O_2 and HCHO levels exceeded measured data by a factor of 4 and 3.4, respectively. Lower NO_x (S1 and S2) had an insignificant effect on the mixing ratios of the modeled trace chemical species including H_2O_2 and HCHO. Higher deposition velocities (S2) resulted in 2.2-fold (H_2O_2) and 3-fold (HCHO) increased levels, respectively. Sensitivity simulations with higher deposition velocities and basic terpene chemistry remain future research objects.

Contents

Abbreviations and nomenclature

General

A. R.	Analytical grade reagent equivalent to the German *pro analysi* (p. a.)
BB	Biomass burning
CA	Chromotropic acid
CAABA-MECCA	Chemistry As A Boxmodel Application Module Efficiently Calculating the Chemistry of the Atmosphere
CCF	Cloud correction factor
CCN	Cloud condensation nuclei
CFC	Chlorofluorocarbon
CIMS	Chemical ionization mass spectrometer
CLD	Chemiluminescence detector
CRM	Comparative reactivity method
DNPH	2,4-Dinitrophenylhydrazine
DOAS	Differential optical absorption spectroscopy
DWD	Deutscher Wetterdienst
EDTA	Ethylenediaminetetraacetic acid
EMAC	ECHAM5/MESSy Atmospheric Chemistry
FTIR	Fourier transform infrared spectroscopy
FT	Free troposphere
GC-ECD	Gas chromatography-electron capture detector
GC-MS	Gas chromatography-mass Spectrometry
GHG	Greenhouse gas
GCM	General circulation model
GFED	Global fire data
HPLC	High performance liquid chromatography
HLUG	Hessisches Landesamt für Umwelt und Geologie
INTA	National Institute for Aerospace Technology
IPCC	Intergovernmental Panel on Climate Change
KHP	Potassium hydrogen phthalate
LC-MS	Liquid chromatography–mass spectrometry, alternatively HPLC-MS
LCW	Liquid core waveguide
LED	Light emitting diode
LIF	Laser induced fluorescence
LIDAR	Light detection and ranging
LOD	Limit of detection
LOPAP	Long path absorption photometer
MASL	Metres above sea level, also m a. s. l.
MBL	Marine boundary layer
MESSy	Modular Earth Submodel System
MFC	Mass flow controller

MIM	Mainz Isoprene Mechanism
MIM2MTM	Mainz Isoprene Mechanism 2 Mainz Terpene Mechanism
MoLa	Mobiles Aerosolforschungslabor (Engl. mobile aerosol research laboratory)
MODIS	Moderate-resolution imaging spectroradiometer
MPIC	Max Planck Institute for Chemistry, Mainz, Germany
NaOH	Potassium hydroxide
NCAR	National Center for Atmospheric Research, Boulder, Colorado
NIST	National Institute of Standards and Technology, Gaithersburg, Maryland
NOP	Net ozone production
P	Precision at a certain concentration or mixing ratio
PD	Permeation device
PBL	Planetary boundary layer
PE	Polyethylene
PerCA	Peroxy radical chemical amplification
PFA	Perfluoroalkoxy
PMT	Photomultiplier tube
PLS	Partial least squares regression
POH	Primary OH production
POPHA	p-Hydroxyphenylacetic acid
ppbv	Parts per billion by volume: nmol per mole
ppbm	Parts per million by volume: mmol per mole
pptv	Parts per trillion by volume: pmol per mole
PSS	Photostationary state
PTFE	Polytetrafluoroethylene
PTR-MS	Proton-transfer-reaction mass spectrometry
RSD	Relative standard deviation
SMEAR II	Station for Measuring Ecosystem-Atmosphere Relation
SOA	Secondary organic aerosols
SS	Steady state
slpm	Standard liter per minute
TCPO	Chemiluminescence technique using bis-(2,4,6-trichlorophenyl)oxalate
TDLAS	Tunable diode laser absorption spectroscopy
TMU	Total measurement uncertainty
UHEL	University of Helsinki
UTC	Universal time, coordinated
UV	Ultra violet
V25	NEC V25 microcontroller
WHO	World Health Organization

Atmospheric chemical species

BVOC	Biogenic volatile organic compounds, e. g., isoprene ($CH_2 = C(CH_3)CH = CH_2$)
CH_4	Methane
CH_3	Methyl radical

CH_3O	Methoxy radical
CH_3O_2	Methyl peroxy radical
CO	Carbon monoxide
H	Hydrogen
HCO	Formyl radical
H_2O_2	Hydrogen peroxide
H_2SO_4	Sulfuric acid
HCHO	Formaldehyde
HMHP	Hydroxymethyl hydroperoxide ($HOCH_2OOH$)
HO_2	Hydroperoxy radical
HO_x	OH and HO_2
MACR	Methacrolein ($H_2C=C(CH_3)CHO$)
MHP	Methyl hydroperoxide (CH_3OOH)
MVK	Methyl vinyl ketone ($CH_3C(O)CH=CH_2$)
NMHC	Non-methane hydrocarbons
NO	Nitric (mono)oxide
NO_2	Nitric dioxide
NO_x	NO and NO_2
NO_y	Total reactive nitrogen: $NO_x + NO_3 + 2\,N_2O_5 + HNO_2 + HNO_3 + HNO_4 + HONO +$ PAN + other organic nitrates
NO_z	$NO_y - NO_x$
O	Atomic oxygen
O_2	Molecular oxygen
O_3	Ozone
OH	Hydroxyl radical
oVOC	Partly oxidized volatile organic compounds, e. g., formaldehyde (HCHO)
PAA	Peracetic acid ($CH_3(O)OOH$)
PAN	Peroxy acetic nitrate ($CH_3COOONO_2$) or peroxyacyl nitrates (PANs)
PNA	Peroxynitric acid (HO_2NO_2)
ROOH	Organic hydroperoxides (R is an organic rest), e. g., methyl hydroperoxide (CH_3OOH)
$RO\cdot$	Alkoxy radical (R is an organic rest)
$RO_2\cdot$	Organic peroxy radicals (R is an organic rest), e. g., methyl peroxy radical (CH_3OO)
RO_x	Organic oxy and peroxy radicals comprising HO_x: $HO_2 + OH + RO_2 + RO$
VOC	Volatile organic compounds, e. g., propane ($CH_3 - CH_2 - CH_3$)

Field measurement campaigns

DOMINO	Diel Oxidant Mechanisms in Relation to Nitrogen Oxides
HUMPPA	Hyytiälä United Measurements of Photochemistry and Particles in Air
PARADE	Particles and Radicals: Diel Observations of the Impact of Urban and Biogenic Emissions

Fundamental constants

N_A	Avogadro constant	$6.022\,141\,29 \times 10^{23}\ \mathrm{mol^{-1}}$
R	Ideal gas constant	$8.314\,462\,1\ \mathrm{J\ mol^{-1}\ K^{-1}}$
V_m	Molar volume at standard temperature ($T_n = 273.15\ \mathrm{K}$) and pressure ($p_n = 101\,325\ \mathrm{Pa}$)	$24.465\,433\ \mathrm{L\ mol^{-1}}$

Nomenclature

α	Stripping or collection efficiency	(%)
ϵ	Catalase efficiency	(%)
μ	Volume mixing ratio through liquid calibration	(ppbv)
ξ	Volume mixing ratio for the species i: $\xi_i = \frac{c_i}{c_{total}}$, $1\ \mathrm{ppbv} \approx 2.46 \times 10^{10}\ \mathrm{cm^{-3}}$ at 298 K.	
c	Molar concentration	$\left(\mathrm{mol\ L^{-1}}\right)$
E_S	Sum of systematic errors	(ppbv or %)
K_H	Henry coefficient	(mol/L/atm)
n	Molar amount of substance	(mol)
$\dot{n}$	Molar flow rate	$\left(\mathrm{mol\ min^{-1}}\right)$
p	Atmospheric pressure	(Pa)
P	Instrumental precision	(ppbv or %)
S	Instrumental sensitivity	$\left(\mathrm{ppbv\ V^{-1}}\right)$
P	Instrumental precision	(ppbv or %)
τ	Atmospheric lifetime	(e. g., h)
t	Time	(s)
T	Thermodynamic temperature, related to the Celsius scale (ϑ): $T = \left(\frac{\vartheta}{1\,°\mathrm{C}} + 273.15\right)\mathrm{K}$	(K)
R	Recovery	(%)
U	Instrumental signal, actually as a function of time $U(t)$	(V)
V	Volume	(L)
$\dot{V}$	Volumetric flow rate	$\left(\mathrm{L\ min^{-1}}\right)$

1. Introduction

1.1. Why tropospheric hydrogen peroxide and formaldehyde are important

Hydrogen peroxide (H_2O_2), the most abundant organic hydroperoxide (CH_3OOH) and formaldehyde (HCHO) are both sink and source of odd-hydrogen radicals (OH, HO_2, CH_3O_2) in the troposphere. The reactions they are involved in lead to the production of odd-oxygen (O, O_3). Therefore, as reservoir species, they reflect the amount of ambient radicals and indicate the oxidising capacity. Contrary to HCHO, hydroperoxides are direct oxidants by producing sulphuric acid in the aqueous phase. However, losses of hydroperoxides due to deposition or aqueous phase chemistry lead to a decrease in the oxidising capacity, while an increase has the opposite effect. Particularly climate change is caused by an imbalanced atmospheric composition, e. g., the increase of GHGs compared to the paleoclimatic background. This leads to higher variability of extreme synoptic conditions, such as floods and droughts, while an impact on precursor species is highly likely (Stocker et al., 2013).
There are excellent reviews on hydroperoxides (Gunz and Hoffmann, 1990; Hua et al., 2008a; Jackson and Hewitt, 1999; Lee et al., 2000; Reeves and Penkett, 2003) and HCHO (Carlier et al., 1986). This thesis is based on a comprehensive data set which allows focusing on the following scientific issues:

1. There are many observations of ambient hydroperoxides and HCHO under different pollution levels in the troposphere. Which trends can be identified for three different locations in Europe and how are they linked to the oxidising capacity?
2. There are few budget calculations on ambient H_2O_2 and HCHO in the boreal forest. Is the current understanding of sources and sinks able to explain the ambient levels and variability?
3. Although the 3-D model EMAC is limited in reproducing local photochemistry, it shows good agreement for large scale transport processes. How does it simulate physical phenomena that affect ambient H_2O_2 and HCHO in the boreal forest?

Thesis outline. This introducing part briefly summarises chemical and physical processes in the troposphere. The materials and methods chapter focuses on (i) site descriptions, (ii) instruments and procedures for measuring ambient H_2O_2 and HCHO, (iii) methods for observing related species and how (iv) back-of-the-envelope calculations and (v) model simulations were performed. The results and discussion chapter highlights new outcome in comparison to the literature. Starting with describing (i) the trends in three different European locations, over (ii) examining the photochemistry in the boreal forest and ending with the (iii) model evaluation for the large scale transport of biomass burning plumes. Each scientific section ends with a summary and conclusions part that (i) reflects the thesis statements, (ii) provides answers to the research questions, (iii) points out the limitations, (iv) identifies the implications with respect to the overall area and (v) provides perspectives for future research.

1.2. The Earth's atmosphere

1.2.1. Atmospheric vertical structure and composition

The gaseous layer retained by Earth's gravity is referred to as its atmosphere. The atmospheric pressure follows an exponential decrease with altitude. However, physical and chemical processes cause different compositions and temperatures leading to a high stratification as depicted in Figure 1.1. About 90 % of the total atmospheric mass is situated in the troposphere, which is the lowest part of the atmosphere spreading from surface to the tropopause (ca. 10 to 18 km). That is also the part where weather phenomena mostly occur. Except for the highly variable abundance of water vapour, the troposphere is well-mixed and consists of 78 % nitrogen (N_2), 21 % oxygen (O_2), 0.95 % argon (Ar) and 0.036 % carbon dioxide (CO_2) by volume as listed in Table 1.1. Gases which are found below 1 %, such as argon, carbon dioxide – including H_2O_2 and HCHO – are trace gases. Representing volume mixing ratios by the parts-per notation is more practical for those quantities (Table 1.2).

Table 1.1.: Tropospheric composition of dry air. Number concentrations (cm^{-3}) are given for standard conditions. Water vapour accounts for 15 000 ppmv or 3.7×10^{17} cm^{-3} (1.5 %).

Species Unit	Mixing ratio ppmv	Fraction %	Number concentration cm^{-3}
Nitrogen (N_2)	780 840	78	1.9×10^{19}
Oxygen (O_2)	209 460	21	5.2×10^{18}
Argon (Ar)	9 460	0.95	2.3×10^{17}
Carbon dioxide (CO_2)	320	0.0320	7.9×10^{15}
Methane (CH_4)	1.8	—	4.4×10^{13}
Carbon monoxide (CO)	0.1	—	2.5×10^{12}
Ozone (O_3)	0.03	—	7.4×10^{11}
Formaldehyde (HCHO)	0.0001 to 0.01	—	2.5×10^{9} to 2.4×10^{11}
Hydrogen peroxide (H_2O_2)	0.0001 to 0.005	—	2.5×10^{9} to 1.2×10^{11}

Table 1.2.: Units of (volume) mixing ratios as used in this thesis.

Percent	%	1 in 100	1×10^{-2}
Parts per million	ppmv	1 in 1×10^{6}	1×10^{-6}
Parts per billion	ppbv	1 in 1×10^{9}	1×10^{-9}
Parts per trillion	pptv	1 in 1×10^{12}	1×10^{-12}
Parts per quadrillion	ppqv	1 in 1×10^{15}	1×10^{-15}

1.2.2. Atmospheric spatial and temporal scales

Atmospheric gases undergo versatile physical and chemical change processes, the so-called geochemical cycles. Gas sources can be atmospheric chemistry, anthropogenic and biogenic emissions, volcanoes and radioactive decay. Possible removal processes are chemistry, biological activity, particle formation, deposition and uptake by the oceans and land masses. Since ambient mixing ratios are the result of differences between source and sink terms, the average atmospheric lifetime of a gas

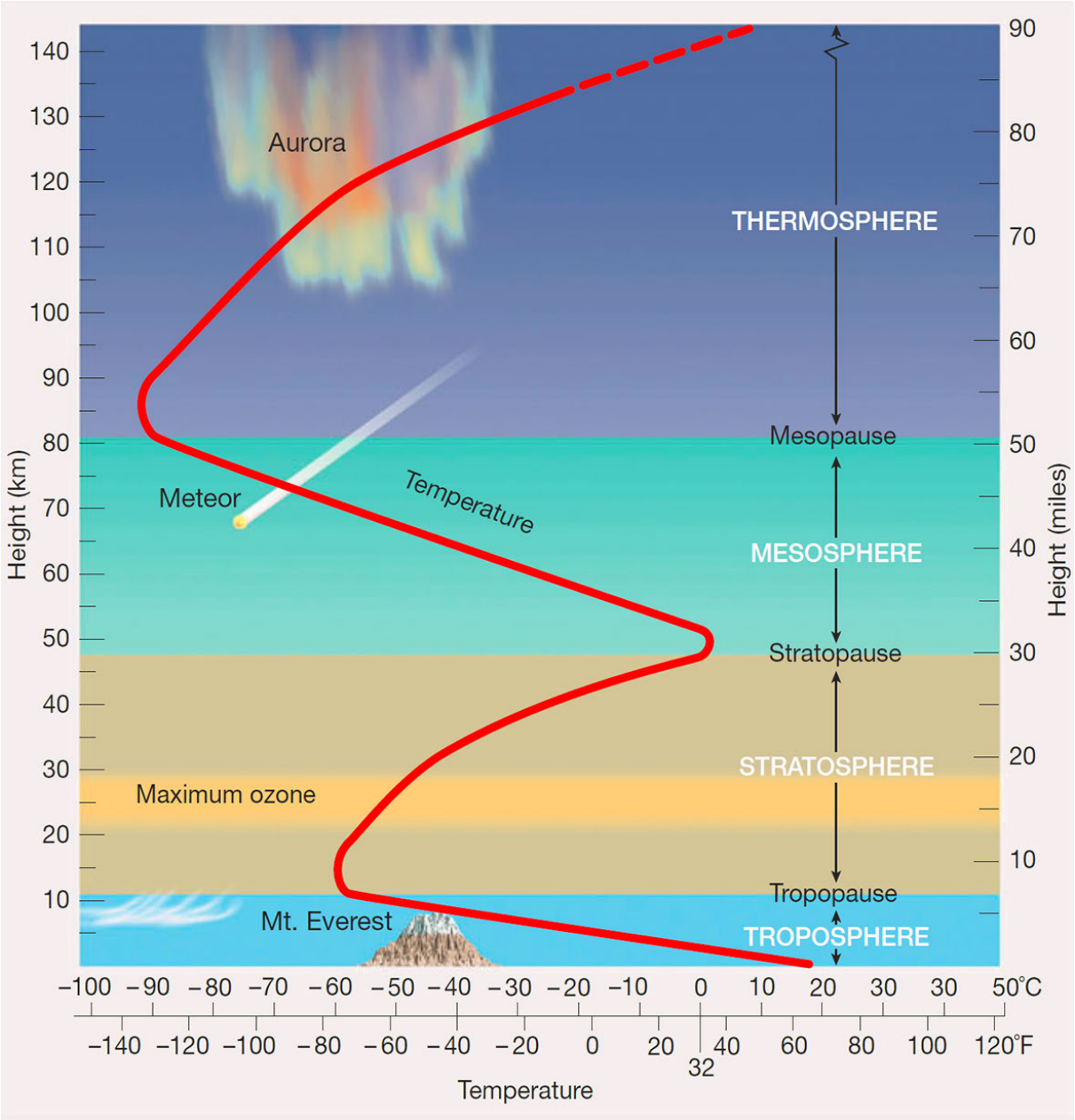

Figure 1.1.: Vertical structure of the atmosphere. Reprinted from Lutgens et al. (2013).

molecule (species) can range from seconds to millions of years. Including atmospheric dynamics (e. g., horizontal and vertical transport), a species can be distributed over certain ranges: microscale (0 to 100 m), mesoscale (tens to hundreds of km), synoptic scale (hundreds to thousands of km) and global scale (5000 km).

Figure 1.2 depicts the temporal and spatial relation of atmospheric species. Radical species (e. g., OH and HO_2) are short-lived (below 1 h) and move solely over hundreds of meters. Hydroperoxides and HCHO are moderately long lived species – that means their life times range from hours to days. Physical transport effects such as vertical motion within the boundary layer and advection up to hundreds of kilometers become relevant then and cannot be neglected. This group also includes atmospheric aerosols. Accompanied by CO, those can also undergo intra-hemispheric dispersion. Long-lived species, such as methane, nitrous oxide (N_2O) and CFCs, are able to move between the two hemispheres due to their life time ranging from one to hundreds of years.

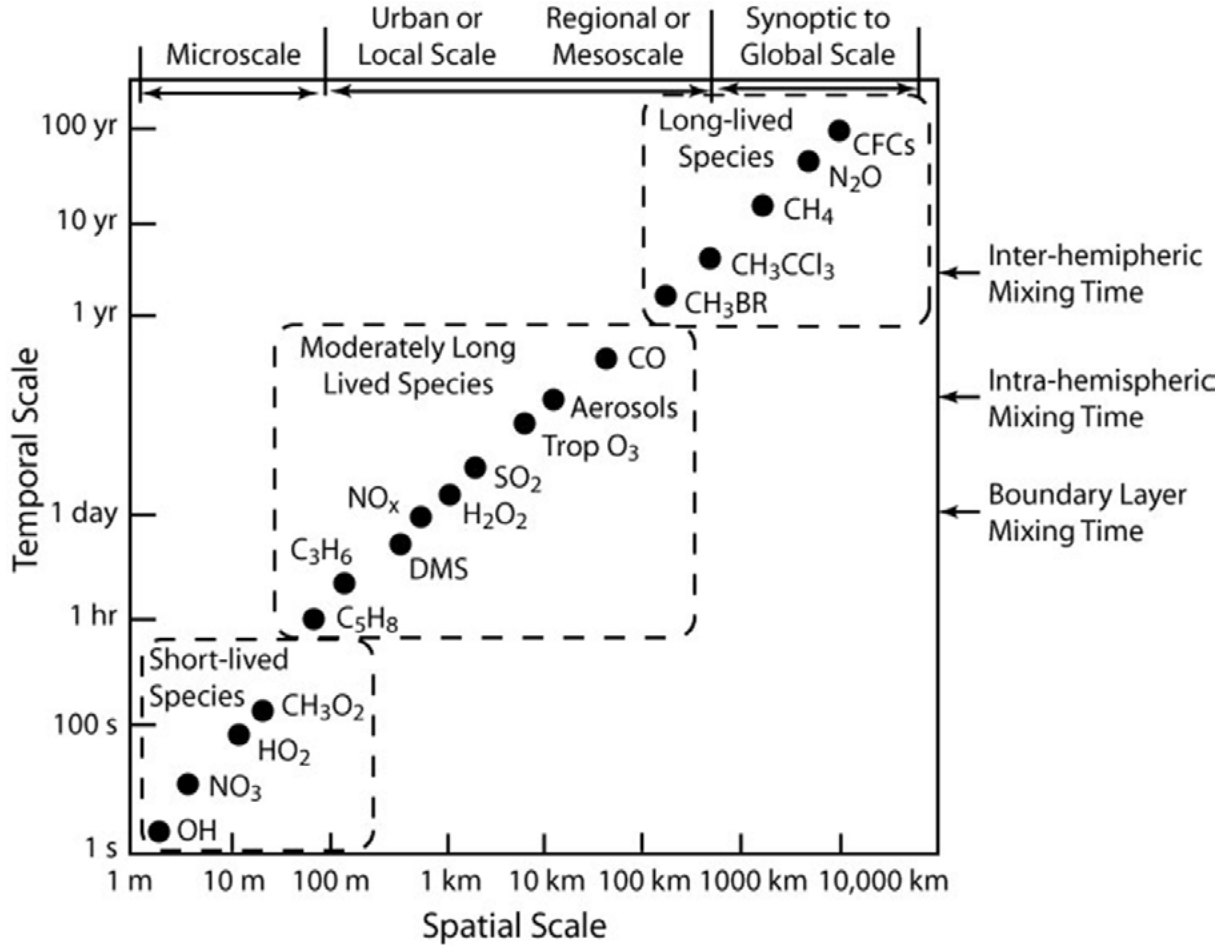

Figure 1.2.: Atmospheric spatial and temporal scales. Adapted from Seinfeld and Pandis (2006).

1.3. Vertical, latitudinal and seasonal trends of hydroperoxides and formaldehyde

Tropospheric hydroperoxides are found in ranges from approximately 0.01 to 20 ppbv (Lee et al., 2000) with a strong dependence on altitude, latitude and season. H_2O_2 and methyl hydroperoxide show maximum levels from 2 to 4 km, then decreasing with higher altitudes (Heikes et al., 1987). At ground level, deposition is the major sink causing mixing ratios below the maximum (Hall et al., 1999). H_2O_2 shows a negative trend with increasing latitude – from south to north (Heikes et al., 1987; Jacob and Klockow, 1992) – of approximately 0.04 to 0.05 ppbv per degree (van Valin et al., 1987). This was also observed for methyl hydroperoxide (Klippel et al., 2011). H_2O_2 shows annual peak mixing ratios in summer and a low in the winter for different chemical regimes and continents (e. g., Ayers et al., 1996; Fels and Junkermann, 1994; Serves, 1994; van Valin et al., 1987; Watanabe et al., 1996). The annual cycling also applies for organic hydroperoxides (Fels and Junkermann, 1994; O'Sullivan, 2004), while maximum levels of hydroxymethyl hydroperoxide (HMHP) were observed in May and methyl hydroperoxide in autumn (O'Sullivan, 2004).

Tropospheric levels of ambient HCHO range from approximately 0.05 ppbv to two-digit numbers (ppbv) (Carlier et al., 1986; Harder et al., 1997; Salthammer et al., 2010). The vertical distribution of HCHO shows a maximum at the surface, while the levels decrease with increasing height (Arlander et al., 1995; Heikes et al., 2001; Snow et al., 2007). Note that convection may cause a further

increase in the free troposphere (Fried et al., 2008; Heikes et al., 2001; Stickler et al., 2006). Surface HCHO is formed in many oxidation processes of emitted VOCs from bio- and anthropogenic sources (Carlier et al., 1986). Biomass burning also injects carbonyl species into the troposphere (Lee et al., 1997), just as traffic (Viskari, 2000). However, dry deposition is a major physical sink. HCHO – as hydroperoxides – shows a latitudinal variation: ambient mixing ratios decrease from the tropics to the poles (Arlander et al., 1995; Fried, 2003; Weller et al., 2000). Besides, it undergoes an annual cycling with a maximum in summer and a minimum in the winter for continental (Tanner and Meng, 1984) and marine (Zhou et al., 1996) conditions.

1.4. Sources and sinks of hydroperoxides and formaldehyde in the troposphere

As discussed before, trace chemical species undergo large temporal and spatial variations in Earth's oxidising atmosphere. For understanding the source and sink processes of hydroperoxides and HCHO, the key pathways will be shown here as simply as possible: starting with the simplest scenario – the marine boundary layer excluding halogen chemistry – then, adding nitric oxides (NO_x) and more complex volatile organic compounds. First, a set of common definitions is provided below.

Definition of the terms "source," "sink," and "budget." Sources are divided into two major categories: primary and secondary. Direct emissions of anthropogenic and biogenic compounds are primary, while secondary deem a production through atmospheric chemistry. Sinks, however, are classified into deposition and photochemistry. Deposition can be both, wet and dry physical loss processes. Photochemistry means loss processes and chemical conversion through photolysis and oxidation, respectively. Budget calculations employ sources and sink terms. If the balance of a species lies more on the source side, ambient mixing ratios will increase, otherwise they decrease. For budget considerations, physical transport through advection or convection has to be considered (continuity equation).

Definition of atmospheric lifetime. Atmospheric lifetime (τ) is the average time that a molecule remains in the atmosphere before it is chemically or physically removed. Lifetimes range from several seconds (e. g., OH) to a few years (CH_4) and even more. Sometimes the term is used to define the time it takes for an emitted trace chemical species to return to natural ("background") concentrations. The global lifetime is defined as the atmospheric burden (total density) divided by the integrated loss rate of a chemical species.

Principles of radical chemistry. Atoms or molecules with at least one unpaired electron are known as free radicals. They are highly chemically active with short lifetimes. However, they are reasonably stable under certain conditions, such as low concentrations in inert media or low temperatures. Radical chemistry is characterized by typical chain reactions including the following three major steps:

1. Initiation (e. g., $O_3 + h\nu \longrightarrow O(^1D) + O_2(^1\Delta_g)$),
2. Propagation (e. g., $CH_4 + OH \longrightarrow CH_3 + H_2O$),
3. Termination (e. g., $HO_2 + HO_2 \longrightarrow H_2O_2 + O_2$).

In atmospheric chemistry, photolysis is the most relevant initiation step leading to net radical formation from closed shell molecules (or atoms). The chain propagates through the collision of the radical with another closed shell molecule (or atom). This step is characterised by no change in the number of free radicals. Radicals can recombine under net destruction and form a closed shell molecule (chain termination).

1.4.1. Photochemistry of the background atmosphere

A closer look at the marine boundary layer (MBL) is the best approach for understanding key chemical processes of the background atmosphere (Figure 1.3). Here, the "natural" background of trace gases consists of methane (CH_4), carbon monoxide (CO) and ozone (O_3), free radicals from photochemistry and hydroperoxides with HCHO as chain terminations. For simplicity, nitric oxides (NO_x) and halogen chemistry will be totally omitted.

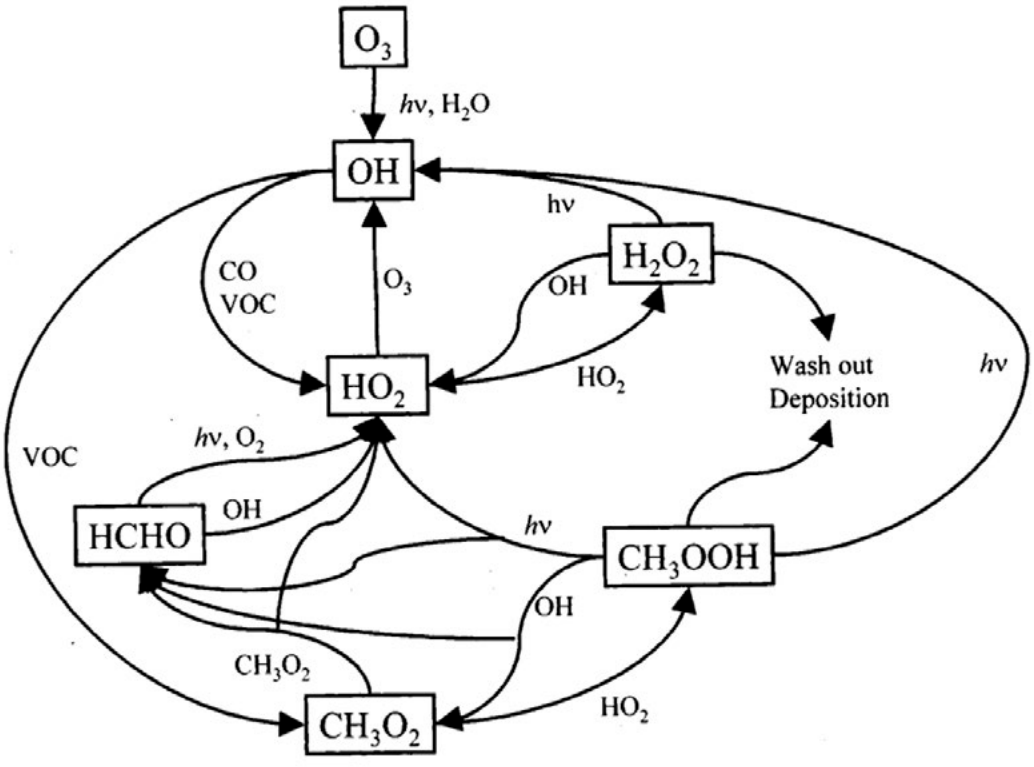

Figure 1.3.: NO_x independent chemical pathways of the background atmosphere. Note that the scheme includes only methane chemistry. Reprinted from Reeves and Penkett (2003).

Production of hydroxyl radicals (OH). Oxidation chemistry is hereby initiated by hydroxyl radicals (OH) which are formed via the photolysis of ozone (Levy, 1971) in the presence of water vapour. Hereby, ozone undergoes vertical transport from the free troposphere into the marine boundary layer (entrainment, Ayers et al., 1997). The produced $O(^1D)$ in Equation 1.1 can be deactivated by

collisions with N_2 and O_2 (both % level). In the marine boundary layer about 10 % of the $O(^1D)$ form OH (Fischer et al., 2003).

$$O_3 + h\nu \xrightarrow{\lambda < 340\,nm} O(^1D) + O_2(^1\Delta_g) \tag{1.1}$$

$$O(^1D) + H_2O \xrightarrow{fast} 2\,OH \tag{1.2}$$

$$O(^1D) + M \xrightarrow{slow} O(^3P) \tag{1.3}$$

The hydroxyl radicals then react with CO (70 ppbv) yielding hydroperoxy radicals (HO_2). Analogously, the reaction with methane (CH_4, 1.7 ppmv) leads to methyl peroxy radicals (CH_3O_2) in a much slower reaction. Due to their abundancy, CO and methane are the most important sinks for hydroxyl radicals on a global scale (Lelieveld, 2002; Logan et al., 1981; Thompson, 1992).

$$OH + CO + O_2 \xrightarrow{faster} HO_2 + CO_2 \tag{1.4}$$

$$OH + CH_4 + O_2 \xrightarrow{slower} CH_3O_2 + H_2O \tag{1.5}$$

Sources of hydroperoxides and formaldehyde. The newly formed HO_2 can react with O_3 (Equation 1.6). Under background conditions, HO_2 has a lifetime of $\tau_{O_3}^{HO_2} \approx 17$ min. Note that this pathway and Equation 1.7 lead to catalytic net ozone destruction in the MBL.

$$HO_2 + O_3 \longrightarrow OH + 2\,O_2 \tag{1.6}$$

$$OH + O_3 \longrightarrow HO_2 + O_2 \tag{1.7}$$

Even though the peroxide channel is less favoured ($\tau_{HO_2}^{HO_2} \approx 53$ min), the recombination of HO_2 forms a significant amount of H_2O_2. Water vapour increases hereby the yield of H_2O_2.

$$HO_2 + HO_2 \xrightarrow{H_2O} H_2O_2 + O_2 \tag{1.8}$$

Methyl peroxy radicals from Equation 1.5 react analogously ($\tau_{HO_2}^{CH_3O_2} \approx 18$ min) and form methyl hydroperoxide (MHP).

$$CH_3O_2 + HO_2 \longrightarrow CH_3OOH + O_2 \tag{1.9}$$

However, for most recombination reactions there is more than one pathway. A rather insignificant branch (Equation 1.10, $\tau_{HO_2}^{CH_3O_2} \approx 2.7$ h) directly produces HCHO following Equation 1.11, even though methoxy radicals react rapidly with ambient O_2 yielding HCHO and HO_2.

$$CH_3O_2 + HO_2 \longrightarrow HCHO + O_2 + H_2O \tag{1.10}$$

$$CH_3O_2 + CH_3O_2 \longrightarrow 2\,CH_3O + O_2 \tag{1.11}$$

$$CH_3O + O_2 \xrightarrow{fast} HCHO + HO_2 \tag{1.12}$$

Photochemical sinks of hydroperoxides and formaldehyde. H_2O_2 and organic hydroperoxides are photolysed (Table 1.3) recycling OH (Equation 1.13) and forming RO (Equation 1.14), respec-

tively. Thus, they are also called "reservoir species" for HO_x and RO_x. Especially the methoxy radical (CH_3O) is a significant source of HCHO in the MBL (via Equation 1.12).

$$H_2O_2 + h\nu \longrightarrow 2\,OH \tag{1.13}$$

$$CH_3OOH + h\nu \longrightarrow CH_3O + OH \tag{1.14}$$

Another major sink of hydroperoxides is the reaction with hydroxyl radicals, which basically recycles HO_2 and RO_2. However, most organic hydroperoxides react via either two pathways, here for example methyl hydroperoxide forming CH_2OOH in one branch (Equation 1.17).

$$H_2O_2 + OH \longrightarrow HO_2 + H_2O \tag{1.15}$$

$$CH_3OOH + OH \longrightarrow 0.7\ CH_3O_2 + 0.3\ OH + 0.3\ HCHO \tag{1.16}$$

$$\longrightarrow CH_2OOH + H_2O \tag{1.17}$$

Analogously to hydroperoxides, HCHO undergoes photolysis through two channels (Table 1.3): the "radical" (Equation 1.18) and the "molecular" (Equation 1.19).

$$HCHO + h\nu \xrightarrow{\lambda < 330\,nm} H + HCO \tag{1.18}$$

$$HCHO + h\nu \xrightarrow{\lambda < 330\,nm} H_2 + CO \tag{1.19}$$

While photolysis accounts for ca. 45 % of the total photochemical HCHO loss, another significant sink, the reaction with OH, causes 55 %.

$$HCHO + OH \longrightarrow HCO + H_2O \tag{1.20}$$

The intermediates H and HCO instantaneously produce HO_2 via the reaction with molecular oxygen. Thus, HCHO is an additional source of HO_2.

$$H + O_2 \xrightarrow{fast} HO_2 \tag{1.21}$$

$$HCO + O_2 \xrightarrow{fast} HO_2 + CO \tag{1.22}$$

Deposition of hydroperoxides and formaldehyde. As discussed before, the formation of hydroperoxides and HCHO does not necessarily lead to radical chain terminations since photolysis and the reaction with OH recycle HO_x and RO_x. On the contrary, deposition is able to permanently cleanse these species from the atmosphere. It is an important physical sink process responsible for the removal of trace gas species to a wet or dry surface. In more detail, wet deposition means "washout" by rain and fog droplets or wet aerosols while dry deposition is the transfer by air motions to the surface. Especially hydroperoxides show high variety in the individual solubilities, thus washout and adsorption are expected to be dominant loss processes (Gunz and Hoffmann, 1990; O'Sullivan et al., 1999; Watkins et al., 1995a).

1.4.2. The influence of nitric oxides (NO_x) and non-methane hydrocarbons (NMHCs)

In contrast to background conditions, the polluted atmosphere contains nitric oxides (NO_x = NO_2 + NO) and versatile VOCs. These include all organic compounds present in the gas phase, while the so-called non-methane hydrocarbons (NMHCs, here $R-CH_2-H$) exclude methane and partially oxidised organic species.

The oxidation of alkanes by OH. Equation 1.5 has already shown the oxidation of methane via hydroxyl radicals which is essential for its removal from the atmosphere. Hence, the initiative step of NMHC oxidation via OH forms an intermediate $R-CH_2$ radical (Atkinson, 1997; Atkinson and Arey, 2003a) which instantaneously reacts with molecular oxygen yielding a peroxy radical ($R-CH_2O_2$).

$$OH + R{-}CH_2{-}H \longrightarrow R{-}CH_2 + H_2O \tag{1.23}$$

$$R{-}CH_2 + O_2 \xrightarrow{M} R{-}CH_2O_2 \tag{1.24}$$

This recombines predominantly with HO_2 or another peroxy radical yielding H_2O_2 (Equation 1.8) and higher organic hydroperoxide ($R-CH_2OOH$, compare to Equation 1.9), respectively.

$$R{-}CH_2O_2 + HO_2 \longrightarrow R{-}CH_2OOH + OH \tag{1.25}$$

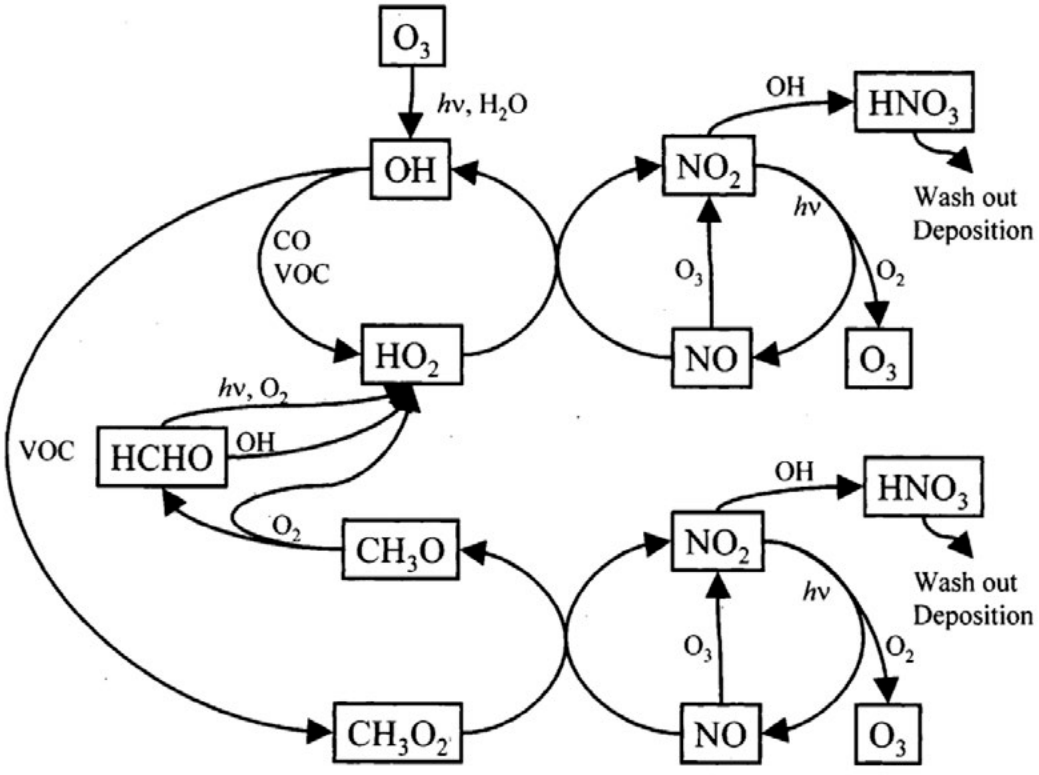

Figure 1.4.: NO_x dependent chemical pathways of polluted atmosphere. Reprinted from Reeves and Penkett (2003).

The role of nitric oxide (NO). Under polluted conditions (high NO_x), peroxy radicals predominantly oxidise NO to NO_2 so hydroperoxide formation is suppressed (Figure 1.4). So nitric oxide plays a crucial role recycling OH (Equation 1.26). Organic peroxy radicals, such as CH_3O_2 (Equation 1.27) and $R-CH_2O_2$ (Equation 1.28), where R is any organic rest, react differently: HCHO or any aldehyde can be formed in a fast reaction involving intermediate alkoxy radicals ($R-CH_2O$). This case results in a shortened organic peroxy radical ($R^{'}O_2$).

$$HO_2 + NO \longrightarrow NO_2 + OH \tag{1.26}$$

$$CH_3O_2 + NO \xrightarrow{+O_2} NO_2 + HCHO + HO_2 \tag{1.27}$$

$$R{-}CH_2O_2 + NO \xrightarrow{+O_2} NO_2 + \text{aldehyde} + R'O_2 \tag{1.28}$$

The reaction with OH (Equation 1.29) is a significant daytime sink for NO_2, yielding nitric acid (HNO_3), which shows deposition rates comparable to H_2O_2. In addition, the equilibrium in Equation 1.30 leads to peroxyacetyl nitrate (PAN) for example. As a reservoir species, it can act in both ways, as source and sink of NO_2 (Singh et al., 1992). The analogous reaction with HO_2 (Equation 1.31) is practically unimportant in the troposphere since $k_{1.26}$ is 2 times higher.

$$OH + NO_2 \longrightarrow HNO_3 \tag{1.29}$$

$$CH_3C(O)O_2 + NO_2 \overset{M}{\rightleftharpoons} CH_3C(O)O_2NO_2 \tag{1.30}$$

$$HO_2 + NO_2 \xrightarrow{M} HNO_4 \tag{1.31}$$

Net source of ozone (O_3). The photolysis of NO_2 (Table 1.3) leads to the formation of O_3. Note that peroxy radicals play a crucial role in producing net ozone, since the reaction of O_3 with NO ($O_3 + NO \longrightarrow O_2 + NO_2$) yields a null cycle.

$$NO_2 + h\nu \xrightarrow{\lambda < 420\,nm} NO + O(^3P) \tag{1.32}$$

$$O(^3P) + O_2 \xrightarrow{M} O_3 \tag{1.33}$$

As a result, ozone production and destruction is a non-linear process which depends on the amount of peroxy radicals (and thus VOCs) and NO_x.

The oxidation of alkenes by OH. Isoprene plays an important role for this thesis. Here, the oxidation of C-C double bonds is further discussed as shown in the following scheme (Figure 1.5). In the first initiative step, OH adds to the 1 and 4 positions and yields two allylic 1-hydroxy-2-alkyl radicals (Atkinson, 1997; Atkinson and Arey, 2003a; Paulson et al., 1992) which instantaneously react with molecular oxygen (not shown in the scheme). In the presence of NO two hydroxyalkoxy radicals and NO_2 are formed. One branch decomposes to methacrolein (MACR, $CH_3C(O)CH=CH_2$) and HCHO plus HO_2. The isomerization pathway yields two hydroxycarbonyls ($HC(O)C(CH_3)=CHCH_2OH$ and $HOCH_2C(CH_3)=CHCHO$) as well as two HO_2 radicals. Note that three HO_2 radicals are potentially produced per isoprene molecule under NO-rich conditions.

Table 1.3.: Photolysis reactions, rates and life time of selected species. Tropospheric photolysis reactions (Atkinson et al., 2004) and photolysis rates (Jacobson, 2005) were modeled for an unpolluted atmosphere (solar zenith angle of 0°, surface albedo of 0.03).

Photolysis reaction	Wavelengths / nm	Photolysis rate $/s^{-1}$	Life time $\tau_{h\nu}$
$O_3 + h\nu \longrightarrow O(^1D) + O_2^*$	< 325	5.1×10^{-5}	5.4 h
$CH_3CHO + h\nu \longrightarrow CH_3 + HCO$	< 335	6.4×10^{-6}	1.8 d
$HCHO + h\nu \longrightarrow H + HCO$[a]	< 340	3.3×10^{-5}	8.4 h
$CH_3OOH + h\nu \longrightarrow CH_3O + OH$	< 350	5.7×10^{-6}	2.0 d
$H_2O_2 + h\nu \longrightarrow 2\,OH$	< 350	7.7×10^{-6}	1.5 d
$HCHO + h\nu \longrightarrow H_2 + CO$[b]	< 360	4.4×10^{-5}	6.3 h
$HONO + h\nu \longrightarrow OH + NO$	< 400	1.9×10^{-3}	8.8 min
$NO_2 + h\nu \longrightarrow NO + O(^3P)$	< 420	8.8×10^{-3}	1.9 min

[a] Radical channel.

[b] Molecular channel.

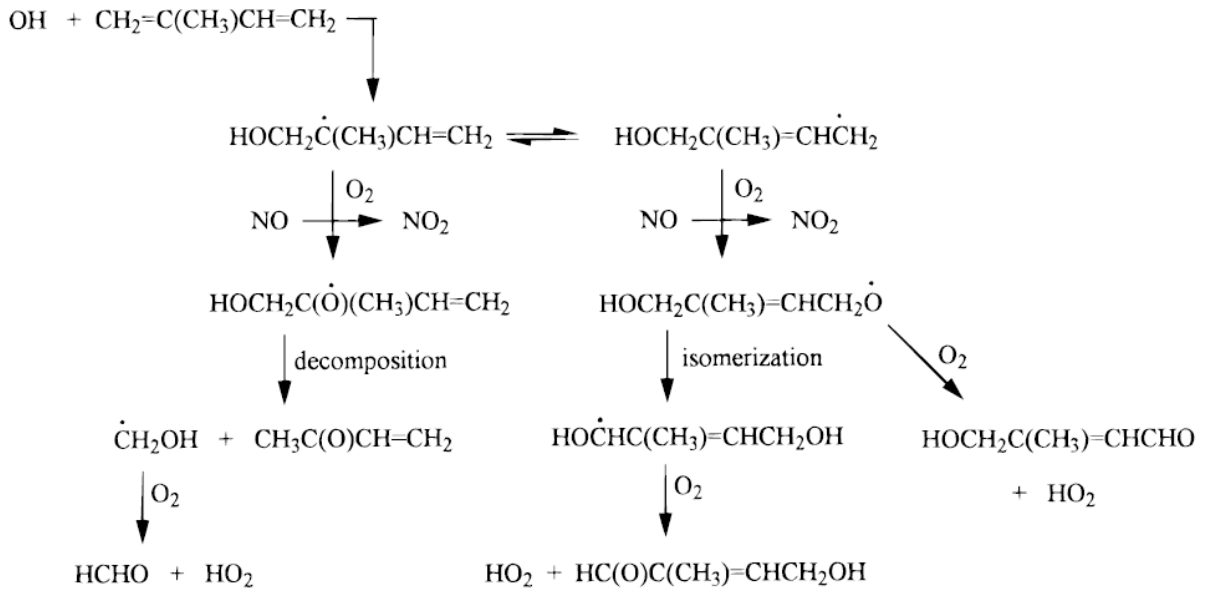

Figure 1.5.: Isoprene oxidation by OH radicals. Reprinted from Atkinson and Arey (2003a).

Ozonolysis of alkenes. The oxidation of alkenes by ozone is an important removal process (Niki et al., 1987). Especially isoprene and monoterpenes (Figure 1.6) are key VOCs of this work. The oxidation process is initiated by addition of ozone to the double bond, which forms the primary ozonide. It decomposes to an excited Criegee intermediate (or bi-radical): $R\dot{C}H_2O\dot{O}^*$ and an aldehyde (e. g., HCHO). Now $R\dot{C}H_2O\dot{O}^*$ either decomposes directly to other products (OH, acids, etc.) or an excited hydroperoxide (hydroperoxide channel). On the other hand, the stabilised Criegee bi-radical can react with water vapour to an α-hydroxy hydroperoxide or add to an aldehyde yielding a secondary ozonide. However, that shows that HCHO, H_2O_2 and organic hydroperoxides are formed depending on the corresponding alkene.

$$\text{Alkene} + O_3 \xrightarrow{H_2O} \alpha\,\text{HCHO} + \beta\,H_2O_2 + \text{products} \tag{1.34}$$

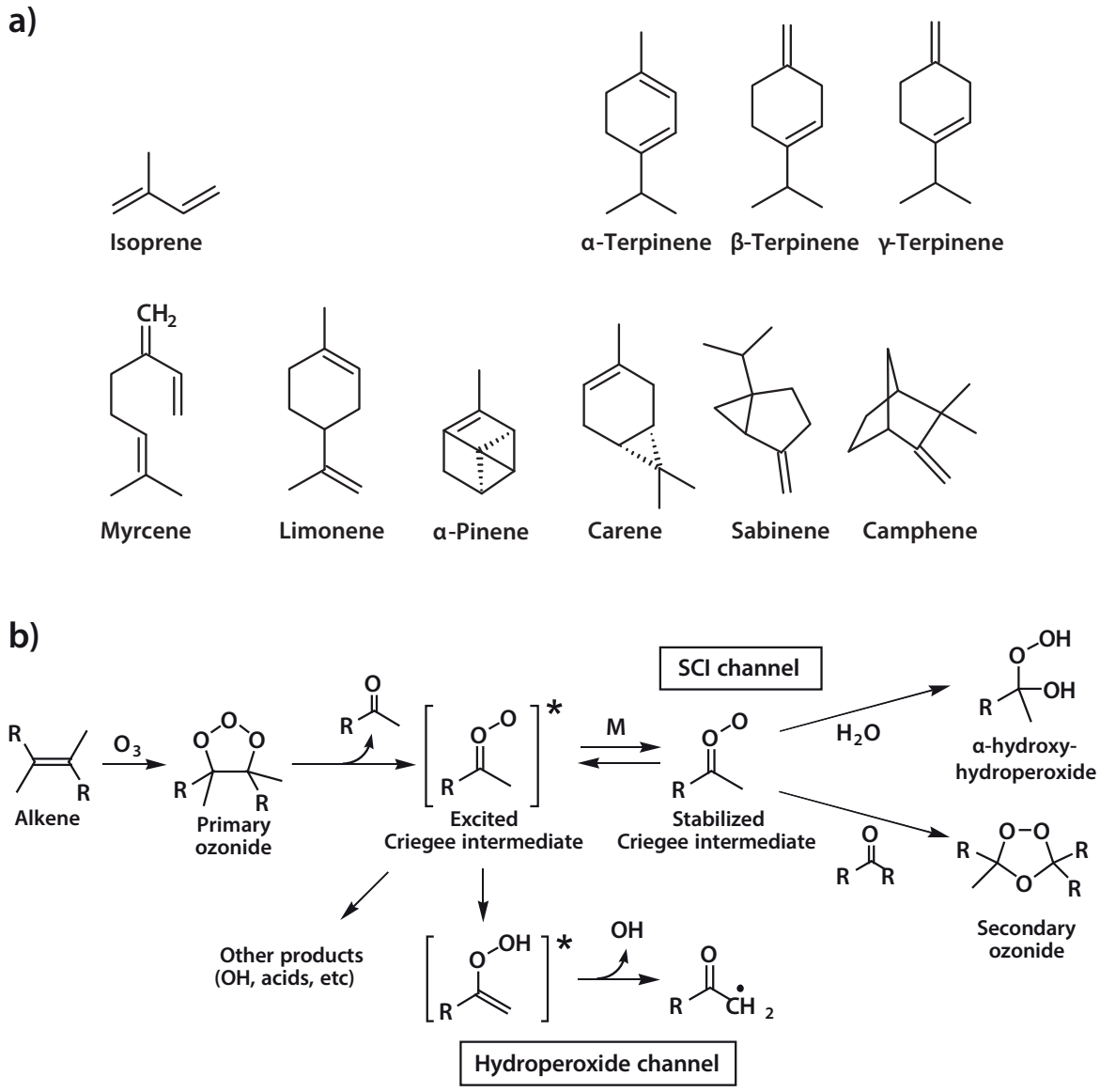

Figure 1.6.: Atmospheric relevant terpenes and ozonolysis of alkenes. Isoprene and some typical monoterpenes (**a**). Oxidation scheme for the ozonolysis of alkenes (**b**). Adapted from Kroll and Seinfeld (2008).

Other reactions. The oxidation of aliphatic alcohols, such as methanol, by OH radicals also plays an important role in the atmosphere. The initiative step is the abstraction of a hydrogen atom forming two species: hydroxymethyl (CH_2OH, 85 %) and methoxy (CH_3O, 15 %) radicals, respectively.

$$OH + CH_3OH \longrightarrow CH_2OH + H_2O \tag{1.35}$$

$$OH + CH_3OH \longrightarrow CH_3O + H_2O \tag{1.36}$$

Those instantaneously react with oxygen to form HCHO and HO_2. Note that hydroperoxy radicals recycle OH via the reaction with NO.

$$CH_2OH + O_2 \xrightarrow{M} HCHO + HO_2 \tag{1.37}$$

$$CH_3O + O_2 \xrightarrow{M} HCHO + HO_2$$

In addition, the presence of NO can lead directly to the production of 1,2-hydroxyalkoxy radicals and OH plus an aldehyde. Besides, the photolysis of acetaldehyde (CH_3CHO) and its oxidation by OH radicals also plays an important role for the budget of HCHO (Atkinson and Arey, 2003a). The first step yields an acetyl radical (CH_3CO) which then reacts with oxygen and forms the acetyloxyl radical (CH_3CO_2). After reacting with NO, it decomposes fast into HCHO, carbon dioxide (CO_2) and NO_2.

$$CH_3CHO + OH \longrightarrow CH_3CO + H_2O \tag{1.38}$$

$$CH_3CO + O_2 \xrightarrow{M} CH_3CO_2 \tag{1.39}$$

$$CH_3CO_2 + NO \longrightarrow HCHO + NO_2 + CO_2 \tag{1.40}$$

1.4.3. The link to aerosols

Atmospheric aerosols are suspended liquid or solid particles in air. They have a high impact on Earth's radiation budget (scattering and absorption of sunlight) and are relevant loci for chemical reactions (heterogeneous chemistry). However, the key role of aerosols is the formation of clouds: once they reach a certain size, aerosols can become cloud condensation nuclei (CCNs). Depending on the source, aerosols are classified into primary and secondary particles. Primary particles are directly emitted from sources such as biomass burning, combustion of fossil fuels, volcanic eruptions, wind-driven suspension of soil, mineral dust, sea salt and biological materials. Secondary particles are formed by processes such as nucleation, condensation, heterogeneous and multiphase chemistry. In particular, secondary organic aerosols (SOAs) are produced through heterogeneous chemistry of anthropogenic and biogenic VOCs. That involves H_2O_2, organic hydroperoxides (especially HMHP and MHP) and to some extent aldehydes, such as HCHO (Hallquist et al., 2009; Hua et al., 2008b).

Sources of secondary organic aerosols. As shown before, the gas-phase oxidation of VOCs is initiated by OH radicals, O_3, NO_3 radicals (during night-time) or via direct photolysis. Particularly in case of terpenes the degradation occurs predominantly by an addition mechanism introducing multiple polar functional groups. As a consequence, the products are less volatile and more water soluble (Kroll and Seinfeld, 2008). The change of volatility is complex and includes several processes over several cycles: (i) oxidation in the gas phase, (ii) reactions in the particle phase and (iii) multiphase chemistry. However, the water-soluble organic compounds contribute to the formation of SOA and are anti-correlated to H_2O_2 and organic hydroperoxides, especially HMHP and MHP (Hua et al., 2008b). That fact is rather new and completes the classic picture of H_2O_2 as an aqueous phase oxidant of SO_2 leading to sulfate aerosols (Finlayson-Pitts and Pitts, 1986; Penkett et al., 1979).

$$SO_2 + H_2O \rightleftharpoons HSO_3^- + H^+ \tag{1.41}$$

$$H_2O_2 + HSO_3^- \longrightarrow HSO_4^- + H_2O \tag{1.42}$$

1.4.4. Night-time chemistry

Since this work focuses on daytime chemistry, night-time sources of hydroperoxides and HCHO will be only briefly reviewed just for completeness. However, understanding the processes is essential for understanding diurnal profiles (Section 1.4.5).

Sources and sinks of NO_3 radicals. The nitrate radical (NO_3) is the most important night-time oxidant formed via the reaction of NO_2 and O_3 (Monks, 2005).

$$NO_2 + O_3 \xrightarrow{\text{slow}} NO_3 + O_2 \tag{1.43}$$

The recombination with NO_2 forms dinitrogen pentoxide (N_2O_5), which can react with water vapour yielding two nitric acid molecules (HNO_3). Those equilibrium reactions are important night-time sinks for NO_3 and thus for NO_x.

$$NO_3 + NO_2 \overset{M}{\rightleftharpoons} N_2O_5 \tag{1.44}$$

$$N_2O_5 + H_2O \rightleftharpoons 2\,HNO_3 \tag{1.45}$$

However, during daytime, NO_3 is not existent due to the following three reactions:

$$NO_3 + h\nu \longrightarrow NO + O_2 \tag{1.46}$$

$$NO_3 + h\nu \longrightarrow NO_2 + O(^3P) \tag{1.47}$$

$$NO_3 + NO \longrightarrow 2\,NO_2 \tag{1.48}$$

General scheme for the oxidation of alkanes by NO_3 radicals. NO_3 is less reactive with alkanes in comparison to OH. As for the oxidation with OH, the H-atom abstraction by NO_3 is an initiative step forming alkyl radicals (R). As previously discussed, those instantaneously react with molecular oxygen yielding organic peroxy radicals. The consecutive reaction with another NO_3 forms alkoxy radicals (and NO_2), which form, analogously to the daytime reaction, aldehydes and HO_2. This night-time HO_2 is depleted either by O_3 or by NO_3 radicals. Those reactions are expected to be the sole night-time sources of OH.

$$NO_3 + \text{organic compound} \longrightarrow RO_2 + \text{products} \tag{1.49}$$

$$R + O_2 \xrightarrow{M} RO_2 \tag{1.50}$$

$$RO_2 + NO_3 \longrightarrow RO + NO_2 + O_2 \tag{1.51}$$

$$RO + O_2 \longrightarrow \text{aldehyde} + HO_2 \tag{1.52}$$

$$HO_2 + O_3 \longrightarrow OH + 2\,O_2 \tag{1.53}$$

$$HO_2 + NO_3 \longrightarrow OH + NO + O_2 \tag{1.54}$$

Unlike the recycling of daytime OH radicals as a catalytic cycle for the oxidation of organic molecules, NO_3 is only an initiator: the higher the amount of reactive compounds, the more it is suppressed.

General scheme for the oxidation of alkenes. Analogously to the daytime oxidation of alkenes by OH radicals, the initiative step is the addition of NO_3 to the C=C double bond forming nitrooxyalkyl peroxy radicals. Those can either react with NO, NO_2, HO_2 and organic peroxy radicals. Product can be PANs, hydroperoxides, aldehydes (potentially HCHO) and alcohols. In addition, depending on the size of the initial organic molecule, second line radicals can be formed. Their isomerisation and decomposition, respectively, yields hydroperoxy radicals as by-products, which might be a night-time source of HO_2.

$$NO_3 + CH_3CH{=}CH_2 \xrightarrow{M} CH_2CHCH_2(ONO_2) \tag{1.55}$$

$$NO_3 + CH_3CH{=}CH_2 \xrightarrow{M} CH_2CH(ONO_2)CH_2 \tag{1.56}$$

1.4.5. Understanding diurnal profiles

After discussing basic tropospheric chemistry it is important to understand the influences of dynamics (atmospheric motion) and physical deposition on the ambient concentration of a photochemical species. As a matter of fact, many scientific results within this work are presented as diurnal profiles (time-series of mixing ratios for a day or as a mean of several days). Those imply information about photochemistry and effects coupled with the evolution of the planetary boundary layer (PBL).

The continuity equation as shown below describes the mixing ratio $[\mathrm{X}]$ of a chemical trace gas species X (e. g., ozone; note that the continuity equation is also applicable for hydroperoxides and HCHO) for infinitesimal time changes, including photochemical production $\mathrm{P(X)}$ and losses $\mathrm{L(X)}$, as well as other effects. Those comprise emissions, entrainment, deposition (expressed as the deposition velocity v_d), which depend on the height of the continental boundary layer H as well as advective and convective terms.

$$\frac{d\,[\mathrm{X}]}{d\,t} = \mathrm{P(X)} - \mathrm{L(X)} \pm \text{other} \approx 0 \tag{1.57}$$

Evolution of the planetary boundary layer (PBL). The height of the continental boundary layer H follows a diurnal cycle driven by solar radiation as shown in Figure 1.7. At sunrise, thermal heat flux increases H leading to convective fluctuations (boundary layer breakup). In case of ozone, which has higher mixing ratios in the free troposphere, that causes an injection effect into the PBL (entrainment). This is basically possible for H_2O_2 as well.

However, H reaches a maximum (1 to 2 km in mid-latitudes) by the early afternoon causing a well-mixed PBL, which is "capped" by an inversion layer. Note that H positively correlates with the mixing volume, which is relevant for calculating the "dilution" of emissions (e. g., industrial areas), even if the emission rates are constant.

By sunset, as the surface cools down, the boundary layer height deceases. This leads to the formation of a residual layer from the day and a nocturnal boundary layer. In mid-latitudes it measures several hundreds of meters at most. The low height plays an important role for physical deposition since the deposition velocity is directly dependent on H.

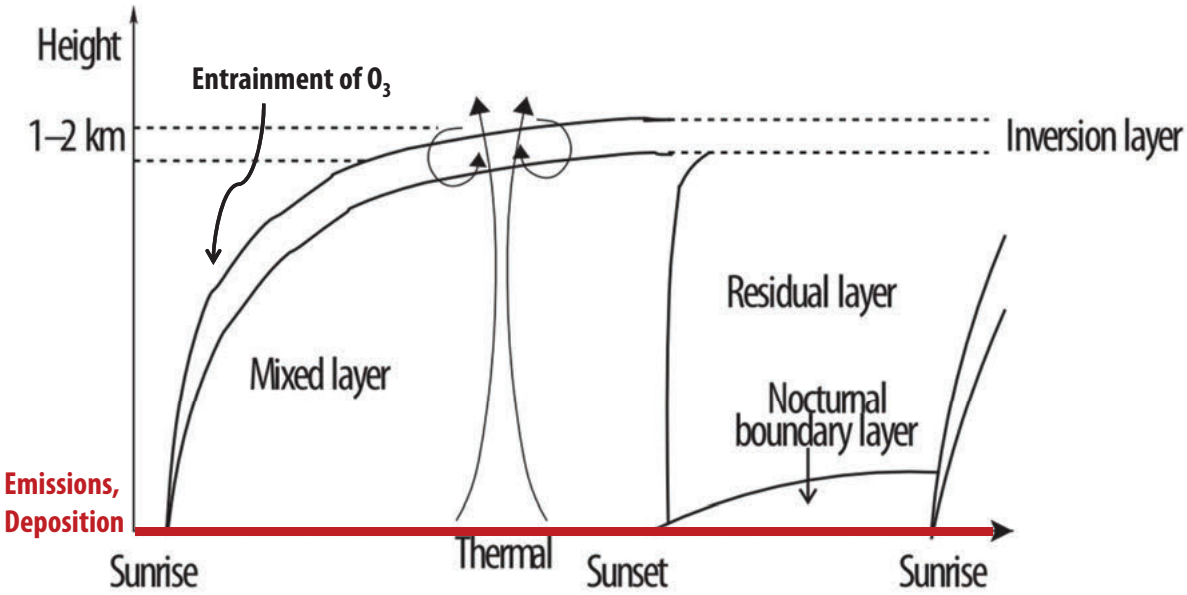

Figure 1.7.: Evolution of the planetary boundary layer. Adapted from Stull (1988).

Trends in diurnal profiles. Figure 1.8 shows how the combined effects of photochemistry and physics manifest themselves in three different diurnal profiles of O_3 (Ayers et al., 1992, 1996; Penkett et al., 1997). Although hydroperoxides and HCHO have other photochemical source and sink reactions as well as different deposition velocities, the following principles are comparable. Starting in the early morning with the injection of ozone-rich air from the free troposphere into the boundary layer (boundary layer breakup), three different scenarios are possible:

$P(O_3) > L(O_3)$: Production under high NO_x conditions. Photochemical production $P(O_3)$ adds to the background mixing ratio, while the losses $L(O_3)$ are insignificant. Ozone accumulates as long as deposition effects during the night are gaining significance.

$P(O_3) = L(O_3)$: Equilibrium. Photochemical production equals the loss rates leading to a constant mixing ratio.

$P(O_3) < L(O_3)$: Destruction under low NO_x conditions. Since significant photochemical production mechanisms are missing, sink reactions dominate (e. g., photolysis) during daytime and deposition during night-time. The mixing ratio reaches a minimum.

1.5. The importance of atmospheric modeling

A mathematical model (hereafter: model) performs simulations of highly complex, non-linear physical and chemical processes in the atmosphere. They allow "switching" on and off specific processes leading to a better qualitative and quantitative understanding of the response. Models can be classified by their dimensionality, such as box (0D) up to three-dimensional (3D). In a box model, mixing ratios of species are equally distributed and thus only a function of time. Three-dimensional models, however, simulate fields of mixing ratios depending on the (x, y, z)-coordinates and time on a global scale. The life times of atmospheric trace chemical species range over several orders of

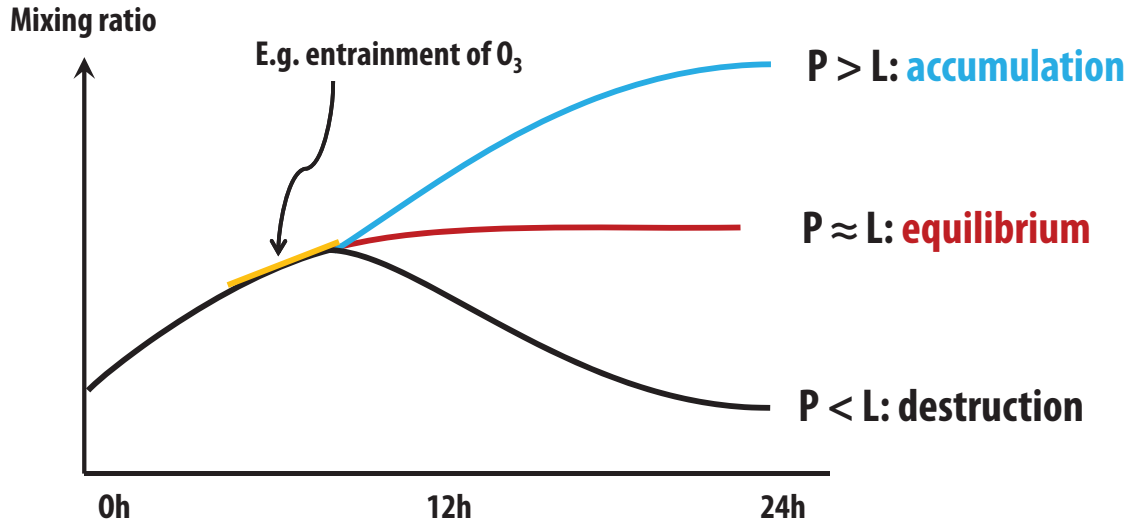

Figure 1.8.: Understanding diurnal profiles.

magnitudes and thus simple steady-state assumptions (as in box models) for long-lived species are questionable, where transport plays an important role. Depending on the scientific requirements such as studying emissions, dynamical and chemical transformations, 3D models are more suitable. However, all types of numerical models give trends and no proofs, thus permanent comparisons to in-situ observations lead to improvements in accuracy and performance. Nonetheless, that requires high-quality field measurements performed by reproducible and robust methods. Further, the kinetic rate coefficients used in the models are derived from laboratory studies including potential artifacts and uncertainties.

2. Materials and methods

2.1. Geographical context

This work is based on three field measurement campaigns in Europe: DOMINO in Spain (2008), HUMPPA in Finland (2010) and PARADE in Germany (2011). Figure 2.1 and the following paragraphs describe the geographical and temporal context.

DOMINO 2008. The DOMINO 2008 (Diel Oxidant Mechanisms in Relation to Nitrogen Oxides) field measurement campaign (Diesch et al., 2012) took place from Nov 20 to Dec 9, 2008 at the Spanish atmospheric research station "El Arenosillo" (37°50′ N, 6°44′ W, 40 m a. s. l.) operated by the INTA (National Institute for Aerospace Technology). The station is influenced by a coastal pine forest, approximately 400 m north, while the vicinity shows irregularly distributed trees (5 to 6 m height) on sandy ground. The Atlantic Ocean was located only 300 to 1000 m south of the measurement site. Although the station is located in a protected natural area, three different source regions influence the site: the Atlantic Ocean, the town of Huelva (20 km distance, population: 149 000) and the nearby National Park of Doñana. The Atlantic Ocean shows heavy ship traffic in the Strait of Gibraltar, Huelva is an industrialized town (oil refineries) as well as the highly populated Seville (70 km distance, population: 704 000). In addition, tourism activities at the Cádiz gulf coast are expected to be rather low due to off-season. Measurements were performed on a 10 m scaffold tower, resulting in 12 m inlet height.

HUMPPA 2010. The HUMPPA field measurement campaign was performed at the SMEAR II station (Station for Measuring Ecosystem-Atmosphere Relation) in Hyytiälä (61°51′ N, 24°18′ E, 181 m a. s. l.), Southern Finland from Jul 12 to Aug 12, 2010. Generally, SMEAR II is a background location, operated by the UHEL (University of Helsinki). The homogeneous boreal forests around Hyytiälä consist mainly of Scots pine and Norway spruce and show as well characteristics of a deciduous forest (Birch trees and woodland scrub: Willows, Aspen). Hyytiälä is located North-West from Helsinki (220 km distance, population: 605 000) and the nearest industrial city is Tampere (60 km distance, population: 220 000) in the North-East. Occasionally, SMEAR II is influenced by pollutant transport from those cities accompanied by local emissions from the station buildings (0.5 km distance). Trace gas species, in particular H_2O_2, HCHO, NO_x and CO were measured above the canopy on a tower (21 m height), with an inlet height about at 24 m.

PARADE 2011. The PARADE 2011 (Particles and Radicals: Diel Observations of the Impact of Urban and Biogenic Emissions) field measurement campaign was performed from Aug 15 to Sep 10, 2011 on the summit of the Mt. Kleiner Feldberg (50°13′ N, 8°26′ E, 825 m a. s. l.) at the "Taunus Observatory", which is operated by the Institute of Meteorology and Geophysics at the Johann Wolfgang Goethe University, Frankfurt am Main, Germany. The Taunus highlands range from southwest to northeast as a northern barrier of the Upper Rhine Valley. Mt. Kleiner Feldberg is located about 30 km northwest from Frankfurt am Main, within the heavily industrialized Rhine-Main region

(population: 2.5 million). In contrast, the area about 50 to 100 km to the north of Kleiner Feldberg is only lightly populated in comparison. The vicinity of the observatory is dominated by mixed forest which is crossed accompanied by smaller towns within a radius of 5 km. Besides the low frequented access road, a main road passes several hundred metres below the observatory, where road works were performed during the campaign period. Meteorological conditions and flow patterns are impacted by two other neighbouring mountains: the Großer Feldberg (878 m a. s. l.; 1.3 km NE of the Kleiner Feldberg) and the Altkönig (798 m a. s. l.; 2.7 km ESE). The measurement site is covered with low lying vegetation, such as grasses and bushes, with a few smaller trees. Higher conifers (15 to 20 m) surround the summit at a distance of approximately 30 m. Measurements were performed on a platform (8 m high), resulting in 10 m inlet height.

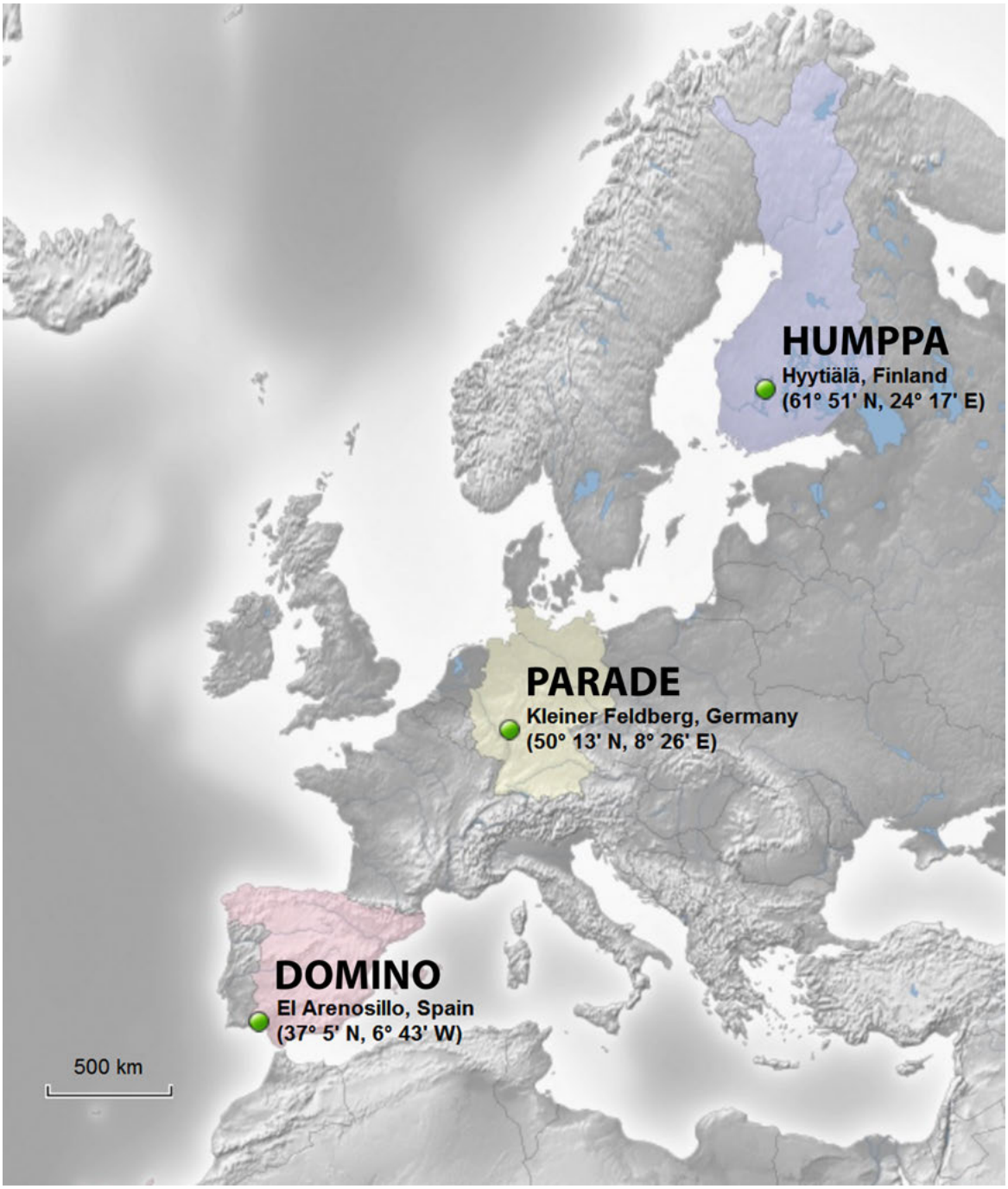

Figure 2.1.: Location map for DOMINO, HUMPPA and PARADE.

2.2. Experimental set-up

2.2.1. Hydrogen peroxide and formaldehyde measurements

This section focuses on H_2O_2 and HCHO measurement techniques addressing the following questions:

1. Instrument requirement specification.
2. Why were the herein presented methods used?
3. What is the instrumental performance?
4. What are the measuring ranges and limitations?

2.2.2. Instrument requirements

The quantification of H_2O_2 and HCHO plays an essential role for this work and implies the following requirements. First, the measurement technique shall be established in the atmospheric science community. This includes long-term experiences in the form of relevant technical and scientific publications for having a broad comparative data set. Secondly, the instrumental range should be linear and cover the atmospheric levels of hydroperoxide and HCHO (usually between the LOD to ca. 10 ppbv). In addition, the technique should provide time series via continuous in-situ measurements. That requires instrumental integration times (i) below the atmospheric life time of hydroperoxides and HCHO (e. g., 6 to 12 h) and (ii) below the time intervals for averaging specified for merged campaign data sets (e. g., 5 min). Continuous operation also allows minimizing artifacts related to storage/tube wall material, e. g., as caused by discontinuous cartridge techniques. In addition, a minimum of (spectroscopic) interferences with other absorbers, for example other aldehyde interfering with HCHO, is required for a selective quantification method.
Since an aircraft based application was envisaged, the two instruments shall be lightweight, small and low in power consumption. That fact is accompanied by easy transportation without a long process of re-adjustment for campaign operation. In the case of instrumental failure, simple and fast repair under field campaign conditions should be possible. Simple data retrieval and calculation from raw to final data also play an important role, especially for in-field data quality control. Low costs of procuring and for operating the instrument should not be neglected. The two wet-chemical commercial instruments, AL2021 and AL4021 (hydroperoxide and HCHO monitor), comply with these requirements as presented in the following sections.

Hydroperoxide measurement techniques. Many continuous and discontinuous methods for quantifying hydroperoxides were used before (Gunz and Hoffmann, 1990; Jackson and Hewitt, 1999; Lee et al., 2000; Sakugawa et al., 1990). Nevertheless, the following section focuses on techniques that allow to obtain in-situ time series of atmospheric mixing ratios in the gas-phase. Table 2.1 gives a comprehensive overview by listing the most important parameters, such as LOD and time resolution, sorted by technique and frequency of use. The majority of the established methods are based on wet chemical and chromatographic techniques either detecting fluorescence or chemiluminescence. The commercial AL2021 based on the dual-enzyme technique is the best compro-

mise concerning those parameters, handling properties and acquisition costs. Recently, new methods have been discussed, such as LED-Ti(IV) absorbance (Li and Dasgupta, 2003) and chemical ionization mass spectrometry (CIMS, Crounse et al. (2006)).

Table 2.1.: Brief summary of common wet chemical and spectroscopic techniques for gas-phase measurements of hydroperoxides. The methods are sorted according to relevance. LODs and time resolutions are listed as typical values only. Wet chemical methods comprise p-hydroxyphenylacetic acid (POPHA), bis-(2,4,6-trichlorophenyl)oxalate (TCPO), luminol, colorimetry (Ti(IV) and the reaction with the Fenton reagent (oxidation of Fe(II)). Tunable diode laser absorption spectroscopy (TDLAS) is hereby the only spectroscopic technique.

Method	Technique	Selective for	Detection limit	Time res.	Reference
Wet chemical methods					
POPHA	dual enzyme fluorescence	H_2O_2, ∑ROOH	< 0.1 ppbv	2 min	Lazrus et al. (1985, 1986)
HPLC-POPHA	post column derivatization	H_2O_2, ROOH	< 0.1 ppbv	30 min	Hellpointner and Gäb (1989)
TCPO	chemiluminescence	H_2O_2	—	—	Jacob et al. (1987)
Luminol	chemiluminescence	H_2O_2	0.5 ppbv	—	Kok et al. (1978b)
Colorimetry	nonenzymatic fluorescence	H_2O_2	< 0.1 ppbv	—	Kok et al. (1978a)
Fenton	chemiluminescence	H_2O_2	< 0.1 pptv	—	Lee et al. (1990)
Spectroscopic methods					
TDLAS		H_2O_2	< 0.3 ppbv	1 min	Slemr et al. (1986)

Formaldehyde measurement techniques. Since environmental control policies exert pressure to study ambient HCHO, new measurement techniques had to be developed. Comprehensive methodical overviews are given in the literature (Salthammer et al., 2010; Vairavamurthy et al., 1992). Table 2.2 contains LODs and time resolutions, sorted by technique and frequency of use. The majority of the established methods is based on wet chemical and chromatographic techniques. GC-MS is generally suitable for the quantification of aldehydes and ketones. However, for low ambient levels of HCHO, wet chemical methods including HPLC dominate, although they lead to higher maintenance costs. On the other side, higher ambient mixing ratios, for example in industrial plants, allow the use of automated techniques such as FTIR. The commercial AL4021 reaches the best compromise between performance, handling properties and acquisition costs.

The working principle of the wet chemical methods. Generally, the "internal" mixing ratio $\xi'(t)$ (ppbv) for a single channel can be expressed as a function of time t. It depends on the difference between the instantaneous photomultiplier (PMT) $U(t)$ (V) and the contiguous zero signal U_0 (V). The sensitivity S (V ppbv^{-1}) is hereby derived from the signal ΔU_{LS} and the mixing ratio μ_{LS} of the internal standard (further referred to as liquid standard), respectively:

$$\xi(t) = \underbrace{\frac{U(t) - U_0}{S}}_{\xi'(t)} \cdot \underbrace{\frac{1}{R}}_{\alpha \text{ and other effects}} \tag{2.1}$$

$$S = \frac{\Delta U_{LS}}{\mu_{LS}} \tag{2.2}$$

Table 2.2.: Brief summary of common wet chemical, chromatographic, spectroscopic and mass spectroscopic techniques for gas-phase measurements of HCHO. The methods are listed after relevance for ambient mixing ratios and continuous operation mode. LODs and time resolutions are given as typical values only. Common abbreviations: 2,4-dinitrophenylhydrazine (DNPH), gas chromatography coupled with mass spectrometry (GC-MS, Fourier transform infra red spectroscopy (FTIR), tunable diode laser absorption spectroscopy (TDLAS) and proton transfer reaction coupled with mass spectrometry (PTR-MS).

Method	Technique	Detection limit	Time resolution	Reference
Wet chemical methods				
Hantzsch reaction	derivatization	< 50 pptv	2 min	Kelly and Fortune (1994a)
Chromatographic methods				
HPLC-DNPH	post column derivatization	0.5 ppbv	120 min	Vairavamurthy et al. (1992)
GC-MS	GC coupled with MS	0.3 ppbv	15 min	Yokouchi et al. (1979)
Spectroscopic methods				
FTIR	infrared absorption	0.4 ppbv	5 min	Hak et al. (2005)
TDLAS	infrared absorption	< 50 pptv	1 min	Harris et al. (1992)
Mass spectroscopic methods				
PTR-MS	ionization with H_3O^+	low sensitivity	1 min	Lindinger and Jordan (1998)

The recovery R factor, however, plays a crucial role, since the instruments transfer ambient air samples to the liquid phase. Thus, the "real" gas-phase mixing ratio $\xi(t)$ depends on both: R and the stripping efficiency α. Those terms and principles will be subjects of discussion in the next sections.

2.2.3. The commercial Aero–Laser AL2021 hydroperoxide analyzer

2.2.3.1. Basic principle of the dual-enzyme method

The two-channel and dual-enzyme technique (Figure 2.2), respectively, allows a quantification of H_2O_2 and an estimation of bulk organic hydroperoxides (ROOH). Channel A measures the sum of all hydroperoxides while channel B quantifies bulk organic hydroperoxides by use of the catalase to selectively destroy H_2O_2 with the efficiency ϵ (Lazrus et al., 1985, 1986).

A $\sum$ [hydroperoxides]

B $\sum$ [hydroperoxides] − ϵ [hydrogen peroxide]

Figure 2.3 depicts the chemical reaction scheme. The sample molecules are stripped (Section 2.2.5) into a potassium hydrogen phthalate buffer (KHP), which contains HCHO and ethylenediaminetetraacetic acid (EDTA) to prevent interferences from sulfur dioxide (SO_2) and metal ions.
Consecutively, the liquid flow is divided into two glass reaction coils. For both, the fluorescent solution is added, which consists of the enzyme peroxidase and p-hydroxyphenylacetic acid (POPHA) in KHP buffer. The fast reaction yields equimolar fractions of the POPHA fluorescence dimer, 6,6'-dihydroxy-3,3'-biphenyldiacetic acid, with respect to the hydroperoxides. In one channel, the enzyme catalase is added to the fluorescent solution and H_2O_2 is selectively destroyed.

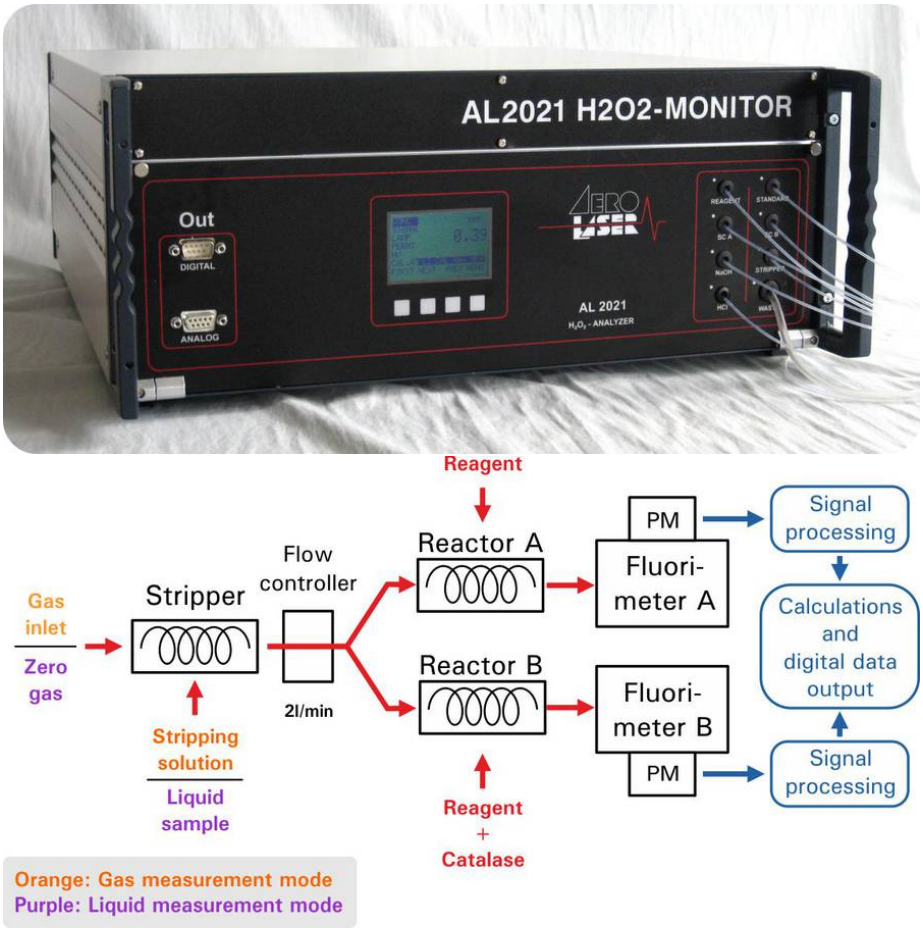

Figure 2.2.: The Aero-Laser 2021 hydroperoxide analyzer. Image (**a**) and flow chart of the two-channel online fluorescence technique (**b**). (Courtesy of Aero-Laser GmbH, Garmisch-Partenkirchen, Germany). The sum of gas-phase hydroperoxides are stripped into a potassium hydrogen phthalate KHP buffer via a glass stripping coil. A phase separator divides the liquid flow stream from the gas phase and splits it into two channels A (total hydroperoxides) and B (total hydroperoxides except H_2O_2). In both reactors peroxidase/POPHA is added, while channel B also uses catalase, which decomposes H_2O_2 specifically. Consecutively, the fluorescence signal of the liquid phase is quantified in the fluorimeters A and B.

Afterwards, a NaOH solution deprotonates the fluorescence dimers of both channels by adjusting the pH to levels above 10. The fluorescence is measured in a flow through cell at an excitation wavelength of $\lambda = 326\,\text{nm}$ (Cadmium Pen-Ray® lamp). The signal is detected at $\lambda = 410\,\text{nm}$ via one photomultiplier (model H957-01, Hamamatsu Photonics GmbH, Herrsching, Germany) per channel.

2.2.3.2. Calibration, linearity and interferences

The linearity of the instrument for atmospheric mixing ratios has been discussed before (Lazrus et al., 1985, 1986). Liquid calibrations as internal standards are crucial for determining the catalase efficiency ϵ as shown in Section 2.2.6.3. Besides, they allow the correction of instrumental drifts e. g., due to altering of the solutions. Additionally, the manufacturer has equipped the instrument with an internal gas-phase H_2O_2 permeation source, which was deactivated. A custom-built external permeation source was used instead (Section 2.2.6.2).

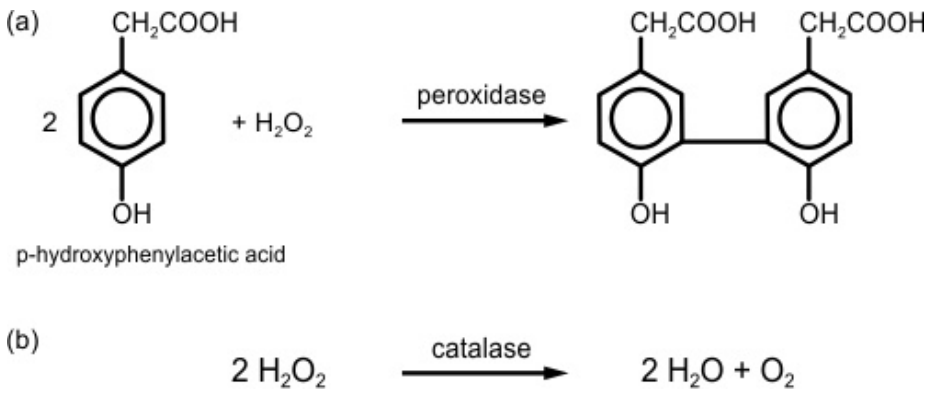

Figure 2.3.: Reaction scheme for conversion of the hydroperoxides to the fluorescence dye for both channels of the AL2021. Reaction (**a**) takes place in both channels. Here, two mol fractions of p-hydroxyphenylacetic acid (POPHA) react with one mol of H_2O_2 or higher hydroperoxides, yielding equimolar fractions of the fluorescence dye. In the second channel (**b**) catalase is used in addition, which specifically decomposes H_2O_2. Kinetically, the catalase destroys H_2O_2 faster than the fluorescence dye is formed by the peroxidase.

The manufacturer reports an interference of 30 pptv ppbv^{-1} (H_2O_2 per 100 ppbv of O_3) and 12 pptv ppbv^{-1} (H_2O_2 per 100 ppbv of NO), while other atmospheric relevant species (e. g., SO_2, NO_2 and HCHO) do not significantly affect the measurements (AL2). Since, in the context of this work, O_3 plays an important role for all field studies and thus the interference was quantified in the laboratory (Section 2.2.6.5).

2.2.4. The commercial Aero–Laser AL4021 formaldehyde analyzer

2.2.4.1. Basic principle of the Hantzsch reaction

The one-channel technique (Figure 2.4) allows a quantification of HCHO via the Hantzsch reaction (Dong and Dasgupta, 1987; Kelly and Fortune, 1994a). Figure 2.5 depicts the chemical reaction scheme of the Hantzsch reaction. HCHO is stripped (Section 2.2.5) into a sulfuric acid solution at 10 °C.

Consecutively, ammonium acetate (NH_4OAc) and acetylacetone (a β-ketone) are added into the reaction coil (tempered at 65 to 70 °C). It yields equimolar fractions of the fluorescence dye (α,α'-dimethyl-β,β'-diacetylpyridine), with respect to HCHO. The fluorescence is measured in a flow through cell at an excitation wavelength of λ = 400 nm (LED). The signal is detected at λ = 510 nm via the photomultiplier (model H957-01, Hamamatsu Photonics GmbH, Herrsching, Germany).

2.2.4.2. Linearity, liquid and gas-phase calibrations

The linearity of the instrument for atmospheric mixing ratios has been discussed before (Kelly and Fortune, 1994a). Liquid calibrations as internal standards are used only for determining instrumental drifts. Similar to the hydroperoxide monitor, the manufacturer has equipped the instrument with an internal permeation source (paraformaldehyde), which was deactivated. A custom-built external permeation source was used instead (Section 2.2.6.2).

The manufacturer reports potential interferences solely for O_3, H_2O_2 and glyoxal (AL4). However, only ozone can play a significant role under ambient conditions causing an positive artifacts of

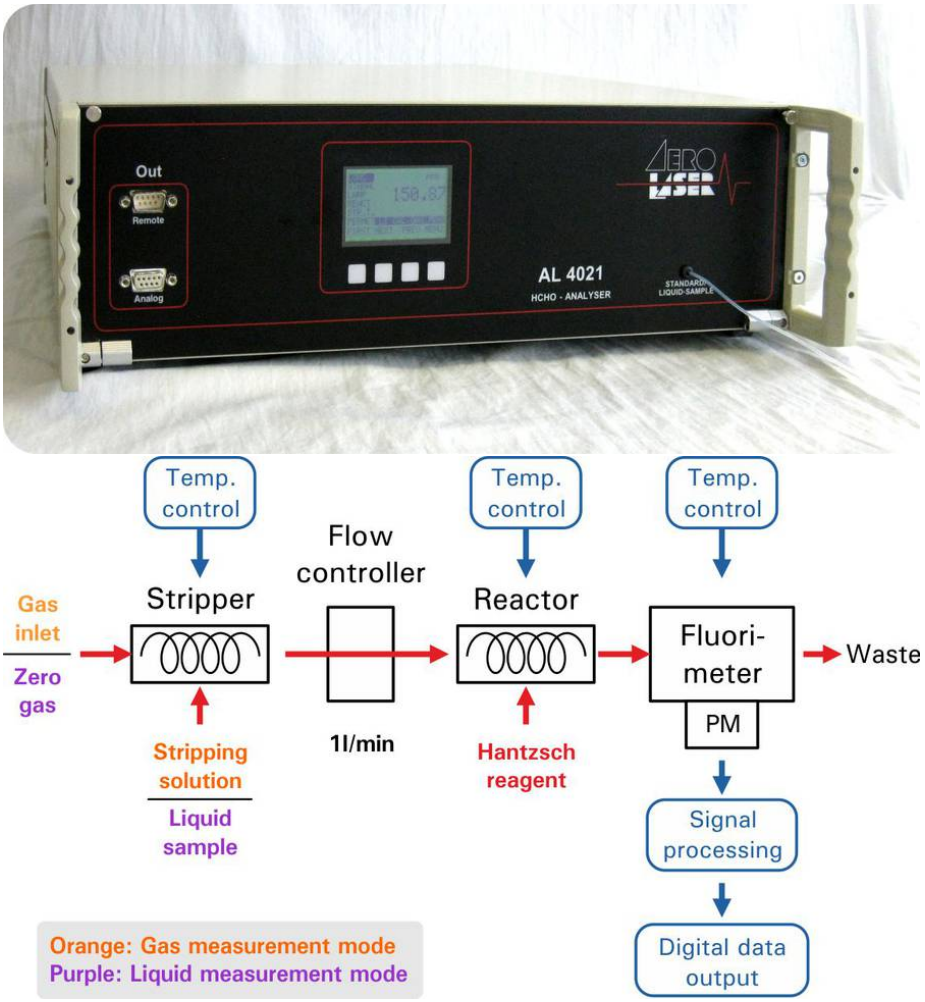

Figure 2.4.: The Aero-Laser 4021 formaldehyde analyzer. Image (**a**) and flow chart of the single-channel on-line fluorescence technique (**b**). Courtesy of Aero-Laser GmbH (Garmisch-Partenkirchen, Germany). Gas-phase HCHO is stripped at 10 °C via a glass stripping coil into the liquid phase. Consecutively, the temperature-controlled reactor coil (65 to 70 °C) controls the Hantzsch reaction yielding equimolar fractions of the fluorescence dye. The fluorescence is quantified in the fluorimeter.

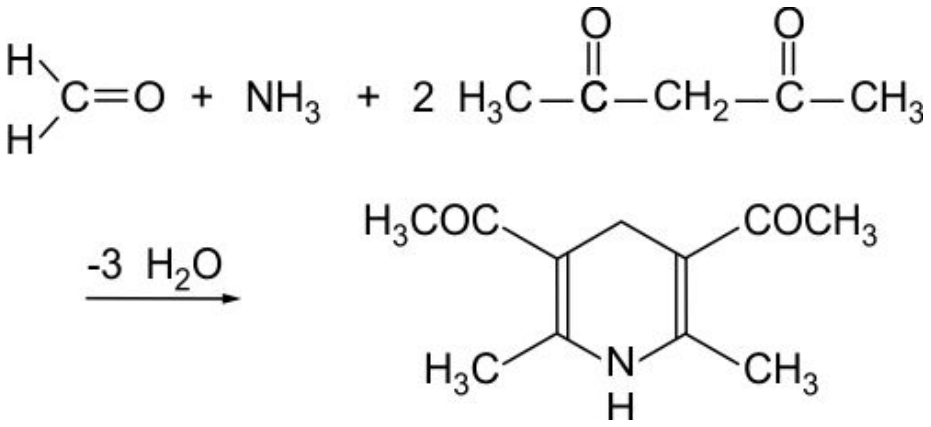

Figure 2.5.: Reaction scheme for the Hantzsch reaction.

200 pptv ppbv^{-1} (HCHO per 100 ppbv of O_3). Section 2.2.6.5) discusses an insignificant O_3 interference quantification for the herein performed field studies.

2.2.5. The glass stripping coil compared to other inlet devices

Since this work is based on liquid chemical measurement techniques, an efficient and reproducible transfer of the sample molecules from the gas to the liquid phase plays a major role. Table 2.3 shows a comprehensive literature overview on various continuous and batch techniques. Glass stripping coils are the best compromise concerning manageability, reproducibility and continuous operation as long as the Henry coefficient of the sample molecule is high enough (O'Sullivan et al., 1996). Other techniques, such as nebulizers require the quantification of the sampling solution loss due to evaporation (Sauer, 1997). Cryogenic traps are technically inconvenient (Campos and Kok, 1996) and cause positive artifacts of H_2O_2 (Campos and Kok, 1996; Staffelbach et al., 1996). Membrane diffusion scrubbers are affected by particle deposition and thus a changing collection efficiency of the sample molecules (Dasgupta et al., 1990). Midget impingers, however, show a significant O_3 interference (Heikes, 1984).

Table 2.3.: Sampling methods for atmospheric measurements of hydroperoxides. Gas-phase compounds are either enriched (batch) and subsequently detected or continuously transferred into the liquid phase with direct on-line analysis.

Method	Technique	Reference
Cryogenic trap	cold gas trap cumulation over several hours with subsequent wet chemical analysis (batch)	Campos and Kok (1996) Hewitt and Kok (1991) Jacob et al. (1990) Hellpointner and Gäb (1989) Sakugawa and Kaplan (1987)
Impinger	sequential bubbling through several midget impingers (continous)	Tanner et al. (1986) Kok et al. (1978a) Kok et al. (1978b)
Membrane diffusion scrubber	gas-phase diffusion though a membrane into liquid phase (continous)	Dasgupta et al. (1990) Tanner and Shen (1990)
Nebulizing nozzle	stripping by ambient air/mist of liquid phase (continous)	Sauer (1997) Cofer and Edahl (1986) Cofer et al. (1985)
Stripping glass coil	gass coil covered by a thin liquid film while being flushed with gas-phase (continous)	Lee et al. (1995) Heikes (1992) Lee et al. (1990) Lazrus et al. (1986) Kok et al. (1978b)

Aero-Laser has already equipped the instruments (AL2021 and AL4041) with stripping glass coils. Therefore, that method will be further discussed. This process is designated as "stripping" in the following sections. The glass stripping coil is based on Henry's law (Equation 2.3) which describes the partitioning of a chemical compound between the gas (partial pressure p in atm) and liquid phase (concentration c in mol L^{-1}) at a certain temperature T (K). It is valid for diluted solutions at equilibrium, while the temperature dependency of the Henry coefficient, K_H (here mol L^{-1} atm^{-1}), is expressed by the van't Hoff equation (Equation 2.4). The constants a and b are empirical and

available in technical overview documents (e. g., Sander, 1999). For example, the coefficients for hydroperoxides spread over several orders of magnitude (O'Sullivan et al., 1996).

$$(K_H)_T = \left(\frac{c}{p}\right)_T \tag{2.3}$$

$$K_H(T) = \exp\left(\frac{a}{T} - b\right) \tag{2.4}$$

An easily comprehensible example for calculating the stripping efficiency α (stripping glass coil) by use of Henry's law is given in the literature (Lazrus et al., 1986) for ambient H_2O_2 measurements. Alongside HCHO it is highly soluble even at room temperature ($\alpha > 99.9\,\%$). However, in case of methyl hydroperoxide (MHP), which is one of the most important organic hydroperoxides, a stripping efficiency of solely 60 % can be achieved theoretically (Lazrus et al., 1986).

The stripping efficiency for the AL2021. Specifically for this measurement technique (Lazrus et al., 1986), the stripping coil and its efficiency has been thoroughly discussed in the literature (Claiborn and Aneja, 1991; O'Sullivan et al., 1996; Staffelbach et al., 1996). However, some assumptions are made for the two-channel set-up: (i) the peroxidase completely converts H_2O_2 and organic peroxides into the fluorescence dye, (ii) the catalase is specific for H_2O_2 and (iii) the rate coefficient of the peroxidase converting H_2O_2 is significantly lower than for methyl hydroperoxide (MHP). In fact, about 7 % of MHP is decomposed erroneously by catalase (Riedel, 2001).
Equation 2.5 expresses the relation of the "real", ambient mixing ratio $\xi_{H_2O_2}$, the equilibrium mixing ratio $\xi'_{H_2O_2}$ (inside the H_2O_2 channel) and the stripping efficiency $\alpha_{H_2O_2}$,

$$\xi_{H_2O_2} = \frac{\xi'_{H_2O_2}}{\alpha_{H_2O_2}} \tag{2.5}$$

which leads, assuming that $\alpha_{H_2O_2} \approx 1$ to the simple expression:

$$\xi_{H_2O_2} = \xi'_{H_2O_2} \tag{2.6}$$

In the catalase channel, the AL2021 estimates only the sum of organic hydroperoxides $[\mathrm{ROOH}]$ or ξ_{ROOH} (ppbv) consisting of individual mixing ratios ξ'_i and stripping efficiencies α_i:

$$\xi_{ROOH} = \sum_{i=1}^{n} \alpha_i^{-1}\, \xi'_i \tag{2.7}$$

Thus, an upper approximation for methyl hydroperoxide (MHP) can be obtained by implying $\alpha_{MHP} \approx 0.6$ (Lazrus et al., 1986; Lee et al., 2000). The calculation improves by the use of other specific hydroperoxide measurements (e. g., peracetic acid, PAA) as discussed later.

The stripping efficiency for the AL4021. Since the AL4021 relies on a one-channel method, the stripping efficiency is based solely on the Henry's law coefficient of HCHO. A crucial step is the

formation of a hemiacetal under acidic conditions (Section A.2.2) removing the HCHO through shifting the equilibrium towards the aqueous phase:

$$HCHO_{(aq)} + H_3O^+ \rightleftharpoons HO{-}CH_2{-}OH_{(aq)} + H^+ \tag{2.8}$$

Equation 2.9 shows the relation of the ambient HCHO mixing ratio, ξ_{HCHO} and the equilibrium concentration ξ'_{HCHO} (inside tempered stripping glass coil at 10 °C), while $\alpha_{HCHO} \approx 1$.

$$\xi_{HCHO} = \frac{\xi'_{HCHO}}{\alpha_{HCHO}} \tag{2.9}$$

2.2.6. Typical instrumental set-up

Typical measurements were carried out with the by-pass line mounted on a tower. During operation, the AL2021 and AL4021 were set in a protected 19 inch rack providing power (24 to 28 V, reactant cooling and external gas-phase zeroing (second rack).

Set-up during field measurement campaigns tests. Figure 2.6 shows the whole concept map for in-situ measurements from a tower to the field laboratory (here MPI white container) including the 8 to 24 m long, unheated by-pass tube (1/2 inch) and the connected instruments. The inlet (no filter) was protected by a PTFE funnel and mounted heading away from metal surfaces in an angle in which rain water was not sucked into the tubing. An air volume flow rate of approximately 18 slpm leads to a residence time below 10 s for avoiding artifacts or losses caused by the wall material (PFA or PTFE), since the atmospheric life times of most of the species is significantly higher.

Set-up for laboratory tests. Figure 2.6 (orange box) shows the by-pass line providing external gas-phase zeros via two three-way valves. One way allowed direct pass-through of ambient air, the other leads air though two zeroing cartridges (silica gel and Hopcalite), while gas-phase calibrations were performed manually through a following T-piece (2 x 1/4 inch and 1 x 1/8 inch) connected to the permeation device (PD). However, both instruments were operated side-by-side though another T-piece (1/4 inch). In standard operation, the hydroperoxide and HCHO rack sucked in 3 slpm.

2.2.6.1. Gas-phase zeroing

The instruments are operating with in-situ zero gas measurements (synthetic air free of H_2O_2 and HCHO) accounting for potential instrumental offsets. Thus, once operational, the first parameter to characterise is the level of the zero signal. Later, together with the calibrations, the limit of detection (LOD) is deduced from the reproducibility of the zero measurements.
In principle, there are two different ways for gas-phase zeroing: “internal” and “external”. Internal is achieved via two small filter cartridges (Infiltec GmbH, Speyer, Germany), one filled with orange gel, the other with Hopcalite (50 % MnO, 30 % CuO, 15 % Co_2O_3 and 5 % Ag_2O), in the gas flow path of the instrument itself. External zeros were performed every 3 h 20 min via two big filter cartridges (Infiltec GmbH, Speyer, Germany) inside the by-pass flow path. Orange gel is necessary to dry the ambient air, since the Hopcalite is deactivated by water. Internal zeros were performed

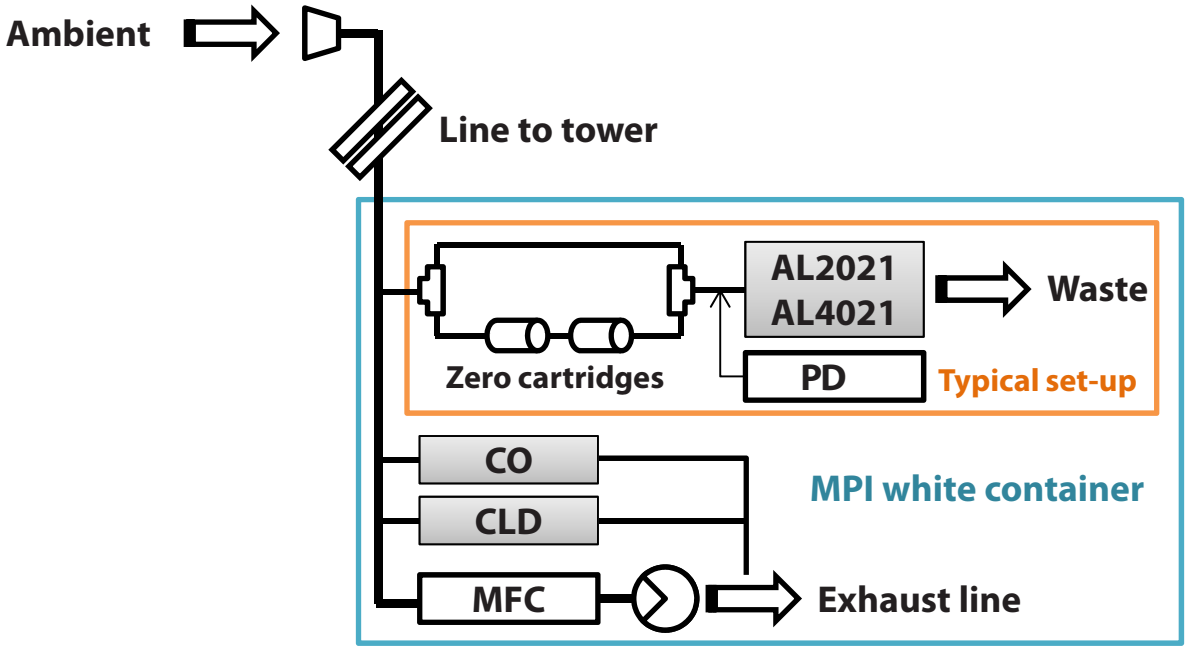

Figure 2.6.: Flow chart of the set-up. Typically, ambient air was sampled at a measurement tower connecting the MPI white container via a by-pass (1/2 inch tubing, e. g., 11 to 25 m length). The hydroperoxide (AL2021) and formaldehyde (AL4021) set-up sampled was equipped with an automated by-pass itself (zero cartridges) allowing gas-phase calibrations by the permeation device (PD). However, the instruments (e. g., CO, AL2021 and AL4021, CLD) were connected by 1/4 inch tubes to the big by-pass line. The flow before the pump was regulated by a MFC to 18 L min^{-1} and the excess air conducted away through a pipe (downwind) as well as the individual instrumental exhaust air.

automatically by the instruments at each liquid calibration, external zeros for 30 min were activated on demand by two magnetic valves controlled by a V25 controller (MPIC custom-built).

2.2.6.2. Primary gas-phase standards

The herein employed instruments for gas-phase measurements are based on wet chemical methods. Thus, for transition from gas to liquid phase basically two effects have to be considered: (i) the physicochemical process of stripping the sample depending on Hery's law and (ii) artifacts or losses caused by wall effects, leakages, dust or pressure fluctuations. Therefore, in addition to the liquid calibrations that are used gas phase standards are needed, consisting two permeation sources for H_2O_2 and HCHO, respectively. Those have to be reliable enough over a longer period of time and easy to calibrate by a direct method which is (i) admitted as accurate and (ii) simple enough to be performed in the field. The permeation sources were integrated in the permeation and data logging device (as a single 19 inch module).

The permeation and data logging device. The permeation device (Figure 2.7) consists data logging unit based on the NEC V25 microcontroller and of two small shielded ovens. Two custom-built impingers fit into the ovens.

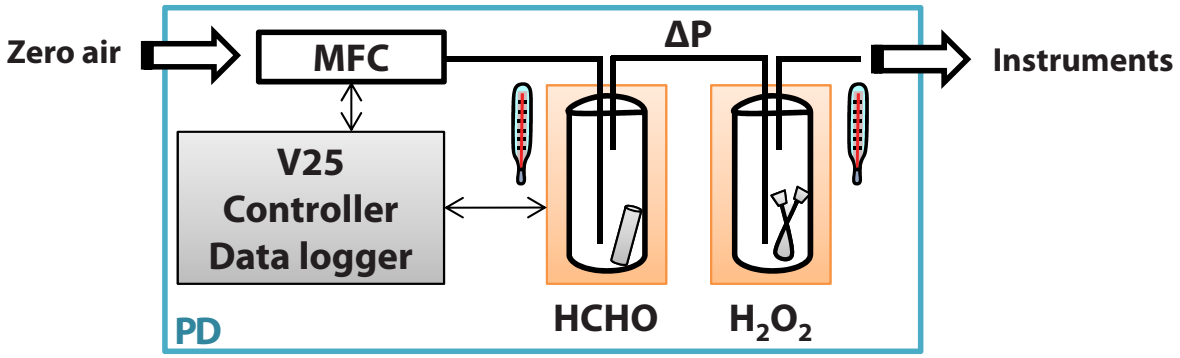

Figure 2.7.: Flow chart of the permeation device (PD). Two permeation sources (paraformaldehyde for HCHO and Perhydrol® 30 % for H_2O_2, respectively) are located in two separate glass impingers. Two ovens control the temperature (31 °C and 70 °C). Zero air (40 to 60 sccm), controlled by a MFC) is flushed through the first (paraformaldehyde) and subsequently through the second (H_2O_2) by series-connection. The whole device consists of a the permeation sources and a V25 data logging and control unit (19 inch component). A pressure gradient (ΔP) is crucial for normal operation. The calibration gas is introduced into the instrumental by-pass (compare to Figure 2.6).

Preparation of the H_2O_2 permeation source. The permeation source consisted of a 1/2 inch PE tube (15 cm length) capped on both ends that is filled with 30 % stabilized H_2O_2 solution. It was prepared in the preparation period before each campaign according to the following procedure:

1. The chunk (15 cm length), PFA fittings and caps are cleaned in an ultrasonic bath filled with ultrapure water for approximately half an hour.
2. The dry tube is filled with H_2O_2 solution.
3. Both ends are capped carefully that no bubbles emerge.
4. The permeation tube is cleaned on the outside with ultrapure water and dried afterwards. This procedure is repeated 2 times.
5. The tube is inserted into the glass flask avoiding any kinks.

The new permeation source provides a signal outside the measurable range of the instrument. Thus, the oven temperature is set to 80 °C for a period of approximately 2 to 5 d. Resetting to the "normal" operational temperature (31 °C) leads to a stable signal over days that allows photometric quantification.

Photometric calibration of the H_2O_2 source with the $TiCl_4$ method. Validating the permeation source as a primary gas calibration standard requires a well approved and direct calibration method. Since the latter has to be simple, sensitive and robust even under campaign conditions, the titanium tetrachloride ($TiCl_4$) method was applied in this work (Pilz and Johann, 1974). Equimolar fractions of H_2O_2 and titanium tetrachloride form the yellow complex $[H_2TiO_2Cl_4]^{2-}$ in aqueous hydrochloric acid solution. Limit of quantification, linearity and range have been shown before (Pilz and Johann, 1974). The study evaluated a sufficient H_2O_2 stripping efficiency after one of five series-connected impingers: gas phase containing H_2O_2 ("saturated") was passed with 2 L min^{-1} through the five impingers which were filled with 50 mL of the 22 wt % $TiCl_4$ solution. Even us-

ing cooled ultrapure water for as stripping solution shows a sufficient stripping efficiency in the first impinger and shows a stable concentration of H_2O_2 (ca. 98 %) over one week of cold storage (Hafermann and Reiffs, 2013).

The reagent is prepared by dissolving $TiCl_4$ (116 mL) slowly in concentrated hydrochloric acid water (500 mL) under cooling and stirring (amber glass flask). The obtained solution (22 wt %) is stable for an unlimited amount of time if stored light-protected.

The calibration procedure (Pilz and Johann, 1974) was slightly changed and thus the following paragraph describes all steps. Two impinger flasks, one blank (B) and one measurement (M), are filled each with 20 mL ultrapure water (Titripac®), the meniscus marked and then precooled to 4 to 8 °C. The outlet tube of the permeation rack (1/8 inch, gas flow ca. 40 to 60 sccm) is inserted into the measurement flask, while the blank is connected to zero air and the timer is started. The tube should be positioned as deeply as possible while the bubbling appears regular. After approximately 24 h the tube is removed, the timer stopped and meniscus checked whether a significant amount of water evaporated. Then, 5 mL of solution (B) are withdrawn twice, once to condition the volumetric pipette, secondly to be inserted into a 10 mL volumetric flask (amber glass). This step is repeated for solution (M) preparing a second volumetric flask. Next, 1 mL of the 22 wt % $TiCl_4$ solution is added to both volumetric flasks and consecutively filled to 10 mL.

The extinction of solution (M) is measured thrice at 415 nm (extinction coeff. $\epsilon = 735\,\mathrm{L\,mol^{-1}\,cm^{-1}}$, cuvette path $d = 1\,\mathrm{cm}$), while (B) is used for zeroing the photometer. The emission of the permeation source is calculated after Equation 2.10, accounting for the absorption (A), the volume of the measurement solution (V_M) and the volume stream of the air ($\dot{V}_{Air}$). The mixing ratio of the permeation source ($\xi_{H_2O_2}$, Equation 2.10) is obtained by the fraction of the molar H_2O_2 flow ($\dot{n}_{H_2O_2}$) and the molar zero air flow ($\dot{n}_{Air}$) rate implying the dilution from the stripping to the measurement solution. Calculated total uncertainty of the method: 10.6 % at 207 ppbv (precision P = 2.03 %, systematic error E_S = 8.6 %).

$$\xi_{H_2O_2} = \overbrace{\left(\frac{10}{5}\right)}^{\text{Dilution factor}} \cdot \overbrace{\left(\frac{A_M \cdot V_M}{\epsilon \cdot d \cdot t}\right)}^{\dot{n}_{H_2O_2}} \cdot \overbrace{\left(\frac{22.414\,\mathrm{L\,mol^{-1}}}{\dot{V}_{Air}}\right)}^{\dot{n}_{Air}^{-1}} \tag{2.10}$$

Reliability of the H_2O_2 permeation source. Permeation tubes as described before were prepared before each campaign, HUMPPA (2010) and PARADE (2011). Since even stabilized H_2O_2 solutions (30 %) are known to be unstable, a chemical decay of the solution in the permeation source is likely. Figure 2.8 shows the long-term stability in the H_2O_2 mixing ratios for HUMPPA (2010) and PARADE (2011). Laboratory as well as in-field calibrations are included in the plot show the average mixing ratio (±1σ) over the time period which is in case of HUMPPA 5.310 ± 0.688 ppbv and PARADE 3.510 ± 0.287 ppbv. Each calibration point is depicted with the value and the precision of the photometric quantification (1σ). Except for some outliers, the calibrations do not significantly exceed the 1σ interval of the long time average and a loss trend of ca. 0.5 % d^{-1} is estimated.

The formaldehyde permeation source. A commercial permeation tube containing paraformaldehyde powder was used: VICI® Valco Instruments Co. Inc., Schenkon, Switzer-

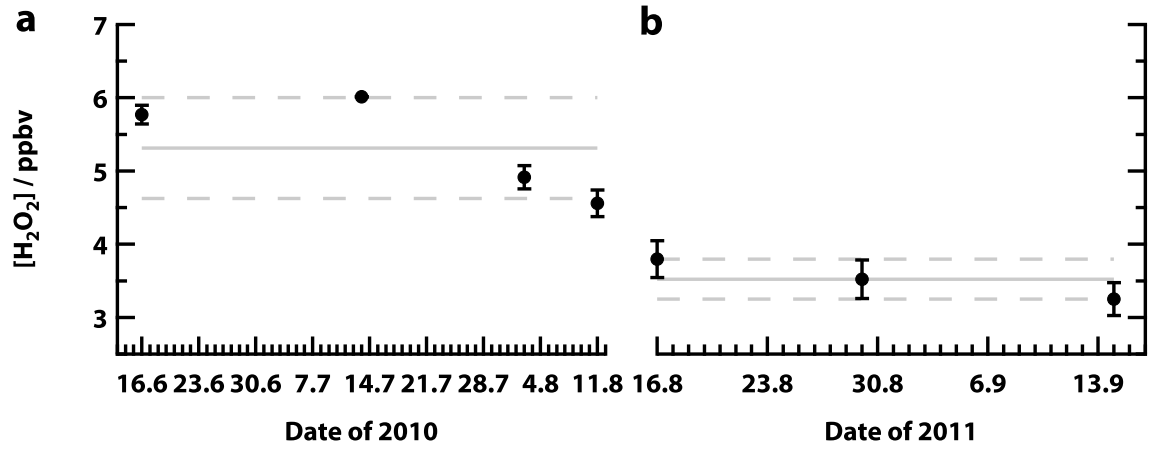

Figure 2.8.: Stability of two different batches of H_2O_2 permeation sources inside the permeation device. Time lines for HUMPPA (**a**) and PARADE (**b**) with the mixing ratios (precisions of the photometric quantification shown as 1σ error bars) normalized by the dilution factor. The latter is the ratio of the total instrumental air flow (e. g., 3000 sccm) and the permeation source zero air flow (e. g., 40 to 60 sccm). Campaign averages are depicted as grey lines (including the 1σ standard deviation, dashed). Statistical outliers are indistinguishable from chemical decomposition although there is a downward trend as expected.

land (PD 100-009-2300-T53-U80, 99 ng min^{-1} at 80 °C). Paraformaldehyde decomposes to HCHO under thermal stress as shown in Equation 2.11. One tube was used from HUMPPA (2010) to PARADE (2011) with the batch number HCHO-RA-20100511.

$$OH(CH_2O)_nH \xrightarrow{T = 70\,^{\circ}C} n\,HCHO \quad n = 8 - 100 \tag{2.11}$$

Photometric calibration of the HCHO source with the chromotropic acid method. Validating the permeation source as a primary gas phase calibration standard requires a well approved and direct calibration method. Since the latter has to be simple, sensitive and robust even under field campaign conditions, the chromotropic acid (CA) method was applied in this work. HCHO and CA condense in an impinger flask containing sulfuric acid (H_2SO_4) which acts as both, a dehydrant and an oxidant (Figure 2.9). The reaction yields chromophor in equimolar fractions to HCHO. Limit of quantification, linearity and the measurement range have been tested before (Bricker and Johnson, 1945; Sawicki et al., 1962; West and Sen, 1956). The extinction coefficient (UV-VIS) has been measured (Wagner, 2000). In the following, the procedure after Wagner (2000) is used, referred as the "campaign method".

The chromotropic acid solution is freshly prepared for each use (−0.036 % activity loss per day). Ultrapure water (Titripac®, 10 mL) and chromotropic acid (20 mg) are prepared in a heat-proof glass flask with agitator. Then concentrated H_2SO_4 (90 mL) is slowly added under ice-cooling and stirring. The CA solution is ready-to-use once all colloidal rests disappear. It should be stored light-protected conditions.

For the calibration procedure two impinger flasks (one blank and one measurement solution) are filled each with 10 mL of the chromotropic acid solution and tempered to (70 °C) by a small oven. The outlet tube of the permeation rack (1/8 inch) is inserted into the measurement flask (M), while the blank (B) is connected to zero air and the timer is started. The tube should be positioned as

deeply as possible until the bubbling appears regular. The procedure (max. 180 min) causes a colour change from colourless to pale violet. Eventually, the tube is removed and the timer stopped. Then the flask is sealed with Parafilm and cooled quickly to room temperature. The extinction of solution (M) is measured at 580 nm (extinction coefficient $\epsilon = 1.76 \times 10^4\,\mathrm{L\,mol^{-1}\,cm^{-1}}$, cuvette path $d = 1\,\mathrm{cm}$), while (B) is used for zeroing the photometer (model: U-1100, Hitachi, Tokyo, Japan). The emission of the permeation source is calculated after Equation 2.12, accounting for the absorption (A), the volume of the measurement solution (V_M) and the volume flow of the air ($\dot{V}_{Air}$). The mixing ratio of the permeation source (ξ_{HCHO}) is obtained by the fraction of the molar HCHO flow ($\dot{n}_{HCHO}$) and the molar zero air flow ($\dot{n}_{Air}$) rate. Calculated total uncertainty of the method: 7 % at 523 ppbv (precision P = 0.33 %, systematic error E_S = 6.7 %).

$$\xi_{HCHO} = \overbrace{\left(\frac{A_M \cdot V_M}{\epsilon \cdot d \cdot t}\right)}^{\dot{n}_{HCHO}} \cdot \overbrace{\left(\frac{22.414\,\mathrm{L\,mol^{-1}}}{\dot{V}_{Air}}\right)}^{\dot{n}_{Air}^{-1}} \tag{2.12}$$

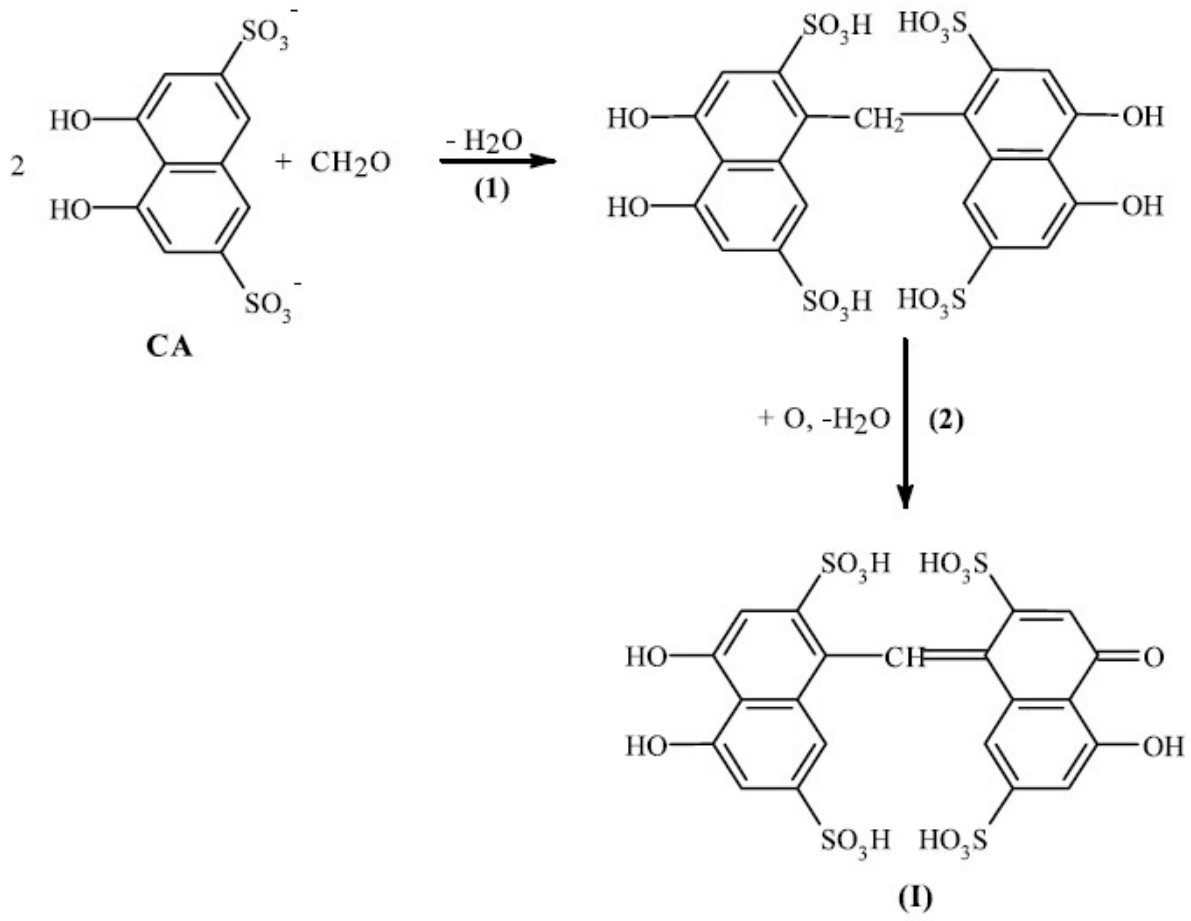

Figure 2.9.: Reaction scheme for the condensation of chromotropic acid and HCHO. Two molecules of the acid react with one HCHO under oxidizing conditions to the one chromophor (Fagnani, 2003).

Reliability of the HCHO permeation source. Figure 2.10 shows the stability in the HCHO mixing ratios. The commercial permeation tube (batch HCHO-RA-20100511) was solely used during this work over the two campaigns HUMPPA and PARADE from 2010 to the end of 2011. Data on permeation rates were obtained with the chromotropic acid method, as described in this para-

graph. Laboratory as well as in-field calibrations are included in the plot showing the average mixing ratio (±1σ) over the time period which is in case of HUMPPA 8.350 ± 0.383 ppbv and PARADE 5.930 ± 0.382 ppbv, respectively. In addition, each calibration point is shown with the precision (1σ). Except for some outliers, the calibrations do not significantly differ from the long time average. This makes it difficult to distinguish between a potential chemical decay and the reproducibility of the individual calibrations.

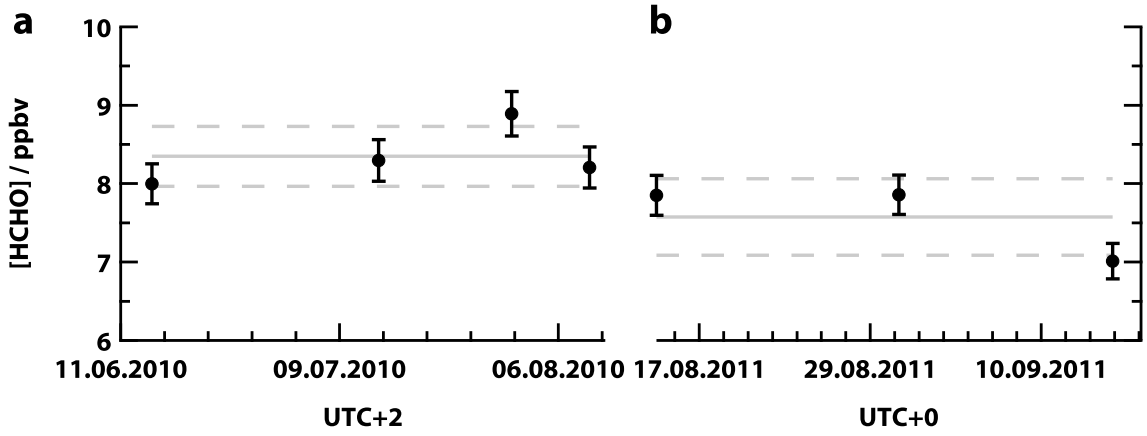

Figure 2.10.: Stability of the HCHO permeation source (batch HCHO-RA-20100511) inside the permeation device over two years. Time lines for HUMPPA (**a**) and PARADE (**b**) with the mixing ratios (precisions shown as 1σ error bars) normalized by the dilution factor, which is the ratio of the total instrumental air flow (e. g., 3000 sccm) and the permeation source zero air flow (e. g., 40 to 60 sccm). Campaign averages are visualized as grey lines (including the 1σ standard deviation, dashed). For instance, (**a**) shows one outlier (8.8 ppbv). However, the mixing ratios show a decreasing trend, potentially caused by (i) chemical decomposition of the paraformaldehyde and (ii) different dilution factors between HUMPPA and PARADE, thus they are incomparable directly.

2.2.6.3. Internal liquid-phase standards

As mentioned before liquid calibrations were performed for both the AL2021 and the AL4021 to correct instrumental drifts. However, in case of the AL2021, liquid calibrations play a crucial role for determining the catalase efficiency. For guaranteeing a maximum stability over weeks, the stock solution was always cooled between 4 to 8 °C. Regular titrations were performed approximately every two weeks.

The H_2O_2 stock solution. The stock solution has a theoretical concentration of 1000 M and is prepared by precooling 0.95 L of ultrapure water (Titripac®) in an amber glass volumetric flask. Then exactly 1 mL of Perhydrol® (30 % H_2O_2) is added and the flask is filled to exactly 1 L. The stock solution is ready-to-use after mixing.

Instrument calibrations were performed with a freshly prepared two-step dilution series of 1 : 100 and 1 : 100 (maximum theoretical concentration 100 nmol L^{-1} yielding a calibration signal about 9.5 ppbv for H_2O_2).

H_2O_2 stock solution: wet chemical quantification of the molar concentration by redox titration (potassium permanganate). The H_2O_2 concentration of the stock solution is quantified via redox titration against $KMnO_4$ as shown in Equation 2.13. Therefore 10 mL (V_{Stock}) are withdrawn and acidified with ca. 3 drops concentrated H_2SO_4 and immediately titrated against $KMnO_4$ solution (c_{KMnO_4} = 0.002 M). The colour change from colourless to pale purple indicates the equivalence point.

$$5\,H_2O_2 + 2\,MnO_4^- + 6\,H_3O^+ \longrightarrow 5\,O_2 + 2\,Mn^{2+} + 14\,H_2O \tag{2.13}$$

Equation 2.14 shows the calculation of the stock solution concentration c_{Stock} including the volume of consumed potassium permanganate solution, V_{KMnO_4}, as well as the stoichiometric coefficient of Equation 2.13.

$$c_{Stock} = \frac{5}{2} \cdot \frac{c_{KMnO_4} \cdot V_{KMnO_4}}{V_{Stock}} \tag{2.14}$$

For a calibration cycle, the stock solution is diluted twice 1 : 100 ($c_{Stock} \rightarrow c_{LS}$). Employing the instrumental parameters such as the stripping $\dot{V}_{Stripper}$ (mL) and the air flow $\dot{V}_{Gas}$ (mL) leads to the the signal of the liquid standard µ (ppbv) with a calculated total uncertainty of 8 % at 6 ppbv (precision P = 6 %, systematic error E_S = 2 %).

$$\mu_{LS} = \underbrace{\frac{c_{LS}}{100 \cdot 100}}_{\text{Dilution factor}} \cdot \frac{22.414\,\text{L mol}^{-1}\,\dot{V}_{Stripper}}{\dot{V}_{Gas}} \cdot \overbrace{10^9}^{\text{nmol mol}^{-1}\rightarrow\text{ppbv}} \tag{2.15}$$

Liquid calibration of the AL2021. A calibration cycle as depicted in Figure 2.11 is divided into three major parts: (a) HCl-flush cleaning of both channels from potential catalase remnants, (b) quantifying the sensitivities S_A and S_B (e. g., in V ppbv^{-1}) for channels A and B, respectively, and (c) calculating the catalase efficiency ϵ. Hereby, $U_{A,LS} - U_{A,0LS}$ and $U_{B,LS} - U_{B,0LS}$ represent the difference of the signal in V for the liquid standard per channel:

$$S_A = \frac{U_{A,LS} - U_{A,0LS}}{\mu_{LS}} \tag{2.16}$$

$$S_B = \frac{U_{B,LS} - U_{B,0LS}}{\mu_{LS}} \tag{2.17}$$

Equation 2.18 describes ϵ taking the alteration of the solution during the calibration cycle into account (standard correction term). Here, U_A and U_B represent the liquid calibration signals, whereas $U_{A,0}$ and $U_{B,0}$ the zeros without catalase. The same applies to the catalase cycle: $U_{A,0C}$ and $U_{B,0C}$ (zero), $U_{A,C}$and $U_{B,C}$ (liquid calibration signals). However, for quantifying ϵ, the sensitivities cancel out.

$$\epsilon = 1 - \overbrace{\left(\frac{U_{B,C} - U_{B,0C}}{U_B - U_{B,0}}\right)}^{\text{Efficiency term}} \cdot \overbrace{\left(\frac{U_A - U_{A,0}}{U_{A,C} - U_{A,0C}}\right)}^{\text{Standard correction term}} \tag{2.18}$$

As a result, the H_2O_2 mixing ratios $\xi'_{H_2O_2}$ deduced from a calibration is given by

$$\xi'_{H_2O_2} = \overbrace{\left(\frac{U_A - U_{A,0}}{S_A}\right)}^{\text{Sum of hydroperoxides}} - \overbrace{\left(\frac{\epsilon \cdot (U_B - U_{B,0})}{S_B}\right)}^{\text{Catalase channel}} \tag{2.19}$$

and for ξ'_{ROOH}:

$$\xi'_{ROOH} = \frac{\epsilon \cdot (U_B - U_{B,0})}{S_B} \tag{2.20}$$

Note that here the stripping efficiency α and the recovery R are not accounted for.

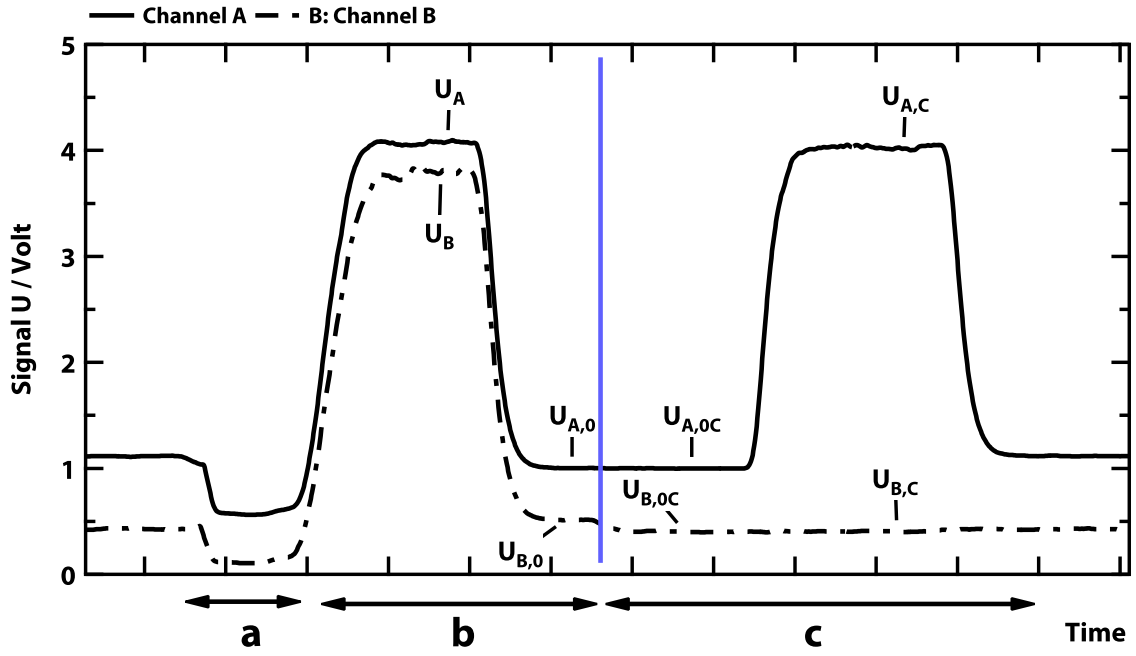

Figure 2.11.: Eight point liquid calibration cycle to quantify the catalase efficiency. The signal (V) of both channels A (total hydroperoxides) and B (total hydroperoxides minus H_2O_2) are visualized. Inequalities in the liquid path and photomultipliers (PMTs) cause absolute differences of the channels. The calibration cycle is divided into three parts: (**a**) the HCl flush to clean both channels from potential catalase artifacts, (**b**) to quantify the sensitivity (e. g., in V ppbv^{-1}) for channel A and B and (**c**) to calculate the catalase efficiency ϵ. However, the points are: U_A and U_B for the liquid calibration signals without catalase and $U_{A,0}$ and $U_{B,0}$, respectively, for the zeros without catalase. Then, catalase is introduced to channel B: $U_{A,0C}$ and $U_{B,0C}$ as zero and $U_{A,C}$ and $U_{B,C}$ as the liquid calibration signals.

The HCHO stock solution. The stock solution has a theoretical concentration of 1000 M and is prepared by precooling 300 mL of ultrapure water (Titripac®) in an amber glass flask. Then, exactly 1 mL of 37 % HCHO is added and the flask filled to exactly 375 mL. The stock solution is ready-to-use after mixing.

Instrument calibrations were performed with a freshly prepared two-step dilution series of 1 : 250 and 1 : 250 (maximum theoretical concentration 600 nmol L^{-1} yielding a calibration signal about 8.5 ppbv for HCHO).

HCHO stock solution: wet chemical quantification of the molar concentration by iodometric redox titration. The HCHO concentration of the stock solution is quantified via redox titration against iodine (I_2) in two major steps as shown in the following equations. Therefore 5 mL (V_{Stock}) are withdrawn and acidified with ca. 3 drops of concentrated H_2SO_4 and immediately titrated against $KMnO_4$ solution (c_{KMnO_4} = 0.002 M).

$$\mathrm{HCHO + Na_2SO_3 + H_2O \xrightarrow{0\,^\circ C,\,7\,min,\,pH\,9.3\text{-}10.5} HO{-}CH_2{-}SO_3{-}Na + NaOH}$$

$$\mathrm{Na_2SO_3 + I_2 + H_2O \xrightarrow{pH\,4.5} Na_2SO_4 + 2\,HI}$$

$$\mathrm{HO{-}CH_2{-}SO_3{-}Na + I_2 \xrightarrow{pH\,4.5} no\ reaction}$$

The colour change from colourless to pale purple indicates the equivalence point.

$$\mathrm{HO{-}CH_2{-}SO_3{-}Na + Na_2CO_3 \xrightarrow{pH\,9\text{-}10} HCHO + Na_2SO_3 + NaHCO_3} \tag{2.21}$$

$$\mathrm{Na_2SO_3 + H_2O + I_2 \xrightarrow{1\,\%\,Starch} Na_2SO_4 + 2\,HI} \tag{2.22}$$

Equation 2.23 shows the calculation of the stock solution concentration c_{Stock} including the volume of consumed potassium permanganate solution, V_{KMnO_4}, as well as the stoichiometric coefficient of Equation 2.13.

- Equation 2.21 shows how Na_2SO_3 and HCHO are produced in equimolar fractions as the sodium HCHO bisulfite decomposes.
- the Na_2SO_3 is titrated against c_{I_2} = 0.025 M (Equation 2.22)

$$c_{Stock} = \frac{c_{I_2} \cdot V_{I_2}}{V_{Stock}} \tag{2.23}$$

Liquid calibration of the HCHO. sensitivity of the channel towards the fluorescence dye is:

$$S = \frac{U_{LS} - U_0}{\mu} \tag{2.24}$$

where μ is the expected signal for the liquid standard (in ppbv). $\dot{V}_{Gas}$ is usually in orders of 1 L min^{-1}.

$$\mu = \underbrace{\frac{c_{LS}}{250 \cdot 250}}_{\text{Dilution factor}} \cdot \frac{22.414\ \mathrm{L\ mol^{-1}}\ \dot{V}_{Stripper}}{\dot{V}_{Gas}} \cdot \overbrace{10^9}^{\text{nmol mol}^{-1}\rightarrow\text{ppbv}} \tag{2.25}$$

2.2.6.4. Quantification of the inlet line losses

The equipment was usually placed in a field laboratory or the MPI white container for avoiding artifacts. Thus a 1/2 inch tube was necessary to connect the instruments to the inlet which was usually installed on a measurement tower (e. g., HUMPPA tower, compare Section 2.2.6). Especially gas-phase H_2O_2 and HCHO to a lesser extent might be effected by (i) wall and (ii) humidity effects. Table 2.4 shows a comprehensive overview on the results of this work and literature. In addition, it

has been find out that the transmission of PFA or PTFE line changes during the campaign time by altering (e. g., aerosol load caused by adhesion).

Table 2.4.: Line losses for H_2O_2 and HCHO measurements performed in this work as well as from literature. Configurations of the inlet tubing comprise the outer diameter, material, filter or heating usage as well as the length and residence time depending on the air volume flow rate. Line losses are given in: 100 % – transmission in %. The data of this work were corrected in case of a significant loss.

Species	Configuration	Line loss / %	Reference
H_2O_2	1/2 inch PFA (no filter), 24 m, 6.3 s	insignificant	this work (HUMPPA)
	1/2 inch PFA (no filter), 15 m, 3.2 s	0 to 39.9 %	this work (PARADE)
	PFA (no filter), 3 m, 2 s	insignificant	Balasubramanian and Husain (1997)
	PFA, 41 m, 8 s	0 to 7 %	Hall and Claiborn (1997)
	PFA (no filter), 3 m, 1.2 s	insignificant	Sauer (1997)
	PFA (heated), 1.3 s	0 to 90 %[a]	Lee et al. (1991)
	1/4 inch PFA, 6 m, 8.9 s[b]	40 %	Dasgupta et al. (1990)
HCHO	1/2 inch PFA (no filter), 24 m, 6.3 s	insignificant	this work (HUMPPA)
	1/2 inch PFA (no filter), 15 m, 3.2 s	insignificant	this work (PARADE)
	1/4 inch PFA, 6 m, 8.9 s[b]	40 %	Dasgupta et al. (1990)

[a] High losses might be caused by the measurement technique itself.

[b] Deposition of particles observed.

Figure 2.12 depicts the experimental set-up. The quantification of the relative losses was accomplished by the procedure described in the following. The tubing was removed from the tower and cut into a short (S) and a long (L) part. Short, in that case, means several meters from the by-pass line heading to the instruments, while long is the rest. Then, dry synthetic air was flushed in excess through the tube at approximately half of the usual flow (9.8 slpm) restricted by the maximum flow of the pressure reducer or mass flow controller (MFC). The loss quantification for other species (e. g., ozone) was performed for several hours by alternating between (L) and (S). Next, all other calibration gases were removed and the permeation sources were connected for (L). Usually two line loss calibrations were performed per campaign, one in the beginning and one at the end.
The line loss quantification showed consistent results with those cited in literature (Table 2.4). Significant losses were found for PARADE, where the H_2O_2 line loss increased from 0 to 39.9 ± 5.0 % throughout the field campaign. Thus the data were corrected via linear interpolation. In all other cases, either for H_2O_2 and HCHO during HUMPPA and HCHO during PARADE, were within the error range of ca 5 %, indicating no significant losses.

2.2.6.5. Quantification of the ozone interference in the laboratory

Ozone Interference. An ozone interference causing an overestimation of H_2O_2 mixing ratios has been observed before (Heikes, 1984), which disagrees with the values given by the manufacturer (0.3 pptv ppbv^{-1}). In addition, in case of HCHO, O_3 artifacts of about 2.5 pptv ppbv^{-1} were reported (Kormann et al., 2003). Therefore the interference was quantified in the laboratory for both instruments under field measurement campaign conditions.

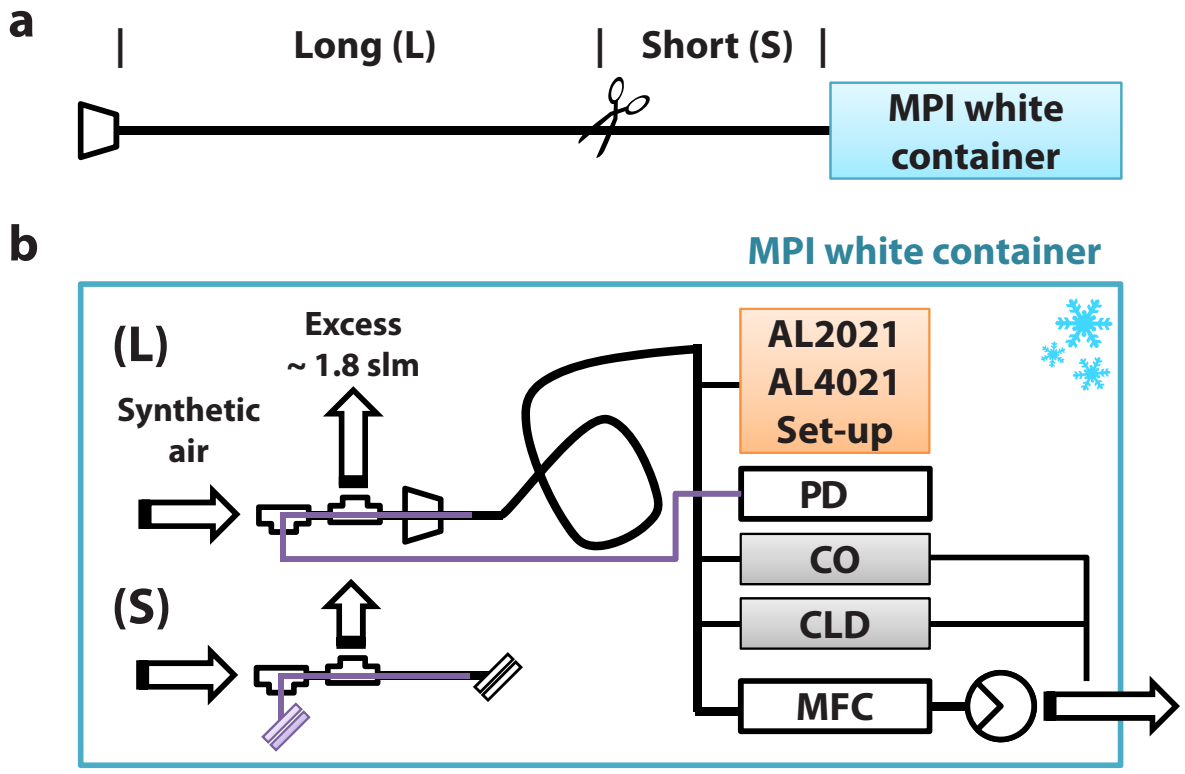

Figure 2.12.: Set-up for the relative line loss quantification for H_2O_2 and HCHO measurements. The procedure consists of two major steps: (**a**) demounting the line from the tower and cutting it somewhere between the tower and the MPI white container into a long (L) and a short part (S), e. g., 3 m. Secondly, the relative loss between L and S is quantified (**b**). Therefore, chunk L is flushed with synthetic air, while introducing calibration gas against ambient pressure from the permeation device (PD) through a mixing tee. Once the signal is stable, the same steps is performed with part S. Both were flushed with synthetic air and gas phase standard. However, the instrumental set-up remains unchanged (compare to Figure 2.6).

Figure 2.13 depicts the set-up for the ozone interference quantification in the laboratory for both instruments, the AL2021 (H_2O_2) and the AL4021 (HCHO) as previously described (Stickler et al., 2006). Zero air (free from methane) is flushed though the ozone calibrator (Model 49PS, Thermo Environmental Instruments Inc., Franklin, MA, USA) with an excess flow higher than 3 slpm. The surplus of air is released over a tee (one side open against atmospheric pressure). Then the instruments follow as described in Section 2.2.6.

Next, a well-defined mixing ratio of ozone is set. The ozone calibrator is operated for approximately one hour at 1000 ppbv to remove oxidable artifacts (e. g., hydrocarbons) covering the insides of the tubes. Meanwhile external and internal gas-phase zeros and calibrations are performed for both instruments.

The ozone cross-sensitivity test is initiated by running a liquid and consecutive gas-phase calibration for both instruments (set point ozone calibrator: 0 ppbv). Then, the ozone level is set to 200 ppbv until the interference signal of H_2O_2 stabilises (usually after 20 to 40 min). Next, the ozone mixing ratio is decreased by 20 ppbv until equilibrium. That decreasing procedure is performed until a set-point of 0 pptv of O_3 is reached. Potential drifts at the end of the interference quantification are checked by setting once again an ozone mixing ratio of 200 ppbv as well as performing liquid,

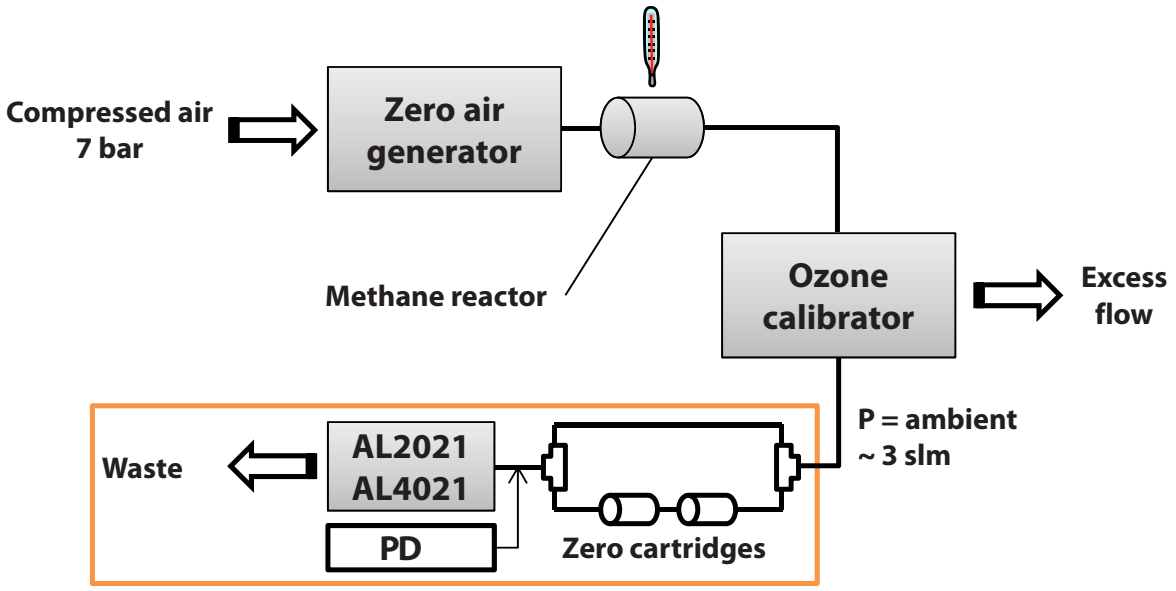

Figure 2.13.: Set-up for the quantification of the ozone interference for both, the AL2021 and the AL4021. Zero air is generated in a zero air generator and consecutively scrubbed from methane (Stickler et al., 2006). As it reaches the ozone calibrator, a well-defined mixing ozone is adjusted and from that point the set-up works under ambient pressure (excess flow). Thus, the AL2021 and the AL4021 can undergo zeroing (via the by-pass flow) and calibrations (liquid and gas phase via the PD) as described in the campaign procedures. The interference quantification is performed by measuring the artifact in H_2O_2 and HCHO at a ramp from 0 to 200 ppbv of O_3.

gas-phase calibration and a zero measurement. Figure 2.14 shows typical regression plots (here for the instrumental parameters of HUMPPA) in case of both instruments.

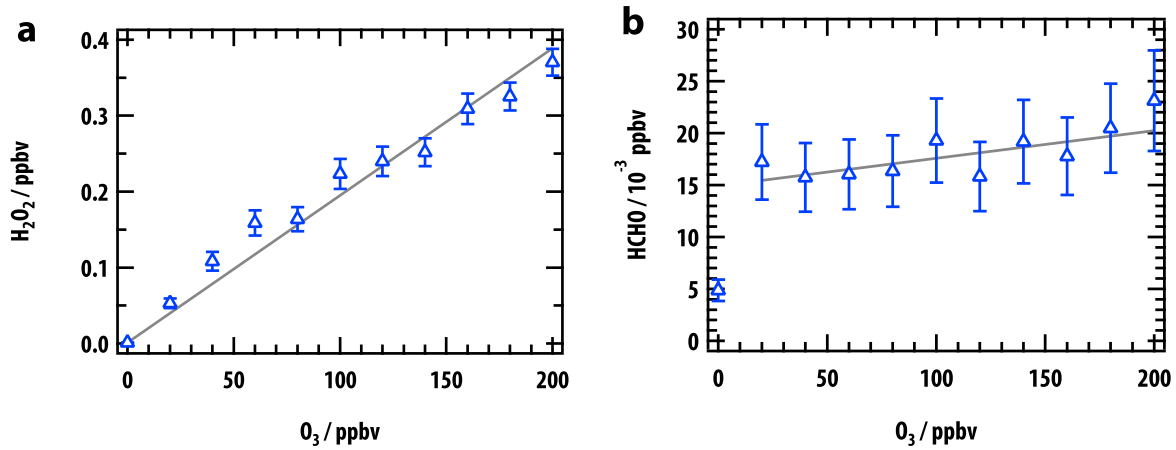

Figure 2.14.: Ozone interference versus ozone mixing ratios for H_2O_2 and HCHO measurements exemplary for HUMPPA. Instrumental variabilities in the respective averaging intervals (3 min) are depicted as error bars (1σ). The AL2021 (H_2O_2) shows a significant ozone interference about 1.74 pptv per ppbv of ozone (**a**). In case of the AL4021 (HCHO), the interference is rather constant (e. g., 15.0 ± 2.5 pptv), showing orders about the instrumental LOD (9 to 15 pptv), both for a time resolution of 3 s) (**b**). The data point at 4.9 pptv is below the LOD and remains unconsidered.

H_2O_2 measurements are significantly interfered by ozone with a slope of 1.7200 ± 0.0834 pptv ppbv^{-1} and an insignificant intercept. HCHO measurements, however, show evidence for a constant interference around the LOD of the instrument (17 pptv offset), as expected from literature (Kormann

et al., 2003). Table 2.5 shows an exemplary summary on the interference at relevant atmospheric mixing ratios of ozone for the herein performed field studies.

Table 2.5.: Ozone interference quantification for DOMINO, HUMPPA and PARADE. The interference is given per ppbv of O_3 with the 1σ standard deviation (%). Negative values indicate that the H_2O_2 values needed to be downward-corrected. In addition, the interference is given for an ozone mixing ratio of 40 ppbv

Field campaign	O_3 interference $\frac{\text{pptv}\,(H_2O_2)}{\text{ppbv}\,(O_3)}$	Standard deviation (1σ) %	Interference at 40 ppbv of O_3 / pptv (H_2O_2) pptv (H_2O_2)
DOMINO[a]	1.78	3.48	71.2
HUMPPA	1.73	4.83	69.1
PARADE[b]	1.72	2.73	68.8

[a] Stickler (2006).

[b] Hafermann (2011).

2.2.6.6. Other potential interferences for the AL2021 and AL4021

Hydrogen peroxide measurements (AL2021). Sulfur dioxide (SO_2, S(IV)), a medium soluble trace gas is known to undergo liquid phase chemistry with H_2O_2 and organic hydroperoxides (Kelly and Fortune, 1994b; Lee et al., 1991), both causing H_2O_2 losses by yielding sulfuric acid (H_2SO_4, S(IV)).

$$SO_2 + H_2O \rightleftharpoons HSO_3^- + H^+ \tag{2.26}$$

$$H_2O_2 + HSO_3^- \longrightarrow HSO_4^- + H_2O \tag{2.27}$$

For prevention, HCHO is added to the KHP solution, which reacts with SO_2 to the hydroxymethanesulfinate ($HOCH_2SO_3H$) at pH 6, before the fluorescence dye is produced in the liquid flow system (Lazrus et al., 1986).

$$SO_{2(aq)} + HCHO_{(aq)} + H_2O \longrightarrow HOCH_2SO_3H_{(aq)} \tag{2.28}$$

Since H_2O_2 is a strong oxidizing agent, it undergoes redox reactions with metal ions (e. g., Fe(II)) causing its decomposition (Lazrus et al., 1985). Thus, EDTA masks metal ions via the chelate effect (max. 68 µmol, 1.2 ppmv in the liquid phase of the solutions of the hydroperoxide analyzer).
In addition, the ozonolysis of PTFE was reported to cause positive artifacts (Heikes, 1984), which is also potentially for PFA. An interference from such reactions in the inlet line is unlikely since: (i) the residence time is about 6 s and (ii) rather losses of H_2O_2 or HCHO were observed (Section 2.2.6.4). However, the POPHA-peroxidase system is known to interfere with NO leading to negative artifacts, due to the production of 3-nitrohydroxypenylacetic acid instead of the fluorescence dimer (Ischiropoulos et al., 1996). Consequently, adding excess NO to the air sample stream for decreasing the O_3 interference via titration ($NO + O_3 \longrightarrow NO_2 + O_2$) might rather be counterproductive. However, effects caused by NO play a minor role concerning the manufacturer (AL2).

Finally, hydroperoxyl radical-water reactions can potentially lead to the production of H_2O_2 causing positive measurement artifacts in aqueous solutions via two pathways (Bielski et al., 1985):

$$HO_2 + HO_2 \longrightarrow H_2O_2 + O_2 \tag{2.29}$$

$$HO_2 + O_2^- + H_2O \longrightarrow H_2O_2 + O_2 + OH^- \tag{2.30}$$

One limitation hereby is the solubility of HO_2. Its liquid-phase concentration has a major influence on the partitioning to the superoxide (O_2^-). However, for simplicity, Table 2.6 assumes that HO_2 yields instantaneously equimolar fractions of H_2O_2. It accounts for the Henry law coefficient, a representative ambient level and the corresponding mixing ratio in the liquid phase resulting in 20 pptv of H_2O_2.

Besides, ozone-alkene reactions can lead to positive artifacts of H_2O_2 and even two different aldehydes ($R^1(R^2)C=O$ and $R^3(R^4)C=O$) as shown in Equation 2.31 (e. g., Zhang et al. (2009) and the herein cited articles).

$$R^1(R^2)C{=}C(R^3)R^4 + O_3 \xrightarrow{H_2O} R^1(R^2)C{=}O + H_2O_2 + O{=}C(R^3)R^4 \tag{2.31}$$

Table 2.6 lists very low solubilities and mixing ratios in the liquid phase for both O_3 and terpenoids due to their low Henry coefficient (Sander, 1999). The latter are hereby the limiting compound. Assuming three potential double bonds of the terpenoid for ozone-alkene reactions, where each double bond yields equimolar fractions of H_2O_2, an interference of 4.8 pptv is expected. However, those potential positive artifacts are rather insignificant compared to the impact of O_3.

Table 2.6.: Calculated partitioning of selected species causing a potential liquid phase interference at equilibrium. The Henry coefficient K_H is listed for HO_2, O_3 and bulk terpenoids (as a rough estimate, Sander, 1999). Assuming typical tropospheric mixing ratios (ppbv), the stripping efficiency (%) can be calculated. However, if not mentioned otherwise, it is assumed that one stripped molecule instantaneously yields equimolar fractions of H_2O_2. That results in an upper limit of artifact H_2O_2 of 26 pptv for ambient conditions.

Species	Henry coefficient k_H	Ambient mixing ratio ppbv	Stripping efficiency %	Mixing ratio in liquid phase pptv
HO_2	5.7×10^3	0.02	98	20
O_3	1.3×10^{-2}	40	0.012	4.7
Terpenoids[a]	3.0×10^{-2}	2	0.027	1.6[b]

[a] Reacting with ozone in the aqueous phase.

[b] Assuming three potential double bonds for ozone-alkene reactions in average, each yielding 100 % of H_2O_2.

Formaldehyde measurements (AL4021). Besides the reported ozone interference, no detectable interferences were found from: acetone, acetaldehyde, SO_2, NO_2, NO and isobutane (AL4; Dong and Dasgupta, 1987; Kelly and Fortune, 1994a). However, H_2O_2 could cause an interference about 10 pptv ppbv^{-1} under ambient conditions (AL4).

2.2.6.7. Data processing procedure in WaveMetrics IGOR Pro 6

Time, signal (V) and other parameters such as the instrumental state, lamp voltage and ambient temperature were logged at a resolution of 3 s in ASCII format with the V25 data acquisition integrated in the permeation device rack. Data processing and analysis require an easy-to-use procedure (Figure 2.15.) which is able to cope with large files. Therefore, WaveMetrics IGOR Pro 6 was used with a featured procedural programming language. For calculating mixing ratios out of the raw signal via the discussed zeroing and calibration methods a procedure was previously developed (C. Gurk and T. Klippel, priv. comm. 2010) and enhanced as a part of this work. The different instrumental states (zero, calibration or ambient measurement) are automatically sorted with the possibility of manual adjustment, while the time shift delay caused by the liquid flow path is corrected (90 to 120 s). Then the procedure performs linear interpolation between internal and external zeros as well as liquid calibrations once the signal to the respective mode is stable. However, gas-phase calibrations and line loss corrections were applied manually. In a consecutive step the averaging of the data to the time resolution requested for filing is done. The O_3 interference correction was applied manually if necessary.

2.2.6.8. Methodical and instrumental performance for the field studies

After discussing the laboratory procedures, the following section focuses on parameters which describe the methodical and instrumental performance in the field. Table 2.7 gives a summary for the field measurement campaigns DOMINO, HUMPPA and PARADE.

Duty cycle. Duty cycles quantify the operational time of an instrument as a fraction of the entire campaign time. Interruptions include calibration cycles, instrumental failure and power cuts. Typical values range from 50 to 60 % for the AL2021 and the AL4021. The one exception was during PARADE, where the HCHO instrument failed approximately after the middle of the field campaign.

Time resolution. The time resolution is the minimal interval that allows to distinguish between two different mixing ratios. It is determined by the time difference between 10 % (start) to 90 % (end) of the maximum peak value for the liquid calibration running. Due to the peristaltic pump speed being adjusted from campaign to campaign, this time varies. Typical values are 2 to 3 min for hydroperoxide and 2 to 4 min for HCHO measurements. The following parameters will be averaged for an integration time of 5 min.

Limit of detection (LOD). The limit of detection (LOD) was obtained by the automated 30 min zeroing procedure as described in Section 2.2.6.1 for H_2O_2, organic hydroperoxides and HCHO measuremts. In each case, the last 3 min of the interval was averaged and interpolated to perform a drift-correction. The 3σ (pptv) of all the zero measurements were included here.

$$\mathrm{LOD} = 3\sigma(\xi_0) \tag{2.32}$$

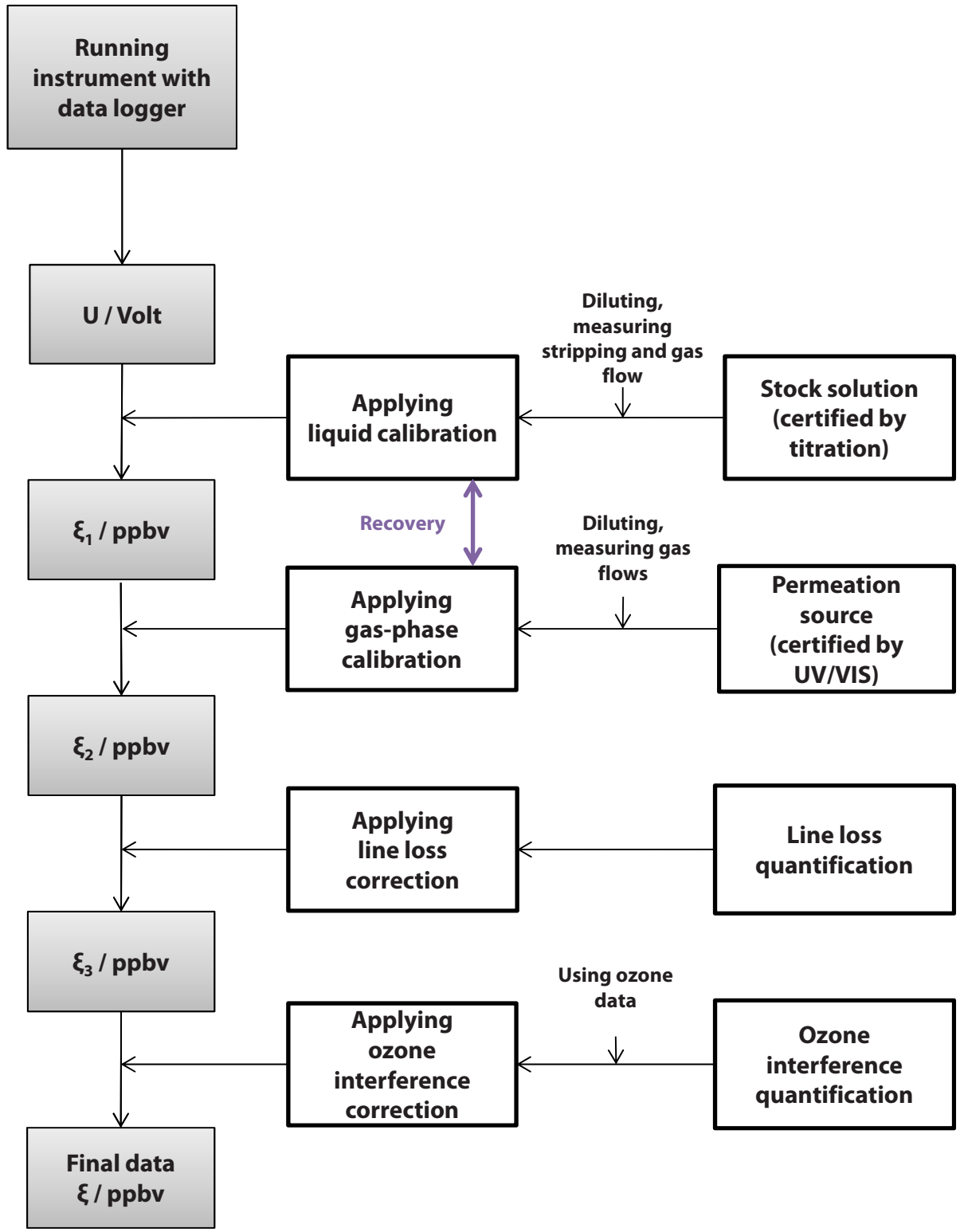

Figure 2.15.: Flow chart for the data processing steps performed on H_2O_2 and HCHO measurements to calculate ambient mixing ratios (ppbv) **from the raw signal** (V)**.** Variables and units are shown (**left**). The data is logged by the V25 in V yielding mixing ratios, ξ_1 (in ppbv), after applying the liquid calibration. Further, the apparent recovery (due to primary gas-phase standards) is quantified obtaining ξ_2. Then, line loss and ozone corrections are performed if necessary in consecutive steps (**middle**). The methods to obtain the different variables are given (**right**).

Recovery R of the internal versus the gas-phase standards. Since both measurement techniques are based on wet chemistry, stripping the sample molecules plays a crucial role. That requires pri-

mary (external, gas-phase) and secondary (internal, liquid-phase) standards leading to small negative differences between quantifying a gas-phase sample via the two standards. Potential causes of sample losses can be:

1. sorption effects on the inside of the tubes of Figure 2.6,
2. heterogeneous chemistry depending on humidity and aerosol load of the tubes,
3. fluctuations in pressure influencing the stripping efficiency
4. and deposited impurities inside the stripping coil.

However, the recovery R (Equation 2.33) is defined as the difference of the gas-phase calibration signal ξ (ppbv) compared to the result using the internal standard μ (ppbv):

$$R = \frac{\mu_{LC}}{\xi_{GC}} \tag{2.33}$$

Under laboratory and campaign conditions from 70 to 80 % of the H_2O_2, while over 88 % of the HCHO is recovered. Thus the correction term is defined as:

$$\frac{1}{R} = \frac{\xi_{GC}}{\mu_{LC}} \geq 1 \tag{2.34}$$

Precision P quantified with gas-phase standards. Each measurement is afflicted with statistical errors likewise gas-phase calibrations, which are the primary calibration method. Thus, the precision for a data resolution of 5 min quantified by gas-phase standards will solely be referred to. It is given as the relative standard deviation (1σ) of the drift corrected signal (ppbv) at a respective mixing ratio and represents the reproducibility of the gas-phase calibration under unchanged conditions. In addition, the figures 2.16 and 2.17 depict a test for the type of distribution for the AL2021 and AL4021, respectively. As a result, the two channels for hydroperoxide measurements show a normal distribution. On the contrary, the data of the HCHO monitor is log-normal distributed due to air bubbles in the liquid flow system. However, they do not affect the herein discussed parameters, since average and median show a difference of solely 0.53 %.

Accuracy as the sum of systematic uncertainties E_S. Systematic errors occur nevertheless how precise the instrument works. Thus, the accuracy is defined as the closeness of the measurement towards the "true" value. In other words, it accounts for the uncertainties of all herein performed corrections and quantifications. These are typical values for both, the AL2021 and the AL4021:

- 8 % at 6 to 7 ppbv for liquid titrations (if not mentioned otherwise),
- 5 % at 0.5 to 4 ppbv for the line loss quantifications,
- 7 % at 5 to 7 ppbv for calibrations of permeation sources (if not mentioned otherwise)
- and 5 % below 200 pptv for the ozone interference.

The list shows the main contributors and quantifying the accuracy, however, is the most difficult point due to other potential systematic uncertainties. Especially in case of the organic hydroperoxides the exact composition and thus the stripping efficiencies are unknown. Consequently, the accuracy was estimated to roughly 50 % (e. g., a moderately soluble hydroperoxide similar to MHP).

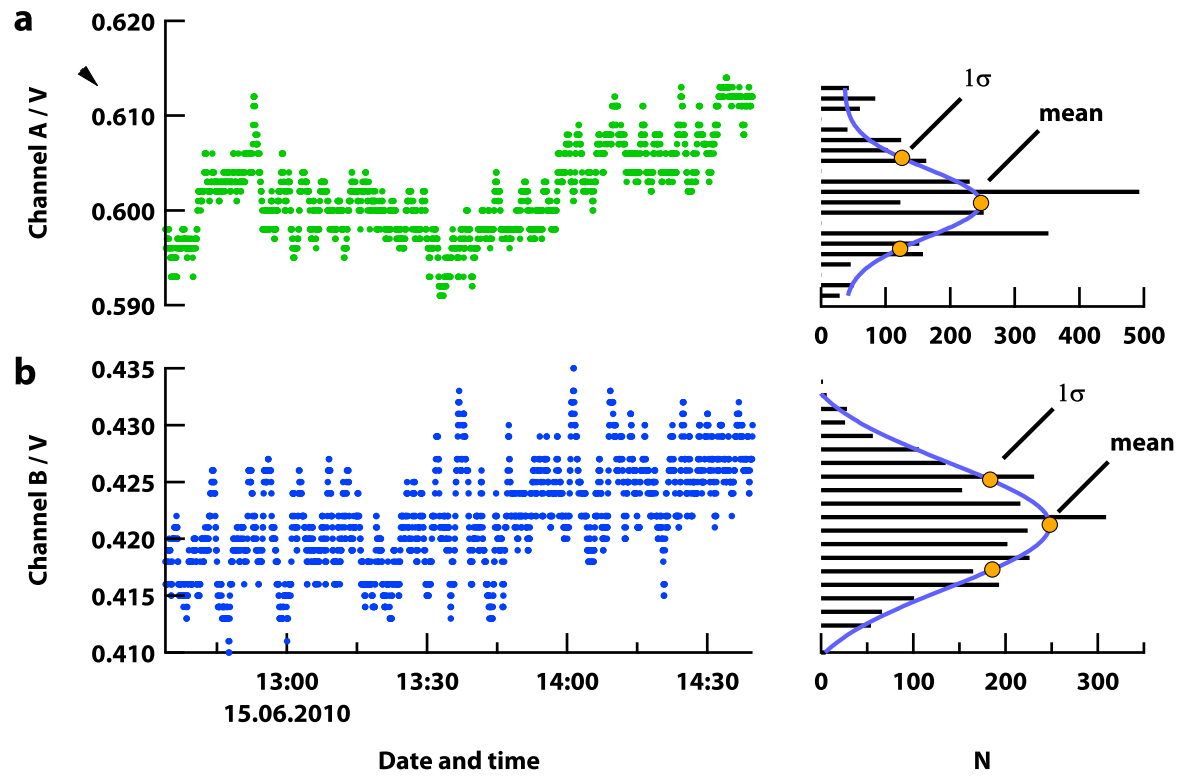

Figure 2.16.: **Normal distribution of the AL2021 for a gas-phase calibration with HUMPPA parameters.** Raw signal (V) of the total peroxide (**a**) and organic channel (**b**) with 3 s readings of a gas-phase calibration (H_2O_2 permeation source at ca. 4 ppbv) for a time period of approximately 3 h (**left**). The horizontal data gaps are caused by the analogue-to-digital converter. Fitted histogram (**right**) including the mean and the 1σ standard deviation (orange dots).

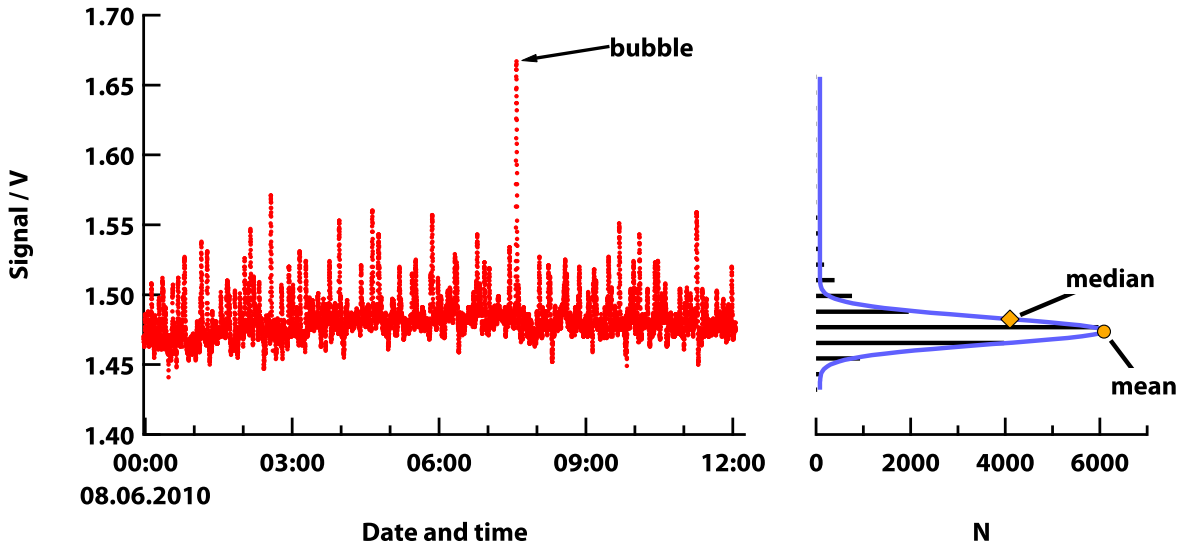

Figure 2.17.: **Log-normal distribution of the AL4021 for a gas-phase calibration with HUMPPA parameters.** Raw signal (V) with 3 s readings of a gas-phase calibration (HCHO permeation source at ca. 6 ppbv) for a time period of approximately 12 h (**left**). The histogram (**right**) includes the most frequently occurring signal, here 1.47 V (orange dot) and the arithmetic mean, here 1.48 V (orange diamond) showing a deviation of 0.53 %. The log-normal distribution is presumably caused by air bubbles which bias the calibration signal to higher values.

Typical accuracies for H_2O_2 are in orders of 16 % (at the same mixing ratios as given for the precision). The one exception is DOMINO which lacks a line loss quantification and thus accounts for 20 % of uncertainty. For HCHO typical accuracies show values of 13 %.

Total measurement uncertainty (TMU). The absolute propagation of errors is shown in Equation 2.35 with the terminology of Section 2.2.6.7, where Δx_i is the uncertainty in the data process step i yielding $\Delta\xi$

$$\Delta\xi = \sqrt{\sum_{i=1}^{n}\left(\frac{\partial\xi}{\partial x_i}\cdot\Delta x_i\right)^2} \tag{2.35}$$

Some transformations lead to the relative uncertainty:

$$\frac{\Delta\xi}{\xi} = \sqrt{\sum_{i=1}^{n}\left(\frac{\Delta x_i}{x_i}\right)^2} \tag{2.36}$$

However, in the context of the definition paragraphs above, the relative total measurement uncertainty (TMU) in % at a corresponding mixing ratio ξ is obtained by embodying the precision P as well as the sum of systematic errors $\sum E_S$ at certain gas-phase mixing ratio (e. g., H_2O_2, 4 ppbv; HCHO, 6 ppbv):

$$TMU^2 = P^2 + \sum E_S^2 \tag{2.37}$$

Including the previously discussed precision and accuracy, typical TMUs for a time resolution of 5 min are dominated by systematic uncertainties. As a result, hydroperoxide are afflicted with roughly 16 %, HCHO measurements with 13 % total uncertainty.

2.2.7. Instruments and performances for other species

Studying H_2O_2 and HCHO requires various information on physical parameters, chemical precursor and sink species. Table 2.8 lists measurements techniques, performances and operators for the herein used instrumental data, which were provided at 5 min resolution for HUMPPA and 10 min for DOMINO and PARADE.

Meteorological parameters. Meteorological parameters, such as temperature, pressure, relative humidity, wind speed and direction, during DOMINO and PARADE were determined by the MoLa (mobile aerosol research laboratory) (Diesch et al., 2012). The vehicle is equipped with a commercial weather station (model: WXT520, Vaisala, Finland) and other instruments for observing aerosols and trace gases (O_3, SO_2, CO, CO_2, NO and NO_2). Wind data for PARADE was intercompared to those from the HLUG (Hessisches Landesamt für Umwelt und Geologie), evaluated in this work. However, the SMEAR II station (HUMPPA) is equipped with a mast (73 m high) which is located several hundred meters from the site. It allows gradient measurements of meteorological and physical parameters in addition to determining trace gas fluxes at 6 different heights (4.2, 8.4, 16.8, 33.6, 50.4 and 67.2 m) by various instruments. However, only relevant measurements will be further considered. Temperature and pressure were measured with a ventilated and shielded Pt-100 sensor (16.8 m) and a digital barometer at ground height (Druck series, model: DPI 260; Transcat,

Table 2.7.: Summary of the instrumental performances during the field measurement campaigns. The performance for hydroperoxides (AL2021) and formaldehyde (AL4021) is given depending on the field studies: DOMINO, HUMPPA and PARADE. For comparability reasons all parameters are given for a data resolution of 5 min. The duty cycle quantifies the on-line time throughout the whole campaign. Time resolution means the minimum time of distinguishing between two different ambient mixing ratios. Accuracy in this case means the sum of systematic uncertainties $\sum E_S$. All values given in % are related to the respective mixing ratio of the precision P. The latter means the reproducibility of the primary gas-phase calibration. As a result of the propagation of errors the total measurement uncertainty (TMU) is given as TMU = $\sqrt{P^2 + {E_S}^2}$.

	DOMINO 2008	HUMPPA 2010	PARADE 2011
Location	El Arenosillo, Spain	Hyytiälä, Finland	Kleiner Feldberg, Germany
Period	Nov to Dec	mid-Jul to mid-Aug	Aug to Sep
AL2021 (H_2O_2)			
Duty cycle	57 %	53 %	66 %
Time resolution / s	189	114	135
LOD (3σ) / pptv	13.9	37.6	73.9
Recovery	70.9 %	75.0 %	82.6 %
Precision (3σ)	3.05 % at 3.73 ppbv	1.74 % at 4.25 ppbv	9.90 % at 3.78 ppbv
Accuracy	24.2 %[a]	15.5 %	15.5 %
TMU	24.4 %	15.6 %	18.4 %
AL2021 (ROOH)			
LOD (3σ) / pptv	33.1	71.7	93.6
Precision (3σ)	6.10 % at 69.4 pptv	3.48 % at 479 pptv	19.8 % at 84.6 pptv
Accuracy[b]	50.5 %	50.5 %	50.5 %
TMU	50.9 %	50.6 %	54.2 %
AL4021 (HCHO)			
Duty cycle	69 %	52 %	35 %
Time resolution / s	141	186	219
LOD (3σ) / pptv	80.8	20.8	122
Recovery	87.7 %	96.5 %	88.8 %
Precision (3σ)	2.26 % at 10.5 ppbv	3.02 % at 6.42 ppbv	14.2 % at 6.82 ppbv
Accuracy	12.8 %	12.8 %	12.8 %
TMU	13.0 %	19.0 %	19.1 %

[a] Line loss quantification unavailable. Assuming a moderate value of 20 % according to Table 2.4.

[b] Assuming 50 % of systematic uncertainty due to missing stripping efficiency α, O_3 interference and line loss quantification.

Rochester, NY, USA), respectively. Wind speed and direction were determined at 16.8 m by an ultrasonic anemometer (Adolf Thies GmbH & Co. KG, Göttingen, Germany). Relative humidity was obtained indirectly by a chilled mirror dew point monitor (model: Hygro E4, GE General Eastern, CT, USA).

j(NO_2) – Filter radiometer. Radiometry is a common method employing optical instruments with photoelectric detectors for measuring the photodissociation of molecules, for instance O_3 and NO_2:

$$O_3 + h\nu \longrightarrow O(^1D) + O_2^*, \lambda < 325\,nm \quad (2.38)$$

$$NO_2 + h\nu \longrightarrow NO + O(^3P), \lambda < 420\,nm \quad (2.39)$$

The photolysis rate of NO_2 (j(NO_2)) was determined by two (up- and downward) 2π-steradian filter radiometers which quantify the the UV actinic flux (Junkermann et al., 1989). Calibrations were performed once per campaign versus an actinic spectral radiometer in cooperation with the Forschungszentrum Jülich, Germany (R. Koenigstedt, priv. comm. 2011) and were stable within a range of 2 % for one year. The instrument has a total uncertainty of roughly 12 %. Other photolysis rates such as j(H_2O_2), j(HCHO) and j(HONO) were parametrised by use of the measured j(NO_2) and j(O^1D) data (Holland, 2003).

NO, NO_2 and O_3 – Chemiluminescence detector (CLD). Nitric oxides, NO and NO_2 were measured by a modified (Hosaynali-Beygi, 2010) three-channel chemiluminescence detector (model: CLD 790 SR; ECOPhysics, Durnten, Switzerland). NO is quantified via the reaction with excess O_3 yielding equimolar fractions of an excited NO_2* (channel 1): $NO + O_3 \longrightarrow NO_2^* + O_2$. The relaxation of NO_2* to NO_2 emits a photon which is quantified. Measuring NO_2 (channel 2) itself is performed with preceding photolytic conversion to NO in a blue light converter (Droplet Measurement Technologies, Boulder, CO, USA).
Although the technique is able to quantify O_3 through excess NO (channel 3), it was measured conventionally via UV-absorption (model: 49C; Thermo-Electron, Waltham, MA, USA) for HUMPPA and PARADE due to an instrumental failure of the CLD ozone channel. Calibrations are performed with a NIST-NO standard. Ozone was measured with a LOD of 1 ppbv by the MoLa instrumentation (model: Airpointer; Recordum GmbH, Wiener Neudorf, Austria) during DOMINO.

OH and HO_2 – Laser-induced fluorescence (LIF). OH is crucial for estimating the oxidising capacity. It is highly reactive and its life time is short (maximum 10 s) and thus ambient mixing ratios are of the order of pptv. The LIF instrument is based on laser-induced fluorescence of OH providing high time resolution and sensitivity (Hard et al., 1984; Holland et al., 1995). The technique converts HO_2 with NO to OH. The fast reaction of $RO + O_2 \longrightarrow R'CHO + HO_2$ yields hydroperoxy radicals, which may cause a positive interference for the HO_2 signal. Consequently, depending on the mixing ratios of RO_2, interferences up to 95 % are possible (Fuchs et al., 2011).
DOMINO is a special case due to a potential interference in the OH mixing ratios of about 60 % between 10 and 15 hours (UTC) (E. Regelin, priv. comm. 2011). Thus, OH and HO_2 data are considered as upper limits.

OH reactivity – Comparative reactivity method (CRM). The total OH-reactivity was measured using the CRM method (Sinha et al., 2008). Pyrrole is absent in ambient air and therefore useful to measure the concentration drop-down by the reaction with artificial OH in zero air (calibra-

tion). The pyrrole is quantified with a PTR-MS instrument. However, immediate flush with ambient air including ambient VOCs and constant pyrrole yields the OH reactivity by the changed concentration drop-down. It is caused by competition of ambient VOCs with pyrrole (ambient measurement). The difference between the calibration and the ambient signal yields allows the determination of the OH reactivity.

HCHO – Differential optical absorption spectroscopy (DOAS). The DOAS technique used for the herein presented data is a spectroscopic technique which uses an artificial light source such as a high-pressure Xe lamp or a laser (Platt and D. Perner, 1980). The light travels over a well-known path length of several hundred meters to kilometers to a reflector and then back to the source. The detector retrieves the absorbance, which allows to obtain trace gas mixing ratios by Beer-Lambert law. As every molecule has its individual absorption properties, several trace gas species can be quantified simultaneously depending on the used light source.

HONO – Long path absorption photometer (LOPAP). This technique quantifies nitrous acid (HONO) using a stripping coil and continuous liquid flow chemistry (Heland et al., 2001). HONO is sampled and converted into an azo dye, which is consecutively detected in a long path absorption photometer: the absorption cell consists of a long Teflon tube, where visible light is focused via fiber optics on one side, while the other is equipped with the liquid core waveguide (LCW). Then, another glass fiber transmits the light to the minispectometer.

Biogenic VOCs – GC-MS. H_2O_2 and HCHO are major products of radical chain terminations. VOCs are oxidizes by OH and O_3 yielding RO_x and play therefore a crucial role on versatile radical budgets. Thus, comprehensive VOC measurements are necessary. Gas chromatography with mass spectrometry detection is a reliable tool for analyzing complex gas-phase mixtures. It combines the benefits of a gas chromatograph and a mass spectrometer: the trace chemical species are separated on the column and consecutively ionized by an ion source. Separation and detection take place for instance in a quadrupole mass spectrometer and depends on mass-to-charge ratio. A GC-MS can quantify many sample molecules specifically, sensitively and simultaneously typical analysis times limit the time resolution to approximately 1 h. Methane was quantified by a novel technique (fast GC), while monoterpenes and isoprene employing GC-MS. One exception is the isoprene data set during PARADE, which was obtained by PTR-MS.

Table 2.8.: Measurement techniques and performances.

Species	Technique	LOD	TMU	Reference
DOMINO 2008				
H_2O_2	dual-enzyme	see Table 2.7	see Table 2.7	this work[a]
HCHO	Hantzsch	see Table 2.7	see Table 2.7	this work[a]
O_3	UV	1 ppbv	—	(Diesch et al., 2012)
NO, NO_2	CLD	6 pptv, 8 pptv	5 %, 8 %	(Z. Beygi, priv. comm. 2012)
PAN	GC-ECD	50 pptv	—	(E. Liakakou, priv. comm. 2012)
HONO	LOPAP	2.5 pptv	12 %	(Soergel et al., 2011)
OH, HO_2	LIF	16 ppqv, 0.33 pptv	18 %, 18 %	(Regelin, 2011)
OH reactivity	CRM	3.5 s^{-1}	20 %	(Sinha et al., 2012)
Biogenic VOCs	GC-MS	—	—	(Song et al., 2012)
Meteorology	Vaisala WXT510	—	—	(Diesch et al., 2012)
j(NO_2)	filter radiometer	—	15 %	Meteorologie consult, Königstein, Germany
HUMPPA 2010				
H_2O_2	dual-enzyme	see Table 2.7	see Table 2.7	this work
HCHO	Hantzsch	see Table 2.7	see Table 2.7	this work
O_3	UV	1 ppbv	4 ppbv or 1.6 %	(Williams et al., 2011)
NO, NO_2	CLD	10.3 pptv, 14.2 pptv	5 %, 6 %	(Williams et al., 2011)
PAN	CIMS	—	10 pptv or 4 %	(Phillips et al., 2013)
HONO	LOPAP	5 pptv	10 %	(R. Oswald, priv. comm. 2012)
OH, HO_2	LIF	—, —	30 %, 30 %	(Williams et al., 2011)
OH reactivity	CRM	3.5 pptv	16 %	(Nölscher et al., 2012b)
Biogenic VOCs	GC-MS	10 pptv	15 %	(Yassaa et al., 2012)
Meteorology	SMEAR II	—	—	(Williams et al., 2011)
j(NO_2)	filter radiometer	—	15 %	(Williams et al., 2011)
j(O^1D)	filter radiometer	—	15 %	(Williams et al., 2011)
Other photolysis	parametrization	—	10 %	(B. Bohn, priv. comm. 2012)
PARADE 2011				
H_2O_2	dual-enzyme	see Table 2.7	see Table 2.7	this work
HCHO	Hantzsch	see Table 2.7	see Table 2.7	this work
	DOAS	50 pptv[b]	5 %	(D. Pöhler, priv. comm. 2012)
O_3	UV	1 ppbv	4 ppbv or 1.6 %	(Reiffs, 2012)
NO, NO_2	CLD	4 pptv, 55 pptv	4 %, 10 %	(Reiffs, 2012)
PAN	CIMS	—	20 %	(G. Phillips, priv. comm. 2012)
HONO	LOPAP	7 pptv	10 %	(L. Xin, priv. comm. 2012)
OH, HO_2	LIF	—, —	30 %, 30 %	(K. Hens, priv. comm. 2012)
OH reactivity	CRM	4 s^{-1}	—	(Nölscher et al., 2012a)
Biogenic VOCs	GC-MS	1 pptv	15 %	(W. Song, priv. comm. 2012)
Meteorology	MoLa	—	—	(J. Fachinger, priv. comm. 2012)
j(NO_2)	filter radiometer	—	15 %	(R. Koenigstedt, priv. comm. 2011)
j(O^1D)	filter radiometer	—	15 %	(R. Koenigstedt, priv. comm. 2011)
Other photolysis	parametrization	—	10 %	(B. Bohn, priv. comm. 2012)

[a] Measurements performed by Heiko Bozem.

[b] Typical LOD.

3. Data analysis, results and discussion

3.1. Observations in Europe

Several physical and photochemical factors influence the budgets of hydrogen peroxide (H_2O_2), organic hydroperoxides (ROOH), formaldehyde (HCHO) and ozone (O_3). However, nitric oxides (NO_x) and volatile organic compounds (VOCs) have a high impact on photochemistry and the ambient levels of those species. This section is based on comprehensive data from three field measurement campaigns: DOMINO (Spain), HUMPPA (Finland) and PARADE (Germany). First, location, meteorology, ambient levels and transport for day- and nighttime are described. Then, the focus is set on the daytime trends for H_2O_2, HCHO and O_3. The data set shows evidence for different regimes concerning the NO_x and VOC levels. The discussion includes the role of nitric monoxide (NO), if the production of hydroperoxides or aldehydes is favored.

3.1.1. Back-of-the-envelope calculations for the trend analysis in Europe

This section focuses on calculations beyond descriptive statistics for DOMINO, HUMPPA and PARADE which are an integral part of Section 3.1 in Chapter 3: deviations from the photostationary state and hydroxyl radical (OH) production rates for daytime.
All the following calculations are based on the steady-state assumption (Equation 3.1). It is assumed that the production $P(X)$ and loss terms $L(X)$ are approximately at equilibrium for infinitesimal changes of mixing ratios for a species X (e. g., O_3, H_2O_2 or HCHO) with time t.

$$\frac{d[X]}{dt} = P(X) - L(X) \approx 0 \tag{3.1}$$

That allows to estimate missing observational data and to enrich the scientific overview. One central aspect is the determination of total peroxy radical mixing ratios, $[RO_x]$ ($= [HO_2] + \sum_i [R_iO_2]$) and their impact on O_3, ambient hydroperoxides and HCHO.

3.1.1.1. Deviations from the photostationary state

If O_3 is the sole oxidant for NO (Equation 3.2), ambient NO, NO_2 and O_3 can be assumed to be at photostationary state for constant radiation levels when local NO_x sources are absent. As a consequence, after NO_2 photolysis (Equation 3.3), O_3 is recycled (Equation 3.4).

$$O_3 + NO \longrightarrow NO_2 + O_2 \tag{3.2}$$

$$NO_2 + h\nu \longrightarrow NO + O(^3P) \tag{3.3}$$

$$O(^3P) + O_2 \xrightarrow{M} O_3 \tag{3.4}$$

Moreover, the mixing ratio of O_3, $[O_3]$, can be expressed by Equation 3.5 or as the Leighton ratio ϕ (Equation 3.6, Leighton, 1961). In general, ϕ equals to 1 in photostationary state and expresses the ratio between O_3 production and loss rates (ppbv h^{-1}).

$$[O_3] = \frac{j(NO_2)[NO_2]}{k_{3.2}[NO]} \tag{3.5}$$

$$\phi = \frac{j(NO_2)[NO_2]}{k_{3.2}[O_3][NO]} \tag{3.6}$$

However, other species apart from O_3 can oxidize NO, e. g., hydroperoxy (HO_2) and all organic peroxy radicals (R_iO_2), such as methyl hydroperoxy (CH_3O_2), acetyl ($CH_3C(O)O_2$) and halogen monoxides (XO).

$$HO_2 + NO \longrightarrow NO_2 + HO \tag{3.7}$$

$$R_iO_2 + NO \longrightarrow NO_2 + R_iO \tag{3.8}$$

$$XO + NO \longrightarrow NO_2 + X \tag{3.9}$$

When considering these reactions, the values for ϕ are above unity and that requires an extension of Equation 3.6 (Hauglustaine et al., 1999).

$$\overbrace{\frac{j(NO_2)[NO_2]}{k_{3.2}[O_3][NO]}}^{\phi} = 1 + \frac{(k_{3.7}[HO_2] + k_{3.8,i}\sum_i [R_iO_2])\,\cancel{[NO]}}{k_{3.2}[O_3]\cancel{[NO]}} \tag{3.10}$$

Observations usually comprise $j(NO_2)$, NO, NO_2 and O_3 data. Equation 3.10 has two unknowns, $[HO_2]$ and $\sum_i [R_iO_2]$, and thus allows solely the estimation of $[RO_x]$. However, HO_2, CH_3O_2 and $CH_3C(O)O_2$ (to a lesser extent) are the most abundant peroxy radicals (Cantrell et al., 1996; Lightfoot et al., 1992). Their rate coefficients for the reaction with NO are similar (see Table E.1 in the appendix Chapter E). That allows to express $k_{3.7}$ and $k_{3.8,i}$ as k' which is weighted by the abundance of HO_2, CH_3O_2 and $CH_3C(O)O_2$. In addition, the contribution of halogen monoxides and unknown oxidants is neglected for DOMINO, HUMPPA and PARADE ($k_{3.9}[XO] \approx 0$) yielding the following expression

$$[RO_x] = \frac{j(NO_2)\,[NO_2] - k_{3.2}\,[O_3]\,[NO]}{k'\,[NO]} \tag{3.11}$$

Sources of uncertainty for ϕ. The use of ϕ as a central point for other calculations requires an error estimation. The relative uncertainty $\frac{\Delta\phi}{\phi}$ is expressed by

$$\frac{\Delta\phi}{\phi} = \sqrt{\left(\frac{\Delta j(NO_2)}{j(NO_2)}\right)^2 + \left(\frac{\Delta NO_2}{NO_2}\right)^2 + \left(\frac{\Delta k'}{k'}\right)^2 + \left(\frac{\Delta O_3}{O_3}\right)^2 + \left(\frac{\Delta NO}{NO}\right)^2} \tag{3.12}$$

This includes the uncertainties of the measured parameters ($\Delta j(NO_2)$, ΔNO_2, ΔO_3 and ΔNO). However, $\frac{\Delta k'}{k'}$ was estimated: assuming fractions of 50 % $[HO_2]$ ($k_{3.7} = 8.5 \times 10^{-12}$ cm^3 s^{-1}), 25 %

of $[CH_3O_2]$ ($k_{3.8} = 7.7 \times 10^{-12}$ cm^3 s^{-1}) and 25 % of $[CH_3C(O)O_2]$ ($k_{3.8} = 2.0 \times 10^{-11}$ cm^3 s^{-1}) of total $[RO_x]$ leads to $\frac{\Delta k'}{k'} = 31.5\,\%$ at 8.5×10^{-12} cm^3 s^{-1} that was used for the calculations.
Peroxyacetyl nitrate (PAN), as an NO_2 source through thermal decomposition, has an influence on the calculated daytime ϕ: 2.60 % (DOMINO, [PAN] = 0.566 ppbv), 9.31 % (HUMPPA, 0.241 ppbv) and 1.47 % (PARADE, 0.401 ppbv). However, the observed mixing ratios of O_3 and NO_x are higher than in those reported in previous studies; therefore PSS is assumed to be established (relevant for DOMINO); the typical XO mixing ratios contribute for only 3 % to ϕ.
All the discussed effects add to relative 1σ uncertainties on ϕ as follows: 202 % for DOMINO, 132 % for HUMPPA and 168 % for PARADE.

3.1.1.2. Calculations of hydroxyl radical production rates

Due to the lack of comprehensive OH observations for DOMINO, HUMPPA and PARADE, a different approach was required to study this aspect of oxidation chemistry. Therefore, primary and secondary OH production rates were calculated. The primary quantifies OH radicals produced from O_3 photolysis, whereas the secondary quantifies OH radicals produced from other sources, for instance $HO_2 + NO \longrightarrow NO_2 + OH$.

Primary OH production. The primary OH production is determined by the O_3 photolysis, while the intermediate $O(^1D)$ is either quenched by air molecules or reacts with water vapor yielding OH (Warneck, 1975).

$$O_3 + h\nu \longrightarrow O(^1D) + O_2(^1\Delta_g) \tag{3.13}$$

$$O(^1D) \xrightarrow{N_2} O(^3P) \tag{3.14}$$

$$O(^1D) \xrightarrow{O_2} O(^3P) \tag{3.15}$$

$$O(^1D) + H_2O \longrightarrow 2\,OH \tag{3.16}$$

Therefore, the primary OH production rate $P_0(OH)$ is expressed as:

$$P_0(OH) = \frac{2k_{3.16}[H_2O]j(O^1D)[O_3]}{k_{3.14}[N_2] + k_{3.15}[O_2] + k_{3.16}[H_2O]} \tag{3.17}$$

Secondary OH production. There is no uniformity in the usage of the term "secondary OH production rate" (here $P_S(OH)$ in ppbv h^{-1}). However, the following reactions play a crucial role as secondary hydroxyl sources (Lelieveld, 2002).

$$HO_2 + NO \longrightarrow NO_2 + OH$$

$$HO_2 + O_3 \longrightarrow 2\,O_2 + OH \tag{3.18}$$

$$HONO + h\nu \longrightarrow NO + OH \tag{3.19}$$

$$H_2O_2 + h\nu \longrightarrow 2\,OH \tag{3.20}$$

$$ROOH + h\nu \longrightarrow RO + OH \tag{3.21}$$

$$O_3 + BVOC \longrightarrow products + OH \tag{3.22}$$

The production terms of equations 3.7 and 3.18 show the highest overall contribution on secondary OH. Thus, $P_S(OH)$ is defined as the sum of the production terms, if not mentioned otherwise in the following chapters.

3.1.1.3. Calculations of the hydrogen peroxide budget

Table 3.1 lists the production and sink terms that were used in the following discussions. The considerations are completely based on the mean daytime measurements listed in Table 2.8. Due to incomplete observations for all the three campaigns, the effect of alkene oxidation via O_3 and OH was neglected. As discussed in the HUMPPA chapter, alkene-OH reactions have an insignificant impact on H_2O_2 production. In contrast, the omission of alkene-O_3 reactions possibly underestimates H_2O_2 production by approximately 20 %. Compared to DOMINO and PARADE, the HUMPPA campaign had the highest levels of BVOCs. On the sink side, the H_2O_2 photolysis rate $j(H_2O_2)$ was parametrized (Holland, 2003) using filter radiometer data (Table 2.8).

Table 3.1.: Calculation of the H_2O_2 budget.

Reaction	Expression
Production (P)	
$HO_2 + HO_2 \longrightarrow H_2O_2 + O_2$	$k[HO_2][NO]$
Losses (L)	
$H_2O_2 + h\nu \longrightarrow 2\,OH$	$j(H_2O_2)[H_2O_2]$
$H_2O_2 + OH \longrightarrow H_2O + HO_2$	$k[H_2O_2][OH]$

3.1.1.4. Simplified calculation of the formaldehyde budget

Table 3.2 lists the simplified production and sink terms for HCHO. The considerations are completely based on the mean daytime measurements listed in Table 2.8. Due to incomplete observations for all the three campaigns, the effect of alkene oxidation via O_3 and OH was neglected, except for the isoprene–OH reaction. As discussed in the HUMPPA chapter, alkene–OH and alkene–O_3 reactions possibly affect HCHO production up to 15 %. Compared to DOMINO and PARADE, HUMPPA had the highest levels of BVOCs and therefore it can be seen as an upper estimate. On the sink side, the HCHO photolysis rate, j(HCHO), was parametrized (Holland, 2003) by using filter radiometer data (Table 2.8).

Table 3.2.: Simplified calculation of the HCHO budget.

Reaction	Expression
Production (P)	
$CH_3O_2 + NO + O_2 \longrightarrow HCHO + NO_2 + HO_2$	$k[CH_3O_2]_{SS}[NO]$
$CH_3OH + OH + O_2 \longrightarrow HCHO + H_2O + HO_2$	$k[CH_3OH][OH]$
Isoprene + OH $\longrightarrow$ 0.6 HCHO + products	$0.6\,k$[Isoprene][OH]
Losses (L)	
$HCHO + OH \longrightarrow HCO + H_2O$	$k[HCHO][OH]$
$HCHO + h\nu \longrightarrow HCO + H_2O$	$j(HCHO)_{rad}[HCHO]$
$HCHO + h\nu \longrightarrow H_2 + CO$	$j(HCHO)_{mol}[HCHO]$

3.1.2. Meteorology during the field campaigns

Table 3.3 and Figure 3.1 give an overview on daytime meteorological parameters, such as the photolysis rates for NO_2 ($j(NO_2)$ in s^{-1}) and O_3 ($j(O^1D)$ in s^{-1}), temperature (°C), relative (%) and absolute humidity (ppmv), wind speed ($m\,s^{-1}$) and ambient pressure (hPa) during DOMINO, HUMPPA and PARADE. $j(NO_2)$ was in comparable ranges for all field campaigns, where DOMINO showed peak values ($4.21 \times 10^{-3}\ s^{-1}$), just as for $j(O^1D)$ (7.75×10^{-6}). Highest average daytime temperatures were observed during HUMPPA (20.8 °C), whereas DOMINO was coldest (13.3 °C). The relative humidity was comparable for DOMINO and HUMPPA (64.5 to 69.1 %), although highest values were observed during PARADE (75.1 %). On the contrary, DOMINO significantly showed lowest levels of absolute humidity (9717.4 ppmv) in comparison to HUMPPA (17 344 ppmv) and PARADE (14 522 ppmv). The wind speed was comparable for DOMINO ($2.6\,m\,s^{-1}$) and HUMPPA ($2.1\,m\,s^{-1}$) with maximum values for PARADE ($3.6\,m\,s^{-1}$). Highest ambient pressure was observed during DOMINO (1011.7 hPa) and lowest during PARADE (921 hPa).

Table 3.3.: Daytime averages of observed meteorological parameters for DOMINO, HUMPPA and PARADE. Average values are given with relative variabilities in % (1σ).

		DOMINO		HUMPPA		PARADE	
Species	Unit	Average	1σ / %	Average	1σ / %	Average	1σ / %
jNO_2	s^{-1}	4.21×10^{-3}	74.0	3.57×10^{-3}	71.5	3.74×10^{-3}	73.3
$jO(^1D)$	s^{-1}	3.95×10^{-6}	104	6.44×10^{-6}	95.0	7.57×10^{-6}	99.5
Temperature	°C	13.3	28.6	20.8	19.9	15.4	29.7
Rel. humidity	%	64.5	29.7	69.1	25.2	75.1	20.4
Abs. humidity	ppmv	9717.4	33.6	17 344.7	19.7	14 522.3	25.5
Wind speed	$m\,s^{-1}$	2.6	45.9	2.1	44.9	3.6	46.7
Amb. pressure	hPa	1011.7	0.500	993.6	0.400	921.0	0.300

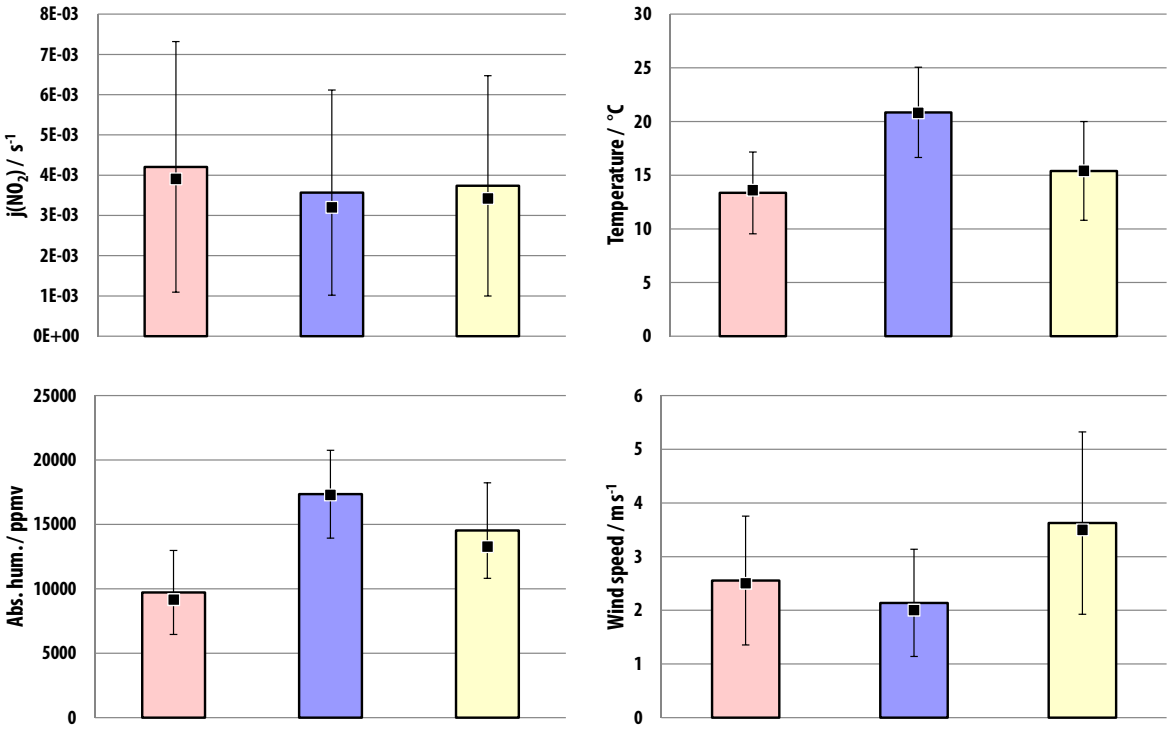

Figure 3.1.: Bar charts representing the observed daytime trends of meteorological parameters for DOMINO (red), HUMPPA (blue) and PARADE (yellow). Bars show averages, markers medians and error bars variabilities (1σ) of all available data points (5 min time resolution for HUMPPA and 10 min for DOMINO and PARADE). $j(NO_2)$ shows no significant differences for all field campaigns. However, ambient temperatures and absolute humidity were highest during HUMPPA, followed by PARADE and DOMINO. Minimum values for wind speed were observed during HUMPPA, followed by DOMINO and PARADE. DOMINO shows the coldest (13.3 °C, Mediterranean winter) and HUMPPA the warmest (20.8 °C, Northern summer) conditions, while the radiation levels vary with season, latitude and wavelength. jNO_2 are comparable in case of HUMPPA and PARADE, whereas the highest values were observed for DOMINO (4.21×10^{-3} s^{-1}). The highest relative humidity and wind speed were observed during PARADE (75.1 % and 3.6 m s^{-1}, respectively).

3.1.3. Observations of H_2O_2, HCHO and selected trace gases

3.1.3.1. Time series of H_2O_2 and HCHO

Figure 3.2 shows the time series of H_2O_2 and HCHO mixing ratios (both in ppbv) including $j(NO_2)$ (s^{-1}) for DOMINO (Nov 21-Dec 9 2008), HUMPPA (Jul 12-Aug 12 2010) and PARADE (Aug 15-Sep 10 2011). In addition, Table 3.4 lists the daytime average values for H_2O_2 and HCHO and related chemical trace gas species for the entire campaigns.

DOMINO 2008. H_2O_2 levels showed pronounced diurnal cycles during the first 5 days (Nov 21-25) of the field campaign, contrary to the rest of the time. Daytime mixing ratios were 82 ± 59 pptv on average (median: 68 pptv) and reached maximum levels of 306 pptv (minimum below the LOD). HCHO underwent cycles as well, especially from Nov 21-29, while it followed less the day-night rhythm in comparison to H_2O_2. After that period only two days, Nov 28 and Dec 3, showed significant daytime increases of the mixing ratios. The daytime averages were 569 ± 337 pptv

(median: 539 pptv), with maximum values of 2.37 ppbv (minimum below the LOD).

No direct comparative data for in-situ gas-phase hydroperoxides and HCHO measurements were available for the DOMINO site. However, several observations in the Mediterranean (Central Portugal) were performed in summer, ranging from below the LOD to 630 pptv (Jackson and Hewitt, 1996).

HUMPPA 2010. Throughout the entire field campaign, H_2O_2 mixing ratios showed very pronounced diurnal cycles. Average daytime mixing ratios were 639 ± 648 pptv (median: 409 pptv) and maximum levels of 3.86 ppbv were reached from Jul 12-15 and on Jul 26. The observed HCHO mixing ratios varied smoother with a daytime average of 465 ± 558 pptv (median: 276 pptv). Maximum values of 5.66 ppbv (minimum: 34 pptv) were reached between Jul 26 and 31.

So far, H_2O_2 measurements have not been performed at the SMEAR II site (Hyytiälä). However, ambient mixing ratios in Canadian and Swedish boreal forests were reported for midsummer: H_2O_2 ranged from 0.5 to 1.5 ppbv (Nipawin, Saskatchewan, 53 54 °N 104 31 °E, 579 m a.s.l.; Hall and Claiborn, 1997), respectively from 0.05 to 2 ppbv in a remote coniferous forest (Jädraås, 60°48′ N, 16°30′ E, 185 m a.s.l.; Ross et al., 1992). HCHO, among other aldehydes and ketones, was observed before during springtime (2003) in Hyytiälä at levels of 358 pptv (24 h average; Hellén et al., 2004). Considerably higher average levels in Jul (967 pptv) and (671 pptv) Aug were reported in Norway (Birkenes, 58°20′ N, 8°14′ E; Solberg et al., 1996).

PARADE 2011. H_2O_2 followed the day-night rhythm with pronounced periods from Aug 15-27 and Sep 2-4 reaching daytime maximum values of 1.77 ppbv (minimum below the LOD). The other days varied smoother. On an average, daytime levels were 323 ± 264 pptv (median: 236 pptv). HCHO data were only available from Aug 16 to 30 due to an instrumental failure. However, it showed a significant diurnal cycling reaching a daytime maximum of 5.2 ppbv (minimum below the LOD). The average levels were 1.56 ± 1.06 ppbv (median: 1.40 ppbv).

In comparison, hydroperoxide concentrations above limit of detection (50 to 500 pptv) were observed in Oct 2000 on the mount Kleiner Feldberg (Wiesufer et al., 2002). At a comparable site in Germany, Papstthum (around Berlin), maximum H_2O_2 mixing ratios of 1.4 ppbv were reported for the afternoon (Aug 1998; Grossmann, 2003). The HCHO levels of 4.5 ppbv (Mihelcic, 2003) are comparable to the herein presented results. Besides, 0.33 ppbv of H_2O_2 and 1.97 ppbv of HCHO were observed in a Norway spruce forest during Jun 2001 in north-east Bavaria, Germany (775 m a.s.l.; Klemm et al., 2006). A comparable study during summer 2002 reported up to 6.5 ppbv of HCHO also in a Norway spruce forest (research station "Waldstein" in the Fichtelgebirge, Germany; Müller et al., 2006).

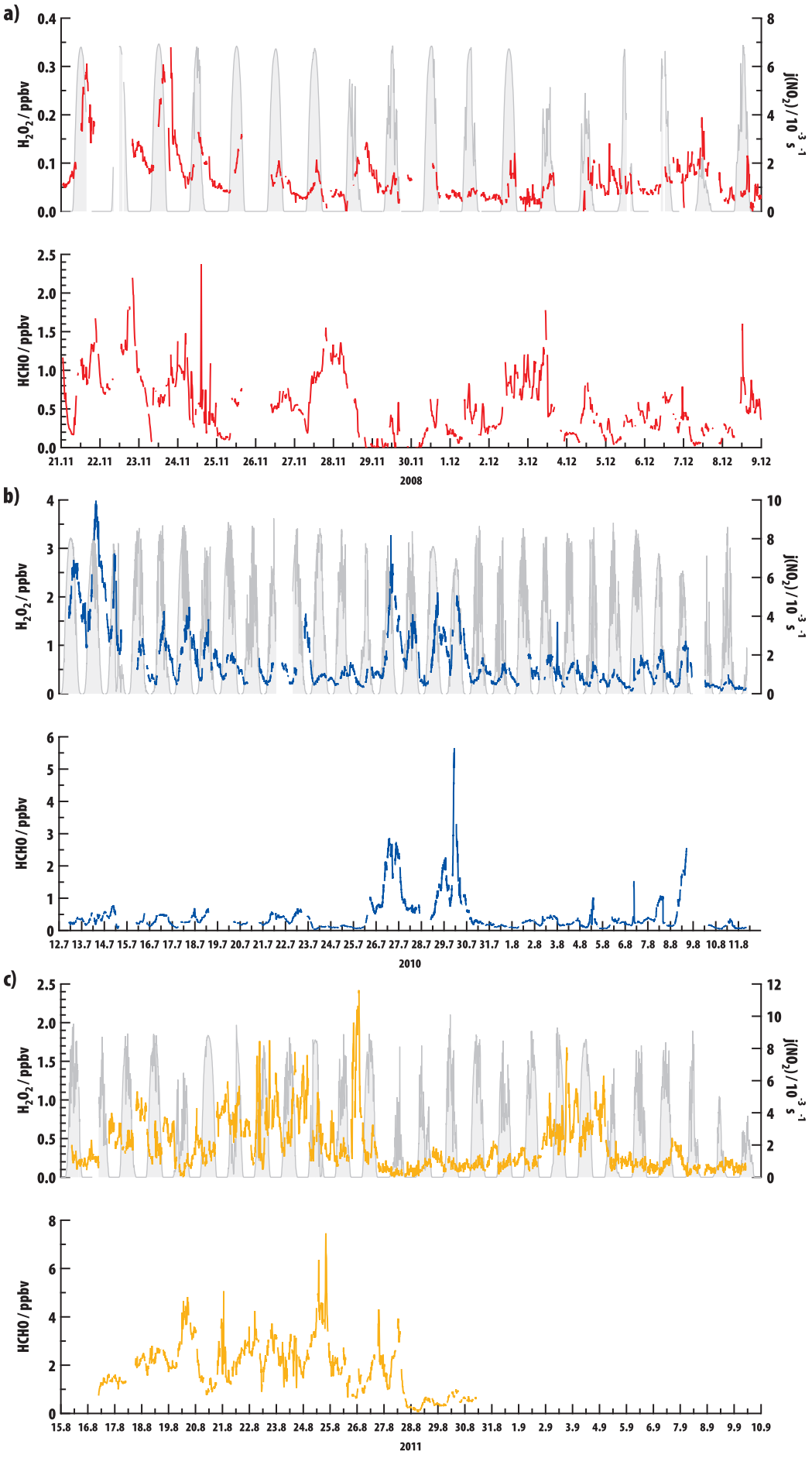

Figure 3.2.: Time series of observed H_2O_2 and HCHO mixing ratios (ppbv) **for DOMINO (red), HUMPPA (blue) and PARADE (yellow).** Photolysis rates of NO_2 ($j(NO_2)$ in s^{-1}) are depicted in grey.

3.1.3.2. Campaign averages of nitric oxides, HO_x, isoprene and methanol mixing ratios for daytime

Table 3.4 lists the average daytime values for selected trace gases including the relative variability (1σ). Data from DOMINO, HUMPPA and PARADE with a time resolution of 10, 5 and 10 min, respectively, were included without filtering.

The O_3 levels were comparable for HUMPPA and PARADE (43 and 45 ppbv) while lowest levels were observed during DOMINO (33 ppbv). HUMPPA showed the smallest variation (25 %). Highest NO_x was measured during PARADE (2.7 ppbv), followed by DOMINO (2.2 ppbv) while HUMPPA showed evidence for the lowest levels and variability (370 pptv, 59 %). The behaviour of NO was comparable: 41 pptv were observed for HUMPPA (smallest variability), while mixing ratios were similarly high for DOMINO (480 pptv) and PARADE (450 pptv) with high variation (150 % and 120 %, respectively). The NO to NO_2 ratio showed evidence for a high fraction of "fresh" NO for DOMINO and PARADE (0.25 and 0.20). Particularly for DOMINO, the NO_x trends were consistent with previous observations from 2008-2011 identifying traffic and nearby industrial areas as sources (Notario et al., 2013). In contrast, a very low ratio was observed during HUMPPA (0.15). The highest PAN mixing ratios were measured during DOMINO (570 pptv), followed by PARADE (400 pptv) and HUMPPA (240 pptv). The trends of HONO are similar: lowest levels were observed during HUMPPA (27 pptv), then DOMINO (45 pptv) and PARADE (95 pptv).

The average daytime mixing ratios of hydroperoxy radicals (HO_2) showed an increasing trend from PARADE (2.2 pptv) to DOMINO (2.8 pptv) to HUMPPA (20 pptv). Significant variation of 280 % was observed for HUMPPA. Further, highest OH values were measured during DOMINO (0.078 pptv), then HUMPPA (0.033 pptv) and PARADE (0.017 pptv) accompanied by a high variability (100 %). It is noteworthy, that HO_2 (and OH) data covered only a few days for HUMPPA and PARADE, thus the fact that highest HO_2 levels correlate with lowest NO_x deserves critical attention.

Daytime isoprene levels were highest during HUMPPA (88 pptv) followed by PARADE (51 pptv) and DOMINO (17 pptv) with highest variation (110 %). Reliable measurements of methanol were missing for DOMINO, while HUMPPA shows highly variable intermediate values of 4 ppbv (120 %). The highest levels (5.2 ppbv) were observed during PARADE.

Table 3.4.: Daytime averages for observations of selected trace gases. Missing and preliminary values are referred to as N/A and brackets, respectively.

		DOMINO		HUMPPA		PARADE	
Species	Unit	Average	1σ / %	Average	1σ / %	Average	1σ / %
H_2O_2	ppbv	0.0820	72.0	0.639	102	0.323	81.7
HCHO	ppbv	0.569	59.2	0.465	120	1.56	68.0
O_3	ppbv	32.8	21.3	43.1	25.1	44.6	33.3
NO_x	ppbv	2.23	111	0.371	58.9	2.68	83.3
NO	ppbv	0.480	149	0.0410	82.5	0.449	117
NO_2	ppbv	1.77	108	0.331	61.4	2.25	84.1
$\frac{NO}{NO_2}$		0.246	71.7	0.148	73.5	0.198	75.6
PAN	ppbv	0.566	53.0	0.241	52.2	0.401	65.0
HONO	pptv	45.1	98.0	27.0	68.5	95.4	73.4
HO_2	pptv	2.76	64.2	20.0	284	(2.2)	N/A
OH	pptv	0.0780	66.1	0.0330	74.4	0.0170	104
CO	ppbv	(680)[a]	N/A	116	41.7	103	17.5
Isoprene	pptv	17.0	115	87.7	53.7	51.2	44.9
Methanol	ppbv	N/A	N/A	3.99	117	5.24	26.6

[a]Level at the Magazon station, Huelva (Sinha et al., 2012).

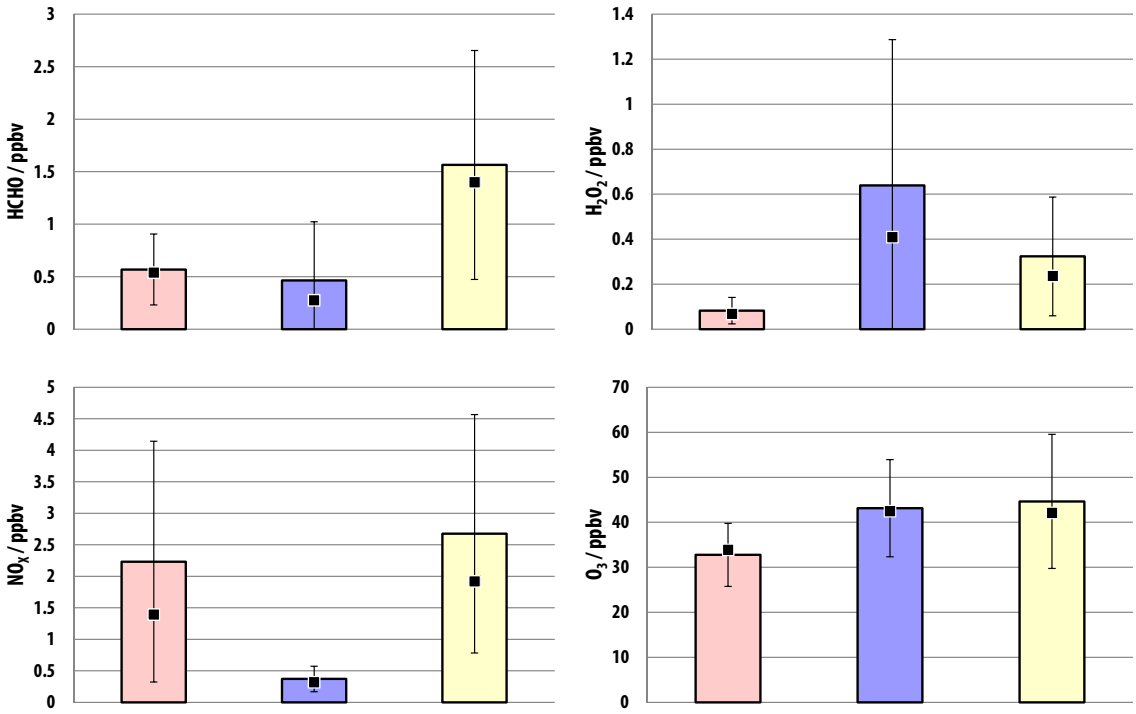

Figure 3.3.: Bar charts representing observed daytime trends of mixing ratios for HCHO, H_2O_2, NO_x and O_3 during DOMINO (red), HUMPPA (blue) and PARADE (yellow). Bars show averages, markers medians and error bars variabilities (1σ) of all available data points (5 min time resolution for HUMPPA and 10 min for DOMINO and PARADE). The HO_2 and OH data did not cover the entire campaign periods for HUMPPA and PARADE.

3.1.3.3. Mean diurnal profiles

Figure 3.4 depicts the diurnal profiles for $j(NO_2)$, H_2O_2, HCHO, O_3 and NO_x that were observed during DOMINO, HUMPPA and PARADE. All available data points included were based on a time resolution of 10 min (except for HUMPPA: 5 min), indicating averages, medians, minimum, maximum values and 1σ variability. The time is given in UTC. The local noon time may be different from 12 UTC, depending on the latitude and season. However, the $j(NO_2)$ levels were comparable for all three campaigns as shown previously, whereby there were differences in day length: shortest for DOMINO and longest for HUMPPA.

The observed H_2O_2 profiles showed pronounced variations with increasing maximum levels in the order of: DOMINO, PARADE and HUMPPA. In general, the minimums were in the morning and maximums in the afternoon for DOMINO (min. from 50 to 70 pptv at 8 a.m., max. at 6 p.m. from 100 to 150 pptv) and HUMPPA (min. at 6 a.m. from 200 to 300 pptv, max. at 4 p.m. ranging from 0.9 to 1.1 pptv). In contrast, PARADE showed an inverse profile with a minimum in the late morning (0.3 ppbv) and peak values at night (0.6 ppbv). This profile was inverse to the diurnal cycle of O_3 as an exception for the observations during DOMINO and HUMPPA.

The HCHO diurnal profiles showed smoother variations in all the three cases with minimums in the morning, reaching a plateau from noon to the night: min. at 8 a.m., max. 12 a.m. to 7 p.m. for DOMINO; min. at 6 a.m., max. 9 a.m. to 10 p.m. for HUMPPA and min. at noon, max. at 4 p.m. for PARADE. Maximum levels were comparable for DOMINO and HUMPPA (0.8 ppbv), while double values were observed during PARADE (2 ppbv).

The observations showed evidence for photochemical O_3 production in all the cases, with low mixing ratios in the morning reaching a maximum in the late afternoon, namely 40 ppbv (DOMINO), 50 ppbv (HUMPPA) and 55 ppbv (PARADE).

The diurnal patterns of NO_x showed high variation in analogy to the previously discussed campaign averages: the maximum NO_x levels during DOMINO and PARADE (max. 5 to 6 ppbv) were 10 times higher than those observed for HUMPPA. DOMINO and PARADE show a similar behavior with peak values in the late morning and early night (late evening, respectively) that could be highly correlated to traffic. Remarkably, the NO_x profile during HUMPPA (min. 0.2 ppbv at 12 a.m., max. 0.6 ppbv at 6 a.m.) was clearly anti-correlated to O_3 without showing evidence of traffic pollution.

The diurnal cycles of H_2O_2 during DOMINO and HUMPPA were comparable to earlier observations, indicating a minimum during the night and peak mixing ratios during the day (Balasubramanian and Husain, 1997; Grossmann, 2003; Jackson and Hewitt, 1996; Sakugawa et al., 1990; Sauer, 2001; Staffelbach et al., 1996). The winter conditions at the DOMINO site favored lower levels, whereas the higher daytime temperature and absolute humidity resulted in higher mixing ratios for HUMPPA and PARADE (Lee et al., 2000). One exception was the inverse profile of H_2O_2 during PARADE that showed similarities to the observations at Pabsttum, Germany (Grossmann, 2003) and Izaña, Tenerife (Zöllner, 2008), where its production was mainly driven by photochemistry and vertically transported in the morning from the residual layer. This result is typical for mountainous sites.

The daily variations of HCHO during all the three field studies were less pronounced than those of H_2O_2. This was observed earlier at coastal sites (Brittany, France Carlier et al., 1990), in the MBL over the Atlantic (Junkermann and Stockwell, 1999; Weller et al., 2000) and in the south Indian Ocean (Wagner, 2002). Moreover, a direct comparison of marine with continental sites is difficult due to a high impact of halogen and aerosol chemistry on HCHO photochemistry. In addition, the diurnal cycle can also be influenced by dynamics (Wagner et al., 2001; Weller et al., 2000). The base levels can be highly different, as shown by comparing PARADE with DOMINO and HUMPPA (including continental observations). Direct emissions and transport within the life time have a high impact on ambient HCHO.

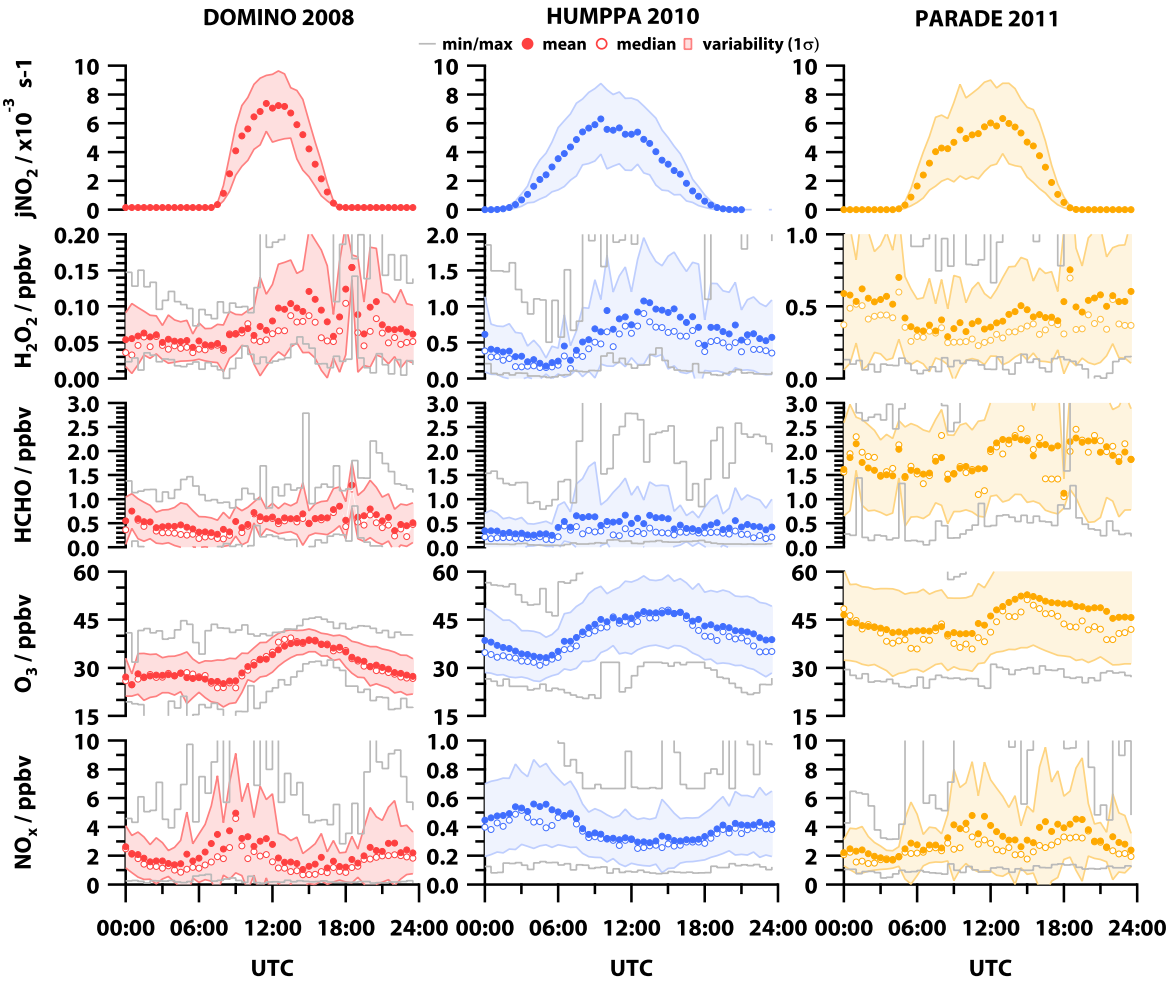

Figure 3.4.: Observed mean diurnal profiles for DOMINO, HUMPPA and PARADE.

3.1.4. Photochemistry and transport

3.1.4.1. Deviations from photostationary state

As previously discussed, hydroperoxy (HO_2) and organic peroxy (RO_2) radicals play major roles in the budget of H_2O_2, organic peroxides and HCHO. When peroxy radical measurements are missing, the Leighton ratio ϕ allows characterizing the photostationary state and thereby, calculating the total peroxy radical concentration ($[RO_x]$). In urban areas with high ambient NO_x, ϕ is close to unity (Carpenter et al., 1997; Thornton, 2002) due to the removal of RO_x by NO. In remote re-

gions with lower NO_x levels, the Leighton ratio deviates from unity (Hauglustaine et al., 1996, 1999; Mannschreck et al., 2004; Parrish et al., 1986; Volz-Thomas, 2003b) due to the fact that low NO concentrations reduce the loss rate of peroxy radicals. As a result peroxy radical levels increase.
Figure 3.5 shows the observed species, such as NO, NO_2, the NO to NO_2 ratio, HO_2 and parameters from the photostationary state calculation (ϕ and RO_x) for DOMINO, HUMPPA and PARADE. As previously discussed, all three sites were affected by relatively clean air masses, whereas DOMINO and PARADE still showed significant amounts of NO_x. One exception is HUMPPA, where especially NO reached minimum levels comparable to the clean MBL. However, the three sites cannot be regarded as "low" NO_x regimes due to NO levels over approximately 40 pptv.
Regarding the Leighton ratio, DOMINO and HUMPPA showed comparable daytime values and variabilities of 1.540 ± 0.263 and 1.540 ± 0.307, respectively. In contrast, 1.160 ± 0.185 were calculated for PARADE. The campaign was dominated by cloudy synoptic conditions thus photostationary state was not established for a major fraction of observed data points. The calculated RO_x was lowest for PARADE (17 ± 13 pptv), followed by DOMINO (31 ± 18 pptv) with highest levels for HUMPPA (55 ± 33 pptv). The observed average HO_2 mixing ratios showed a similar trend: lowest levels during PARADE (2.2 pptv), then during DOMINO (2.8 pptv) and highest for HUMPPA (20 pptv). The HO_2 (and OH) data covered only a few days for HUMPPA and PARADE.

The average ϕ for all the campaigns ranging from 1.2 to 1.5 was consistent with previously published studies that were based on comparable conditions. Those reported values of 1 to 3 for urban (Hauglustaine et al., 1996; Parrish et al., 1986; Volz-Thomas, 2003b) and 1.8 to 1.9 , respectively for rural sites (Ridley et al., 1992; Rohrer et al., 1998). Although the herein applied calculation of RO_x shows disagreements (Cantrell et al., 1997; Hauglustaine et al., 1999; Ridley et al., 1992; Thornton, 2002) to observations (e. g., by peroxy radical chemical amplification, PerCA), the relative trends between the campaigns are assumed to be sufficiently representative: low NO (and low NO_x) correlates with high (calculated) RO_x and high (observed) HO_2. Since those are precursors of hydroperoxides, DOMINO and PARADE showed lowest and HUMPPA the highest ambient levels of H_2O_2, which is in agreement with a previous study (Lee et al., 2000). In case of HCHO, the relationship of peroxy radicals and NO_x is not correlated: low ambient HCHO was observed for DOMINO and HUMPPA, which were both different NO_x regimes, and high for PARADE. This is due to the versatile HCHO sources and transport, as discussed in the next sections.

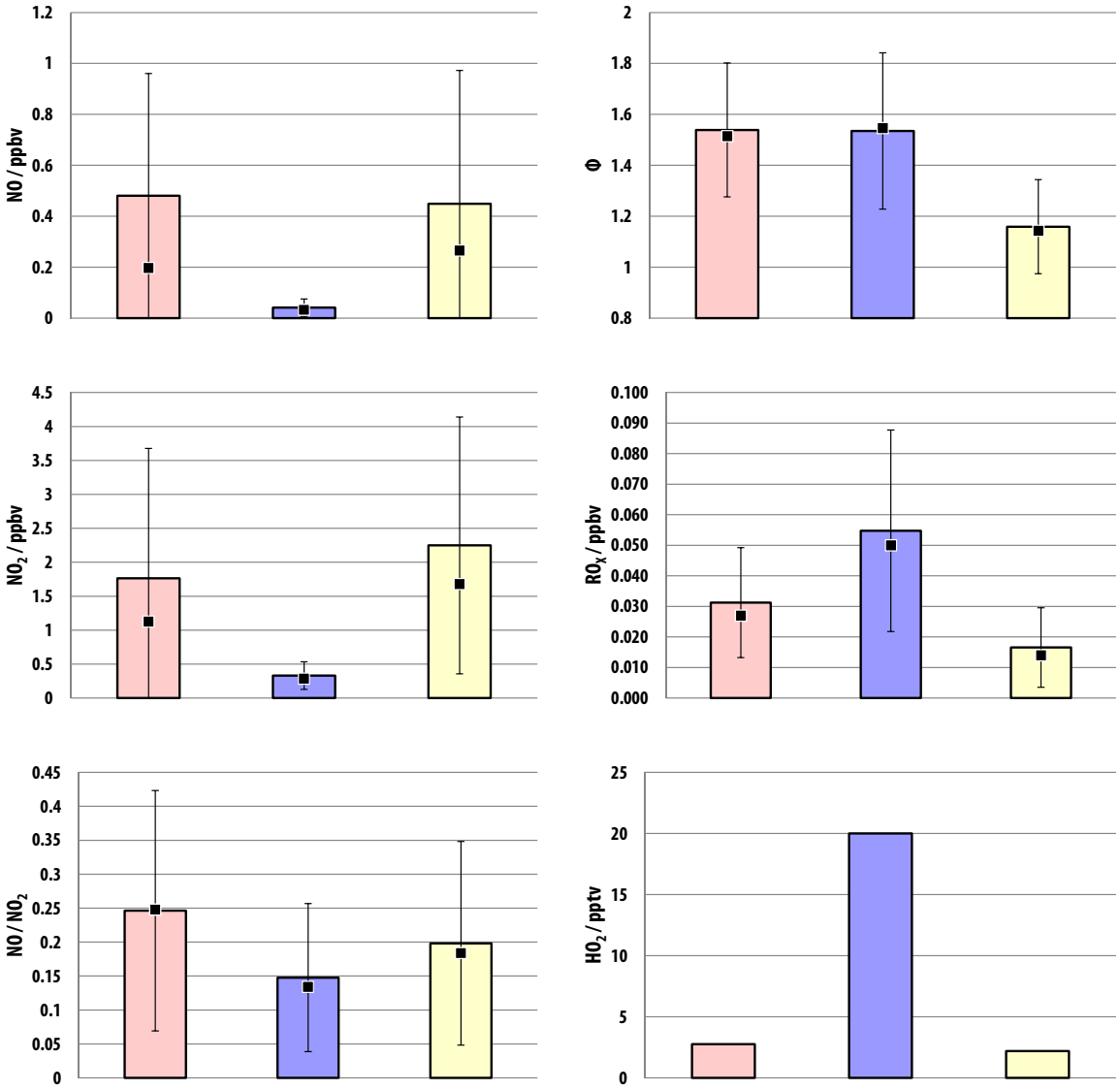

Figure 3.5.: Bar charts representing daytime trends of photostationary state parameters and related species during DOMINO (red), HUMPPA (blue) and PARADE (yellow). The only calculated quantities on the figure are ϕ and RO_x (calculated via the PSS). Bars show averages, markers medians and error bars variabilities (1σ) of all available data points (5 min time resolution for HUMPPA and 10 min for DOMINO and PARADE).

3.1.4.2. Trends in the oxidizing capacity

Daytime oxidizing capacity is defined by the available amount of OH, O_3 and H_2O_2 in the atmosphere (Thompson, 1992). It determines the rate of their removal in reaction with reactants (Y_i) such as VOCs and other inorganic chemical trace constituents (Prinn, 2003). Since the oxidizing capacity is primarily determined by O_3 and OH, whereas the latter is by far more reactive than O_3, it is essential to study the OH turnover.

$$OC = k_{Y_i}[Y_i][OH] \tag{3.23}$$

It is also essential to study the OH reactivity, particularly in case of incomplete VOC measurements, since that quantity can be directly observed (Kovacs and Brune, 2001; Nölscher et al., 2012b; Sadanaga et al., 2004; Sinha et al., 2008) and no [OH] observations are required.

$$R = k_{Y_i}[Y_i] \tag{3.24}$$

Figure 3.6 depicts the observed OH[1] mixing ratios and the OH reactivity for DOMINO, HUMPPA and PARADE. OH levels decreased in the order from DOMINO (0.078 pptv, 2×10^6 cm^{-3}), HUMPPA (0.033 pptv, 8×10^5 cm^{-3}) and PARADE (0.017 pptv, 4×10^5 cm^{-3}). OH reactivity decreased from DOMINO (21 s^{-1}), over HUMPPA to (12 s^{-1}) PARADE (1.7 s^{-1}). OH levels had a positive correlation with OH reactivity; however, no such correlation was observed for other trace gas species.

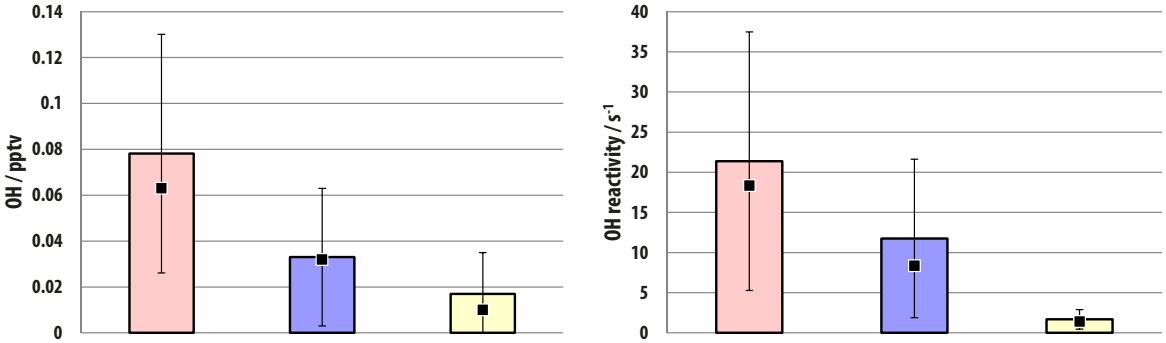

Figure 3.6.: Bar charts representing observed daytime trends of OH mixing ratio and total OH reactivity during DOMINO (red), HUMPPA (blue) and PARADE (yellow). Bars show averages, markers medians and error bars variabilities (1σ) of all available data points (5 min time resolution for HUMPPA and 10 min for DOMINO and PARADE).

Figure 3.7 shows relative values of calculated OH production rates (see Table 3.5 for absolute values) for daytime for all the three campaigns. OH recycling via HO_2 + NO was the dominating pathway for all three campaigns. DOMINO was outstanding (85 %), whereas HUMPPA (65 %) and PARADE (68 %) showed similar values. The primary OH production, P_0(OH), played a minor role for DOMINO (4.1 %), whereas HUMPPA (14 %) and PARADE (15 %) were in the same order. The photolysis of HONO accounted for 9.5 % and 4.0 % of the total OH production for DOMINO and HUMPPA, whereas PARADE took an exceptional position with 15 %. Further, the reaction of HO_2 with O_3 was rather unimportant for DOMINO (1.4 %) and PARADE (1.6 %); however, it played an outstanding role for HUMPPA (16 %). Compared to the OH production pathways discussed so far, the photolysis of H_2O_2 was a minor fraction of the total amount, particularly for DOMINO (0.13 %) and PARADE (0.46 %). However, HUMPPA had the highest value of 0.81 %. Furthermore, the reaction of isoprene with O_3 was negligible (<1 %).

As expected, OH recycling through HO_2 + NO was the major production pathway, since all the three regimes exceed background mixing ratios of NO_x. Consequently, the photolysis of HONO

[1]Note that the duty cycles of the LIF instrument is a couple of days for HUMPPA and PARADE (Table 2.8).

contributed during DOMINO and PARADE in ranges equal or more than the primary OH production. However, HUMPPA showed lowest NO_x levels, thus HONO played a minor role. High ambient HO_2 and low NO favors H_2O_2 formation, which was characteristic for all the three campaigns. The regime "compensated" the lower OH production rate via HO_2 + NO by HO_2 + O_3. Thus, the total OH production during HUMPPA (1.506 ppbv h^{-1}) was comparable with PARADE (1.545 ppbv h^{-1}), although the ambient NO_x was 10 times lower.

Table 3.5.: Calculated OH production rates for DOMINO, HUMPPA and PARADE divided into reaction channels. Production rates (ppbv h^{-1}) were calculated from the daytime averages given in Table 3.4 including combined variabilities (1σ).

		DOMINO		HUMPPA		PARADE	
Species	Unit	Average	1σ / %	Average	1σ / %	Average	1σ / %
HO_2 + NO	ppbv h^{-1}	1.00	160	0.98	300	1.1	150
$P_0(OH)$	ppbv h^{-1}	0.048	110	0.21	110	0.23	140
HONO + hν	ppbv h^{-1}	0.11	160	0.060	140	0.23	140
HO_2 + O_3	ppbv h^{-1}	0.016	68	0.24	290	0.025	110
H_2O_2 + hν	ppbv h^{-1}	0.0020	150	0.012	160	0.0070	150
O_3 + isoprene	ppbv h^{-1}	0	—	0.0010	120	0.0010	61
Sum	ppbv h^{-1}	1.2	—	1.5	—	1.5	—

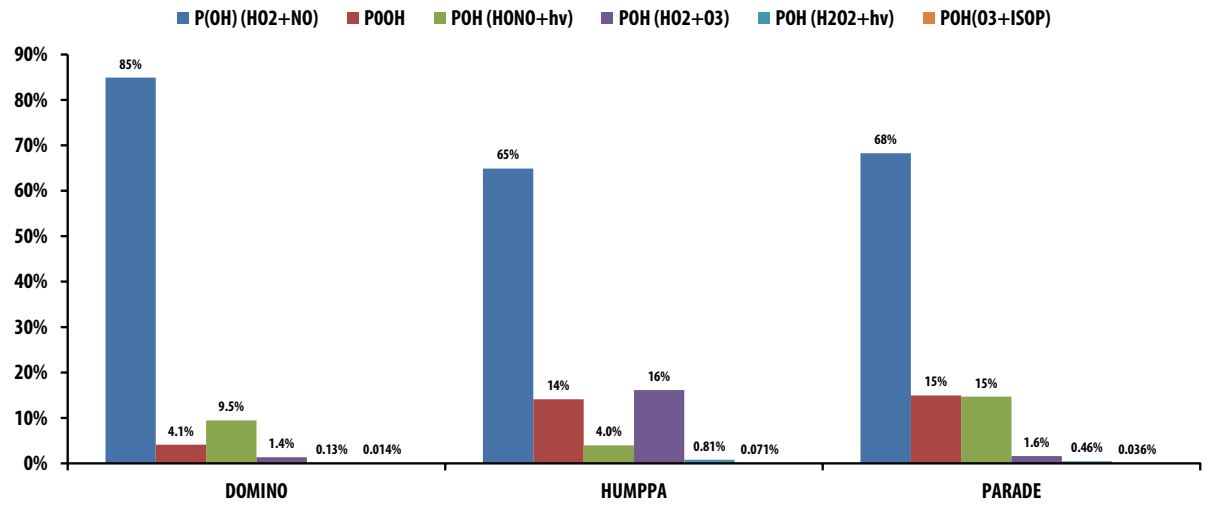

Figure 3.7.: Relative contributions of individual reactions to the OH production for DOMINO, HUMPPA and PARADE.

Further, Figure 3.8 shows the relative contributions of selected chemical pathways to the total OH reactivity for daytime (see Table 3.6 for absolute values). For comparison, only the reactivity of HCHO, CH_4, CO, isoprene and H_2O_2 have been studied. The other reaction pathways were not investigated and are addressed as "rest." In the case of DOMINO, this fraction dominated (90 %) and was followed by the contribution of CO (7.9 %). There was a lack of on-site CO measurements; therefore, the peak levels were assumed to be of 680 ppbv from the Mazagón station (Huelva Sinha et al., 2012). The Huelva province is heavily influenced by local traffic and industrial emissions from the metropolitan area of Seville (Notario et al., 2013). Further, CH_4 accounted for 1.3 % (0.28 s^{-1}) on

the OH reactivity, followed by HCHO (0.57 %, 0.12 s^{-1}) and H_2O_2 (0.39 %, 0.082 s^{-1}). Unfortunately, the original study did not report details on individual contributions of trace chemical species on the total OH reactivity (e. g., Sinha et al., 2012) except for CH_4 (0.3 s^{-1}) and a low impact of biogenic and aromatic VOCs (below 1.5 s^{-1}). The values presented in Table 3.6 are in full accordance (Sinha et al., 2012).

HUMPPA showed a comparable trend with 92 % of the total OH reactivity accounting for non-examined reactions followed by the contributions of CH_4 (2.4 %, 0.28 s^{-1}) and CO (2.3 %, 0.28 s^{-1}). Isoprene oxidation had an impact of 1.8 % (0.22 s^{-1}) followed by HCHO (0.82 %, 0.098 s^{-1}); however, H_2O_2 contribution played a minor role (0.22 %, 0.027 s^{-1}). The original study reported comparable results (Nölscher et al., 2012b): CO (0.406 s^{-1}), CH_4 (0.280 s^{-1}), isoprene (0.222 s^{-1}) and HCHO (0.098 s^{-1}).

In contrast to the trends of other two campaigns, the "rest" fraction solely reached 41 % during PARADE, directly followed by the contribution of HCHO (20 %, 0.34 s^{-1}). The oxidation of CH_4 and CO accounted for 17 % (0.28 s^{-1}) and 15 % (0.25 s^{-1}) of the total OH reactivity, respectively. The contribution of isoprene was 7.5 % (0.13 s^{-1}), whereas that of H_2O_2 was negligible (0.79 %, 0.013 s^{-1}). In agreement, the original study reported generally low daytime values of the total OH reactivity and high relative contributions of BVOCs from 11 to 16 % (Nölscher et al., 2013).

The two regimes with higher total OH reactivity (DOMINO and HUMPPA) showed evidence for negligible HCHO contributions; however, its oxidation had a high impact in the case of PARADE (low total OH reactivity). In general, the H_2O_2 pathway plays no significant role as an OH sink.

Table 3.6.: Calculated contributions of individual reaction channels to the total OH reactivity for DOMINO, HUMPPA and PARADE. Reactivities (s^{-1}) were calculated from the daytime averages given in Table 3.4 including combined variabilities (1σ). The "rest" fraction includes the contribution of NO_x besides other compounds.

		DOMINO		HUMPPA		PARADE	
Species	Unit	Average	1σ / %	Average	1σ / %	Average	1σ / %
OH reactivity	s^{-1}	21	75	12	84	1.7	72
k[HCHO]	s^{-1}	0.12	96	0.098	150	0.34	99
k[CH_4]	s^{-1}	0.28	75	0.28	84	0.28	72
k[CO]	s^{-1}	1.7	90	0.28	94	0.25	74
k[isoprene]	s^{-1}	0.042	140	0.22	100	0.13	85
k[H_2O_2]	s^{-1}	0.082	100	0.027	130	0.013	110
Rest	s^{-1}	19	—	11	—	0.69	—

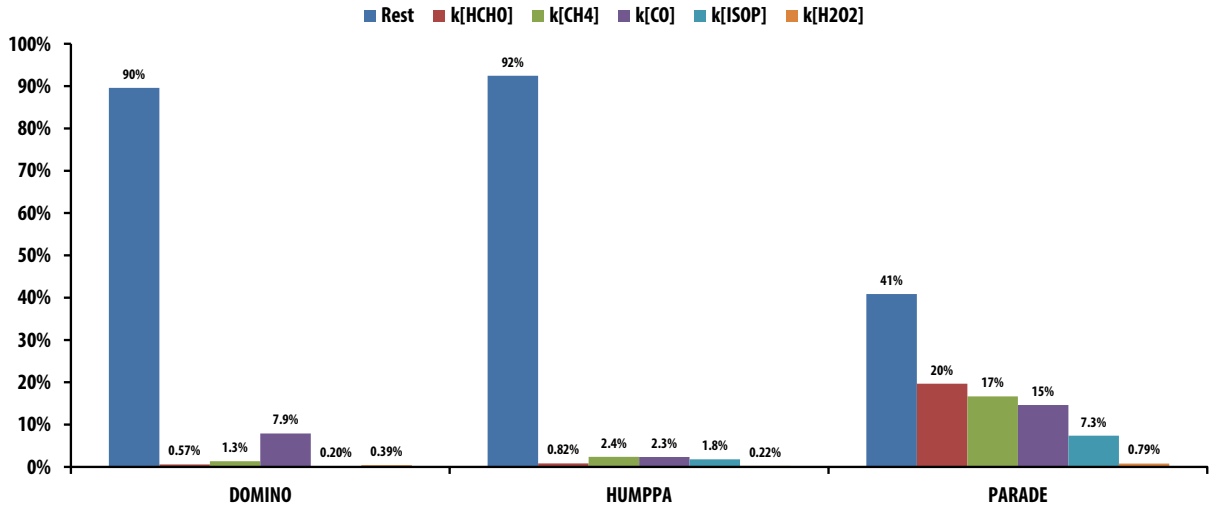

Figure 3.8.: Calculated relative contributions of individual reactions to the total OH reactivity for DOMINO, HUMPPA and PARADE based on Table 3.6. Note that the "rest" fraction includes the contribution of NO_x besides other compounds.

3.1.4.3. Budget considerations and transport for H_2O_2 and HCHO

The aim of this section is to learn how ambient H_2O_2 and HCHO are related to their photochemical sources and sinks under different NO_x conditions. Table 3.7 gives an overview on the production, loss terms and estimates of the steady-state mixing ratios for daytime. Deposition was neglected for both H_2O_2 and HCHO since convectively-mixed boundary layer occurs during daytime. If not mentioned otherwise, all calculations used observed mixing ratios of HO_2 and OH (Table 3.4), even if the data set did not cover the entire campaign periods. Mixing ratios of CH_3O_2 that were intermediately needed were calculated via the steady-state assumption from the oxidation of CH_4, methanol and isoprene.

In comparison to the other campaigns, the H_2O_2 production, $P(H_2O_2)$, during DOMINO was lowest (1.7 pptv h^{-1}) due to the low ambient HO_2 and significantly low absolute humidity. Although DOMINO took place in winter 2008, the more southern latitudes led to higher radiation and OH levels. Therefore, H_2O_2 had the shortest life time (2 d) towards photolysis and oxidation by OH ($\tau^{H_2O_2}_{OH+h\nu}$). However, even after neglecting deposition effects, the calculated steady-state mixing ratio ($[H_2O_2]_{SS}$) of 0.078 ppbv was in the order of the observation (0.082 ppbv), implying that the calculated source and sink terms were reasonable. In addition, daytime transport through advection could be excluded since that would lead to high differences between the calculation and observation.

In contrast, the production of formaldehyde, P(HCHO), showed a slightly different trend: 90 pptv h^{-1} was the highest production rate compared to the other campaigns. This may be due to the high ambient OH. Together with the high radiation level, this caused the shortest HCHO life time ($\tau^{HCHO}_{OH+\sum h\nu}$) of (7 h). For the simple budget consideration of H_2O_2, the steady-state mixing ratio ($[HCHO]_{SS}$) of 0.63 ppbv described the observed value (0.569 ppbv) consistently well. This implies that neither deposition nor advection played a significant role.

Of the three campaigns, the daytime calculations for HUMPPA resulted in the highest production rate for H_2O_2 (54 pptv h^{-1}). This was due to the highest ambient HO_2 and absolute humidity. However, lower ambient OH and radiation, particularly $j(H_2O_2)$), caused a longer life time (2.9 d) compared DOMINO. Therefore, the steady-state calculation led to 3.7 ppbv versus the observed 0.639 ppbv, indicating a non-closed budget. Photochemistry explains 5 times higher mixing ratios than the observations; thus, a strong daytime deposition can be concluded.
Compared to the other two campaigns, the HCHO production was medium (51 pptv h^{-1}). The simple calculation does not take the HCHO yield from the oxidation of higher BVOCs into account, and thus, it may underestimate the values. On the other hand, the HCHO life time was the highest (8.9 h) due to the medium ambient OH and higher latitude. However, the calculated steady-state mixing ratio (0.45 ppbv) agrees well with the observations (0.465 ppbv), thus implying very low daytime influences of deposition and advection on HCHO. However, the HCHO budget shall be discussed in more detail in the next chapter.

PARADE showed the second lowest production rate for H_2O_2 (2.1 pptv h^{-1}) and the highest life time towards oxidation and photolysis (3.1 d) due to the low photochemical activity during the field campaign. The preliminary HO_2 measurements were only available from Sep 04 to Sep 10 2011 (K. Hens, priv. comm. 2013). A steady-state calculation for H_2O_2 yields 0.16 ppbv versus the observed 0.323 ppbv. The two explanations for the non-closed budget are as follows: (i) H_2O_2 was transported during daytime or (ii) HO_2 is not representative due to the low data coverage. However, neglecting deposition, the following back-of-the-envelope calculation gives a lower estimate for daytime HO_2 (HO_{2SS}) by including the observed mixing ratio of H_2O_2 (H_2O_{2obs}) and its photochemical lifetime ($\tau^{H_2O_2}_{OH+h\nu}$) towards photolysis and oxidation by OH. The result of 7.7 pptv is consistent with the observed maximum mixing ratio of 10 pptv (K. Hens, priv. comm. 2013).

$$[HO_2]_{SS} = \sqrt{[H_2O_2]_{obs} \cdot \frac{1}{\tau^{H_2O_2}_{OH+h\nu}\, k_{HO_2+HO_2}}} \approx 7.7\,\text{pptv} \tag{3.25}$$

The photochemical HCHO production during PARADE was the lowest (29 pptv h^{-1}) compared to the other campaigns, whereas its photochemical lifetime (8.8 h) was comparable to HUMPPA. However, the steady-state calculation yields 0.26 ppbv versus the ambient 1.564 ppbv implying that 83.7 % of the HCHO is transported from the nearby industry in the Frankfurt area. In addition, since CO is a tracer for combustion processes, a closer look at the HCHO-to-CO correlation coefficient (R^2 = 0.51) underlines the fact.

Table 3.7.: Daytime averages of calculated production rates, life times and steady-state mixing ratios for H_2O_2 and HCHO during DOMINO, HUMPPA and PARADE. Sources and sinks of H_2O_2 and HCHO are estimated as $P(H_2O_2)$ and P(HCHO), respectively life times $\tau^{H_2O_2}_{OH+h\nu}$ and $\tau^{HCHO}_{OH+\sum h\nu}$. Relative compound variabilities are given as 1σ.

		DOMINO		HUMPPA		PARADE	
Species	Unit	Average	1σ / %	Average	1σ / %	Average	1σ / %
$P(H_2O_2)$	pptv h^{-1}	1.66	90.8	54.4	402	2.13	141
$\tau^{H_2O_2}_{OH+h\nu}$	d	1.97	161	2.86	173	3.07	181
$[H_2O_2]_{SS}$	ppbv	0.0783	—	3.74	—	0.157	—
P(HCHO)	pptv h^{-1}	90.2[a]	200	50.8	126	29.0	166
$\tau^{HCHO}_{OH+\sum h\nu}$	h	6.96	155	8.87	185	8.78	175
$[HCHO]_{SS}$	ppbv	0.628	—	0.451	—	0.255	—

[a] Assuming 4 ppbv of methanol.

3.1.5. Summary and conclusions

[1] Comprehensive ground-based field measurements at three different European sites were performed to study the behavior of H_2O_2 and HCHO under the following different "high" NO_x (NO > 25 pptv) conditions: DOMINO from Nov 20–Dec 9, 2008 (El Arenosillo, Southern Spain), HUMPPA from Jul 12–Aug 12, 2010 (Hyytiälä, Southern Finland) and PARADE from Aug 15–Sep 10, 2011 (Kleiner Feldberg, Germany). Although the temperatures and absolute humidity levels showed distinct differences, the mid-day averages of $j(NO_2)$ were comparable. Synoptic conditions were mostly clear sky (DOMINO), mostly clear with some thunderstorm events (HUMPPA) and variable accompanied by rain (PARADE).

[2] The average daytime levels of H_2O_2 for DOMINO, HUMPPA and PARADE were 82, 639 and 323 pptv, respectively. The night-time mixing ratios reached 59, 99 and 486 pptv, respectively. The mean diurnal profiles of H_2O_2 showed a strong diurnal pronunciation for DOMINO and HUMPPA, with maximum values in the afternoon, whereas an inverse profile was observed during PARADE. In case of HCHO, daytime averages of 569 pptv, 465 pptv and 1.9 ppbv were measured for DOMINO, HUMPPA and PARADE, respectively. The night-time mixing ratios, showing smooth diurnal variations, were 505 pptv, 383 pptv and 1.9 ppbv.

[3] Observations showed high differences in the NO_x averages. The highest levels were measured during PARADE (2.7 ppbv), followed by DOMINO (2.2 ppbv) with a high amount of "fresh" NO. HUMPPA showed evidence for the lowest levels (370 pptv) with a very low fraction of NO (41 pptv). The average daytime O_3 was comparable for HUMPPA and PARADE (43 and 45 ppbv), whereas lowest levels were observed during DOMINO (33 ppbv).

[4] The photostationary state (PSS) and simple steady-state calculations for H_2O_2 and HCHO were performed for all the data sets to study the trends in the oxidizing capacity and transport. The average deviation from PSS for all the campaigns ranging from 1.2 to 1.5 was consistent with previously published studies that were based on comparable conditions. Those studies reported values of 1 to 3 for urban (Hauglustaine et al., 1996; Parrish et al., 1986; Volz-Thomas, 2003b) and 1.8

to 1.9 for rural sites (Ridley et al., 1992; Rohrer et al., 1998). However, the herein applied calculation of RO_x showed disagreements (Cantrell et al., 1997; Hauglustaine et al., 1999; Ridley et al., 1992; Thornton, 2002) with the observations (e. g., by peroxy radical chemical amplification, PerCA) for DOMINO.

[5] The observed OH levels decreased in the order from DOMINO (0.078 pptv, 2×10^6 cm^{-3}), HUMPPA (0.033 pptv, 8×10^5 cm^{-3}) and PARADE (0.017 pptv, 4×10^5 cm^{-3}). Subsequently, the OH reactivity decreased with a comparable trend from DOMINO (21 s^{-1}), over HUMPPA to (12 s^{-1}) PARADE (1.7 s^{-1}). A positive correlation was observed between the OH levels and the OH reactivity. As expected, OH recycling through HO_2 + NO is the major source, whereas the photolysis of H_2O_2 is insignificant. On the OH sink side, the two regimes with higher total OH reactivity (DOMINO and HUMPPA) showed evidence for a low contribution of HCHO as, while it had a high impact during PARADE. H_2O_2 plays a non-significant role throughout all three campaigns. However, HO_2 and OH observations did not cover the entire campaign periods for HUMPPA and PARADE.

[6] The H_2O_2 production increased as follows: DOMINO (1.66 pptv h^{-1}), PARADE (2.13 pptv h^{-1}) and HUMPPA (54.4 pptv h^{-1}). On the other hand, the photochemical life time decreased from PARADE (3.1 d), over HUMPPA (2.9 d) to DOMINO (2.0 d). The HCHO production showed slightly different trends: highest for DOMINO (90.2 pptv h^{-1}), mid for HUMPPA (50.8 pptv h^{-1}) and lowest during PARADE (29.0 pptv h^{-1}). On the sink side, the photochemical life times increased in the order of: DOMINO (7.0 h), PARADE (8.8 h) and HUMPPA (8.9 h). The major amount of daytime H_2O_2 during DOMINO and PARADE can be explained by photochemistry due to the fact that the steady-state mixing ratio match reasonably well with the observations. This simple assumption fails for HUMPPA; therefore the calculated H_2O_2 levels are overestimated by a factor of 6. Furthermore, the ambient HCHO was under photochemical control during DOMINO and HUMPPA. Its production can be expressed by background chemical pathways, such as the oxidation of CH_4, isoprene and methanol by OH radicals. During PARADE, over 80 % of ambient HCHO was primarily emitted from anthropogenic sources and transported.

3.2. Investigation of the photochemical budget of H_2O_2 and HCHO during HUMPPA

The previous chapter compared photochemical regimes of three field measurement campaigns at different European sites (DOMINO, Spain; HUMPPA, Finland; PARADE, Germany). HUMPPA (Hyytiälä, Southern Finland; Summer 2010) has been chosen to study the relationships of net H_2O_2 ($N(H_2O_2)$) and net HCHO (N(HCHO), production tendency) during daytime. This chapter points out the lack of knowledge about H_2O_2 and HCHO (and broaches the organic hydroperoxides) in the boreal forest and sets the field campaign into the context. The aim is to calculate the photochemical budgets and the influence of physical processes (transport, deposition). A high impact of monoterpenes due to their high abundance as well as minor urban anthropogenic influences and pollutants (primary and secondary chemical) from biomass burning events were expected on atmospheric chemistry.

3.2.1. General overview on the synoptic conditions and trace gas levels

The HUMPPA field measurement campaign was performed at the SMEAR II station (Station for Measuring Ecosystem-Atmosphere Relation) in Hyytiälä (61°51′ N, 24°18′ E, 181 m.a.s.l.), Southern Finland from July 12 to Aug 12 2010 (Figure 3.9). A general overview on the meteorological conditions, instrumentation and special events has already been given (Williams et al., 2011). Thus, in the following, only the relevant information concerning this work are summarized.
The boreal forests around Hyytiälä consist mainly of Scots pine and Norway spruce and show as well characteristics of a deciduous forest (Birch trees and woodland scrub: Willows, Aspen) as provided in Figure 3.9. The trace gas species H_2O_2 and HCHO were measured above the canopy on the tower at 21 m with the wet-chemical dual enzyme and Hantzsch on-line fluorescence method, respectively.

Meteorology and general conditions. The day length during HUMPPA was very long (ca. 18 hours from 04:00-23:00 UTC+2) due to the northern summer leading to a short length of the night of (6 h). The average temperatures were anomalously warm (20.20 ± 4.10 °C; min to max: 10.1 to 31.7 °C) above the canopy. The exceptional warm conditions compared to the last years (Williams et al., 2011) may be a future perspective for the climate change. Precipitation levels were below 2 mm d^{-1}, except for Jul 15, Jul 27 and Aug 4 August with heavy thunderstorms (Williams et al., 2011). Air masses originated throughout the whole campaign from the south-west (53.7 %) and south-east (20.7 %) with potential pollutant transport. Note that former trajectory analyses showed that highest concentrations of carbonyls were from the east and the lowest in the air masses cycled a long time over Scandinavia (Hellén et al., 2004). Trajectories from the north-west (10.3 %) indicated "clean" conditions (Williams et al., 2011). On a local scale, the average wind speed above canopy was 3.48 ± 1.37 m s^{-1} (at 33.6 m). Considering the high horizontal homogeneity and assuming constant mid-scale wind speeds, the average atmospheric life times τ (Seinfeld and Pandis, 2006) of the herein discussed species lie within the reach of anthropogenic influences: roughly 300 km for H_2O_2, O_3 and NO_x ($\tau \approx 1$ d), whereas 90 km for HCHO ($\tau \approx 7$ h). Consequently, that makes primary transport for wind directions heading to Tampere, Korkeakoski, Orivesi and even Helsinki possible.

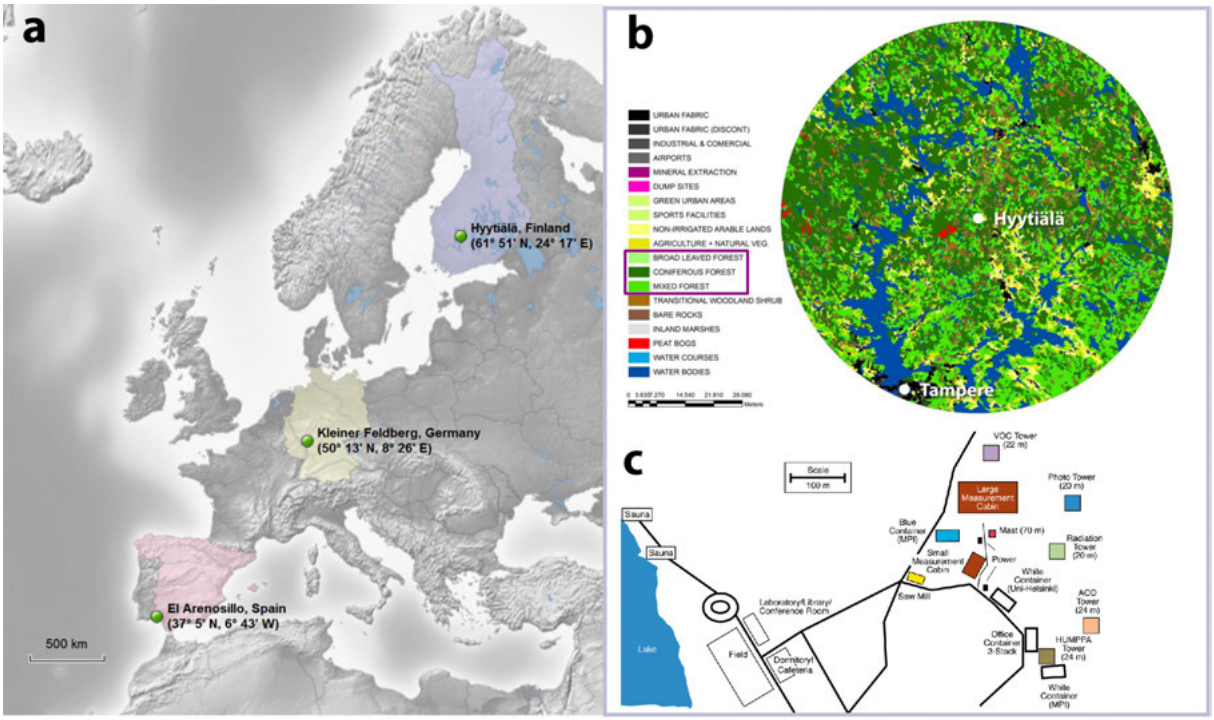

Figure 3.9.: Location and land use map for the Hyytiälä site. Location map (**a**) showing the HUMPPA site (light purple) and the other two campaign positions (DOMINO, PARADE), which are discussed in this work. Land use map (**b**) for a radius of 50 km, where Tampere (population ca. 211 000) also appears on the lower left (Williams et al., 2011). However, it shows a high horizontal homogeneity. The main structures are coniferous (dark green), mixed forests (light green) and water bodies (dark blue). Closer view (**c**) depicting an area of ca. 600 m with the campaign set-up (Williams et al., 2011). H_2O_2 and HCHO measurements were performed on the MPI tower (located in a clearing) at a height of ca. 24 m above the canopy level.

However, as shown later, the NO_x levels were closer to the marine boundary layer (MBL; $[NO] \approx 25$ pptv) than to other European forests (e. g., mount Kleiner Feldberg with $[NO_x] \approx 10$ ppbv, this work). Unlike the MBL, which is dominated by CH_4 (in orders of ca. 1.7 ppmv), typical deciduous forests emit isoprene. Conifers, such as those around the site, are known as monoterpene emitters, especially α-pinene, which dominated ca. 50 % of their emission spectrum (Yassaa et al., 2012). Studies at the SMEAR II station indicated higher ambient isoprene (C_5), monoterpenes (C_{10}) and sesquiterpenes (C_{15}) in summer (Hakola et al., 2003). Consequently for this work, a high impact of monoterpenes on the photochemical budgets is expected (Hakola et al., 2012).

3.2.2. The chemical regimes R1-R4

As mentioned before, the diversity of the chemical regimes requires a classification in time periods for further studying the photochemistry. Concerning OH reactivity, the campaign was divided into three regimes (Nölscher et al., 2012b): (i) stressed boreal (Jul 18-25 2010), (ii) transported pollution (Jul 26-29) and (iii) normal boreal (Aug 1-7). However, aerosol signature (Corrigan et al., 2013) and meteorology (Williams et al., 2011) allow splitting (i) into a period from Jul 23 to 25 since those were the coldest and the cleanest days. Thus the further discussion will consist of the following regimes: stressed boreal (R1, Jul 12-22 2010), cold & clean (R2, Jul 23-25), transported pollution (R3, Jul 26-29) and normal boreal with some short pollution events (R4, Aug 1-12).

Table 3.8 lists daytime statistics of selected chemical trace gas species for the four regimes. That includes basically H_2O_2, HCHO, parameters for studying the photostationary state, such as O_3 and NO_x, and (mono)terpenes.

Results for R1 (stressed boreal). The first regime is characterised by the second highest average radiation and temperature (21.4 °C). H_2O_2 levels are highest (971 pptv) and highly variable (80.1 %). HCHO shows medium mixing ratios (327 pptv) with the lowest variability (42.9 %). O_3 and NO_x were observed in medium values (42.7 ppbv, and 397 pptv), respectively, as well as CO (104 ppbv). A closer look at precursors shows highest mixing ratios for isoprene (128 pptv), α-pinene (117 pptv) and Δ^3-carene (72.7 pptv). The levels of β-Pinene and myrcene are hereby medium high (36.0and 9.51 pptv, respectively). Note that this regime is affected by the highest OH reactivity (22.5 s^{-1}).

Results for R2 (cold & unpolluted). A special aspect of this regime is the low average temperature (17.1 °C) accompanied by a low absolute humidity (13.3×10^3 ppmv). Besides, the pollution levels are very low, especially concerning the CO (87.5 ppbv), NO_x (264 pptv) and O_3 (38.8 ppbv) levels. A backtrajectory analysis indicates "clean" northern air masses. However, H_2O_2 shows medium (391 pptv), whereas HCHO lowest (211 pptv) mixing ratios. Apparently conditions causing similar isoprene levels (125 pptv) as during R1 could be observed. The other monoterpenes show exclusively lowest ambient mixing ratios: α-pinene (51.6 pptv), β-pinene (14.6 pptv), (26.3 pptv) and myrcene (3.67 pptv). Here, the OH reactivity shows a highly variably campaign minimum (6.30 s^{-1}, 103).

Results for R3 (pollution series). This regime is characterised by recurring heat stress and air masses affected by pollution events in Russia. Highest average daytime temperatures (22.4 °C) accompanied by highest absolute humidity (1.91×10^3 ppmv) were observed. In addition, ambient CO and O_3 show peak values (147 ppbv and 45.0 ppbv, respectively), whereas the NO_x mixing ratio is intermediate (360 pptv). The levels of H_2O_2 are medium (767 pptv) with a low variability (72.6 %), whereas HCHO reaches its campaign daytime maximum (1.09 ppbv). In particular, ambient isoprene has its minimum (70.0 pptv), whereas α-pinene is still persistently high (104 pptv). β-Pinene shows a maximum (37.7 pptv) and the other monoterpenes such as Δ^3-carene and myrcene solely intermediate values (59.3 and 7.43 pptv). Consider that the OH reactivity is medium high (13.0 s^{-1}).

Results for R4 (normal boreal). During this regime, the meteorological conditions are comparable to the trends of the last years (Williams et al., 2011): sun, clouds and rain events interchange (lowest $j(NO_2)$ of 2.18×10^{-3} s^{-1} and highest variability of 113 %) and temperature and absolute humidity show only medium values (18.9 °C and 17.1×10^3 ppmv). Noteworthy that some pollution and sawmill events occurred as reflected by the second highest CO mixing ratios (114 ppbv) and the highest variability in α-pinene (174 %). Ambient H_2O_2 has a minimum (295 pptv) accompanied by the lowest variability (67.9 %). The same trend could be observed for HCHO due to its second lowest levels (282 pptv), whereas it varies extensively (113 %). Note that myrcene shows a maximum (10.3 pptv), whereas the other (mono)terpenes occur in medium mixing ratios: isoprene (71.5 pptv), α-pinene (103 pptv), β-pinene (29.3 pptv) and Δ^3-carene (63.6 pptv). Besides, the OH reactivity is medium (7.21 s^{-1}).

Table 3.8.: Observed trace gases for the regimes during HUMPPA. (R1) stressed boreal, (R2) cold and clean, (R3) transported pollution and (R4) normal boreal.

Species	Unit	R1		R2		R3		R4	
		Average	1σ / %	Average	1σ / %	Average	1σ / %	Average	1σ / %
H_2O_2	pptv	971	80.1	391	73.6	767	72.6	295	67.9
HCHO	ppbv	0.327	42.9	0.211	77.4	1.09	77.4	0.282	113
O_3	ppbv	42.7	24.8	38.8	28.0	45.0	30.1	41.4	22.0
NO_x	pptv	397	64.8	264	69.6	360	45.9	417	50.5
CO	ppbv	104	14.4	87.5	15.2	147	38.2	114	41.8
Isoprene	pptv	128	88.8	125	57.7	70.0	132	71.5	94.3
α-Pinene	pptv	117	112	51.6	41.6	104	60.0	104	175
β-Pinene	pptv	36.0	92.8	14.6	54.3	37.7	54.6	29.3	113
Δ^3-Carene	pptv	72.7	115	26.3	57.0	59.3	76.5	63.6	190
Myrcene	pptv	9.51	96.5	3.67	54.9	7.43	90.3	10.3	119

Mean diurnal profiles. Figure 3.10 depicts the diurnal profiles of O_3, NO_x, H_2O_2, MHP, CO and HCHO for the four regimes (R1: black, R2: pale blue, R3: purple, R4: green). Note that the minimums and the maximums are slightly shifted due to the decreasing day length.

O_3 decreases during the night to minimum values in the morning (ca. 6:00 UTC+2) ranging from 30 to 37 ppbv and increases to its maximum between early and late afternoon (ca. 15:00-18:00 UTC+2) throughout the regimes. At the moment of boundary layer breakup the four curves cross in one point (ca. 6:00 UTC+2, 0.55 ppbv). Levels are highest about 55 ppbv for R3 (ca. 18:00 UTC+2) and lowest with 43 ppbv during R2 (ca. 20:00 UTC+2). The two regimes with warm and mixed conditions (R1 and R4) show intermediate maximum values (50 to 51 ppbv) with a time shift of about 4 h. NO_x behaves differently having maximum levels from 0.3 to 0.7 ppbv in the early morning (ca. 4:00-6:00 UTC+2) and minimums from 0.2 to 0.4 ppbv in the late afternoon (ca. 17:00 UTC+2) for R1 to R4. For the early morning, R1 is hereby outstanding by having a peak value of 0.7 ppbv at 4:00 UTC+2. Note that the pollution series (R3) reveal hereby solely moderate diurnal values ranging from 0.3 to 0.6 ppbv.

H_2O_2 shows minimum values around 7 UTC+2 (0.3 to 0.5 ppbv) and maximum (0.5 to 2.2 ppbv) from midday until the afternoon (12-16 UTC+2) throughout three regimes due to insufficient data coverage during R2. In contrast, the mixing ratios spread over a wide range: lowest trends were observed during R4 and highest for R1 and R3, respectively. The MHP estimation follows a comparable trend by having minimums at 6 UTC+2 and minimums around 17 UTC+2. Hereby, lowest values range from the LOD to ca. 0.3 ppbv. In contrast, the maximums range from 0.7 to 1.7 ppbv with lowest R4 and with highest R3 values.

CO behaves differently. R1 shows low variation having a maximum (110 ppbv) at 6:00 UTC+2, whereas minimum values were observed at 21:00 UTC+2 (100 ppbv). The data for R2 covers only a period from 8:00 UTC+2 to midnight. Starting from minimum levels in the morning (80 ppbv), ambient mixing ratios increase almost linearly until midnight (100 ppbv). In contrast, R3 does not

vary from 0-7 UTC+2 and from 22 UTC+2 until 0 UTC+2, whereas it shows maximum levels (120 to 130 ppbv) from noon until the night. However, R2 follows the most striking trend: starting from lowest ambient levels (130 to 140 ppbv) in the night until ca. 8 UTC+2, they increase to a peak at ca. 10 UTC+2 (180 to 190 ppbv). Ambient HCHO is characterised by low variation for R1, R2 and R4: minimum levels (0.2 to 0.3 ppbv) were observed in the early morning, which then reach a plateau between 6 and 21 UTC+2 (0.2 to 0.6 ppbv). In contrast, HCHO shows a similar daytime pattern as CO during R4. The minimum (0.5 ppbv) is in the morning (ca. 7-8 UTC+2), whereas the mixing ratio increase quickly within ca. 3 h to almost 2 ppbv. Then, HCHO "oscillates" between 0.9 and 1.5 ppbv in periods of approximately 3 h (from minimum to minimum). During nighttime, the levels decrease almost linearly from ca. 1.5 to 0.5 ppbv.

The biomass burning series (R3) show evidence for a high, whereas cold and clean air masses (R2) lead to a low photochemical production of O_3. Unexpectedly, highest NO_x was not observed during the pollution series indicating photochemically aged air. The transport time of several days from the biomass burning plumes to the HUMPPA sites is sufficient to remove NO_x. Rain events during R4 might have washed out H_2O_2 and MHP due to their high solubility. The high ambient methyl hydroperoxide during R3 is most likely caused by secondary production from photochemically aged biomass burning plumes. CO and HCHO entrainment (note that those special have a different photochemical behaviour) for R4. The other regimes show no extraordinary behaviour (HCHO). In the case of CO, clean air masses (R2) definitely cause low, whereas intermediate conditions, such as during R1 and R4 (remnants of anthropogenic and/or biogenic emissions) lead to enhanced mixing ratios.

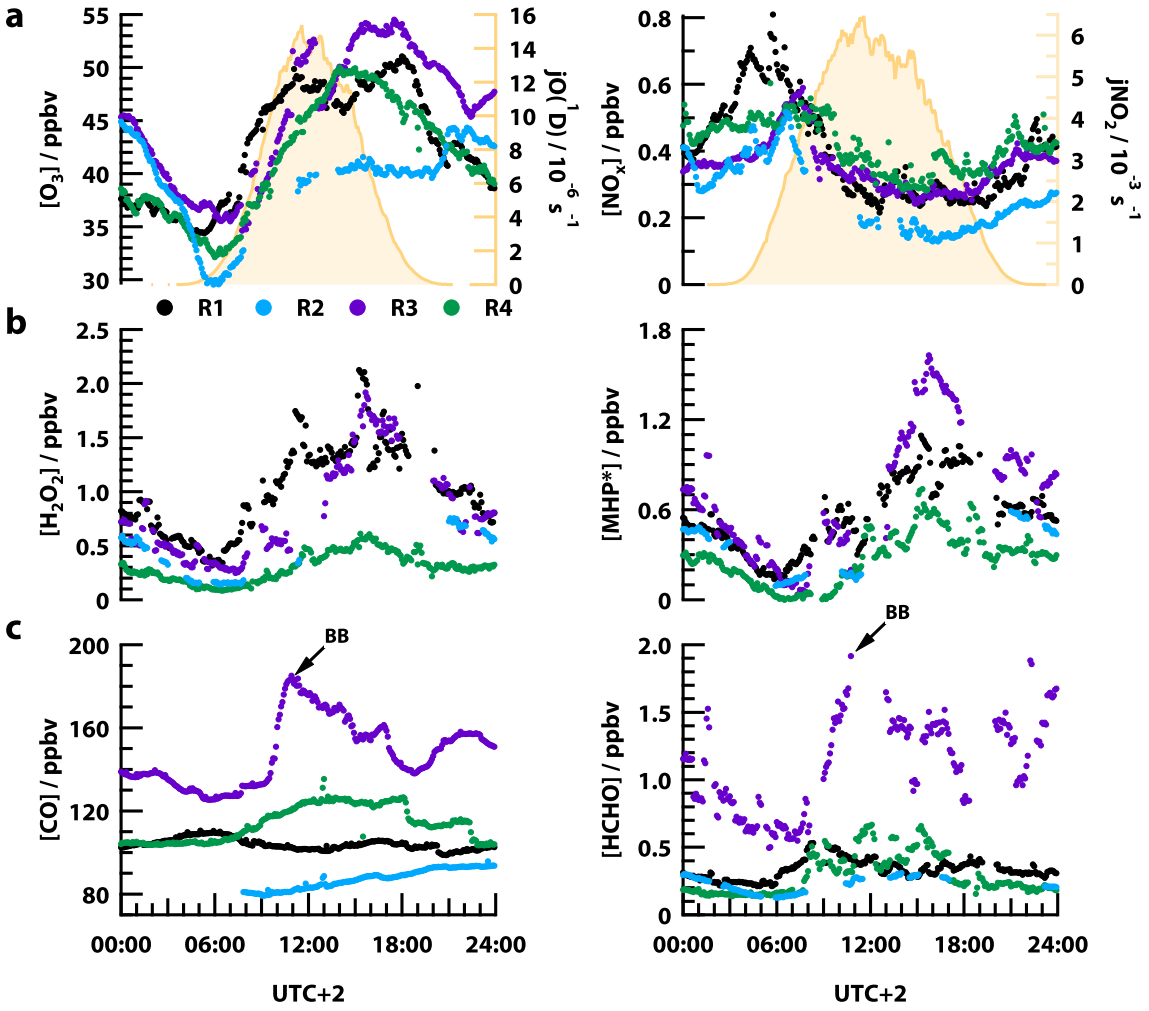

Figure 3.10.: Mean diurnal profiles of $[O_3]$, $[NO_x]$, $[H_2O_2]$, $[MHP]^*$, [CO] and [HCHO] for R1–R4. Mixing ratios of O_3 and NO_x (**a**), hydroperoxides (**b**) as well as CO and HCHO (**c**) are depicted corresponding to the regimes R1 (black), R2 (cyan), R3 (purple) and R4 (green). The arrows point to the time of entrainment when both species entered from biomass burning (BB) plumes into the PBL.

3.2.3. Steady-state calculations of peroxy radicals

For obtaining a comprehensive picture about (i) sources and sinks of H_2O_2, CH_3OOH and HCHO and (ii) the oxidizing capacity during HUMPPA, the following steps needed to be performed for extending the observed OH and HO_2 data (LIF instrument):

1. Calculation of the deviations from photostationary state ϕ and $[RO_x]$ (Section 3.1.1.1).
2. Estimation of the $[HO_2]/[RO_x]$ partitioning to obtain $[HO_2]_{PSS}$ (Section 3.2.3.1).
3. Evaluation of $[HO_2]_{PSS}$ and other calculations (using the [PAA]/[PAN] ratio) via the observed $[HO_2]_{LIF}$ (Section 3.2.3.1).
4. Estimation of the missing OH data by fitting the observed $[HO_2]_{LIF}/[OH]_{LIF}$ ratio and invoking $[HO_2]_{PSS}$ (Section 3.2.3.2).
5. Estimation of important organic peroxy radical mixing ratios, such as $[CH_3O_2]$ and $[AcO_2]$ by using the observations and calculations (sections 3.2.3.4 and 3.2.3.5).
6. Estimation of the H_2O_2 and HCHO budgets (sections 3.2.5 and 3.2.7).

3.2.3.1. Estimation and evaluation of $[HO_2]$ for the entire campaign

HO_2 levels were estimated through two independent approaches: derived from the $[CO]/[CH_4]$ ratio (in the following CO-CH_4 method and $[HO_2]_{PSS}$, respectively) and the [PAA]/[PAN] ratio (Phillips et al., 2013). Afterwards, an evaluation with measured HO_2 ($[HO_2]_{LIF}$) will be performed.

$[HO_2]_{PSS}$ derived from the CO-to-CH_4 ratio assuming steady state conditions. Observations and model studies have shown that the $[HO_2]/[RO_2]$ ratio is relatively constant and close to unity during daytime, regardless of the NO_x levels (Cantrell et al., 2003; Mihelcic, 2003). Thus, the following approach is based on the remote background troposphere, where CH_4 (ca. 1.8 ppmv) and CO (ca. 100 ppbv) dominate assuming that HO_2 and CH_3O_2 are the only components of RO_x.
CO reacts with OH forming an H atom which collides with molecular oxygen and instantaneously produces HO_2.

$$\begin{aligned} CO + OH &\longrightarrow CO_2 + H \\ H + O_2 &\xrightarrow{M} HO_2 \end{aligned} \tag{3.26}$$

CH_4 is oxidized in a similar way by OH, over an intermediate CH_3, which yields methyl peroxy radicals (CH_3O_2).

$$\begin{aligned} CH_4 + OH &\longrightarrow CH_3 + H_2O \\ CH_3 + O_2 &\xrightarrow{M} CH_3O_2 \end{aligned} \tag{3.27}$$

Assuming that the highest fraction of $[RO_2]$ is $[CH_3O_2]$, $[HO_2]$ can be estimated, namely

$$[HO_2]_{PSS} \approx \frac{P(HO_2)}{P(HO_2) + P(CH_3O_2)}[RO_x] = \frac{k_{3.26}[CO]}{k_{3.27}[CO] + k_{3.27}[CH_4]}[RO_x] \tag{3.28}$$

Note that the background mixing ratios of CO and CH_4 are several orders of magnitude higher than other VOCs.

$[HO_2]_{PAA/PAN}$ derived from the PAA-to-PAN ratio assuming steady state conditions. Another approach of estimating $[HO_2]$ takes profit of the peroxyacetyl nitrate (PAN, $CH_3C(O)O_2NO_2$) and peroxyacetic acid (PAA, $CH_3C(O)OOH$) observations during HUMPPA (Phillips et al., 2013).
Hereby, the thermal decomposition of PAN and the oxidation of PAA lead to the formation of peroxyacetyl radicals ($CH_3(O)O_2$).

$$CH_3C(O)O_2NO_2 \xrightarrow{M} CH_3C(O)O_2 + NO_2 \tag{3.29}$$

$$CH_3C(O)OOH + OH \longrightarrow CH_3C(O)O_2 + H_2O \tag{3.30}$$

Those are lost via the reaction with NO forming CH_3O_2 or recombine with NO_2 to PAN. The reaction with HO_2 leads to the thermostable PAA.

$$CH_3C(O)O_2 + NO \longrightarrow CH_3 + CO_2 + NO_2 \tag{3.31}$$

$$CH_3C(O)O_2 + NO_2 \xrightarrow{M} CH_3C(O)O_2NO_2 \tag{3.32}$$

$$CH_3C(O)O_2 + HO_2 \longrightarrow CH_3C(O)OOH + O_2 \tag{3.33}$$

Setting up the steady state equation for the PAA/PAN ratio, simplifying and solving for $[HO_2]$ leads the following expression, namely

$$[HO_2]_{PAA/PAN} = \frac{[PAA]}{[PAN]} \cdot \frac{[NO_2]\, k_{3.32}\, (k_{3.30}\, [OH] + D_{PAA})}{k_{3.33}\, k_{3.29}} \tag{3.34}$$

Since there is no experimental data for $k_{3.30}$, a rate coefficient of approximately 1×10^{-12} cm^3 s^{-1} is assumed. The loss rate $k_{3.30}\,[OH]$ is comparable to the dry deposition D_{PAA} (Baer and Nester, 1992).

Evaluation of the calculations. Figure 3.11 shows an overview on observed HO_2 (LIF instrument) and calculated HO_2. The time series depicts $[HO_2]_{PSS}$ in comparison to $[HO_2]_{LIF}$ for the available period (Aug 1-8 2010). Note that the LIF instrument interferes with $[RO_2]$ and thus HO_2 may be up to ca. 20 % higher (Fuchs et al., 2011). Nonetheless, deviations of $[HO_2]_{PSS}$ from $[HO_2]_{LIF}$ were quantified as follows

$$\Delta[HO_2]_{PSS} = \left(\frac{[HO_2]_{PSS} - [HO_2]_{LIF}}{[HO_2]_{LIF}} \right) \cdot 100\% \tag{3.35}$$

From 8:00-19:00 UTC+2, $[HO_2]_{PSS}$ is in good agreement with the observations showing deviations of ca. −25 to 25 %. However, during rainy days (Aug 3-4), the calculation significantly underestimates HO_2 by −100 %. Photostationary state is unlikely to be fully established for cloudy conditions as discussed before.

The time series for the entire campaign (Jul 12-Aug 12) shows comparable daytime HO_2 levels between 10 and 70 pptv for $[HO_2]_{PSS}$ and $[HO_2]_{PAA/PAN}$. Note that $[HO_2]_{PSS}$ provided the most data points and was used for further studies. $[HO_2]_{PAA/PAN}$ solely served for evaluation.

The correlation plot shows a very good agreement of $[HO_2]_{PSS}$ with $[HO_2]_{LIF}$ ($m = 0.44 \pm 0.029$, $r^2 = 0.71$), although the levels are generally by 56 % lower. $[HO_2]_{PAA/PAN}$ also underestimates by ca. 53 % and agrees less with the observations ($m = 0.47 \pm 0.17$, $r^2 = 0.12$). However, note that the calculated data points depend on the data availability.

As a result, both methods, CO/CH_4 and PAA/PAN, lead to comparable values, particularly for low mixing rations ($HO_2 < 10$ pptv). For the available data points, $[HO_2]_{PAA/PAN}$ underestimates by 53 % with a rather bad correlation, whereas OH lies in similar orders in comparison to the LIF observations. In addition, there is even less agreement during special rain events.

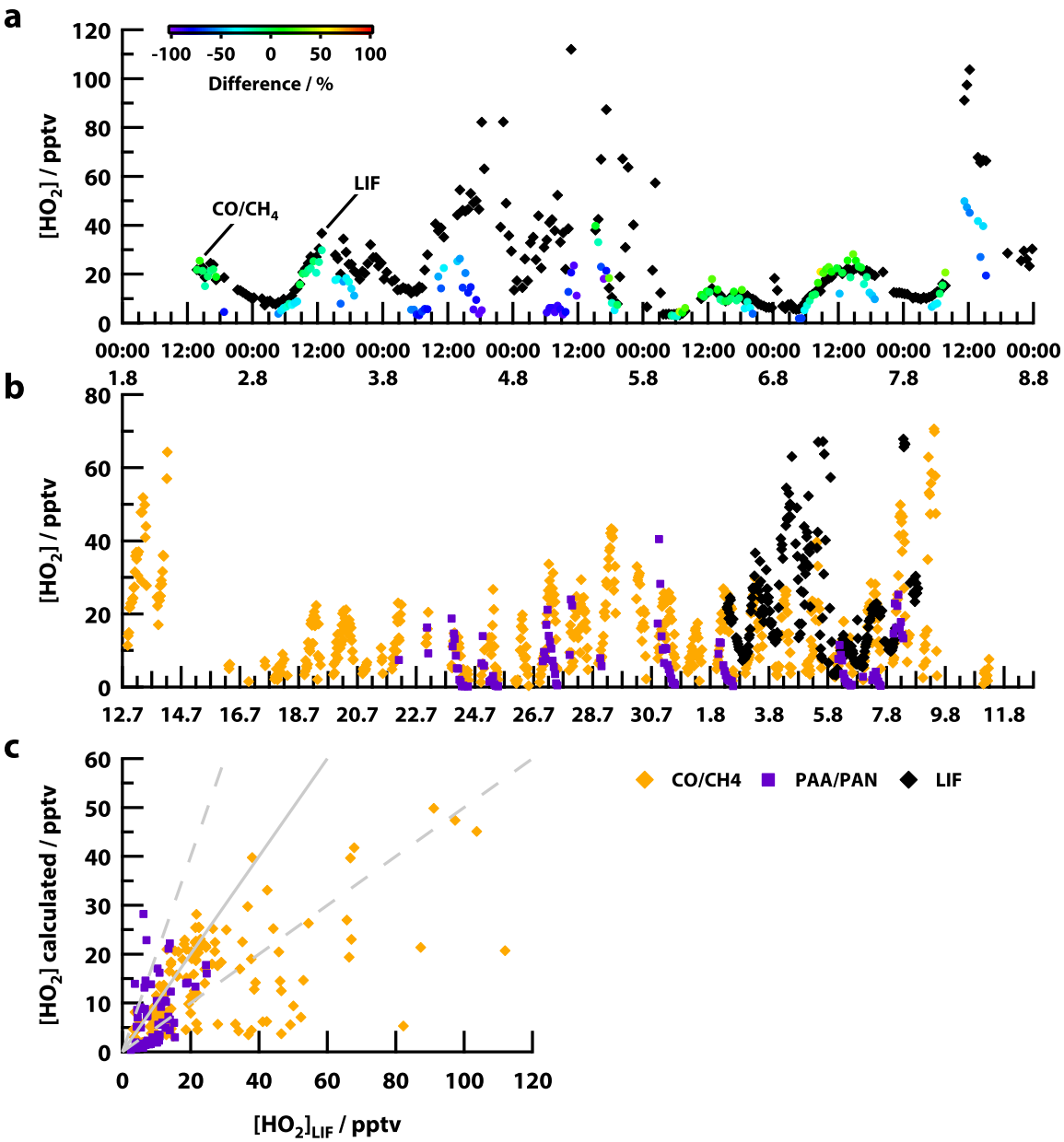

Figure 3.11.: Time series comparison of measured and calculated $[HO_2]$ for HUMPPA. 5 min data derived from the ratio of CO+OH to CH_4+OH ($[HO_2]_{PSS}$) versus LIF measurements ($[HO_2]_{LIF}$), where the colour code indicates the relative difference in % (**a**). HO_2 calculations via the CO to CH_4 and PAA to PAN ratio ($[HO_2]_{PAA/PAN}$), respectively, and LIF measurements (**b**). Correlation plots of estimated $[HO_2]$ versus $[HO_2]_{LIF}$ excluding the biomass burning series (**c**). Parameters: CO to CH_4 (m = 0.44 ± 0.029, r^2 = 0.71) and PAA/PAN (m = 0.47 ± 0.17, r^2 = 0.12).

3.2.3.2. Estimation of daytime [OH] for the entire field campaign

OH measurements performed by the LIF instrument were only available for one week during HUMPPA. That required a suitable method for obtaining complete data. The HO_2/OH ratio is a measure of the OH recycling efficiency and high levels are typical under low NO_x conditions (Hofzumahaus et al., 2009; Mihelcic, 2003; Ren et al., 2006). The ratio is nearly constant until the early morning, whereas it grows quasi-exponentially until the late afternoon.

For HUMPPA data, the logarithm of the $[HO_2]_{LIF}$ to $[OH]_{LIF}$ ratio showed linear growth during three available days (Aug 2, 5 and 6 2010) from the late morning (9:00-11:30 UTC+2) to the late

afternoon (18:00-19:00 UTC+2) as depicted in Figure 3.12. This time window will be further discussed, since calculated HO_2 data ($[HO_2]_{PSS}$) is available. Considering those three days yielded an average slope $\bar{b}$ and intercept $\bar{a}$ of $0.164 \pm 0.0250\ h^{-1}$ (fraction of hour of day starting with 0 at midnight), and 3.44 ± 0.492, respectively. The intercept indicates an early mid-day ratio of $[HO_2]_{LIF}$ to $[OH]_{LIF}$ about $\exp(3.44) \approx 31.2$ (consistent with e. g., Stevens et al., 1997, 15 to 80), whereas it increases over one order of magnitude by late afternoon.

$$\ln\left(\frac{[HO_2]_{LIF}}{[OH]_{LIF}}\right) = \bar{b} \cdot \text{hour of day} + \bar{a} \tag{3.36}$$

As a result, the fit allows to calculate the OH mixing ratio, $[OH]_{PSS}$, in dependence of $[HO_2]_{PSS}$ (Figure 3.13).

$$[OH]_{PSS} = \frac{[HO_2]_{PSS}}{\exp\left(\bar{b} \cdot \text{hour of day} + \bar{a}\right)} \tag{3.37}$$

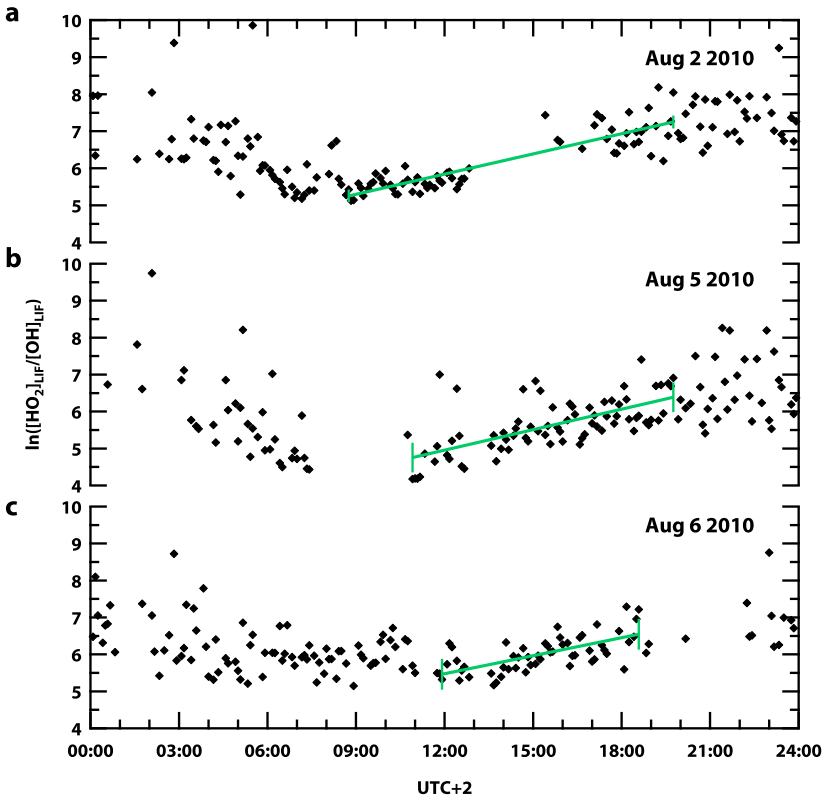

Figure 3.12.: Linear fit of the logarithmic $[HO_2]_{LIF}$ to $[OH]_{LIF}$ ratio for three days during HUMPPA. Clear sky conditions and sufficient 5 min data (LIF instrument) was available Aug 2, 5 and 6. The ratio of HO_2 to OH is given as $\ln\left(\frac{[HO_2]_{LIF}}{[OH]_{LIF}}\right)$ as a function of time. The green line indicates fitted data points.

Evaluation of the calculation. Figure 3.13 shows an overview on observed (LIF instrument) and calculated OH. The time series depicts $[OH]_{PSS}$ in comparison to $[OH]_{LIF}$ for the available period (Aug 1-9 2010). Deviations of $[OH]_{PSS}$ from $[OH]_{LIF}$ were quantified as follows

$$\Delta[OH]_{PSS} = \left(\frac{[OH]_{PSS} - [OH]_{LIF}}{[OH]_{LIF}} \right) \cdot 100\% \tag{3.38}$$

From 6:00-11:00 UTC+2, $[OH]_{PSS}$ overestimates the observations from ca. 50 to 100 %. However, from noon time to 15:00 UTC+2 the calculation agrees well with $[OH]_{LIF}$ (−25 to 50 %). Data points for late afternoon (15:00-19:00 UTC+2) disagree towards lower values (−100 to −25 %).

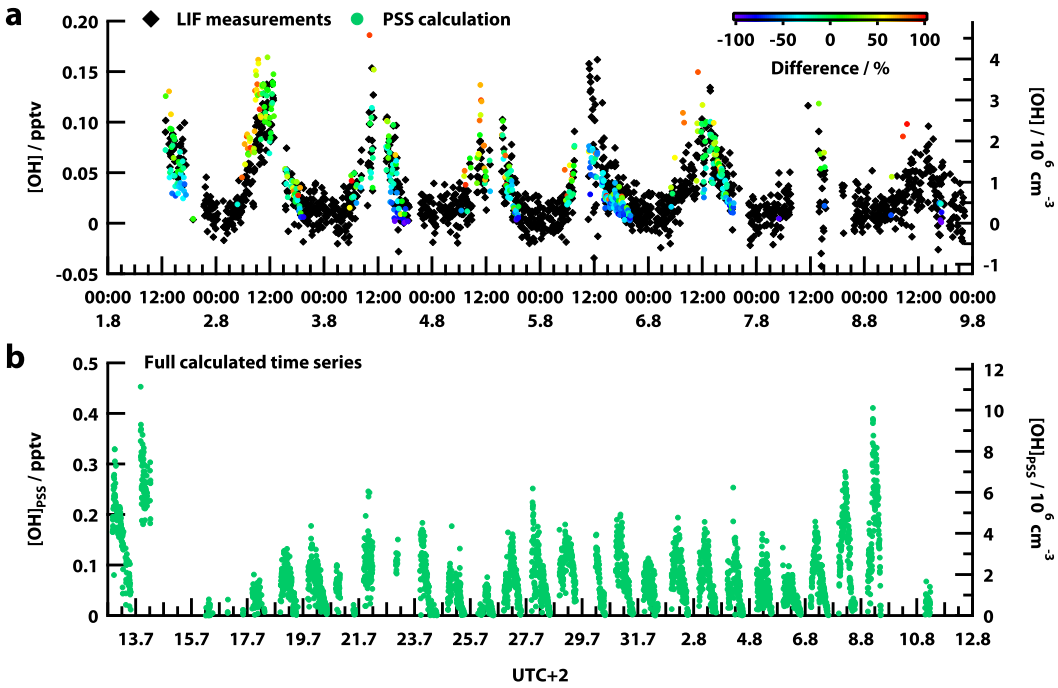

Figure 3.13.: Time series comparison $[OH]_{PSS}$ vs. $[OH]_{LIF}$. Intercomparison of LIF data (5 min resolution) with $[OH]_{PSS}$ (pptv and 1/cm^3). The colour code indicates the deviations of the estimation (**a**). Time series of $[OH]_{PSS}$ (pptv and 1/cm^3) for the entire campaign (**b**).

3.2.3.3. Estimation and evaluation of $[CH_3O_2]$, $[AcO_2]$ and $[RO_2]$

The following sections describe the estimation of organic peroxy radical species which are needed for calculating the HCHO and methyl hydroperoxide budget for the HUMPPA field campaign. The most important are methyl peroxy (CH_3O_2) and peroxyacetyl radicals ($CH_3C(O)O_2$).

3.2.3.4. Steady state calculation of $[AcO_2]$

The peroxyacetyl radical is mainly formed via the oxidation of acetaldehyde by OH and the thermal decomposition of PAN (Choi et al., 2010; LaFranchi et al., 2009).

$$CH_3CHO + OH \longrightarrow CH_3(O)O_2 + H_2O \tag{3.39}$$

$$CH_3C(O)OONO_2 \xrightarrow{M} CH_3(O)O_2 + NO_2 \tag{3.40}$$

Other sources may be the reaction of OH with isoprene, α-pinene and hydrocarbons with acetaldehyde as intermediates (Atkinson and Arey, 2003a; LaFranchi et al., 2009; Phillips et al., 2013). Those will be neglected and the potential contribution of isoprene will be discussed later.
Unless any other peroxy radical, $CH_3O(O)O_2$ reacts one order of magnitude faster with NO yielding $CH_3(O)O$ (Equation 3.41). Note that the decomposition of $CH_3(O)O$ forms CH_3O_2 radicals, $CH_3C(O)O_2 + NO + O_2 \longrightarrow NO_2 + CH_3O_2 + CO_2$ and was taken into account in Section 3.2.3.5. The peroxyacetyl radical also reacts with NO_2 forming PAN (Equation 3.42). Another important reaction is the recombination with HO_2 radicals yielding peracetic acid (Equation 3.43). In a minor pathway, $CH_3O(O)O_2$ reacts with other peroxy radicals to form different products such as CH_3O_2 (Equation 3.44).

$$CH_3C(O)O_2 + NO \longrightarrow CH_3(O)O + NO_2 \tag{3.41}$$

$$CH_3C(O)O_2 + NO_2 \xrightarrow{M} CH_3(O)OONO_2 \tag{3.42}$$

$$CH_3C(O)O_2 + HO_2 \longrightarrow 0.4\ CH_3(O)OOH + 0.4\ OH + 0.4\ CH_3O_2 + \text{products} \tag{3.43}$$

$$CH_3C(O)O_2 + RO_2 \longrightarrow CH_3O_2 + \text{products} \tag{3.44}$$

Now the steady state equation for $[CH_3C(O)O_2]$ can be set up, namely

$$[CH_3C(O)O_2]_{SS} = \frac{k_{3.39}[CH_3CHO][OH] + k_{3.40}[PAN]}{k_{3.41}[NO] + k_{3.42}[NO_2] + k_{3.43}[HO_2]_{SS} + k_{3.44}[RO_2]_{PSS}} \tag{3.45}$$

Note that intermediates of the oxidation of isoprene by OH lead to glyoxal and methyl vinyl ketone which impact $[CH_3C(O)O_2]_{SS}$ towards higher levels. Their contribution on the budget was estimated to account for ca. 40 % (according to LaFranchi et al., 2009) and was corrected.

3.2.3.5. Steady state calculation of $[CH_3O_2]$

The methyl peroxy radical plays a major role in the oxidation pathway of methane (CH_4). However, there are other sources, such as the photolysis of acetaldehyde (CH_3CHO) and reactions involving $CH_3C(O)O_2$. Note that for HUMPPA potential contributions of intermediates from BVOCs and the oxidation of methyl hydroperoxide (CH_3OOH) by OH were neglected.
The oxidation of CH_4 (Equation 3.46) is initiated by OH and produces methyl radicals (CH_3) so as the photolysis of acetaldehyde (Equation 3.47), whereas it reacts instantaneously with molecular O_2 to yield CH_3O_2. As discussed before, $CH_3C(O)O_2$ reacts with NO (Equation 3.48), RO_2 (Equation 3.49) and HO_2 (Equation 3.50) to form acetyl radicals ($CH_3C(O)O$). The equations 3.49 and 3.50 are secondary pathways which do not form hydroperoxides. Especially the recombination

with HO_2 competes with the production of PAA and acetic acid (Atkinson et al., 2006), whereas those account only for ca. 6 % of the CH_3O_2 production (agreeing with Choi et al., 2010).

$$CH_4 + OH \longrightarrow CH_3 + H_2O \tag{3.46}$$

$$CH_3CHO + h\nu \longrightarrow CH_3 + CHO \tag{3.47}$$

$$CH_3C(O)O_2 + NO \longrightarrow CH_3C(O)O + NO_2 \tag{3.48}$$

$$CH_3C(O)O_2 + RO_2 \longrightarrow CH_3C(O)O + \text{aldehydes} + O_2 \tag{3.49}$$

$$CH_3C(O)O_2 + HO_2 \longrightarrow CH_3C(O)O + OH + O_2 \tag{3.50}$$

As do other peroxy radicals, the main loss of CH_3O_2 is caused by the reaction with NO (Equation 3.51) yielding an intermediate methoxy radical which instantaneously produces HCHO (discussed later). The second pathway is the recombination with HO_2 to form methyl hydroperoxide (CH_3OOH). A minor sink is the reaction with other organic peroxy radicals (Equation 3.53).

$$CH_3O_2 + NO \longrightarrow CH_3O + NO_2 \tag{3.51}$$

$$CH_3O_2 + HO_2 \longrightarrow CH_3OOH + O_2 \tag{3.52}$$

$$CH_3O_2 + RO_2 \longrightarrow HCHO + \text{products} + O_2 \tag{3.53}$$

Note that the PAN formation is an additional loss reaction (Equation 3.54), whereas the equilibrium favours CH_3O_2 and thus is neglectable.

$$CH_3O_2 + NO_2 \rightleftharpoons CH_3O_2NO_2 \tag{3.54}$$

Finally, setting up the steady state equation for $[CH_3O_2]_{SS}$ yields the following expression, namely

$$[CH_3O_2]_{SS} = \tag{3.55}$$

$$\frac{k_{3.46}[CH_4][OH] + j(CH_3CHO)[CH_3CHO] + (k_{3.48}[NO] + k_{3.49}[RO_2] + k_{3.50}[HO_2])[AcO_2]_{SS}}{k_{3.51}[NO] + k_{3.52}[HO_2]} \tag{3.56}$$

3.2.3.6. Evaluation of organic peroxy radical estimations

As shown before, photostationary state calculations allow an estimation of $[RO_x]_{PSS}$. It should be noted that an intercomparison with PerCA measurements indicated 23 to 166 % higher levels for $[RO_x]_{PSS}$ under low-NO_x (32 pptv, Mauna Loa Observatory, Hawaii, USA; Hauglustaine et al., 1999) and high-NO_x (4 ppbv, pine plantation in Alabama, USA; Cantrell et al., 1993).
However, concerning the previous sections, the fraction of unknown organic peroxy radicals, $[RO_2]^*$, can be expressed as the difference of $[HO_2]_{PSS}$, $[CH_3O_2]_{SS}$ and $[AcO_2]_{SS}$ from $[RO_x]_{PSS}$, as follows

$$[RO_2]^* = [RO_x]_{PSS} - [HO_2]_{PSS} - [CH_3O_2]_{SS} - [AcO_2]_{SS} \tag{3.57}$$

According to the photostationary state expression, the NO_2 mixing ratio, $[NO_2]_{SS}$, can be calculated including the previously estimated peroxy radicals HO_2, CH_3O_2 and AcO_2 (Hosaynali-Beygi et al.,

Table 3.9.: Life time estimation of RO_x towards the reaction with NO and HO_2 based on typical daytime levels measured during the entire campaign: $[NO] \approx 1 \times 10^9\,cm^{-3}\,s^{-1}$ (41 pptv) and $[HO_2] \approx 5 \times 10^8\,cm^{-3}\,s^{-1}$ (20 pptv). The reactions are sorted after their tendency to react through the NO or HO_2 channel, yielding an alkoxy radical ($RO\cdot$) and a hydroperoxide (ROOH), respectively. Alkoxy radical react rapidly with molecular oxygen to the respective aldehyde.

Reaction	τ_{RO_x}	Ratio $\frac{\tau_{RO_x+NO}}{\tau_{RO_x+HO_2}}$
$HO_2 + NO \longrightarrow OH + NO_2$	117 s	10
$HO_2 + HO_2 \longrightarrow H_2O_2 + O_2$	21 min	
$CH_3C(O)O_2 + NO \longrightarrow CH_3C(O)O\cdot + NO_2$	50 s	7
$CH_3C(O)O_2 + HO_2 \longrightarrow CH_3C(O)OOH + O_2$	5.9 min	
$CH_3O_2 + NO \longrightarrow CH_3O + NO_2$	129 s	3
$CH_3O_2 + HO_2 \longrightarrow CH_3OOH + O_2$	7.2 min	
$HOCH_2O_2 + NO \longrightarrow HOCH_2O + NO_2$	177 s	1.9
$HOCH_2O_2 + HO_2 \longrightarrow HOCH_2OOH + O_2$	5.7 min	
$HOCH_2CH_2O_2 + NO \longrightarrow HOCH_2CH_2O + NO_2$	110 s	1.5
$HOCH_2CH_2O_2 + HO_2 \longrightarrow HOCH_2CH_2OOH + O_2$	169 s	

2011; Mihelcic, 2003; Volz-Thomas, 2003a). The only observed parameters hereby are $j(NO_2)$, $[O_3]$ and $[NO]_{CLD}$ (CLD).

$$[NO_2]_{SS} = \frac{(k_{3.2}[O_3] + k_{3.48}[CH_3C(O)O_2]_{SS} + k_{3.51}[CH_3O_2]_{SS} + k_{3.7}[HO_2]_{PSS})\,[NO]_{CLD}}{j(NO_2)} \quad (3.58)$$

Figure 3.14 shows a time series of $[NO]_{SS}$ for HUMPPA. Daytime mixing ratios show a good correlation of $r^2 = 0.99$ with the observations, $[NO]_{CLD}$. None of the differences are significantly outside ±50 %. Note that the term $k_{3.2}[O_3]$ has a significant impact on Equation 3.58 and thus may "mask" the contributions of the reactions of HO_2, CH_3O_2 and AcO_2 with NO. However, especially AcO_2 reacts one order of magnitude faster than other organic peroxy radicals. The mixing ratio was estimated – as $[CH_3O_2]$ – by steady-state considerations which are independent from the photostationary assumption. The correlation plot of $[NO]_{SS}$ vs. $[NO]_{CLD}$ shows a slope close to unity and as a result, this indicates reasonable levels of peroxy radicals.

The mixing ratio of methyl peroxy radicals may be evaluated by the steady-state calculation of methyl hydroperoxide, CH_3OOH or MHP. It is produced by the recombination of CH_3O_2 with HO_2 (Equation 3.52). Losses are determined by photolysis and the reaction with OH radicals.

$$CH_3OOH + h\nu \longrightarrow OH + CH_3O \quad (3.59)$$

$$CH_3OOH + OH \longrightarrow H_2O + CH_2OOH \quad (3.60)$$

The steady-state equation of methyl hydroperoxide, $[MHP]_{SS}$ (in pptv), is expressed as follows

$$[MHP]_{SS} = \frac{k_{3.52}[CH_3O_2]_{SS}[HO_2]_{SS}}{j(MHP) + k_{3.60}[OH]_{SS}} \quad (3.61)$$

Figure 3.14 shows the comparison of $[MHP]_{SS}$ with an estimation ($[MHP]^*$ in ppbv) from the total hydroperoxide channel, [ROOH] (without correction for unknown stripping efficiencies α) of the AL2021 instrument.

$$[MHP]^* = \frac{[ROOH] - 0.9[PAA]}{0.6} \tag{3.62}$$

[PAA] is hereby the CIMS data measurements of peracetic acid ($CH_3C(O)OOH$ in ppbv). The stripping efficiencies α are 0.6 for methyl hydroperoxide (Lazrus et al., 1986; Lind and Kok, 1994) and 0.9 for peracetic acid (K. Bauer, priv. comm. 2012 Lind and Kok, 1994; O'Sullivan et al., 1996).
The correlation of $[MHP]_{SS}$ with $[MHP]^*$ is good (r^2 = 0.7), whereas the steady-state calculation underestimates by a factor of approximately 2. There are two possibilities: either $[CH_3O_2]_{SS}$ is underestimated or $[MHP]^*$ is overestimated. It is highly likely that the peroxide channel quantifies organic hydroperoxides, which are the sink of intermediates from the isoprene and monoterpene oxidation. However, this consideration assumes methyl hydroperoxide and peracetic acid to be the predominant organic hydroperoxides.

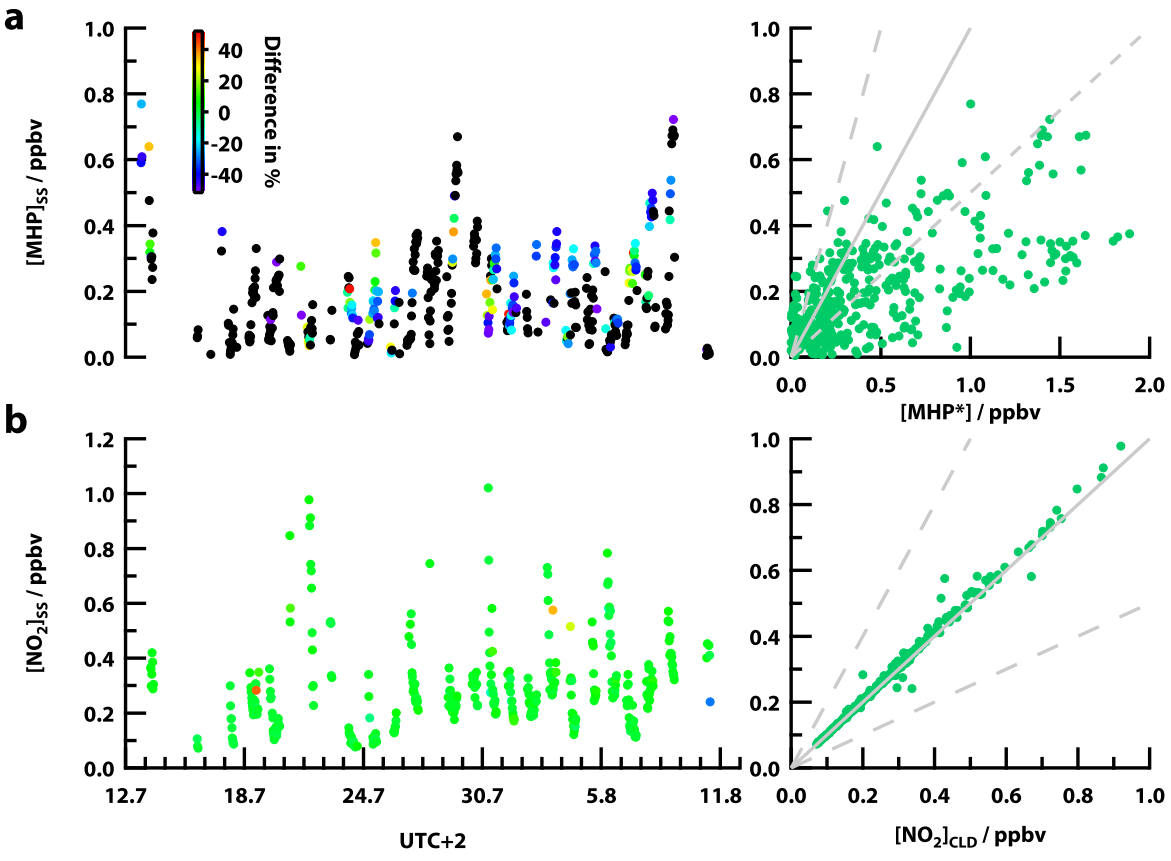

Figure 3.14.: Time series of steady-state calculations for MHP and NO_2 as well as correlation plots versus measurements. Time series and correlation plot (r^2 = 0.7) for $[MHP]_{SS}$ (**a**). The colour code indicates deviations from estimated ambient $[MHP]^*$ in percent, whereas black dots are out of a range from −50 to 50 %. Time series and correlation plot (r^2 = 0.99) for $[NO_2]_{SS}$ (**b**). None of the differences to $[NO_2]_{CLD}$ are significantly outside ±50 %.

3.2.4. Daytime levels and partitioning of [RO_x]

Table 3.10 presents several calculated parameters in accordance to the four regimes, namely the deviation from the photostationary state (ϕ), mixing ratios of hydroperoxy (HO_2), methyl peroxy (CH_3O_3), acetyl peroxy (AcO_2) radicals and the remaining organic peroxy radical fraction (RO_2*). In addition, the net O_3 production rate $N(O_3)$ is given. As described before, the index "PSS" represents parameters derived from photostationary state calculations, whereas "SS" indicates steady-state calculations. The first regime is characterised by a medium ϕ (1.45) accompanied by relatively high HO_2 (26.0 pptv), CH_3O_2 (2.10 pptv), AcO_2 (1.15 pptv) and medium RO_2* (27.2 pptv). This trend is reflected by an average net O_3 production rate (1.06 ppbv min^{-1}). Although cold and clean conditions yield a comparable deviation from photostationary state (1.44), ambient radical mixing ratios achieve solely minimum values: HO_2 (10.6 pptv), CH_3O_2 (1.20 pptv) and RO_2* (14.0), whereas AcO_2 is even insignificant. As a consequence, $N(O_3)$ reaches a minimum (0.501 pptv h^{-1}). The biomass burning series shows a high deviation from photostationary state (1.63) accompanied by the highest peroxy radical mixing ratios: HO_2 (26.3 pptv), CH_3O_2 (2.52 pptv), AcO_2 (2.08 pptv) and RO_2* (24.0 pptv). However, $N(O_3)$ is characterised by medium values (1.44 pptv h^{-1}). The highest ϕ (1.64) was calculated for R4 (normal boreal accompanied by some events). HO_2 values are hereby the highest (27.5 pptv), whereas CH_3O_3 and AcO_2 reach only medium mixing ratios (2.44 pptv and 1.21 pptv), respectively, as well as RO_2* (31.5 pptv). The net O_3 production is remarkably high (1.75 ppbv h^{-1}). Note that the trends of NO_x are comparable to the increase in $N(O_3)$ starting from lowest values for R2 (264 pptv), over R3 (397 pptv) and R1 (360 pptv) up to R4 (417 pptv).

The presented trends reflect that O_3 is net produced at high ambient peroxy and nitric oxide mixing ratios (Sillman, 1999). The regime R4 (normal boreal) plays hereby an outstanding role since $N(O_3)$ is 3.5 times higher than during R2 (cold & clean) as a reference for particularly low NO_x conditions. Besides, those are still exceeded by a factor of 2.4 during the biomass burning series (R3). However, those air masses were photochemically aged, which might have led to the removal of NO_x. The period of stressed boreal conditions (R1) is characterized by relatively low NO_x by coincidence and shows consequently a low net O_3 production. Anyway, the regimes excluding R2 are a proxy for the boreal forest affected by global warming.

Table 3.10.: Calculated $[HO_2]_{PSS}$, $[CH_3O_2]_{SS}$, $[RO_2]^*$ (in pptv) from PSS and SS. (R1) stressed boreal, (R2) cold and clean, (R3) transported pollution and (R4) normal boreal. Daytime values were averages between 12-14 UTC+2 (highest [ROx], best estimation of $[OH]_{PSS}$) of 30 min data, relative values indicate the variability (1σ). The relative contributions of $[HO_2]_{PSS}$, $[CH_3O_2]_{SS}$ and $[RO_2]^*$ to [ROx] is 43.80 ± 2.66 %, 4.060 ± 0.319 % and 52.20 ± 2.38 % throughout all the regimes.

Species	Unit	R1		R2		R3		R4	
		Average	1σ / %	Average	1σ / %	Average	1σ / %	Average	1σ / %
ϕ	—	1.45	29.2	1.44	22.3	1.63	11.6	1.64	11.3
$[HO_2]_{PSS}$	pptv	26.0	60.2	10.6	49.4	26.3	28.5	27.5	67.3
$[CH_3O_2]_{SS}$	pptv	2.10	15.1	1.20	49.6	2.52	25.6	2.44	53.6
$[AcO_2]_{SS}$	pptv	1.15	94.8	—	—	2.08	55.9	1.21	94.5
$[RO_2]^*$	pptv	27.2	9.46	14.0	46.1	33.6	24.0	31.5	27.6
$N(O_3)$	ppbv h^{-1}	1.06	115	0.501	92.1	1.44	29.3	1.75	54.8

3.2.5. Budget calculations for H_2O_2 and HCHO excluding dry deposition

The following section describes the budget calculations of O_3, H_2O_2 and HCHO for Chapter 3. For simplicity, production and loss reactions as well as the kinetic terms were compiled in tables. The corresponding rate coefficients *k* are listed in the appendix Chapter E. Parameters with an index, such as $[HO_2]_{SS}$, $[RO_2]_{PSS}$ and $[OH]_{SS}$ are based on steady-state calculations, whereas the others are direct measurements.

3.2.5.1. Brief overview on source and sink reactions of H_2O_2

Main source. H_2O_2 is produced via the recombination of two HO_2 radicals (Table 3.11). Water plays hereby an important role in accelerating the reaction (Gnauk et al., 1997; Gunz and Hoffmann, 1990) and this effect was considered. Note that NO (above 100 pptv) is a major competitor for the production of H_2O_2 as it destroys HO_2 radicals (Lee et al., 2000), namely

$$HO_2 + NO \longrightarrow OH + NO_2$$

Sources from ozone–alkene reactions. H_2O_2 can also be produced by the ozonolysis of alkenes, such as isoprene and monoterpenes. This pathway involves intermediate Crigée bi-radicals and is independent from HO_2 (Becker et al., 1990, 1993). However, water vapour may influence this reaction as well. The herein used rate coefficients are given in the appendix Chapter E.

Sinks. There are two predominant sinks such as photolysis and the reaction with OH.

Table 3.11.: Calculation of the H_2O_2 budget.

Reaction	Expression
Production (P)	
$HO_2 + HO_2 \longrightarrow H_2O_2 + O_2$	$k[HO_2]_{PSS}[NO]$
Alkene + $O_3 \longrightarrow \alpha\, H_2O_2$ + products	See Table E.2 in the appendix.
Alkene + OH $\longrightarrow \alpha\, H_2O_2$ + products	See Table E.3 in the appendix.
Losses (L)	
$H_2O_2 + h\nu \longrightarrow 2\,OH$	$j(H_2O_2)[H_2O_2]$
$H_2O_2 + OH \longrightarrow H_2O + HO_2$	$k[H_2O_2][OH]_{PSS}$

3.2.5.2. Photochemical sources and sinks of hydrogen peroxide

Hydrogen peroxide sources. Figure 3.15 divides the relative H_2O_2 production through the regimes R1–R4 into two major groups: (i) the recombination of HO_2 and (ii) the ozonolysis of alkenes. Note that absolute production rates, $N(H_2O_2)$, are given in Table 3.12 (appendix Chapter B). Those range from 256 (R4) over 234 (R1) and 185 (R3) to finally 43.5 pptv h^{-1} (R2). So the biomass burning series (R4) shows the highest production, whereas the cold and clean regime (R2) tends to lowest production rates.

The recombination of HO_2 is the only significant H_2O_2 source ranging from 79 (R2) to 96 % (R4). Hereby, the regime with the lowest absolute production rate (R2) has the lowest fraction for the HO_2 recombination (79 %). On the other hand, R4 shows the opposite trend. The two stressed boreal regimes R1 and R3 are not only comparable concerning absolute, but also in relative rates (86 % and 89 %, respectively).

The ozonolysis of alkenes is the second major group of H_2O_2 sources. Note that the absolute values may distort perceptions about the relative contributions. However, R2 is dominated by 21 % (9.20 pptv h^{-1}), whereas the biomass burning series shows the lowest relative contribution with 4 % (10.4 pptv h^{-1}). Again the regimes R1 and R3 are comparable with 14 and 11 %, although absolute production rates differ significantly (R1: 33.0 pptv h^{-1}, R2: 20.9 pptv h^{-1}).

Taking closer look at R1, the ozone-alkene fraction is dominated by the ozonolysis of α-pinene (7.0 %, 16.3 pptv h^{-1}), whereas myrcene and Δ^3-carene play a minor role with 3.8 % (8.78 pptv h^{-1}) and 2.9 % (6.87 pptv h^{-1}), respectively. The ozonolysis of isoprene and β-pinene is of practically no significance (below 1 %) for all regimes. At the beginning of R2 the weather changed quickly towards colder and dryer meteorological conditions. Remnants of ambient monoterpenes from the previous R1 influenced this period of HUMPPA. The ozonolysis of α-pinene significantly accounts for 13 % (only 5.63 pptv h^{-1}) of the relative H_2O_2 production. The contributions of myrcene and Δ^3-carene oxidation is by far lower: 4.3 % (1.87 pptv h^{-1}) and 2.4 % (1.05 pptv h^{-1}), respectively. The next regime (R3) is characterised by a mixture of boreal stressed, biomass burning and rainy conditions. Relative contributions of α-pinene (6.4 %, 11.8 pptv h^{-1}) and myrcene (3.3 %, 6.18 pptv h^{-1}) are comparable to R2 except for Δ^3-carene (1.1 %, 2.10 pptv h^{-1}). As discussed before, the biomass burning series (R4) shows a totally different trend. Monoterpene oxidation chemistry almost plays no role: the α-pinene pathway accounts for solely 2.7 % (6.88 pptv h^{-1}) of the total

relative production. The ozonolysis of myrcene and Δ^3-carene are insignificant contributing 0.63 % (1.61 pptv h^{-1}) and 0.54 % (1.38 pptv h^{-1}), respectively.

The recombination of HO_2 radicals is significantly the main H_2O_2 source through all regimes as expected. Especially for the biomass burning series (R4) it plays a special role for the production of H_2O_2, whereas cold and clean summer conditions (R2) show more importance of the ozonolysis of alkenes. Note that the high ambient monoterpene mixing ratios during this period of HUMPPA were caused by remnants from stressed boreal conditions (R1).

Table 3.12.: Calculated H_2O_2 budget for HUMPPA according to the regimes (R1-R4). Production and loss rates are given in pptv h^{-1} including combined variabilities (1σ). Note that the direct (first level) production of H_2O_2 via the oxidation of alkenes by OH is insignificant.

Reaction	R1		R2		R3		R4	
	Average	1σ / %	Average	1σ / %	Average	1σ / %	Average	1σ / %
Production								
$HO_2 + HO_2$	201	125	34.3	76.8	164	48.2	246	149
O_3 + α-Pinene	16.3	83.5	5.63	30.2	11.8	69.3	6.88	23.1
O_3 + Myrcene	8.77	111	1.87	12.6	6.18	118	1.61	29.1
O_3 + Δ^3-Carene	6.87	145	1.05	30.1	2.10	67.9	1.38	33.2
O_3 + Isoprene	0.411	50.4	0.462	55.7	0.433	154	0.323	47.1
O_3 + β-Pinene	0.691	109	0.180	53.8	0.375	79.9	0.188	25.6
$P(H_2O_2)$	234	265	43.5	118	185	236	256	166
Losses								
$H_2O_2 + h\nu$	22.1	80.6	5.96	15.7	17.7	53.2	6.52	47.6
H_2O_2 + OH	18.3	78.8	1.85	54.3	14.9	56.3	8.31	105
$L(H_2O_2)$	40.4	113	7.81	56.5	32.6	77.4	14.8	115
$N(H_2O_2)$	193	288	35.7	131	152	248	241	202

Hydrogen peroxide sinks. Photochemical H_2O_2 sinks are (i) the direct photolysis and (ii) the reaction with OH radicals basically in a ratio of 1:1 (Lee et al., 2000). Absolute losses decrease in the order of R1 (40.5 pptv h^{-1}), over R3 (32.6 pptv h^{-1}) and R4 (14.8 pptv h^{-1}) and finally R2 (7.81 pptv h^{-1}). A closer look at the partitioning of H_2O_2 sinks for R1 indicates a slight predominance of 54.7 % (22.1 pptv h^{-1}) for the photolysis towards 45.3 % (18.3 pptv h^{-1}) for the oxidation by OH. The cold and dry air masses during R2 lead to another trend: 76.3 % (5.96 pptv h^{-1}) for the photolytic and 23.7 % (1.85 pptv h^{-1}) for the oxidative pathway. Proceeding to R3 shows 54.3 % (17.7 pptv h^{-1}) and 45.7 % (14.9 pptv h^{-1}) for the reaction with OH. Although the relative losses during R4 (photolysis: 44.0, oxidation: 56.0 %) are not comparable to R2, the absolute loss rates show evidence for similar values: 6.52 and 8.31 pptv h^{-1}.

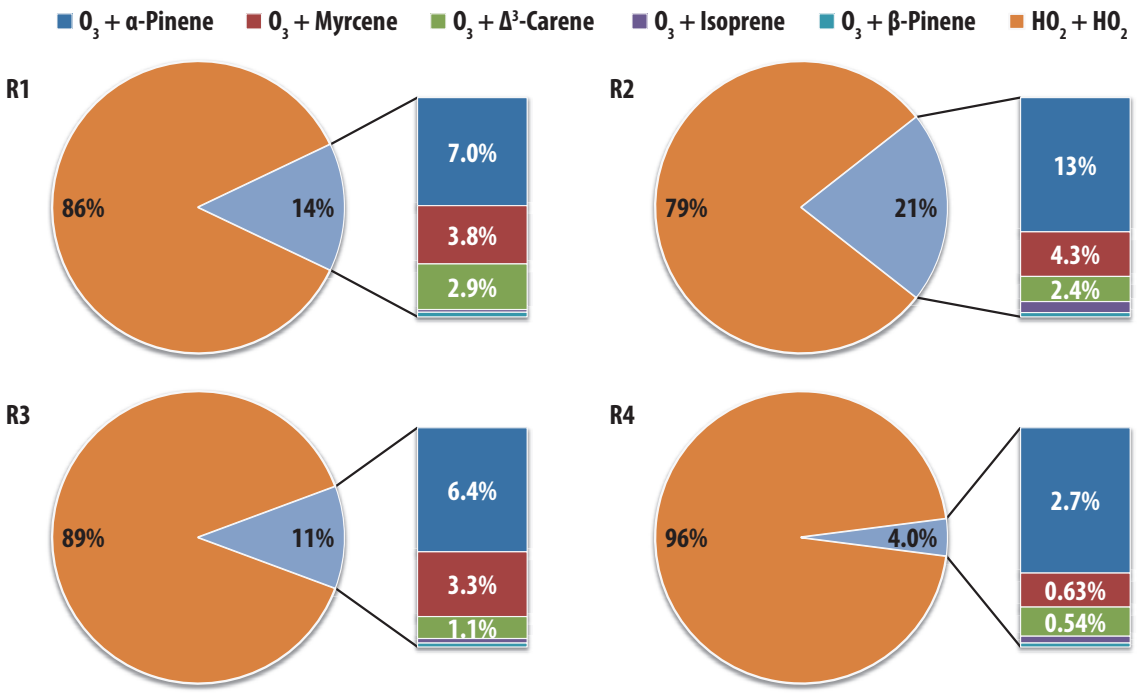

Figure 3.15.: Relative daytime production rates of H_2O_2 according to the regimes (R1–R4). The main producing reaction is the recombination of peroxy radicals (87 %), whereas ozone-alkene reactions play a minor role (13) (**a, b, c, d**). However, the latter contribute from 4 to 21 % and absolute production rates (in pptv h^{-1}) show a high variability throughout the campaign time. Especially R2 shows a high contribution of ozone-alkene reactions due to monoterpene remnants from the previous period (R1: boreal stressed), whereas cold temperatures as well as the lowest absolute humidity caused rather low ambient mixing ratios of peroxy radicals.

As expected, regimes with high radiation and absolute humidity, such as R1 and to a lesser extent R3, show evidence for high loss terms. This is due to increased direct ($j(H_2O_2)$) and indirect photolysis rates ($j(O^1D)$). The latter yields OH depending on the absolute humidity which then acts as a H_2O_2 oxidant.

Net hydrogen peroxide production. The net H_2O_2 production during daytime, $N(H_2O_2)$, generally show positive numbers through the regimes: calculations yield highest levels for R4 (241 pptv h^{-1}), directly followed by R1 (193 pptv h^{-1}). The biomass burning series (R3) shows moderate values of 152 pptv h^{-1}, whereas the cold series (R2) is in stark contrast with only 35.7 pptv h^{-1}.

The results show that the net H_2O_2 production is 5 to 7 times higher during the two stressed boreal periods (R1 and R4) in comparison to the cold series (R2). Note that R2 represents the "normal" boreal summer (Williams et al., 2011), whereas especially R1 and R4 give a good proxy for heatwaves and global warming. Those conditions are accompanied with increased net H_2O_2 production rates for daytime.

3.2.5.3. Brief overview on source and sink reactions of HCHO

Main sources. Major photochemical pathways for the production of HCHO are the reaction of methyl peroxy radicals with NO, the oxidation of VOCs by OH (and O_3) as well as the photolysis of methyl hydroperoxide.
Note that the reaction of methyl peroxy radicals (CH_3O_2) strongly depends on NO. Once a methoxy radical (CH_3O) is formed, it instantaneously reacts with molecular oxygen yielding HCHO.

$$CH_3O_2 + NO \longrightarrow CH_3O + NO_2$$
$$CH_3O + O_2 \xrightarrow{\text{fast}} HCHO + HO_2$$

Sources from ozone–alkene reactions. HCHO can also be produced by the ozonolysis of alkenes, such as isoprene and monoterpenes. The herein used rate coefficients are given in the appendix Chapter E.

Sinks. The major HCHO sinks are the two photolysis channels (radical: $j(HCHO)_{rad}$ and molecular: $j(HCHO)_{mol}$) and the reaction with OH radicals. Note that the "radical" channel instantaneously forms HO_2.

$$HCO + O_2 \xrightarrow{\text{fast}} HO_2 + CO$$

Table 3.13.: Calculation of the HCHO budget.

Reaction	Expression
Production (P)	
$CH_3O_2 + NO + O_2 \longrightarrow HCHO + NO_2 + HO_2$	$k[CH_3O_2]_{SS}[NO]$
$CH_3OH + OH + O_2 \longrightarrow HCHO + H_2O + HO_2$	$k[CH_3OH][OH]$
Isoprene + OH $\longrightarrow$ 0.6 HCHO + products	$0.6\,k[\text{Isoprene}][OH]$
$j(CH_3OOH) + h\nu \longrightarrow CH_3O + OH$	$j(CH_3OOH)[MHP]^*$
Alkene + $O_3 \longrightarrow \alpha$ HCHO + products	See Table E.2 in the appendix.
Alkene + OH $\longrightarrow \alpha$ HCHO + products	See Table E.3 in the appendix.
Losses (L)	
$HCHO + OH \longrightarrow HCO + H_2O$	$k[HCHO][OH]$
$HCHO + h\nu \longrightarrow HCO + H_2O$	$j(HCHO)_{rad}[HCHO]$
$HCHO + h\nu \longrightarrow H_2 + CO$	$j(HCHO)_{mol}[HCHO]$

3.2.5.4. Investigation of daytime sources and sinks of formaldehyde

Formaldehyde sources. Figure 3.16 divides the relative HCHO production through the regimes R1–R4 into four major groups: (i) the reaction of CH_3O_2 with NO, (ii) the oxidation of methanol by OH, (iii) the oxidation of isoprene by OH and (iv) the ozonolysis of alkenes and other reactions. Note that the calculations include only the first-generation production of HCHO and absolute production rates, P(HCHO), are given in Table 3.14 (appendix Chapter B). Those range from 455 (R3)

over 299 (R2) and 277 (R4) to finally 230 pptv h^{-1} (R1). So the biomass burning series (R3) shows the highest production, whereas the beginning of the campaign (R1) tends to lowest production rates. The reaction of methyl peroxy radicals with NO is here significantly accounting for approximately half the production: from 44 (R1) to 56 % (R3). The oxidation of methanol via OH radicals accounts for 25 % (119 pptv h^{-1}) in the case of R2, 26 % for R3 and R4 (119 pptv h^{-1} and 72.1 pptv h^{-1}, respectively) and 30 % (69.1 pptv h^{-1}) for R1. Next, the oxidation of isoprene by OH radicals, has an impact of 13 % (37.1 pptv h^{-1}) during R4, followed by R2 and R1 with 11 % (33.2 and 24.5 pptv h^{-1}, respectively) and finally 7.5 % (33.5 pptv h^{-1}).
Taking a closer look at the "other" fraction of the first period (R1) reveals 3.7 % (8.54 pptv h^{-1}) relative contribution of the methyl hydroperoxide (MHP) photolysis. The ozonolysis of myrcene accounts for 3.3 % (7.60 pptv h^{-1}), followed by the oxidation of α-pinene (2.1 %, 4.88 pptv h^{-1}). According to the calculations, the ozonolysis of isoprene is not significant (1.6 %, 3.70 pptv h^{-1}). In contrast, cold and dry conditions (R2) lead to less relative contribution of the MHP photolysis (2.0 %, 6.02 pptv h^{-1}), whereas the total oxidation of monoterpenes has a higher impact with ca. 7.1 % (25.0 pptv h^{-1}, comparable to R1). Regard that individual reactions of both, the ozonolysis and oxidation via OH, range from 1.1 to 1.4 % (3.31 to 4.25 pptv h^{-1}), where O_3 + myrcene shows the highest value (1.4 %). The pollution series (R3) shows a comparable picture: 2.0 % (9.04 pptv h^{-1}) for the photolysis of MHP and basically 1.2 to 1.5 % (5.29 to 6.90 pptv h^{-1}) for monoterpene reactions. Unlike R2, here the ozonolysis of α-pinene and isoprene play practically no significant role. Finally, R4 shows evidence for the lowest relative MHP (1.4 %, 3.82 pptv h^{-1}) and monoterpene contributions in comparison to the other regimes. The latter include solely the oxidation of α-pinene (1.3 %, 3.55 pptv h^{-1}), the ozonolysis of isoprene (1.0 %, 2.91 pptv h^{-1}) and the oxidation of β-pinene (2.84 pptv h^{-1}). Note that the ozonolysis of β-pinene and Δ^3-carene, its oxidation of Δ^3-carene by OH and the recombination of CH_3O_2 with AcO_2 play practically no role for the HCHO production throughout the four regimes (<1 %).

As a result, the major daytime HCHO sources throughout the regimes can be represented by simple "background" chemistry: the reaction of CH_3O_2 with NO accounts for approximately 50 % of the production rate, despite the low NO_x levels during HUMPPA. Note that the steady-state calculations of CH_3O_2 consider not only the oxidation of CH_4 but also degradation products of the acetaldehyde and the recombination of major peroxy radicals (e. g., AcO_2) except for its first-generation production from the oxidation of monoterpenes. Next, the oxidation of methanol by OH radicals has an impact of ca. 25 %, whereas the oxidation of isoprene contributes with approximately 10 %. The photolysis of MHP plus the monoterpene oxidation via O_3 and OH leads in total to comparable values (10 %). Individual monoterpene reactions always contribute below 2.1 % throughout the regimes and they vary with the emission pattern (Yassaa et al., 2012): higher ambient mixing ratios lead to a higher impact on the budget.

Formaldehyde sinks. The total HCHO sink term, consisting of its two photolysis channels (radical and molecular) as well as the oxidation by OH radicals, spread broadly from the lowest absolute value of 81.7 pptv h^{-1} (R1), over similar during R4 and R2 (126 and 145 pptv h^{-1}, respectively) up to 307 pptv h^{-1} during R3. Investigation of the relative losses shows a nearly constant value for the

Table 3.14.: Calculated HCHO budget for HUMPPA concerning to the regimes (R1-R4). Production and loss rates are given in pptv h^{-1} including combined variabilities (1σ).

Reaction	R1		R2		R3		R4	
	Average	1σ / %	Average	1σ / %	Average	1σ / %	Average	1σ / %
Production								
CH_3O_2 + NO	100	33.4	158	64.9	256	46.7	146	57.1
OH + MeOH	69.1	127	75.7	168	119	161	72.1	142
OH + Isoprene	24.5	47.5	33.2	77.4	33.5	108	37.1	64.6
MHP + hν	8.54	65.2	6.02	87.7	9.04	67.9	3.82	89.4
O_3 + Myrcene	7.60	111	4.25	145	5.35	118	1.40	29.1
O_3 + α-Pinene	4.88	83.5	3.14	88.2	3.55	69.3	2.06	23.1
O_3 + Isoprene	3.70	50.4	3.47	89.0	3.89	154	2.91	47.1
OH + α-Pinene	2.12	22.6	3.71	60.6	5.40	51.7	3.55	47.7
OH + Myrcene	2.07	25.0	3.32	116	6.90	86.1	1.74	33.9
O_3 + Δ^3-Carene	1.83	145	0.826	191	0.559	67.9	0.368	33.2
OH + β-Pinene	1.76	17.3	3.31	71.4	5.29	62.2	2.84	43.6
O_3 + β-Pinene	1.66	109	0.893	129	0.900	79.9	0.452	25.6
OH + Δ^3-Carene	1.12	38.5	2.07	60.6	3.08	53.0	1.98	39.9
CH_3O_2 + AcO_2	0.440	29.2	1.17	133	2.40	73.1	1.04	145
P(HCHO)	230	287	299	424	455	346	277	263
Losses								
HCHO + hν (mol.)	29.0	54.1	49.5	125	118	86.4	38.9	99.7
HCHO + hν (rad.)	23.7	53.9	39.8	125	94.8	86.6	31.1	99.0
OH + HCHO	29.0	21.4	56.1	152	94.5	90.0	56.1	174
L(HCHO)	81.7	79.3	145	233	307	152	126	224
N(HCHO)	148	297	153	484	148	378	151	345

molecular photolysis channel in average about 34 % for all regimes. However, absolute levels spread from 29.0 to 118 pptv h^{-1} (R1 and R3). Comparable results are obtained for the radical photolysis channel with a quite constant average contribution about 25 % throughout the regimes. Again absolute loss rates vary from 23.7 to 94.8 pptv h^{-1} (R1 and R3). In contrast, the oxidation of HCHO by OH indicates more variability accounting for 30.8 % (94.5 pptv h^{-1}) for R3, 35.5 % (29.0 pptv h^{-1}) for R1, 38.6 % (56.1 pptv h^{-1}) for R2 and 44.5 % (56.1 pptv h^{-1}) for R4 of the relative losses.

Excessive ambient HCHO mixing ratios during the biomass burning series (R3) explain the high loss terms. As shown before, a major fraction was secondary HCHO, presumably entrained in the morning hours from the residual layer. Unlike the other regimes, the reaction with OH is less important.

Net formaldehyde production. Although the regimes differ from the meteorological and photochemical point of view, the absolute net HCHO production rate, P(HCHO) ranges only from 148

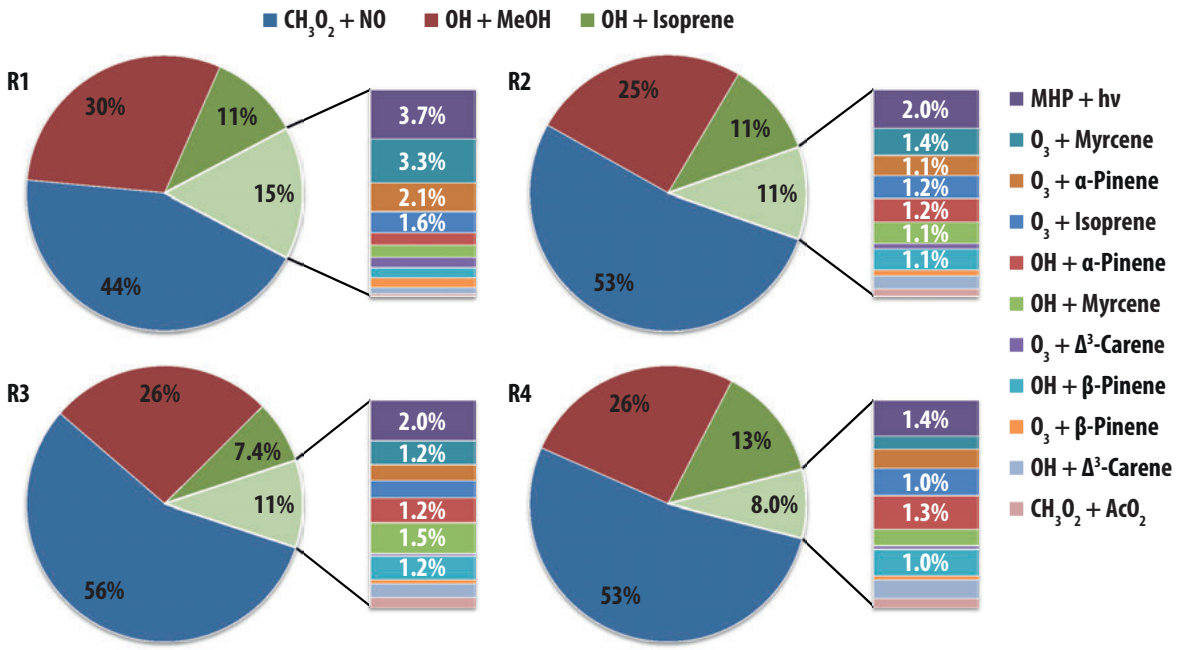

Figure 3.16.: Relative daytime production rates for HCHO according to the regimes (R1–R4). The pie charts depict the different regimes R1–R4 (**a, b, c, d**), whereas R0 is excluded due to missing VOC measurements during that period. Although the absolute production rates (in pptv h^{-1}) show a high variability throughout the campaign, the relative contributions barely differ: HCHO is mainly produced by the reaction of methyl peroxy radicals with NO (52 %), followed by the oxidation of methanol by OH (27 %, NO independent), the oxidation of isoprene (10 %) and finally ozone-alkene and OH-alkene reaction among "others" (11 %).

to 153 pptv h^{-1} (R3-R2). The pollution series (R3) shows evidence for the lowest, whereas cold and clean conditions (R2) favour highest photochemical production.

3.2.5.5. Steady-state calculations of hydrogen peroxide and formaldehyde excluding dry deposition

Figure 3.17 depicts the result for the steady-state calculations for H_2O_2 and HCHO excluding the impact of dry deposition. Black diamonds represent observational, whereas green circles calculated data. In average H_2O_2 is overestimated by a factor of 5 up to an order of magnitude (slope: 4.920 ± 0.512, intercept: 2.250 ± 0.333 ppbv, r^2 = 0.24), whereas HCHO levels exceed the measurements by 3.6 times (slope: 0.6610 ± 0.0899, intercept: 1.1700 ± 0.0781 ppbv, r^2 = 0.26).

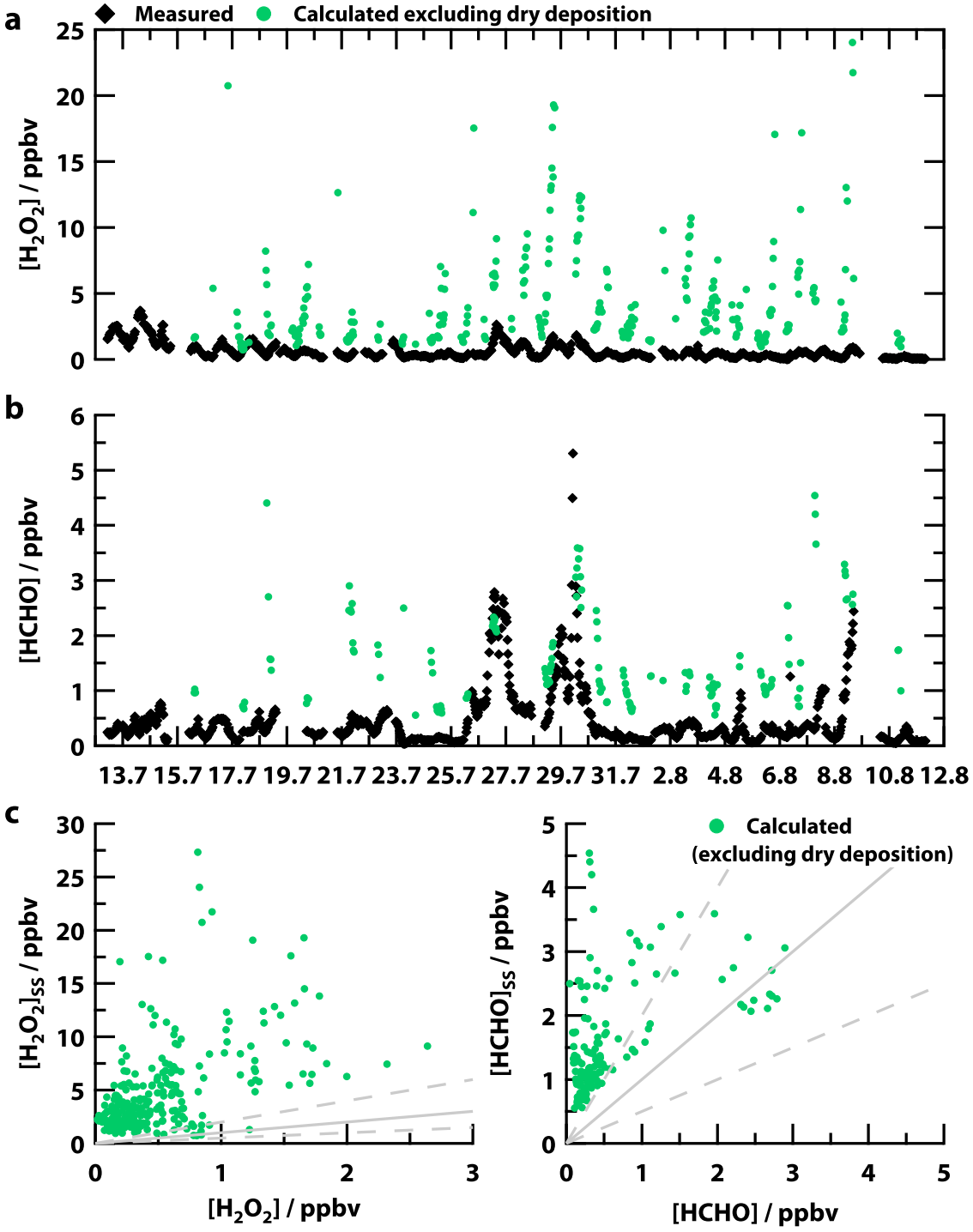

Figure 3.17.: Comparison of steady-state calculations excluding dry deposition versus measurements for H_2O_2 and HCHO. Time series of calculated (green) and observed (black) H_2O_2 and HCHO (**a, b**). Correlation indicating the slopes: 1:1 (grey), 0.5 and 2 (grey, dashed), respectively (**c**).

3.2.5.6. Potential sources of uncertainty for the budget calculations

Measurement uncertainties. Budget calculations consist of many steps and make use of data which is obtained by many different methods as previously discussed in detail (Section 2.2.7). Thus, technical issues such as measurement uncertainties and interferences have a high impact in over- and underestimating ambient mixing ratios. For example, the H_2O_2 data has to be corrected for line losses (ca. 0 to 40 %) and an O_3 interference (ca. 5 %). HO_x data might be still affected by RO_2 (ca. 20 %) artifacts.

Time resolution. Averaging can be a source of "uncertainty" as well. This work usually uses data with a time resolution of r = 5 min (or 10 min). This may be a minor problem for long lived species with $\tau > r$ (e. g., $\tau_{H_2O_2}$ = 12 h) since natural variations on the time scale of averaging remain. Larger time steps may even be helpful for local sources of considered species (e. g., NO) which may cause deviations from steady-state conditions due to a high release during a short time (concentration peaks).
However, very short lived radical species, for example OH (τ_{OH} = 1 to 10 s), might be impacted if $\tau < r$ causing variation to be "smoothed". This fact was considered to find a compromise between the available time resolution of the data and species life times.

Uncertainties in the kinetic considerations. Kinetic calculations consist of concentrations and rate coefficients for obtaining production and loss rates. Rate coefficients are measured under laboratory conditions over certain temperature, pressure and time ranges. The experimental set-up can be a source of artifacts that change the concentrations (e. g., material of chamber wall, permeation of undesired species). Furthermore, measurement methods may have an insufficient time resolution depending on the life time of the reactants and products. All these effects can impact herein used rate coefficients (appendix Chapter E) and are considered in the kinetic data evaluation (Atkinson and Arey, 2003a; Atkinson et al., 2004, 2006).
Photolysis rates are also important for budget calculations. As discussed before, mesoscale (or less) meteorology cause fluctuations in the photolysis rates, e. g., due to passing clouds. Steady-state conditions are not necessarily fulfilled for periods of seconds to minutes.
Besides, some photolysis rates were not observed (e. g., $j(H_2O_2)$, $j(HCHO)_{rad}$ and $j(HCHO)_{mol}$) and needed to be estimated by using the measured $j(NO_2)$. However, for clear sky conditions, the uncertainty can be quantified for ca. 3 % (Holland, 2003).

Calculations for missing observations. Above all, missing data (e. g., HO_2, OH and very short lived BVOCs such as sesquiterpenes) is a large source of uncertainty. Nonetheless, knowing the concentration levels or at least being confident of neglecting non-calculable species is crucial for budget calculations. Assumptions were referred to in the respective sections.

3.2.6. The influence of physical processes on H_2O_2 and HCHO in the boreal forest

After calculating the budgets and steady-state mixing ratios for H_2O_2 and HCHO excluding physical effects the question arises about quantifying dry deposition and transport. The first step is to

obtain an early morning estimate of the daytime deposition velocity V_d via a simple equation including the boundary layer height H and the deposition rate coefficient k_{DDEP} (Equation 3.63). For the determination of V_d other methods are known which require fluxes obtained from vertical concentration gradients (e. g., Eddy diffusivity, resistance models). Those were not available for this work, thus for simplification a linear behaviour of V_d was assumed.

$$V_d = H\, k_{DDEP} \tag{3.63}$$

The boundary layer height H plays an essential role on the deposition velocity. Figure 3.18 shows the profile during the entire campaign time obtained by 132 radio soundings (Ouwersloot et al., 2012). The daytime height was about 906 ± 504 m (median: 850 m) meaning a relative variability (1σ) of 55.5 %. Note that this is a source of uncertainty since the calculation relies only on one day and the result will be used in further sections for the entire campaign. However, the variability of k_{DDEP} is about 200 to 350 % for H_2O_2 and HCHO as implicitly given by the tables 3.12 and 3.14. Now

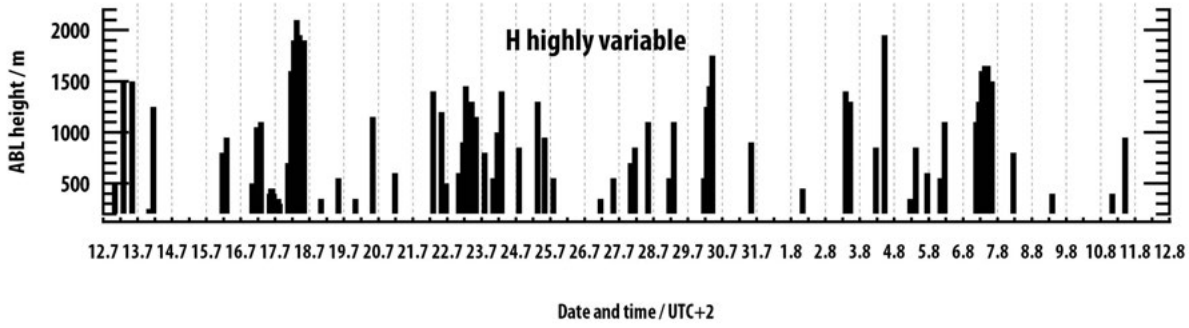

Figure 3.18.: Boundary layer height. After Ouwersloot et al. (2012).

the amount of transport is required to explain the observed changes in H_2O_2 and HCHO. Starting from the continuity equation from the introductory chapter (Equation 1.57), infinitesimal changes in the mixing ratio of a species [X] (e. g., $[H_2O_2]$ and [HCHO], respectively) are expressed by:

$$\frac{d\,[\mathrm{X}]_{obs}}{d\,t} = \overbrace{\mathrm{P(X)} - \mathrm{L(X)}}^{\mathrm{N(X)}} + \mathrm{A(X)} + \mathrm{E(X)} - \mathrm{D(X)} \approx 0 \tag{3.64}$$

Here, the index "obs" denotes observations, so the differential equals the sum of photochemistry and physics, such as advection A(X), vertical transport E(X) (entrainment) and deposition D(X) (e. g., in ppbv h^{-1}). D(X) is by definition a first-order expression consisting of the deposition rate coefficient k_{DDEP} times the mixing ratio (here: $[X]_{obs}$) in steady-state.

$$\mathrm{D(X)} = k_{DDEP}\,[\mathrm{X}]_{obs} \tag{3.65}$$

Note that this differential was obtained by using numerical methods on the observed time series. The production tendency (or net production N(X) if positive), as the difference between production P(X) and loss L(X), quantifies photochemistry. These terms were calculated in the previous section of this chapter for obtaining $[H_2O_2]_{SS}$ and $[HCHO]_{SS}$, respectively. Neglecting advection

$(A(X) \approx 0)$ due to steady meteorological condition leads to the following expression for the entrainment $E(X)$ based upon known terms:

$$E(X) = \frac{d[X]_{obs}}{dt} - \frac{d[X]_{SS}}{dt} + D(X) \tag{3.66}$$

3.2.6.1. Dry deposition

Two previous studies addressed summertime deposition velocities for H_2O_2 in Canadian boreal forests (Hall and Claiborn, 1997; Hall et al., 1999). Note that due to the methods used in those articles the following velocities are given by positive numbers. Both reported a diurnal variation showing night-time minimums and daytime maximums from 10 a. m. to 6 p. m. (local time). Values during the night were generally lower. Levels of 5.0 cm s^{-1} were observed during the day for a coniferous forest in Saskatchewan (Hall and Claiborn, 1997). More comprehensive measurements reported deposition velocities ragging from 5 to 9 cm s^{-1} during July in a Jack pine forest (Saskatchewan, Canada, Hall et al., 1999). For HCHO, previous studies reported daytime deposition velocities from 0.75 to 1.5 cm s^{-1} (Krinke, 1999).

As shown in Equation 3.64 the removal of H_2O_2 and HCHO can be an overlap of dry (and wet), deposition, transport and photodepletion. Thus, a simple consideration of the photochemical budget is not sufficient for the HUMPPA field measurement campaign. The following section presents a simple method for obtaining the dry deposition velocity from mid-night to the early morning in agreement to the literature mentioned above. During the night-time, significant photochemical processes caused by remnant species from the day, strong advection and gas exchange through open plant stomata can be widely excluded. Table 3.15 lists the results of the linear regression on ambient mixing ratios (ξ in ppbv) of H_2O_2 and HCHO between midnight the early morning (5 UTC+2) per regime for obtaining the dry deposition velocity. The obtained slope (ppbv h^{-1}) represents the loss rate for these hours. The deposition rate constant k_{DDEP} (s^{-1}) is normalized by the ambient mixing ratio under the assumption of a linear behavior. The deposition velocity V_d (cm s^{-1}) was obtained according to Equation 3.63 by using the average PBL height of the corresponding regime for these early hours. In the case of H_2O_2, the midnight mixing ratios spread from 305 to 872 pptv reaching minimum values from 99.4 to 485 pptv. Note that the coefficients of determination (r^2) show generally a very good linear behavior, especially during R2 (r^2 = 0.97). The lowest linearity (r^2 = 0.58) was calculated for the biomass burning series (R3). The night-time loss rates range from −93.6 to −36.4 pptv h^{-1}. Normalizing those values provides deposition rate constants from 4.34×10^{-5} to 1.63×10^{-4} s^{-1}. As a result, the linear assumption leads to deposition velocities between 1.69 (R3) and 6.35 cm s^{-1} (R2). The campaign average is 3.52 cm s^{-1} (median: 3.03 cm s^{-1}). For HCHO, the midnight levels spread from 0.176 to 1.14 ppbv, whereas the morning minimums range from 135 to 815 pptv. Same as for H_2O_2 the coefficients of determination indicate a high degree of linearity, especially for R2 (r^2 = 0.99). As a result, the night-time deposition rates show a minimum around –104 (R3) up to a maximum of –7.38 pptv h^{-1} (R4). This leads to deposition rates raging form 1.49×10^{-5} to 7.06×10^{-5} s^{-1} which is in full agreement with literature (Sumner et al., 2001, 9.4×10^{-6} to 5.0×10^{-5} s^{-1}). Considering the PBL height, the deposition velocities spread from 0.580 to 2.75 cm s^{-1} with an average of 1.37 cm s^{-1} (median: 1.08 cm s^{-1}) for the entire campaign.

Table 3.15.: Calculated deposition velocities for H_2O_2 and HCHO in the early morning according to the regimes R1-R4. Mixing ratios (ξ) in ppbv are given for midnight and for 5 UTC+2. A linear regression was performed for this interval to obtain the slope in ppbv h^{-1} and the coefficient of determination (r^2). The deposition rate (k_{DDEP}) in s^{-1} is listed for the early morning. The deposition velocity (V_d) in cm s^{-1} was calculated based on the average PBL height between 4 and 6 UTC+2. Combined variabilities (1σ) were estimated for all quantities.

	ξ at 0 UTC+2 ppbv	1σ %	ξ at 5 UTC+2 ppbv	1σ %	Slope ppbv h^{-1}	1σ %	r^2	k_{DDEP} s^{-1}	1σ %	V_d cm s^{-1}	1σ %
H_2O_2											
R1	0.872	2.28	0.435	90.4	−0.0837	8.20	0.72	5.35×10^{-5}	90.8	2.09	93.6
R2	0.608	1.19	0.160	20.9	−0.0936	2.76	0.97	1.63×10^{-4}	21.1	6.35	31.2
R3	0.718	3.52	0.485	58.6	−0.0759	11.3	0.58	4.34×10^{-5}	59.7	1.69	63.9
R4	0.305	1.80	0.0994	43.7	−0.0364	5.21	0.86	1.02×10^{-4}	44.0	3.96	49.6
Average	0.626	38.3	0.295	65.6	−0.0724	34.7	—	9.04×10^{-5}	60.4	3.52	60.4
Median	0.663	—	0.297	—	−0.0798	—	—	7.76×10^{-5}	—	3.03	—
HCHO											
R1	0.293	1.31	0.220	49.3	−0.0157	8.48	0.70	1.99×10^{-5}	50.1	0.775	55.1
R2	0.303	0.383	0.135	62.7	−0.0344	1.11	0.99	7.06×10^{-5}	62.7	2.75	66.8
R3	1.14	3.44	0.815	58.3	−0.1036	12.9	0.52	3.53×10^{-5}	59.7	1.38	64.0
R4	0.176	1.30	0.138	52.4	−0.007 38	10.7	0.60	1.49×10^{-5}	53.4	0.580	58.1
Average	0.479	93.3	0.327	100	−0.0403	109	—	3.52×10^{-5}	71.6	1.37	71.6
Median	0.298	—	0.179	—	−0.0250	—	—	2.76×10^{-5}	—	1.08	—

3.2.6.2. The role of transport on the budget

Figure 3.19 depicts the entire budget of H_2O_2 for the regimes R1, R2 and R4 ("background" conditions) as stacked columns. The consideration includes the terms discussed for Equation 3.64 presenting the values in pptv h^{-1}: photochemical production (P) and loss (L) as well as transport in the form of advection and entrainment (A and E). Please note that the observed difference (D) between two time steps is shown as diamonds.

For the very early morning hours between 4:15 and 4:45 UTC+2 the observations show a net loss of H_2O_2 from −66.1 to −40.0 pptv h^{-1}. This is due to low photochemical production (20.9 to 24.8 pptv h^{-1}) and a high dry deposition rate (−52.3 to −32.6 pptv h^{-1}). Please note that the photostationary considerations are less reliable at these early hours (compare Chapter 3.1). However, this is the only time window which shows evidence for a significant negative transport (−52.9 to −9.84 pptv h^{-1}), especially around 4 UTC+2. The calculation may include effects caused by wet deposition since H_2O_2 is highly water soluble. According to Figure 3.20, the early morning maximum of relative humidity around 88.70 ± 8.77 % (including variability) is close to the dew point. The first positive peak of transport (44.8 ppbv h^{-1}) around 5:50 UTC+2 is either due to degassing of H_2O_2 from the liquid phase or caused by entrainment of H_2O_2-rich air from above (turbulences, boundary layer breakup). In addition to photochemical production it compensates the dry deposition (−48 pptv h^{-1}) to an accumulation rate of 12.9 pptv h^{-1}. Then, shortly after 6 UTC+2, the change rate is almost at the equilibrium, so as the photochemical production (46.9 pptv h^{-1}) and the dry deposition (51.1 pptv h^{-1}). Diurnal profiles discussed in previous sections underline that fact. In the

course of boundary layer breakup after 7 UTC+2, the entrainment rate elevates to a maximum of 96.7 pptv h^{-1} (ca. 8 UTC+2) exceeding P by a factor of 2.4. On the loss side dry deposition rate remains rather constant (−43.4 to −55.4 pptv h^{-1}), whereas the photodepletion plays a minor role. The peak change rate is 77.1 pptv h^{-1} and ambient H_2O_2 starts accumulating in the morning as a consequence. During the late morning (9 to 11 UTC+2) the differential oscillates between 19.4 to 73.3 pptv h^{-1} and this explains the accumulation of ambient H_2O_2 (compare diurnal profiles). The sources and sinks follow that trend in a sinusoidal shape: photochemistry has a relative impact from 35.6 to 54.1 % on the source and a minor (5 to 12.4 %) on the sink side. For the noon and afternoon hours, the minimum to maximum span for the difference ranges from 31.7 to 136 pptv h^{-1}, which is the highest daytime accumulation rate. On the production side, the major fraction of H_2O_2 is transported (87.7 to 271 pptv h^{-1}), whereas photochemistry accounts for 35.7 % of the total rate in average. This could be an evidence for a very strong entrainment of H_2O_2 rich air from above. On the sink side, dry deposition is predominant with levels spreading form −184 to −115 pptv h^{-1}, which is 92.7 % of the total loss rate in average. Photodepletion only shows values from −20.8 to −7.77 pptv h^{-1}. During the late afternoon, the differential turns from positive (50.5 pptv h^{-1}) to negative rates (−27.3 pptv h^{-1}), which is reflected by declining ambient mixing ratios diurnal profiles. In contrast to the hours before, photochemistry predominates the production side with high rates from 62.7 to 221 pptv h^{-1}. That means 54.7 % of the total (transport ranges from 46.3 to 144 pptv h^{-1}). Here, convective entrainment is less important. On the opposite, deposition reaches its highest level for daytime (−234 pptv h^{-1}) and exceeds even the strongest photochemical production rate (−221 pptv h^{-1}). Note that the photochemical loss rate also achieves values of −16.3 pptv h^{-1}, whereas those account for only 4.48 % in total.

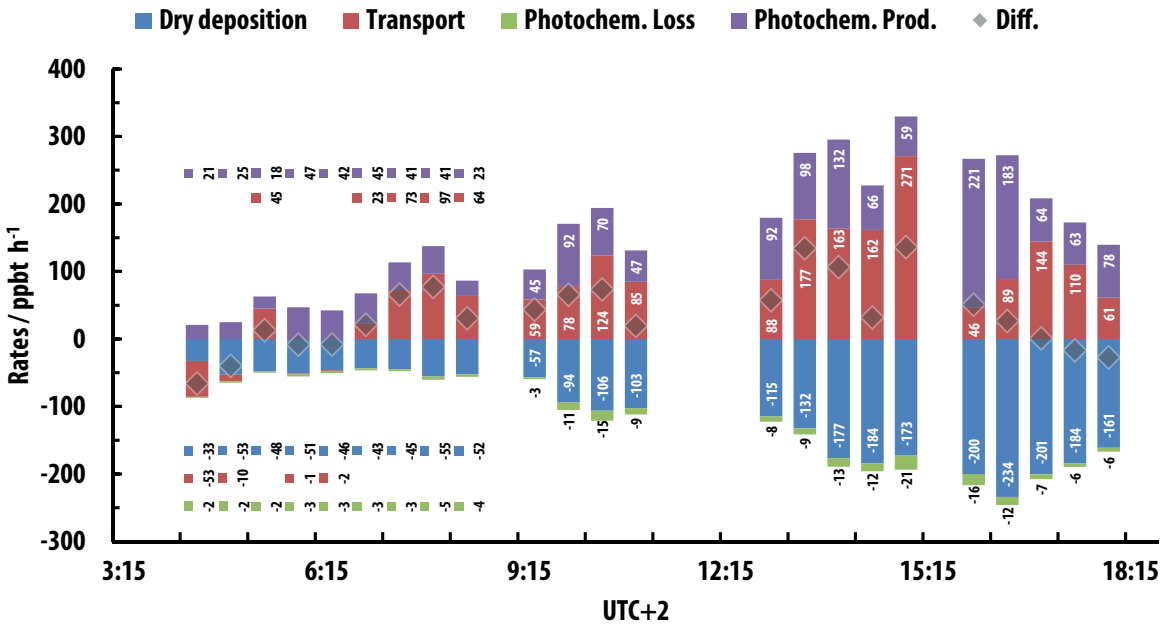

Figure 3.19.: Diurnal profiles of the entire budget for H_2O_2 as stacked columns for background conditions. Mean diurnal profile for R1, R2 and R4 of production, and depletion rates (pptv h^{-1}). Physical processes are broken down to dry deposition and transport (vertical and horizontal), whereas the photochemical side itemizes production and loss. "Diff." quantifies the observed difference between two time steps. Individual rates are indicates by vertical numbers (pptv h^{-1}).

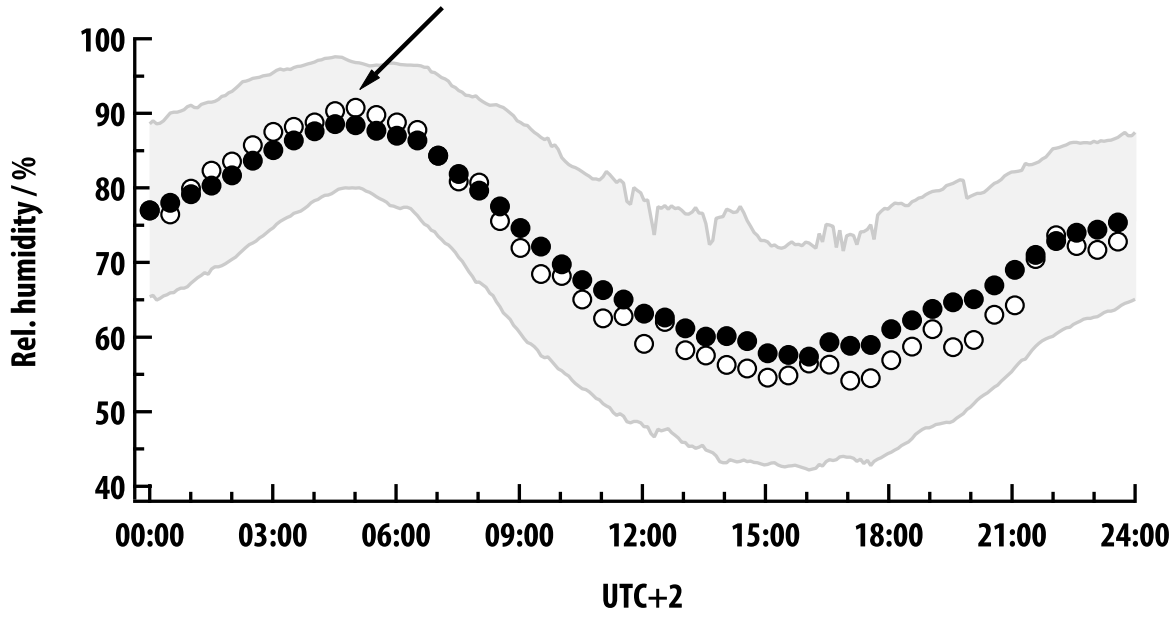

Figure 3.20.: Diurnal profile of the relative humidity for the entire campaign. Observed data provided by the SMEAR II station in a 5 min resolution. Averages (dots), medians (circles) and the 1σ variability (grey shades) are given in percent. Maximum average levels were observed at 4:40 UTC+2 (88.7 %) and minimum at 16:13 UTC+2 (57.2 %).

Figure 3.21 depicts the entire budget of HCHO for the regimes R1, R2 and R4 ("background" conditions) as stacked columns. For the early morning hours (6 to 7:30 UTC+2), the changes in HCHO are minimal but positive (29.5 to 48.4 pptv h^{-1}). On the production side, photochemistry is the sole source with strong levels from 321 to 404 pptv h^{-1}. The sinks are predominated by transport (mean: 88.1 % of total), presumably entrainment of HCHO-poor air from above (−332 to −282 pptv h^{-1}) during the boundary layer breakup. Dry deposition and photochemical losses play a minor role at these hours (−13.3and −13.3 pptv h^{-1} in average, respectively). Around 8 UTC+2, HCHO starts accumulating with 128.2 pptv h^{-1} (reflected in the ambient diurnal profiles). This is caused by less entrainment of HCHO-poor air (−111 pptv h^{-1}). Dry deposition and photodepletion slightly increase without a major impact on the total losses (−34.6 and −47.2 pptv h^{-1}, respectively). The late morning (> 9:45 UTC+2) until the early afternoon (14 UTC+2) is predominated by strong fluctuations of the changes in HCHO spreading from −4.57 to 219 pptv h^{-1}: from close to equilibrium to accumulation. This pattern is reflected in the photochemical production (179 to 357 pptv h^{-1}). However, except for 13 UTC+2, photochemistry is the sole source of HCHO. At that exceptional time, transport accounts for a surplus of 71.8 pptv h^{-1} on the production. The sink side is still predominated by the transport HCHO-poor air, whereas the absolute numbers decrease (131 pptv h^{-1} in average). For those hours, photodepletion plays a higher relative role of ca. 34.0 % in average (−108 to −37.7 pptv h^{-1}). Dry deposition is still rather insignificant. The late afternoon (> 15:45 UTC+2) reflect a declining trend in the differences (132 to −4.10 pptv h^{-1}). On the source side, two data points shows evidence for the transport of HCHO-rich air (82.0and 44.9 pptv h^{-1}, respectively). However, photochemistry is significant (203 to 261 pptv h^{-1}). After 16:45 UTC+2, the photochemical rate drops to ca. half the levels (ca. 96 pptv h^{-1}). On the sink side, photodepletion is predominant from 15:45 to 16:15 UTC+2 ranging from −113 to −163 pptv h^{-1}. Daytime dry deposition achieves its highest daytime

value (−47.2 pptv h^{-1}). From 16:45 UTC+2, photodepletion decreases to ca. −28 pptv h^{-1}, whereas the transport of HCHO-poor air predominates again (−57.0 to −49.3 pptv h^{-1}).

The herein presented results are in full agreement with literature (Sumner et al., 2001). The study examined the HCHO budget at a mixed deciduous/coniferous forest site during summer in Michigan, United States, in a comparable fashion. Ambient mixing ratios ranged from 0.5 to 12 ppbv - values certainly higher then discussed in this chapter. However, for "clean" conditions (north-western air masses), highest total production rates were reported at mid-day (1.76 ppbv h^{-1}) as well as maximum total loss rates (878 pptv h^{-1}). South-eastern air masses under pollutant influence showed evidence for almost double levels for production and sinks, respectively. Qualitatively, the herein presented diurnal profile for the budget is comparable to that time period (high rates from morning to mid-day, decreasing production rates for the evening). Please note that the study (Sumner et al., 2001) did not focus on the transport, whereas the relative fractions of the sinks agree: for daytime photochemical losses equal or are higher than dry deposition.

Another study (Choi et al., 2010) considered advection in the HCHO budget calculations. The late summer campaign took place in a pine forest in Sierra Nevada, United States. Since the site was situated about 75 km north-east of Sacramento, mid-day peak levels from 15 to 20 ppbv and from 8 to 14 ppbv, respectively, for cleaner days were reported. In contrast to this chapter, advection rates exceeding photochemical production by factors between 2 and 3 or even more were reported (total losses up to 3 ppbv h^{-1}). The high ambient mixing ratios lead to correspondingly high loss rates (ca. −7.5 ppbv h^{-1} in total). As a conclusion, the chemical regime is totally different from the discussions above.

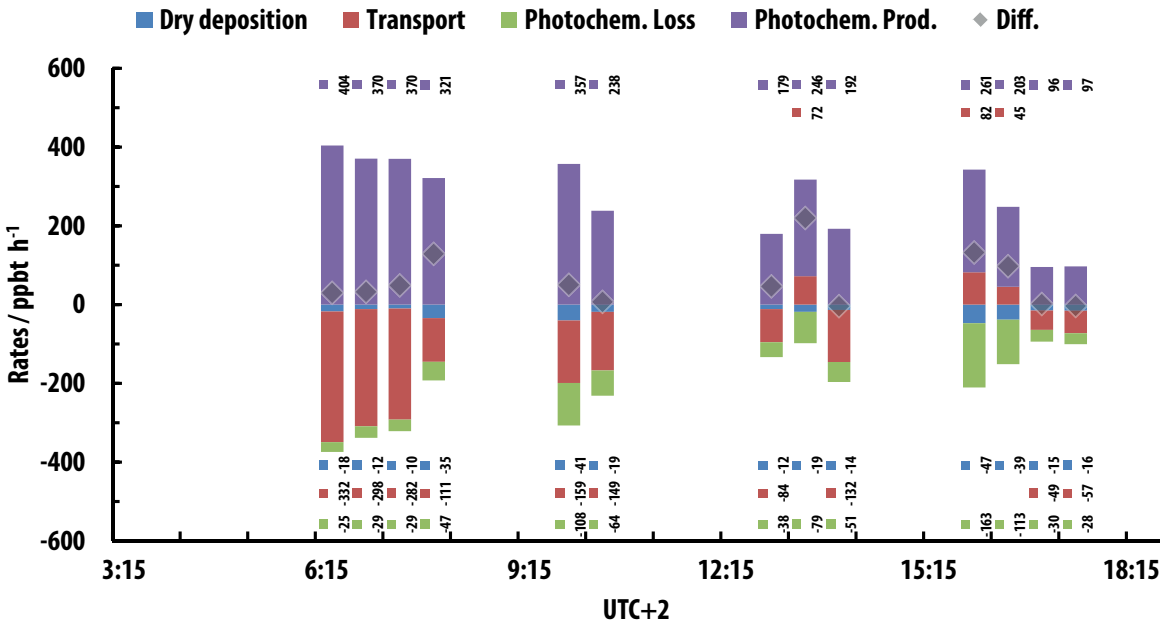

Figure 3.21.: Diurnal profiles of the entire budget for HCHO as stacked columns for background conditions. Mean diurnal profile for R1, R2 and R4 of production and depletion rates (pptv h^{-1}). Physical processes are broken down to dry deposition and transport (vertical and horizontal), whereas the photochemical side itemizes production and loss. "Diff." quantifies the observed difference between two time steps. Individual rates are indicates by vertical numbers (pptv h^{-1}).

3.2.7. Steady–state calculations of hydrogen peroxide and formaldehyde including dry deposition and transport

As discussed in the introduction, a major object of this thesis is to understand sources and sinks for explaining ambient H_2O_2 and HCHO in the boreal forest.

The dry deposition is significant even in the well-mixed daytime boundary profiles (Wesely and Hicks, 2000). Although the continuity equations have multiple unknowns, the previous sections invoked the observed data of H_2O_2 and HCHO for obtaining the deposition velocities by use of the boundary layer profiles (Ouwersloot et al., 2012). Further, the impact of transport on the budgets was discussed. That allows calculating the ambient mixing ratios including physics.

Figure 3.22 depicts the time series of the observed hydrogen peroxide ($[H_2O_2]$) and formaldehyde ([HCHO]) as black diamonds in comparison to their colour-coded[2] steady-state calculations ($[H_2O_2]_{SS}$ and $[HCHO]_{SS}$) taking account for daytime deposition. The results are divided into four periods depending on their chemical regimes: stressed boreal (R1, pale red), cold and clean (R2, pale blue), biomass burning series (R3, pale purple) and normal boreal (R4, pale green). In general, H_2O_2 is underestimated by ca. 100 % in the morning hours (5-10 UTC+2) and in the late afternoon (> 17 UTC+2). As discussed before, the photostationary state calculations are limited for these hours. In contrast, a good match is obtained for the daytime, especially 14 UTC+2. However, there are some outliers up to 200 % in the morning hours (5 UTC+2) of R1 and in the afternoon during R2 and R3, respectively. It is striking that the "boreal normal" regime (R4) shows strong deviations of 200 % from 5 to 10 UTC+2. HCHO shows a more reproducible picture for the morning hours although it is underestimated by 50 to 80 % throughout the regimes. Few outliers about 200 % occur at ca. 7 UTC+2. The strongest underestimation (–100 %) of the calculation is stated during the biomass burning series.

In addition, the figure also presents correlation plots of the steady-state calculations including deposition versus the observations for the entire period. H_2O_2 is reproduced rather well (slope: 0.9520 ± 0.0834, intercept: 0.2330 ± 0.0543 ppbv, $r^2 = 0.30$). Lower mixing ratios (<1 ppbv) tend more to lie outside the limits of the 0.5 to 2 slope than data points above 1 ppbv. The HCHO calculation is reasonable for a major fraction of the results. However, the biomass burning events are not reproduced since HCHO was transported via entrainment, so a physical effect. These points are marked by "BB" (R3) in the correlation plot and lead to a low slope of 0.2320 ± 0.0258 (intercept: 0.2980 ± 0.0224 ppbv, $r^2 = 0.35$). The mean diurnal profiles substantiate that fact in the following section.

[2] $\Delta[X] = \left(\frac{[X]_{SS} - [X]}{[X]} \right) \cdot 100\%$

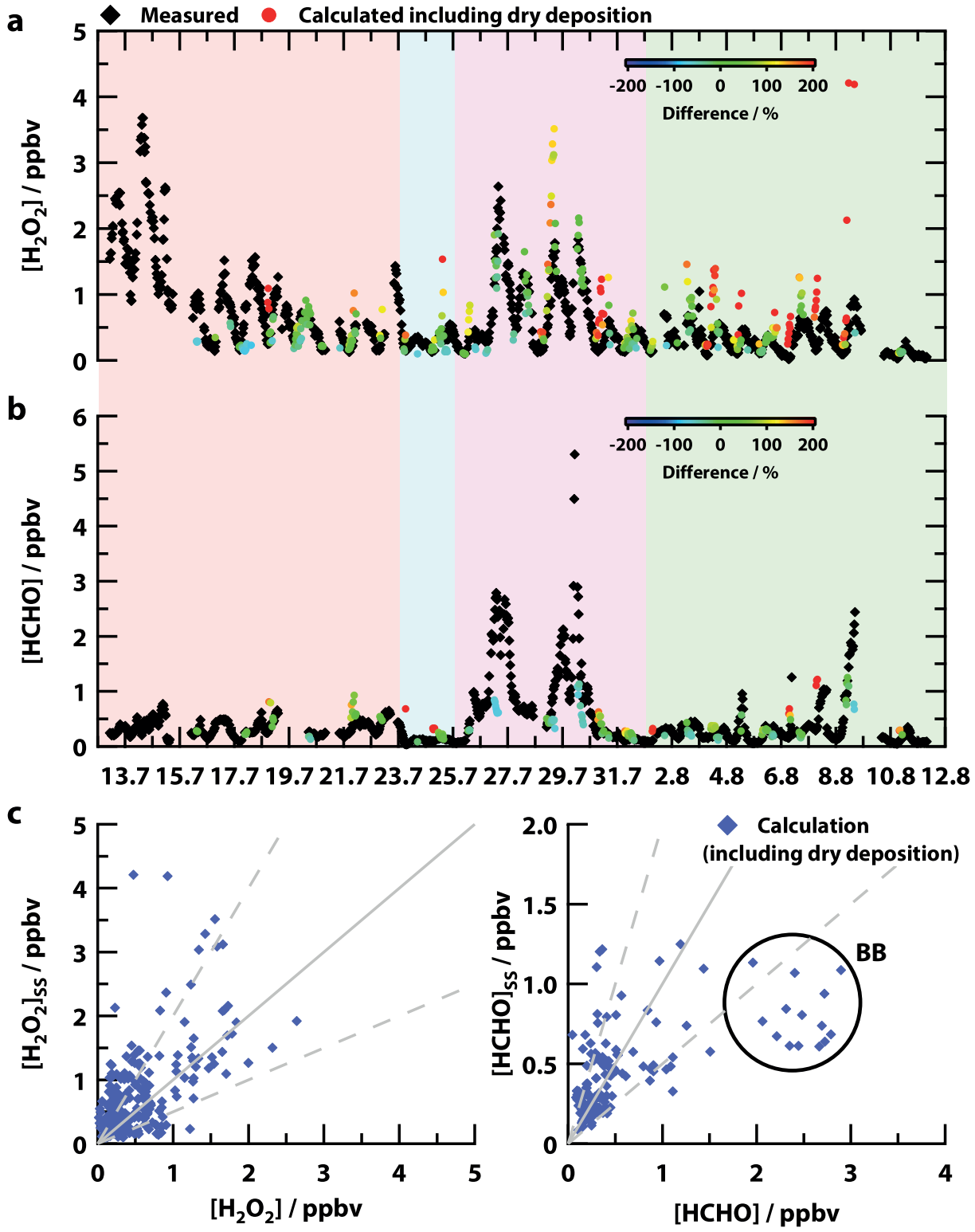

Figure 3.22.: Comparison of steady-state calculations versus measurements for H_2O_2 and HCHO. Time series of calculated (coloured) and observed (black) H_2O_2 and HCHO, respectively (**a, b**). The colour code reflects the relative deviation between observations and calculated data. Dry deposition is taken into consideration. Correlation plots of steady-state (SS) calculations versus observational data for H_2O_2 and HCHO (**c**). Grey lines indicate the 1:1 slope and dashed the 0.5 and 2 slopes. The coefficient of determination is for both species r^2 = 0.3.

3.2.8. Consideration of direct biogenic emissions or absorption of HCHO

As discussed before, non-photochemical excess HCHO during HUMPPA is caused by biomass burning (especially for R3) rather than through the transport of anthropogenic emissions. On

the physical sink side, this study assumes deposition as the sole effect. However, HCHO and acetaldehyde emissions from young seedlings (Stotzky and Schenck, 1976) and trees under stress conditions is known (Kimmerer and Kozlowski, 1982; Kimmerer and MacDonald, 1987; Nondek et al., 1992). More recently, significant direct emissions of HCHO and acetaldehyde from both Mediterranean deciduous trees and conifers were reported (Kesselmeier et al., 1997). On the other side, biogenic sinks also have been taken into consideration for non-conifers under indoor and laboratory conditions (Giese et al., 1994; Wolverton et al., 1984), respectively. Since the biosphere plays a major role in the boreal forest, this fact will be addressed to in the following for evaluation purposes. Figure 3.23 presents the correlation of ambient acetaldehyde (CH_3CHO) versus HCHO as well as the distribution of the relative standard deviation (RSD) for O_3, acetaldehyde and HCHO for the entire campaign. Acetaldehyde is unlikely to be emitted by plants since it is a stronger cell toxin than HCHO. Thus, in case of HUMPPA, ambient CH_3CHO is most probably produced by photochemistry which has similar formation pathways as HCHO. The correlation plot (a), which excludes pollutions events, shows a major fraction of data points up to 1.5 ppbv of acetaldehyde and 1.0 ppbv of HCHO above the 1:1 line. The high coefficient of determination (r^2 = 0.5) indicates similar daytime sources of both aldehydes. Upon reversion, biogenic emissions of HCHO (in the absence of biogenic acetaldehyde emissions) would result in a much lower correlation. In order to underline photochemistry as the sole HCHO source for "clean" days, part (b) of the figure depicts the RSD (variability) of O_3 versus its ambient mixing ratio in intervals of 1.9 ppbv. Excluding transport processes, ambient O_3 is controlled by "pure" photochemistry. The lowest interval (20.9 to 22.8 ppbv) shows the highest variability (ca. 3 %), which then decreases almost linearly down to ca. 0.6 % with increasing intervals. Plotting the acetaldehyde data with the same method (c), where the mixing ratio intervals are narrower (0.08 ppbv), results in a comparable picture indicating full photochemical control: the lowest interval (0.10 to 0.18 ppbv) has an RSD of 28 %, which then decreases strongly to 6 % in the following interval. Mixing ratios above 2 ppbv show almost no variability (<1 %). The trend for HCHO is consistent with that picture (d). Here, the RSD is also depicted versus intervals of 0.08 ppbv. Lowest levels (0.04 to 0.12 ppbv) vary about 24 %, reaching a minimum of 3 % about 1.28 ppbv in a lognormal distribution. Two modes at ca. 2 ppbv are remnants of pollution series and show a RSD of 1 to 2 %. Note that the RSD values are one order of magnitude lower than in case of O_3 with characteristic ambient levels of double-digit mixing ratios.

During non-pollution series, acetaldehyde is likely to be produced by photochemistry rather than emitted by plants. The good correlation with ambient HCHO indicates photochemical control for the latter species as well. That fact is underlined by comparable distributions of the RSD for O_3, acetaldehyde and HCHO.

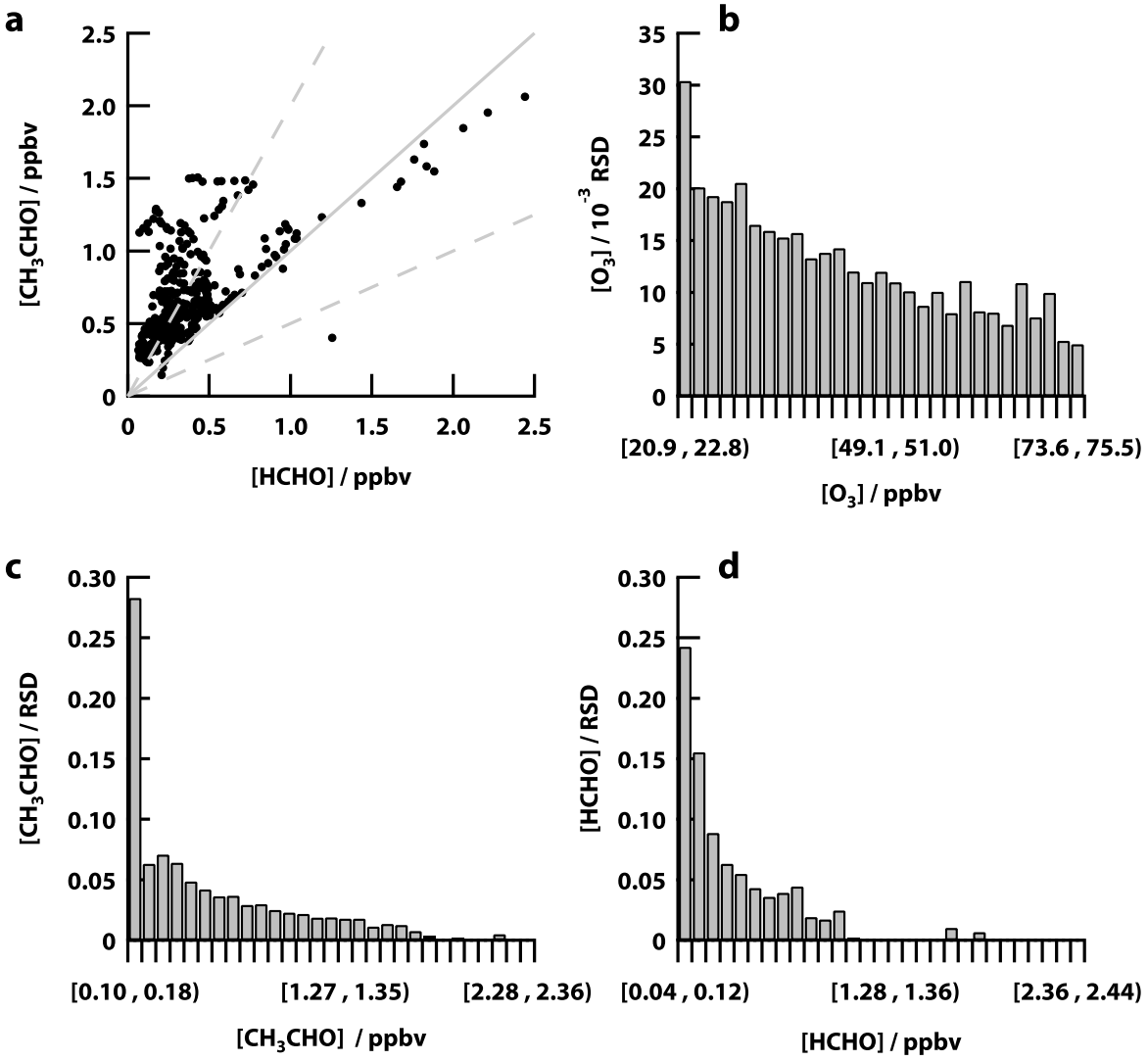

Figure 3.23.: Daytime correlation and distribution of acetaldehyde and formaldehyde. Correlation plot for daytime acetaldehyde versus HCHO (r^2 = 0.5) without the pollution series (**a**). Distribution of the relative standard deviation for O_3 (**b**), acetaldehyde (**c**) and HCHO (**d**). Ambient mixing ratios for all three species are highly influenced by photochemistry, whereas life times and deposition velocities slightly differ.

3.2.9. The NO_x sensitivity of the net hydrogen peroxide and formaldehyde production rate

Figure 3.25 depicts the dependency of the calculated net production rates of H_2O_2, $N(H_2O_2)$, and HCHO, N(HCHO), on the observed ambient NO_x and NO mixing ratio for daytime including all four regimes. So it quantifies basically the NO_x sensitivity of the net production. The two box and whisker plots are based on the data presented in the appendix Chapter B (Figure 3.24). In both cases, the abscissa is divided in 9 bins resulting in steps of ca. 17 pptv for NO_x and ca. 2 pptv for NO. The net H_2O_2 production rate starts with minimum NO_x levels at a median of 48.7 pptv h^{-1} (25^{th} and 75^{th} percentiles: 18.2 and 84.4 pptv h^{-1}, respectively). The maximum is in the subsequent bin at 65.2 pptv h^{-1} (median) ranging from 31.5 to 122 pptv h^{-1} in the NO_x interval 0.24 to 0.41 ppbv. Then $N(H_2O_2)$ approaches asymptotically medians of 24.4 to 34.6 pptv h^{-1} for NO_x mixing ratios between 0.41 and 1.23 ppbv. Note that the 10^{th} and 90^{th} percentiles still reach values of ca. 0.01 and ca. 0.18 pptv h^{-1} for NO_x (0.41 to 0.9 ppbv), respectively. As a result, the H_2O_2 production "needs" a

minimum of NO_x (0.24 to 0.41 ppbv), which lies above clean MBL and below urban mixing ratios for reaching its maximum (65.2 pptv h^{-1}). As expected, $N(H_2O_2)$ then decreases with increasing NO_x.

HCHO, on the other hand, follows a different trend in accordance with the literature. The first bin with an NO mixing ratio from 0 to 0.02 ppbv starts at 68.8 pptv h^{-1} (median) in a narrow distribution. Then it increases almost linearly until 153 pptv h^{-1} in the NO interval 0.05 to 0.07 ppbv. Note that HCHO is here photochemically net destroyed (negative 10th percentile of ca. −50 pptv h^{-1}) during the biomass burning series due to its vertical transport downwards from the plumes. Higher NO mixing ratios (70 to 140 pptv) result in the formation of a plateau ranging from 232 to 265 pptv h^{-1}.

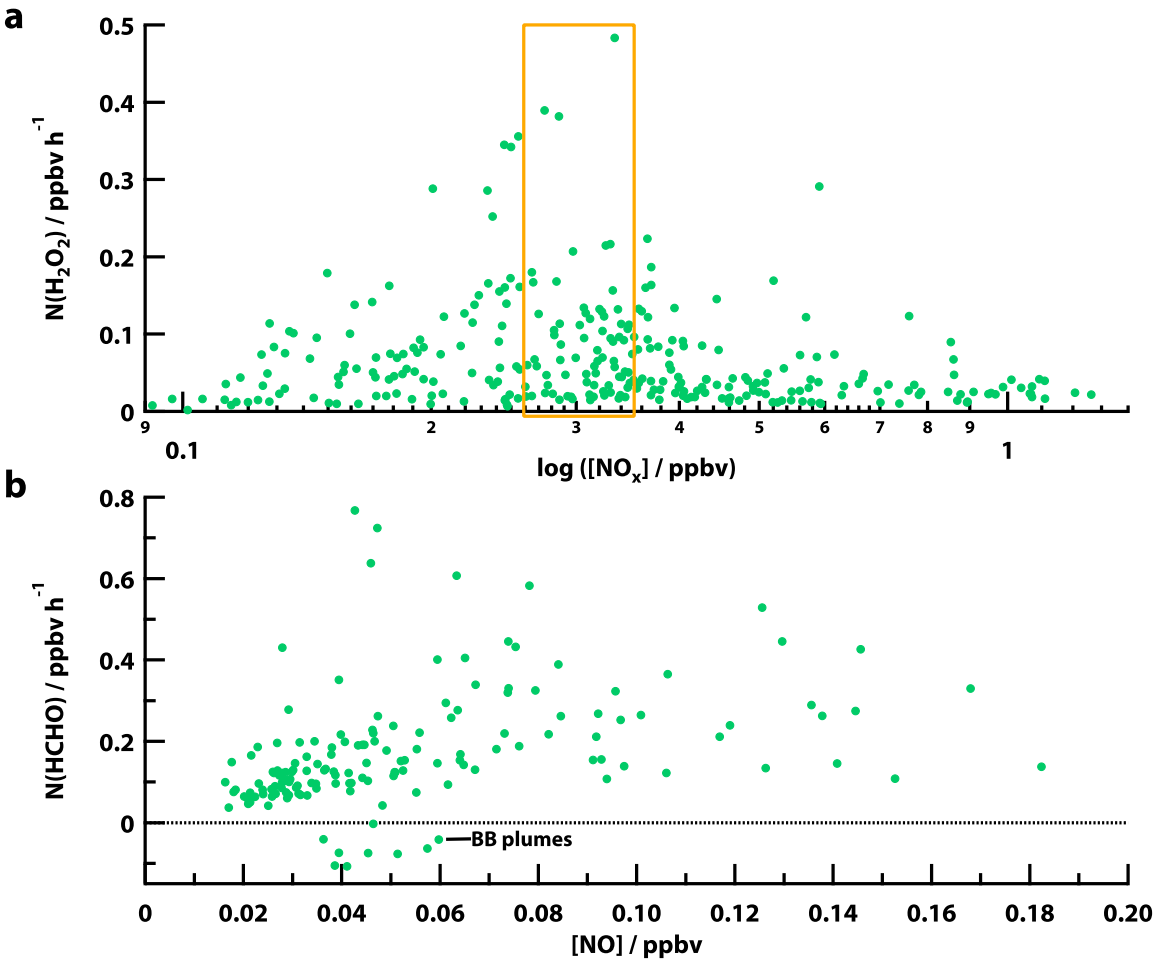

Figure 3.24.: Calculated net production rates of H_2O_2 and HCHO versus [NO_x] and [NO]. Net H_2O_2 production rate, $N(H_2O_2)$, versus the logarithmic NO_x mixing ratio, which shows a turnover point around 0.3 ppbv (**a**). Net HCHO production rate, N(HCHO), versus [NO], which shows increasing rates until ca. 80 pptv (**b**). In case of higher [NO], the production rate scatter irregularly. Net destruction was observed for entrained plumes during the biomass burning series, where secondary produced HCHO was removed by photolysis and the oxidation via OH radicals.

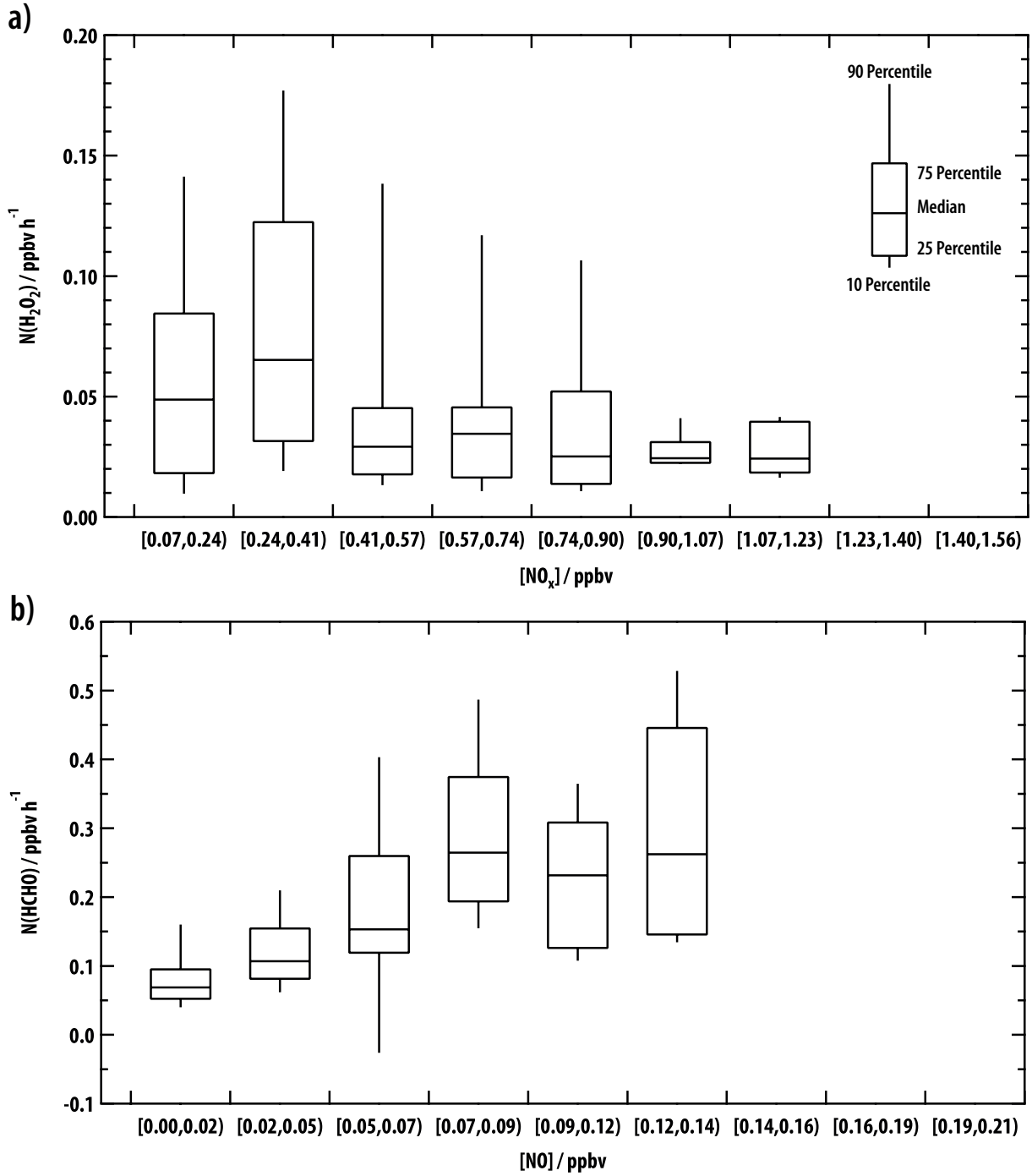

Figure 3.25.: Calculated net production rates of H_2O_2 and HCHO versus NO_x and NO. Net H_2O_2 production rate, $N(H_2O_2)$, versus the NO_x mixing ratio classified in bins of 17 pptv (**a**). Net HCHO production rate, N(HCHO), versus NO which is divided into bins of 2 pptv (**b**).

3.2.10. Summary and conclusions

[1] A comprehensive data set from the field measurement campaign HUMPPA from Jul 12–Aug 12, 2010 (Hyytiälä, Southern Finland) was studied. The following regimes could be identified and used for discussion: stressed boreal (R1, Jul 12-22 2010), cold & clean (R2, Jul 23-25), transported pollution (R3, Jul 26-29) and normal boreal with some short pollution events (R4, Aug 1-12).

During R1, the H_2O_2 levels were highest (971 pptv) and highly variable (80.1 %). HCHO showed medium mixing ratios (327 pptv) and lowest variability (42.9 %). During R2, the low average temperature (17.1 °C) was accompanied by low absolute humidity (13.3×10^3 ppmv). Moreover, the pol-

lution levels were very low, particularly those of CO (87.5 ppbv), NO_x (264 pptv) and O_3 (38.8 ppbv). H_2O_2 had medium mixing ratios (391 pptv), whereas HCHO had the lowest (211 pptv). R3 was characterized by recurring heat stress and pollution-affected air masses from Russia. The highest average daytime temperatures (22.4 °C) characterized by the highest absolute humidity (1.91×10^3 ppmv) were observed. In addition, ambient CO and O_3 showed peak values (147 and 45.0 ppbv, respectively), whereas the NO_x mixing ratio was intermediate (360 pptv). The H_2O_2 levels were medium (767 pptv) with low variability (72.6 %), whereas HCHO reached its campaign daytime maximum (1.09 ppbv). During R4, the meteorological conditions were comparable to the trends observed in the previous years (Williams et al., 2011): sunshine duration, cloud formation and rain events interchange (lowest $j(NO_2)$ of 2.18×10^{-3} s^{-1} and highest variability of 113 %). The temperature and absolute humidity values were only medium (18.9 °C and 17.1×10^3 ppmv). Minimum ambient H_2O_2 levels (295 pptv) were measured with the lowest variability (67.9 %). The same trend could be observed for HCHO due to its second lowest level (282 pptv), whereas it varied extensively (113 %).

[2] The study focused on calculations of the deviations from photostationary state, estimations of $[HO_2]$, $[RO_2]$ and [OH] (due to a low data coverage) and of the H_2O_2 and HCHO budgets. As a result, the calculated $[HO_2]$ is in agreement with the LIF observations (slope: 0.44 ± 0.029, r^2 = 0.71), whereas the OH time series are reasonably reproduced.

[3] Daytime calculations for H_2O_2 and HCHO showed that the recombination of HO_2 was the only significant H_2O_2 source ranging from 79 (R2) to 96 % (R4) of the total production. That source was followed by the ozonolysis of alkenes: R2 was dominated by 21 % (9.20 pptv h^{-1}), whereas the biomass burning series during R3 showed the lowest relative contribution with 4 % (10.4 pptv h^{-1}). R1 and R3 had comparable results with 14 and 11 %; however, the absolute production rates significantly differed (R1: 33.0 pptv h^{-1} and R2: 20.9 pptv h^{-1}). The highest contribution to ozonolysis of alkenes was made by the ozonolysis of α-pinene. H_2O_2 sinks were predominated by photolysis (approximately 55 %), whereas the oxidation by OH accounted for approximately 45 % of the total loss term. Overall, the net H_2O_2 production during daytime, $N(H_2O_2)$, showed highest levels for R4 (241 pptv h^{-1}), followed by R1 (193 pptv h^{-1}), R3 (152 pptv h^{-1}) and R2 (35.7 pptv h^{-1}). $N(H_2O_2)$ was 5 to 7 times higher during the two stressed boreal periods in comparison to the cold series. The HCHO calculations included only the first-generation products. The production rates, P(HCHO), ranged from 455 (R3) to 299 (R2), 277 (R4) and finally 230 pptv h^{-1} (R1). The reaction of methyl peroxy radicals with NO significantly accounted for approximately half the production from 44 (R1) to 56 % (R3). Furthermore, the oxidation of methanol via OH radicals accounted for 25 % for R2 (119 pptv h^{-1}), 26 % for R3 and R4 (119 pptv h^{-1} and 72.1 pptv h^{-1}, respectively) and 30 % for R1 (69.1 pptv h^{-1}). Subsequently, the MHP photolysis and the monoterpene oxidation via O_3 and OH resulted similar values in total (10 %). Consequently, throughout the regimes, the major daytime HCHO sources could be represented by relatively simple background chemical pathways. The total HCHO sink term, consisting of its two photolysis channels (radical and molecular) and the oxidation by OH radicals, broadly spread from the lowest absolute value of 81.7 pptv h^{-1} (R1) to 307 pptv h^{-1} (R3). Although the regimes differed from the meteorological and photochemical point of view, the absolute net HCHO production rate, P(HCHO), ranged only from 148 to 153 pptv h^{-1} (R3-R2). The lowest photochemical production was calculated during the pollution series (R3) and

the highest for cold and clean conditions (R2). Thus R3 was dominated by entrainment of secondary produced HCHO. In general, there is no evidence of biogenic effects on ambient HCHO.

[4] The steady-state budget calculations for H_2O_2 and HCHO excluding dry deposition showed that on an average, H_2O_2 is overestimated by a factor of 5 up to an order of magnitude (slope: 4.920 ± 0.512, intercept: 2.250 ± 0.333 ppbv, r^2 = 0.24). The HCHO values exceeded the observations 3.5 times on an average (slope: 0.6610 ± 0.0899, intercept: 1.1700 ± 0.0781 ppbv, r^2 = 0.26).

[5] The calculations of the deposition velocities for the early morning yielded in median values of 3.03 cm s^{-1} for H_2O_2 (mean: 3.52 cm s^{-1}, 60.4 % 1σ variability) and 1.08 cm s^{-1} for HCHO (mean: 1.37 cm s^{-1}, 71.6 % 1σ variability). The results for H_2O_2 are in agreement with those reported by previous studies in the Canadian boreal forests (Hall and Claiborn, 1997; Hall et al., 1999). Values of 5.0 cm s^{-1} were observed during the day for a coniferous forest in Saskatchewan (Hall and Claiborn, 1997). More comprehensive measurements have reported deposition velocities ranging from 5 to 9 cm s^{-1} during July in a Jack pine forest (Saskatchewan, Canada, Hall et al., 1999). For HCHO, previous studies reported comparable daytime deposition velocities from 0.75 to 1.5 cm s^{-1} (Krinke, 1999).

[6] Transport has a major impact on H_2O_2 and HCHO in the boreal forest. In the very early morning (4 a. m.), dew formation was a significant sink for H_2O_2, followed by a short phase of outgassing (7 a. m.). The rest of daytime was dominated by advection and the entrainment of H_2O_2-rich air from above. A heat wave during the campaign certainly caused a high convective turnover. Occasionally, the transport rates exceeded even the photochemical production. On the sink side, dry deposition was predominating. However, HCHO showed a different picture: the major daytime source was photochemistry, whereas the entrainment of HCHO-poor air from above caused significant losses. On the other hand, the photochemical losses were insignificant, except for those in the late afternoon. Dry deposition showed a relatively small effect for the entire daytime.

[7] The steady-state calculations including deposition and transport revealed a reasonable reproduction of H_2O_2 (slope: 0.9520 ± 0.0834, intercept: 0.2330 ± 0.0543 ppbv, r^2 = 0.30). HCHO showed a more qualitative result including the biomass burning events (slope: 0.2320 ± 0.0258, intercept: 0.2980 ± 0.0224 ppbv, r^2 = 0.35).

[8] The classification of NO_x sensitivity concerning the net H_2O_2 production rate showed a median of 48.7 pptv h^{-1} (low NO_x). The maximum was located in the subsequent bin at 65.2 pptv h^{-1} (median) ranging from 31.5 to 122 pptv h^{-1} in the NO_x interval 0.24 to 0.41 ppbv. Subsequently, $N(H_2O_2)$ asymptotically approached medians of 24.4 to 34.6 pptv h^{-1} for NO_x mixing ratios between 0.41 and 1.23 ppbv. Therefore, the H_2O_2 production in the boreal forest "needs" minimal NO_x levels (0.24 to 0.41 ppbv), which lie above those of the clean MBL and below urban mixing ratios for reaching its maximum (65.2 pptv h^{-1}). As expected, $N(H_2O_2)$ then decreases with increasing NO_x. On the other hand, the HCHO production follows the same trend as reported in literature. The first bin with an NO mixing ratio from 0 to 0.02 ppbv starts at 68.8 pptv h^{-1} (median) in a narrow distribution. Subsequently, it increases almost linearly until 153 pptv h^{-1} in the NO interval 0.05 to 0.07 ppbv. Higher NO mixing ratios (70 to 140 pptv) result in the formation of a plateau ranging from 232 to 265 pptv h^{-1}.

3.3. Comparison of HUMPPA measurements with the EMAC General Circulation Model

A general circulation model (GCM) is a global scale climate model which is able to simulate the physical processes in the atmosphere, oceans, cryosphere and on the land surface. Sub-models can be coupled for reproducing the atmospheric chemistry. Former studies concluded that the 3-D model EMAC realistically simulates stratosphere-troposphere exchange processes and reproduces reasonably the main features of trace gas distributions (Jöckel et al., 2006). This includes especially the seasonal variability of carbon monoxide (CO) in remote regions (Pozzer et al., 2007). Although agreeing with aircraft observations (Klippel et al., 2011), comparisons to ground based measurements show lower correlations (Pozzer et al., 2012). Particularly in the case of H_2O_2, the model has deficits to simulate absolute mixing ratios most probably due to deficits in cloud scavenging (Klippel et al., 2011). A recent study confirmed this behavior for the South Atlantic Ocean (Fischer et al., 2015): an overestimated dry deposition leads to low levels of H_2O_2. In contrast, the model is able to reproduce downward transport of H_2O_2. This section focuses on the third research objective, which is to ascertain the behavior of the model EMAC regarding H_2O_2 and HCHO in the boreal forest.

3.3.1. Model description and set-up for the simulations

ECHAM5/MESSy (hereafter EMAC) combines the general circulation model ECHAM5 (version 5.3.01), which is based on the weather prediction model of the European Centre for Medium-Range Weather Forecasts (ECMWF) (Roeckner et al., 2006) and the Modular Earth Submodel System (MESSy, version 1.9). The latter is a mediator organizing the data streams between the core GCM and the different submodels (Jöckel et al., 2005) as shown in Figure 3.26. Hence, EMAC is able to simulate atmospherical dynamics, thermodynamics and chemistry (e. g., by MECCA, described below).

In this study, the horizontal resolution of the ECHAM5 core model is T106 (approximately 1.1 x 1.1°) with a vertical resolution of 31 layers (up to 10 hPa, ca. 30 km). Meteorological parameters have been "nudged" (Jeuken et al., 1996; van Aalst et al., 2004) towards the reanalysis of the ECMWF for obtaining a more realistic representation particularly of the stratosphere-troposphere exchange processes.

Tropospheric and stratospheric chemistry of the gas and aqueous phase is described by the Module Efficiently Calculating the Chemistry of the Atmosphere (MECCA) sub-model (Sander et al., 2005) which contains 104 gas phase species and 245 reactions, especially basic HO_x, NO_x, CH_4 and non-methane hydrocarbons (NMHCs) chemistry (Kuhlmann, 2003). Hydrocarbon chemistry, including isoprene oxidation pathways, is described by the Mainz Isoprene Mechanism (MIM 1.1), which was developed at the Max Planck Institute for Chemistry (Pöschl et al., 2000). Note that monoterpene oxidation chemistry is not included.

The model includes submodels for dry and wet deposition (Kerkweg et al., 2006a,b; Tost et al., 2006) as well as for aerosol microphysics and gas/aerosol partitioning (Pringle et al., 2010a,b). Biomass burning emissions are tracked by the Global Fire Emissions Database (GFED, version 3.1) (van

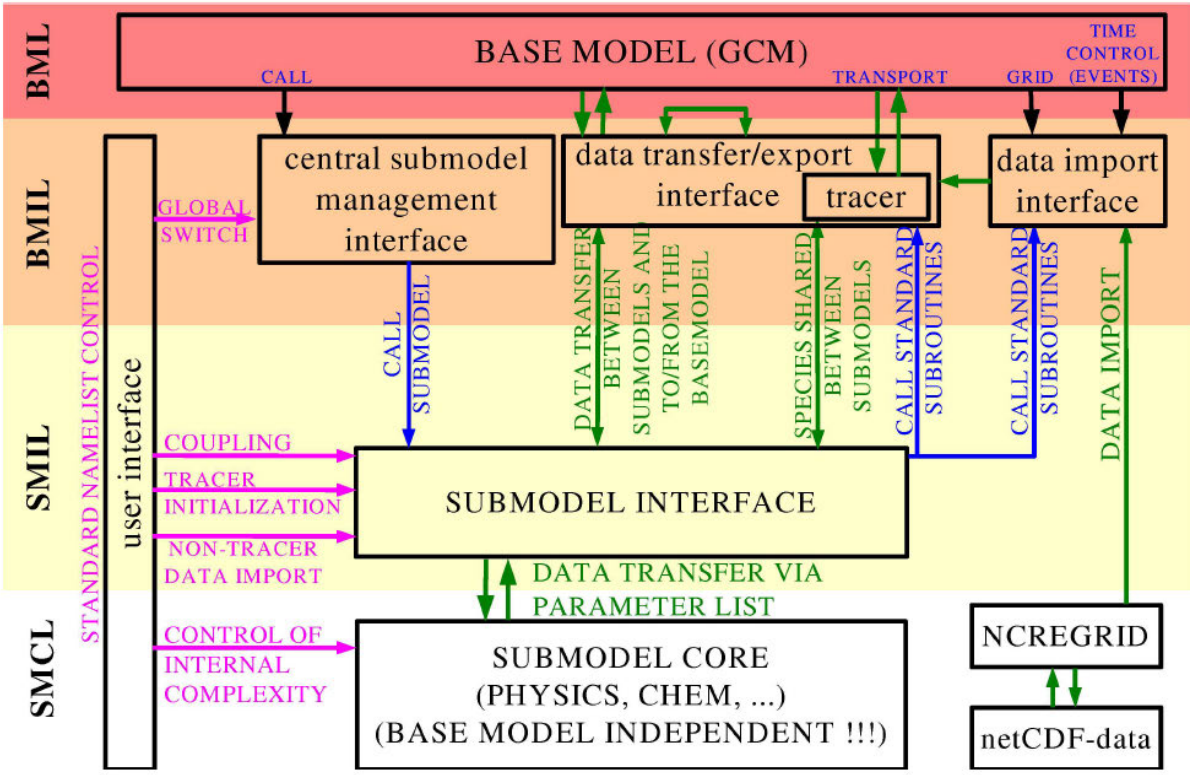

Figure 3.26.: The layered concept of MESSy. Reprinted from Jöckel et al. (2005).

der Werf et al., 2010) averaged from 1997-2010 with monthly time resolution and are based on the Moderate-resolution Imaging Spectroradiometer (MODIS) data.

This set-up (compare Pozzer et al., 2012) was used for the reference simulation (R) of HUMPPA from Jul 12 to Aug 12 2010. The evaluation of ambient NO_x showed that the simulated levels needed to be reduced. Therefore, one sensitivity study (S1) was performed with 50 % – anthropogenic and soil emissions of NO_x. However, the following will show that this has a minor impact on ambient H_2O_2 and HCHO. As a result, a second sensitivity simulation was performed with 50 % NO_x and 200 % deposition velocity for H_2O_2 and HCHO. Table 3.16 summarises the parameters for the reference (R) and the sensitivity simulations (S1 and S2) for this study.

Table 3.16.: Parameters for the reference simulation (R) and the sensitivity studies (S1 and S2). The reference simulation is based on the parameters of Pozzer et al. (2012). Due to overestimated ambient NO_x levels, S1 aimed to lower ambient NO_x via decreasing the emissions by 50 %. Finally, the same parameters were set for S2 including doubled deposition velocities for H_2O_2 and HCHO.

Simulation	Description
Reference (R)	Parameters of Pozzer et al. (2012)
Sensitivity 1 (S1)	50 % of NO_x emissions
Sensitivity 2 (S2)	50 % of NO_x emissions and 200 % deposition velocity for H_2O_2 and HCHO

3.3.2. Large scale evaluation of the reference simulation

3.3.2.1. Synoptic scale meteorology

Figure 3.27 shows the model reproduction of the physics on a synoptic scale over Europe on Jul 30, 2010 00:00 UTC by comparing geopotential height[3] (at 500 hPa) and temperature at about 1.5 km (850 hPa) with data of the NCEP Global Forecast System (GFS) (Whitaker et al., 2008). Main features such as a "double low" over Iceland (550 and 560 gpdm), a low pressure system over Scandinavia and whole Germany (560-580 gpdm), respectively, as well as a wide region of highs from Russia to Greece (590-600 gpdm) are in good agreement with the reanalysis. Focusing on the modeled temperatures at 850 hPa also shows consistent results. The main features here are cold regions over Iceland and vast parts of the North Atlantic Ocean and Central Europe. Warmest temperatures between 25 to 30 °C appear both in the model and in the reanalysis for the south of Spain, North Africa and the eastern Mediterranean. Slight differences in the absolute values for both geopotential height and temperature are expected due to different underlying data sets for the simulation and the reanalysis.

3.3.2.2. Long-range transport of carbon monoxide

The following section discusses in-situ measurements of trace chemical species in comparison to the EMAC simulation. Figure 3.28 depicts a simple cluster analysis of 48 h backtrajectories (NOAA HYSPLIT 4 with GDAS data) (Draxler and Rolph, 2012), CO as the main long-lived indicator for anthropo- and biogenic combustion and CH_4 as an emission predominantly from (anaerobic) biogenic processes.
The first period of special interest is Jul 23-25 dominated by northern air masses showing "clean" conditions focusing on CO with high agreement between model and measurement (AL-5002 CO-VUV, Aerolaser GmbH, Garmisch-Partenkirchen, Germany). Proceeding to Jul 26-31 and during the period from Aug 7-10, the picture is different since SMEAR II was influenced by Central Europe, Northern and Western Scandinavia as well as Russia, which showed evidence of severe biomass burning events around Moscow (not shown here). Though the simulation reproduces the main features, it is not able to show peak values of 440 ppbv on Jul 29 (at midday). These might be caused by strong local sources besides transport from urban areas or an underestimation of the biomass burning since the GFED data has a monthly time resolution. Generally, the simulation overestimates CO in average by 25 ppbv (22 % of the measurement mean). Further, the simulated CH_4)is overestimated by 6 % in average. It shows a diurnal pattern oscillating around a mean level with higher mixing ratios in the night which also sometimes shift a bit towards the morning. On the contrary, the measurements (fast GC) seem to be influenced by local scale emissions (higher variability) which cannot be tracked by the model.

[3]The geopotential height for a single pressure level shows qualitatively where highs and lows are located.

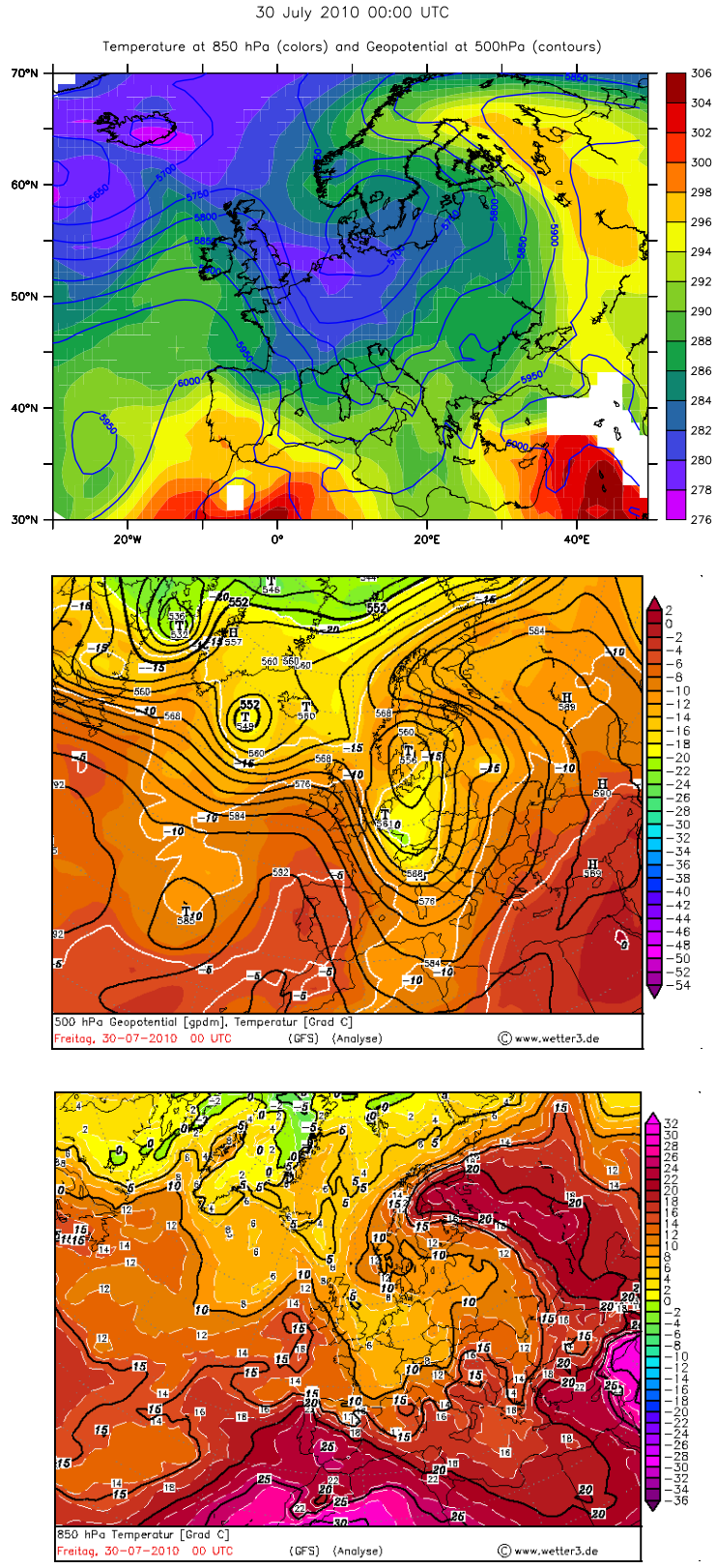

Figure 3.27.: Model and reanalysis of meteorology over Europe for Jul 30, 2010 at 00:00 UTC for the reference simulation. (**top**) EMAC output for temperature (scaling from 276 to 306 K and 3 to 33 °C) at 850 hPa, respectively, and geopotential height (gpm) at 500 hPa. (**middle**) GFS reanalysis of temperature (°C) and geopotential height (gpdm) both at 500 hPa. (**bottom**) GFS reanalysis of the temperature (°C) at 850 hPa.

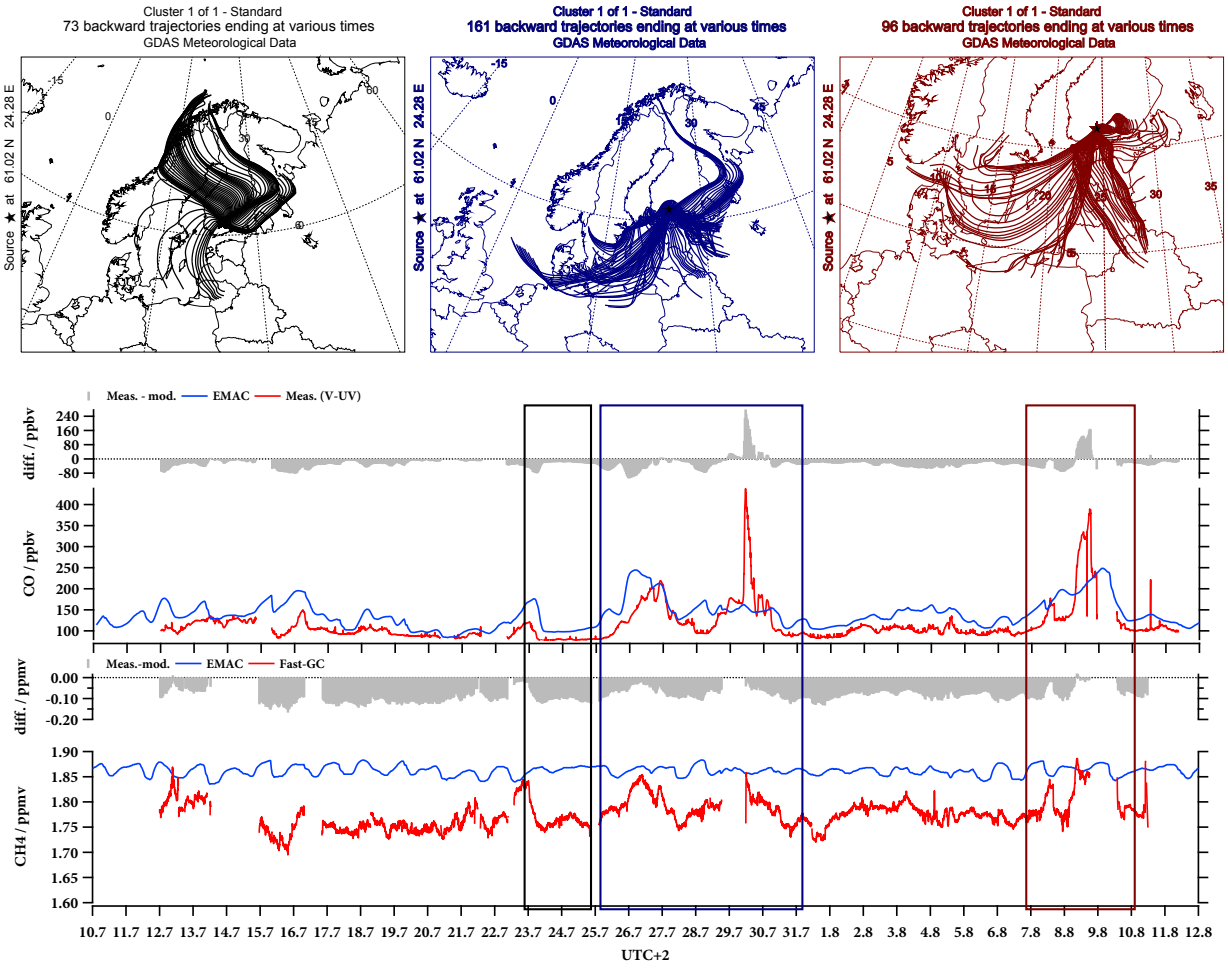

Figure 3.28.: Air mass origins and long-lived trace chemical species for the reference simulation. (**top**) Cluster analysis of 48 h backtrajectories with hourly resolution (NOAA HYSPLIT 4 with GDAS meteorological data) for the periods Jul 23-25 (**black**), Jul 26-31 (**blue**) and Aug 7-10 (**red**) of the year 2010. Simulated and observed CO in ppbv (**middle**) as well as CH_4 in ppbv (**bottom**). The rectangles mark a clean series (**left**) and two biomass burning events (**middle** and **right**).

3.3.3. Why a vicinal model box is used for local scale studies

NO_x (NO and NO_2) is a highly conserved quantity with lifetimes in orders of days until it is removed by OH via HNO_3. It plays a crucial role on the partitioning of peroxy (HO_2 and RO_2) to oxy (OH and RO) radicals and thereby on the O_3 – HO_x – NO_x – VOC chemistry.

$$HO_2 + NO \longrightarrow OH + NO_2$$
$$RO_2 + NO \longrightarrow OH + RO$$

Hence, ambient NO_x needed to be evaluated for the reference simulation before performing sensitivity studies. Other chemical trace gas species are discussed in Section 3.2 in more detail. Figure 3.29 shows extracts of Southern Finland with average values (from Jul to Aug) of the anthropogenic and soil NO_x emission rates. The model grid (1.1 x 1.1°) is indicated by black lines and the anthropogenic emission inventory with a resolution of 0.1 x 0.1° is distinguishable.
Soil emissions spread over several orders of magnitude, namely from 1×10^{-11} to 1×10^{-8} mol s^{-1} m^2 (6.0×10^{12} to 3.8×10^{15} 1/sm^2). The levels are lowest over marine, whereas peak levels are found in inland areas. Anthropogenic emission show a wider range: 1×10^{-11} to $1 \times 10^{-6.2}$ mol s^{-1} m^2 (6.0×10^{12} to 3.8×10^{17} 1/sm^2). Highest values are found around urban areas, such as Helsinki, Tampere, etc.
The HUMPPA site, Hyytiälä, is located in the purple box, right next to Tampere. Figure 3.30 shows the outcome of the first reference run for the purple and vicinal (turquoise) model boxes. A point-by-point comparison of modeled and measured NO_x (ppbv) was performed.
The HUMPPA box shows a spread from several pptv in the late afternoons to 6 ppbv in the early mornings. That causes very high deviations up to a factor of 20 or 5 ppbv of absolute difference. In contrast, the vicinal box shows generally lower modeled NO_x levels, overestimating by a factor between 2 and 8. Highest deviations are found during night time and in the early morning (ca. 1.5 ppbv overestimation by the model).
Consequently, it is highly likely that the HUMPPA box is influenced by NO_x emissions from Tampere, since the simulated parameters are averaged over one model box. Thus the vicinal box was further studied.

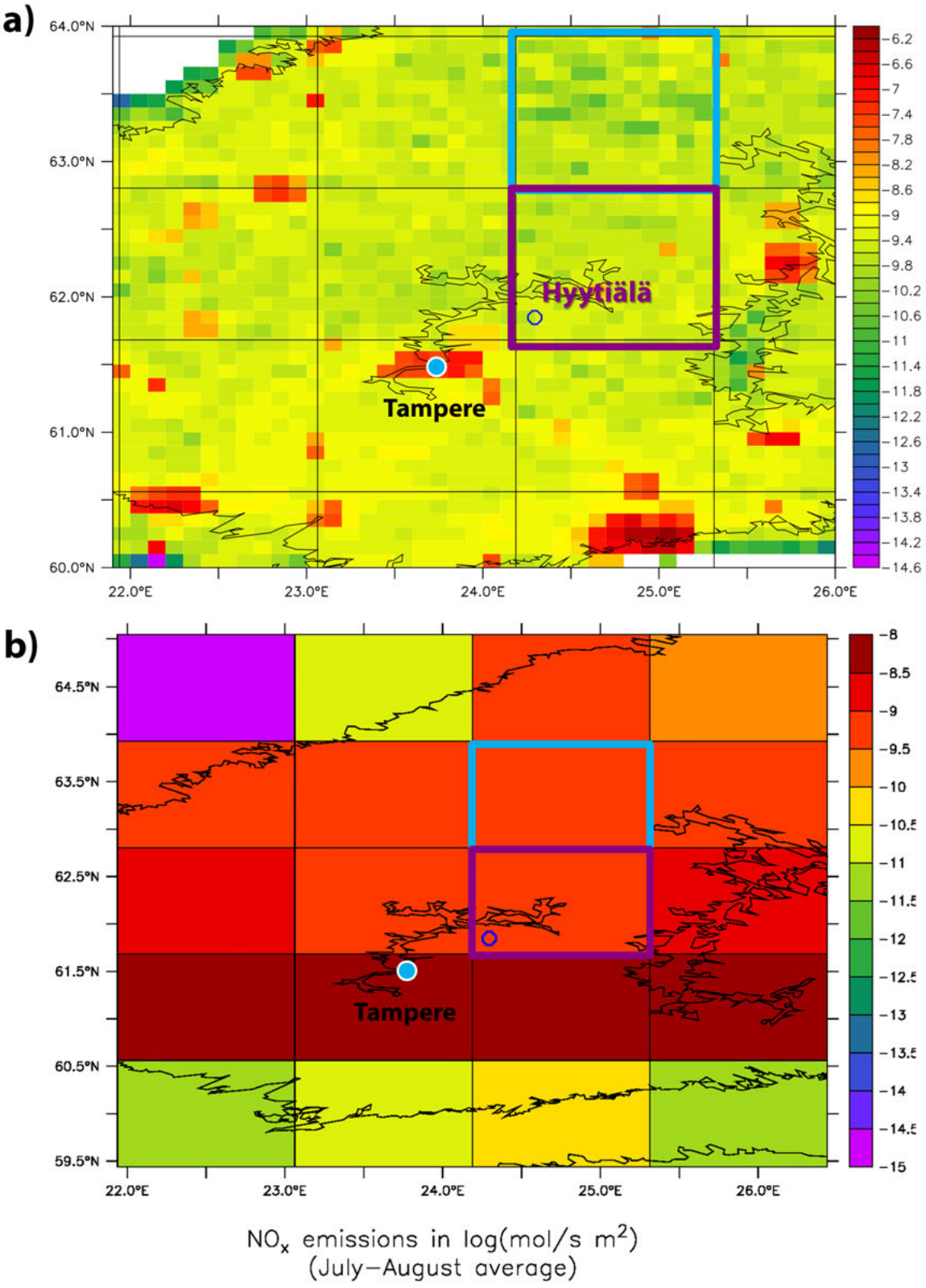

Figure 3.29.: Comparison of anthropogenic and soil emissions rates of NO_x for the HUMPPA EMAC reference simulation. The maps show an extract of Southern Finland. Average values (from Jul to Aug) of the anthropogenic (**a**) and soil (**b**) NO_x emission rates (logarithm of mol s^{-1} m^2; where mol = mole) are depicted in colour code. The HUMPPA site is located within the purple, whereas the turquoise box was used for the model simulations R, S1 and S2 (compare Figure 3.30).

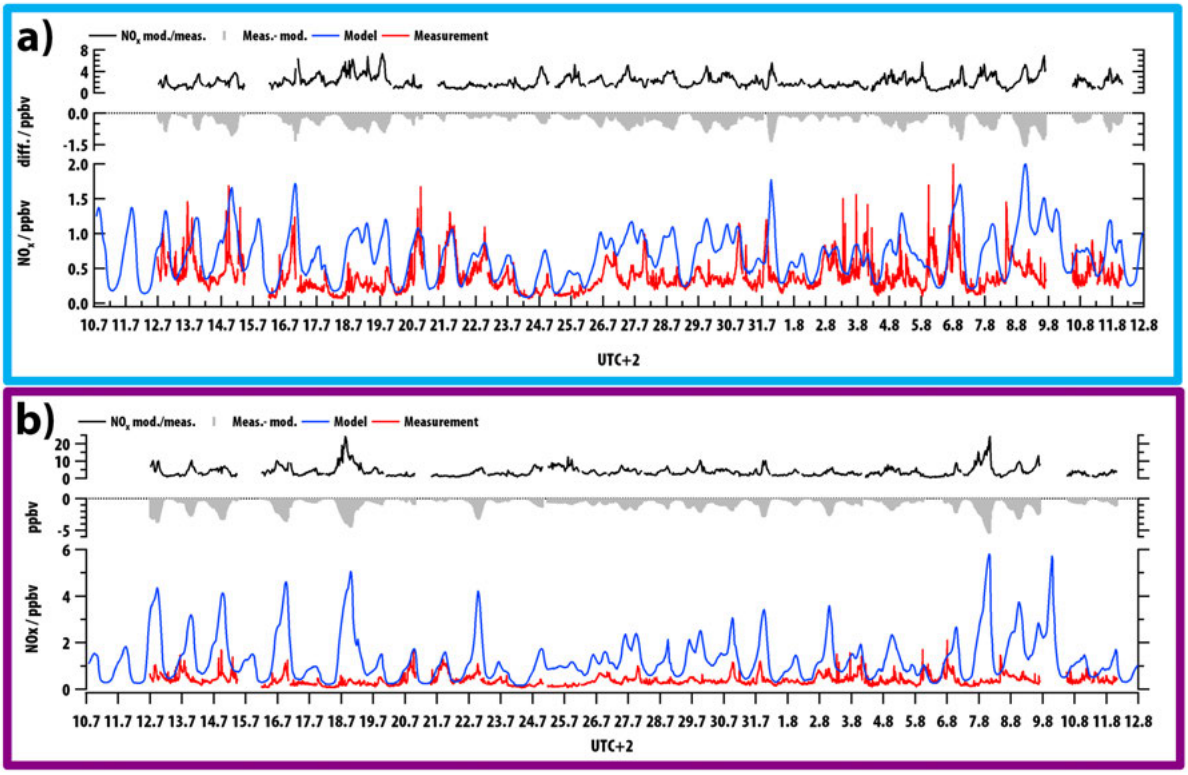

Figure 3.30.: Comparison of NO_x levels between the Hyytiälä and a vicinal box. Time series of measured (red) and modeled (blue) NO_x (ppbv) for a vicinal (**a**) and the HUMPPA site box (**b**). Deviations are shown as the modeled/measured ratio (black) and as differences (grey).

3.3.4. Results for the reference simulation

3.3.4.1. Local meteorological parameters compared to SMEAR II data

Continuing with the local measured meteorological parameters, Figure 3.31 depicts the observed time series of $j(NO_2)$, temperature, pressure, relative humidity and the boundary layer height in comparison to the reference simulation. Since the model reproduces physical processes by the same mechanism, a discussion for the sensitivity studies (S1 and S2) is not necessary. Noteworthy, the measurements were performed in-situ (except for the boundary layer height), whereas the model "nudges" over boxes of 1.1 x 1.1° (approximately 100 x 100 km) leading to expected deviations.
The radiation (here in $j(NO_2)$ values) is reproduced reasonably as it follows the main features. The lengths of day and night overlap showing a clear diurnal profile. However, the simulated daytime values show deviations from typically 16 % (up to 60 %), since clouds and aerosols can lead to changes in radiation by absorption and scattering on a small local and time scale. Interestingly, underprediction occurs for very clean conditions (Jul 23-25), overprediction basically every day during noon. Further, the behaviour of measured temperatures at 16.8, 33.6, 50.4, 67.2 and 84.0 m (above ground level) are reproduced well, though the model overestimates the absolute values in general since the simulation starts from sea level, whereas the SMEAR II station is elevated (181 m a.s.l.)[4]. Especially the difference between modeled surface and temperature at 100 m is higher than the difference between minimum and maximum height on the SMEAR II tower. The model dis-

[4]The lowest vertical box in the model starts at sea level and reaches 100 m.

agrees highest (up to +15 °C) during the coldest days (Jul 23-26) and thunderstorms (Jul 14 and Aug 6). However, the behaviour of measured (at ca. 181 m above sea level) and modeled pressure (at 100 m) is overestimated up to 10 hPa (1 %) which explains the 80 m difference in height[5]. Although temperature, pressure and the relative humidity have a high impact on the absolute humidity, the model reproduces the main features – including the coldest days (Jul 23-26) – very well. However, midday values are overpredicted up to 8 ppmv, whereas the model tends to underpredict absolute humidity for the pollution series about 4 ppmv. In contrast, the relative humidity is underestimated by the model ranging from 20 to 40 %, which could lead to a lower absolute humidity as well potentially effecting chemical reactions involving water molecules. The simulation is only about 20 to 40 % higher during the first period of warm and the coldest days (Jul 11-14 and Jul 24-25, respectively). In addition, the model does not track the rain events (relative humidity around 100 % in the measurements) as it does not exceed values of 90 %. Finally, a critical point for both, measurements[6] and simulation, is the boundary layer height since the balloon sondes detected more than one temperature inversions (not shown here). Nevertheless, there are long periods of very good agreement, especially from Jul 16 to Jul 24 and Jul 26 to 30 (the model overestimates about 44 to 300 m). The only exceptions are Jul 12-13, Jul 24-25 and Aug 4-5.

Meteorology and physics are reproduced reasonably well within the boundary conditions (e. g., comparison of in-situ measurements with a box about 100 x 100 km, nudged data). The weakest period in consideration of the parameters shown in Figure 3.31 is Jul 24-25. The simulation overestimates radiation ($j(NO_2)$), underestimates temperature, overestimates relative humidity and underestimates the boundary layer height.

[5] As a rule of thumb: the pressure drops by 1 hPa each 8 m.

[6] The boundary layer height determination is based on "mixed profiles" (standard mixed boundary layer): temperature, humidity and chemical species are well mixed until the top (Ouwersloot et al., 2012).

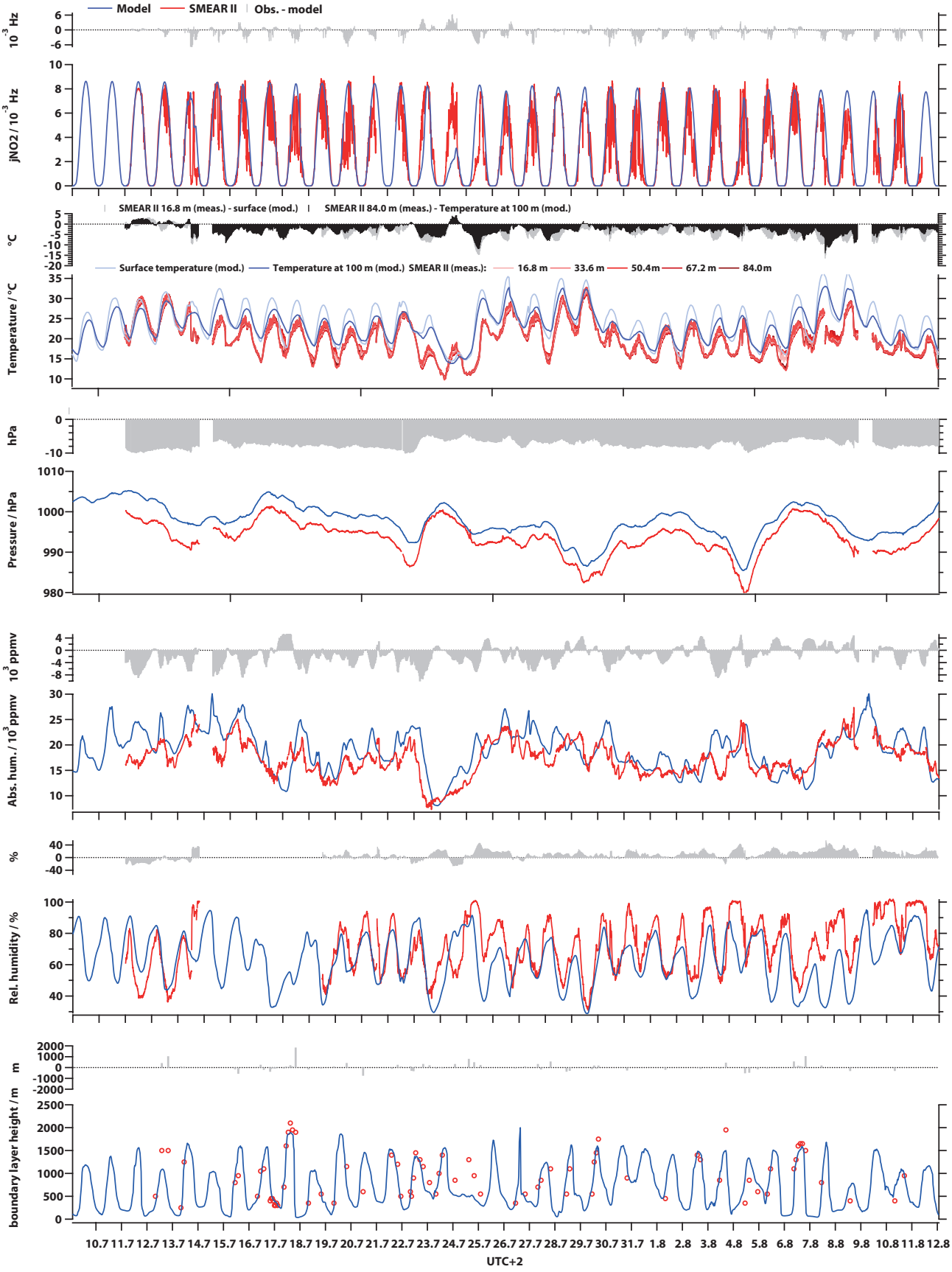

Figure 3.31.: Comparison of modeled and observed meteorological parameters for the reference simulation: j(NO_2) (s^{-1}), temperature (measurements at five different levels, °C), pressure (hPa), absolute and relative humidity (ppmv and %) as well as the boundary layer height (m). Modeled data is always depicted in blue and observations in shades of red. Differences between measurements (meas.) and the model (mod.) are shown in grey (or black if more than one parameter is examined). Positive values result from under-, negative from overestimation of the model.

Scatter plots and linear regression parameters for the local meteorology. Figure 3.32 depicts scatter plots of the simulated daytime temperature T, pressure p and relative humidity versus the observations. Photolysis rates of H_2O_2, HCHO, NO_2 and O_3 include day- and nighttime values. Table 3.17 gives a supplementary overview on the linear regression parameters, such as the coefficient of determination (r^2), the intercept a and the slope b. In addition, $a\ (\bar{x}_{\text{mod.}})^{-1}$ is a simple quantification of the offset. It is the ratio between a and the average simulated quantities for daytime, or day- and nighttime in case of the photolysis rates.

First, the temperature is qualitatively reproduced by the model. However, the PLS based linear regression is tilted for the temperature due to a very high offset (120 % of the average daytime T) with a negative slope (−0.14) and a low coefficient of determination (r^2 = 0.053). In contrast, the pressure shows a very good correlation (r^2 = 0.89) with an insignificant offset (2.1 %) and a slope close to unity (1.02). Relative humidity is reproduced reasonably well (r^2 = 0.34) with a relatively high offset of 55 % of the average daytime value. This is "compensated" by a low slope (0.408). It should be mentioned that temperature and pressure play a major role for the determination of the relative humidity. Thus, this is a qualitatively good result since T is underrepresented in the simulation. Particularly day- and nighttime photolysis rates as well as their trends are generally reproduced accurately. Coefficients of determination decrease in the order: j(O^1D) (r^2 = 0.85), j(HCHO) (r^2 = 0.82), j(H_2O_2) (r^2 = 0.82) and j(NO_2) (r^2 = 0.77). Compared to the other meteorological parameters, the offsets are rather insignificant ranging from 11 to 17 %. Only the slopes deviate negatively from unity, especially for j(H_2O_2) (−26 %), followed by j(O^1D) (−19 %) and j(NO_2) (−10 %). Closest results are obtained for j(HCHO) (−5 %).

Earlier studies have demonstrated that the model represents the physics reasonably well (e. g., Pozzer et al., 2012). This fact is particularly obvious for the photolysis rates and the ambient pressure. However, it should be recalled that the vicinal northern box was used, thus the in-situ "observer" is exposed to a slightly different meteorology. For example, the different solar zenith angle explains deviations up to 5.5 % for the photolysis rates. It is highly likely that clouds and aerosols could explain the other part. Precipitation is closely linked to the relative humidity and the simulation predicts it, quite accurately. However, model does not exceed daytime values of 96 %, whereas the observations recorded rain and thunderstorms (100 %) which can be very local phenomena.

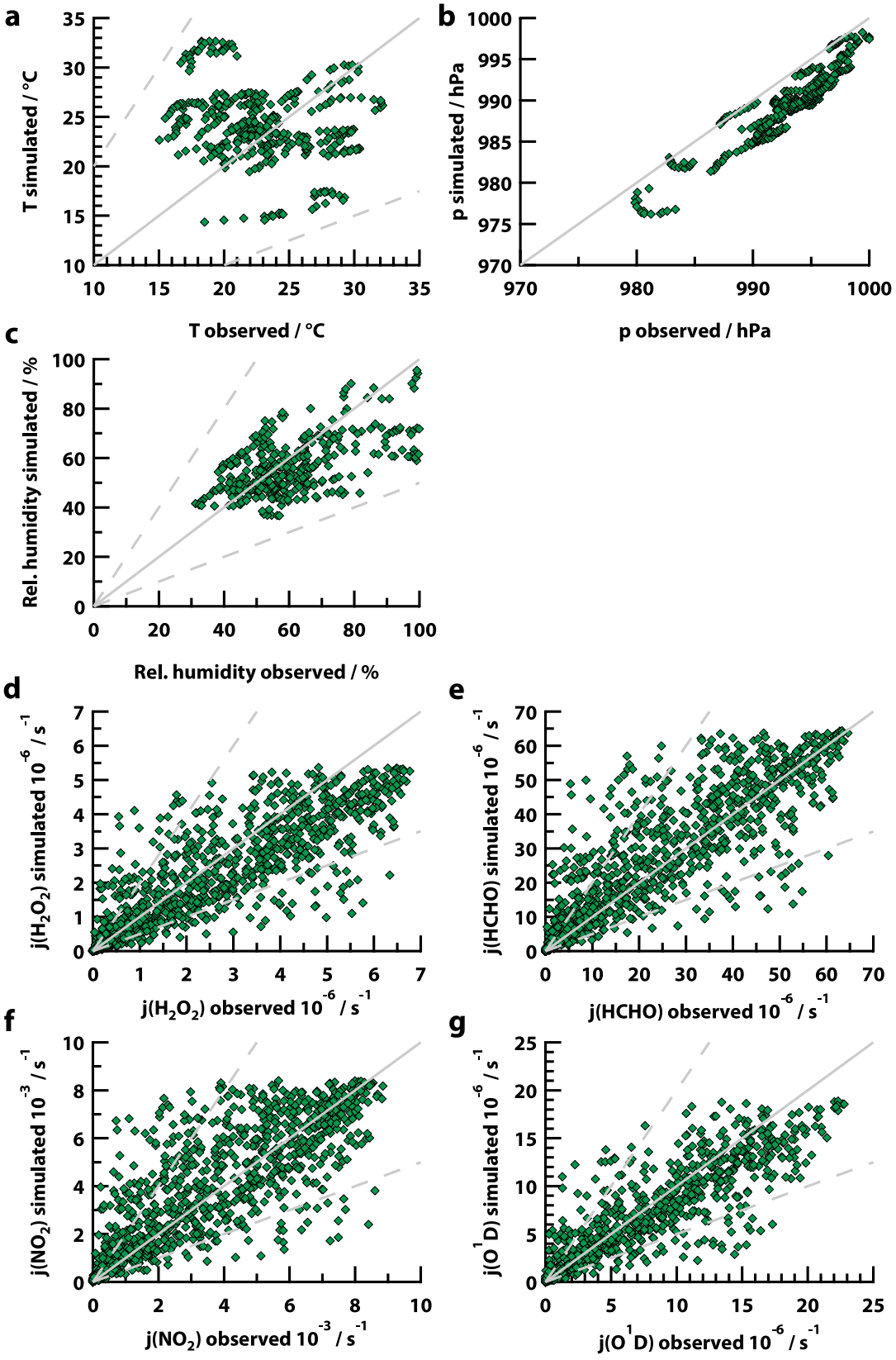

Figure 3.32.: Correlation plots of simulated versus observed meteorological parameters and photolysis rates for the reference simulation. Daytime temperature (T in °C) (**a**), surface pressure (p in hPa) (**b**) and relative humidity (in %) (**c**) are shown as meteorological parameters. Further, day- and night-time $j(H_2O_2)$ (**d**), j(HCHO) (**e**), $j(NO_2)$ (**f**) and $j(O^1D)$ (**g**) are given in s^{-1}. Grey lines represent unity, whereas dashed depict the 0.5 and 2 slopes, respectively. Note that the latter are out of scale in case of p.

Table 3.17.: Determination and linear regression coefficients for physical parameters of the reference simulation versus the observations. Given are the coefficients of determination (r^2) and intercepts a (including the relative 1σ uncertainty Δa) in the corresponding units for the quantities presented in Figure 3.32. The ratio of a to the average daytime value in the model $\bar{x}_{\text{mod.}}$ (in %) is a simple measure of significance for the regression intercept: the higher the value the more significant the offset. The slope is listed as b with the relative 1σ uncertainty Δb.

Quantity	Unit	r^2	a	$a\ (\bar{x}_{\text{mod.}})^{-1}$ / %	Δa / %	b	Δb / %
Temperature	°C	0.053	29.0	120	3.6	−0.214	21
Pressure	hPa	0.89	−21.0	2.1	80	1.02	1.7
Rel. Hum.	%	0.34	32.0	55	5.6	0.408	7.1
$j(H_2O_2)$	s^{-1}	0.82	1.96×10^{-7}	13	13	0.744	1.3
j(HCHO)	s^{-1}	0.82	2.82×10^{-6}	15	11	0.951	1.3
$j(NO_2)$	s^{-1}	0.77	4.78×10^{-4}	17	10	0.901	1.5
$j(O^1D)$	s^{-1}	0.85	4.13×10^{-7}	11	16	0.813	1.1

3.3.4.2. Time series of selected trace chemical species

Proceeding to short-lived trace chemical species, Figure 3.33 depicts the comparison of species related to the O_3 budget as well as HO_x mixing ratios. O_3 characterized by high deviations around ±50 %, especially considering an overestimation of NO_x by the model to peak values of 25 ppbv or a factor of 100. Disagreeing periods in NO_x follow a nighttime cycle, indicating either a strong source or a missing sink (e. g., dry and wet deposition via N_2O_5 to HNO_3; Jacob, 2000; Wesely and Hicks, 2000) in the simulation. Nevertheless, the NO to NO_2 ratio is in agreement with the measurements. Proceeding to H_2O_2, the model overpredicts the observed mixing ratios in general. The measured diurnal behaviour is reproduced with deviations up to 6 ppbv, especially in the night implying an underestimation of the deposition. The daytime values are less overpredicted as expected due to reasonable HO_2 mixing ratios[7]. A related species is HCHO, the major product of CH_4 and isoprene oxidation by OH radicals (Lee et al., 1998b; Tan et al., 2001) as well as directly emitted to a lesser extent. The model generally overestimates HCHO, particularly during the polluted periods by approximately 5 to 7 ppbv.

Further, Figure 3.33 shows the reproduction of hydroxyl (OH) and hydroperoxy (HO_2) radicals, which are very short-lived in the order of seconds and undergo fast changes in concentration depending on meteorology and photochemistry (e. g., Heard and Pilling, 2003; Lelieveld et al., 2004). Thus, it is expected to be difficult for a 3-D model to simulate.

HO_2 levels are consistent with the calculations from photostationary state in Section 3.2 by reaching values up to 30 pptv, which might be due to agreeing NO to NO_2 ratio for both measurement and model. Although the absolute NO_x mixing ratios are overestimated, a ratio implies a reasonable conversion of NO to NO_2 (and back) by peroxy radicals during daytime. In contrast, the model underestimates OH in average by a factor of 9, indicating a missing source or a strong sink of OH.

[7] The major source of H_2O_2 is the recombination of two hydroperoxy radicals:
$HO_2 + HO_2 \longrightarrow H_2O_2 + O_2$ (Lee et al., 2000).

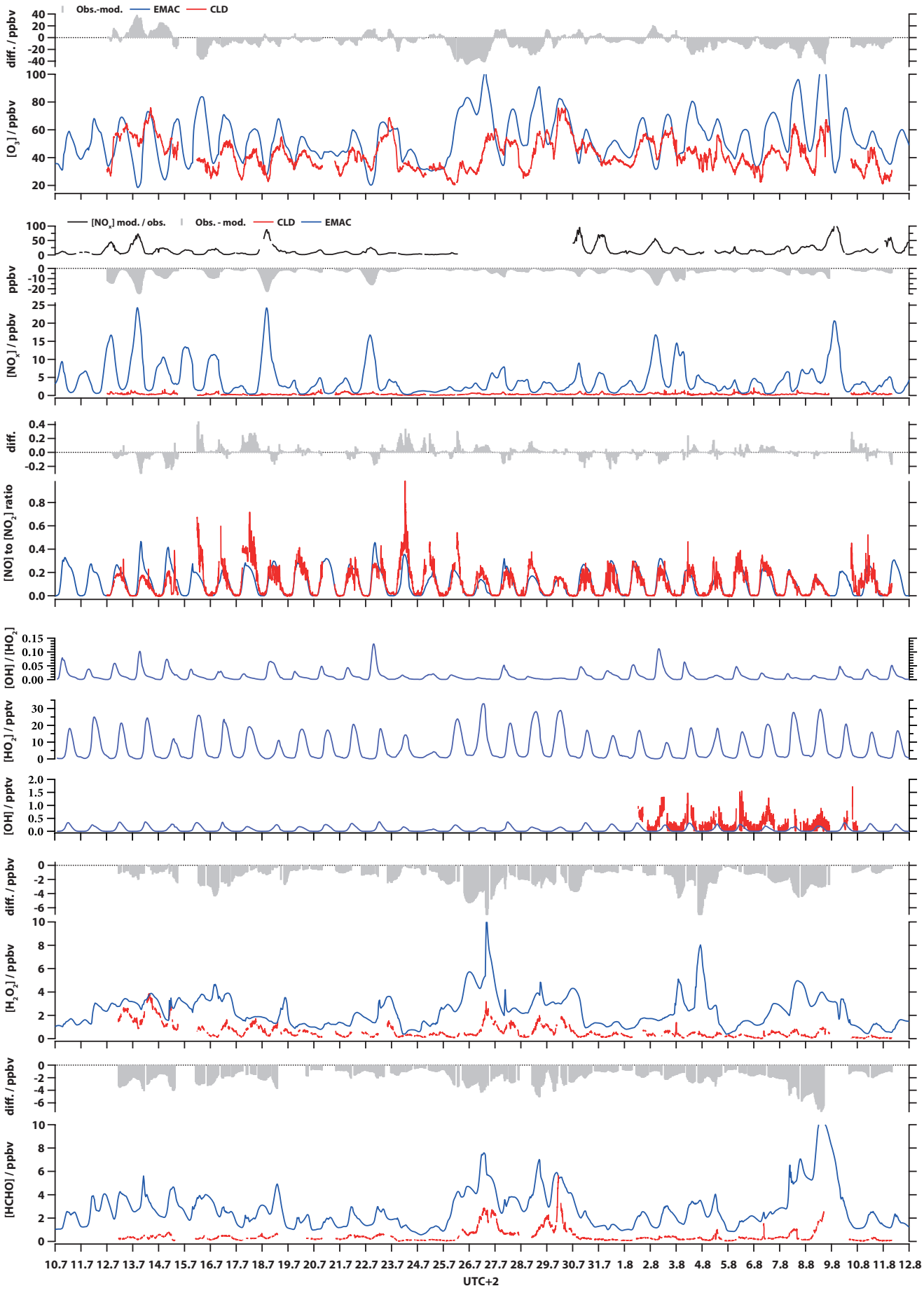

Figure 3.33.: Short-lived trace chemical species. Modeled and measured O_3, NO_x, NO to NO_2 ratio, H_2O_2, HCHO and related trace chemical species.

3.3.5. Sensitivity to changes in NO_x emissions, H_2O_2 and HCHO deposition velocities

3.3.5.1. The trends for H_2O_2, HCHO and related species

Figure 3.34 depicts the time series of all simulations for H_2O_2 and HCHO and highlights clean conditions (Jul 23-25) as well as the two biomass burning events (Jul 25-31 and Aug 7-10). In general, the model reproduces the main features across the three simulations for both species. However, there are differences in the sensitivity to changes in NO_x and the deposition velocity as well as during the pollution series. The following discussion includes daytime averages listed in Table 3.18.

Hydrogen peroxide and other hydroperoxides. In case of H_2O_2, a decrease of anthropogenic and biogenic emissions by 50 % from R to S1 leads to a largely identical time series. This fact is supported by the daytime averages (R: 2.59 ppbv, S1: 2.55 ppbv) concluding a low model sensitivity due to the insignificant change of −2 %. Consequently, S1 still overpredicts the observed H_2O_2 (0.639 ppbv) by a factor of 4. Increasing the deposition velocity from S1 (0.638 cm s^{-1}) to S2 (1.280 cm s^{-1}) results in a significant change to the ambient H_2O_2 (1.440 ppbv, −44 %). Note that the absolute differences between R and S2 depend on the chemical regime: R overestimates minimally the clean conditions (0.2360 ± 0.0974 ppbv in average) and highly biomass burning series (1.630 ± 0.904 ppbv and 1.500 ± 0.721 ppbv in average). This emphasizes the importance of deposition for the pollution series and implies a high model sensitivity. However, the effect is insufficient to meet the observations. Another doubling of the deposition velocity in the model – for example to 2.56 cm s^{-1}, a value within the 1σ interval of the calculations (3.52 ± 2.13 cm s^{-1}) – could indeed lead to reasonable H_2O_2 mixing ratios (ca. 0.813 ppbv). Interestingly, the modeled H_2O_2 does not increase with lower NO_x as expected (Gnauk et al., 1997; Watkins et al., 1995a,b). This feature is also confirmed by calculations on observational data in Section 3.2.
However, all simulations show methyl hydroperoxide (MHP) levels within the uncertainty of the calculation from Section 3.2 (0.435 ± 0.405 ppbv). Especially the reference simulation underpredicts MHP by 6 % (409 ppbv). S1 and S2 lead to a small increase towards higher values (504 and 500 ppbv). A similar trend is reflected for peroxy acetic acid (PAA): an increase from higher (R: 0.246 ppbv) to lower NO_x (S1: 0.347 ppbv), whereas the observations are overestimated (0.206 ppbv).

Formaldehyde. The reference simulation overpredicts ambient HCHO by a factor of 3.4 (Obs.: 0.465 ppbv, R: 1.580 ppbv). The model reacts to the decrease in NO_x with a slight drop of 8 % in the simulated levels as reflected in the daytime averages (S1: 1.460 ppbv). Note that the NO_x emissions were cut by 50 %, which should have a more significant impact since NO is positively correlated with photochemically produced HCHO. As for H_2O_2, the sensitivity to a decrease of NO_x emissions is rather low. Increasing the deposition velocity of HCHO (S2, 1.150 cm s^{-1}) leads to an insignificant response of solely 3 % (or 0.05 ppbv) as well (S2: 1.410 ppbv). However, the absolute differences between R and S2 indicate a dependency of the chemical regimes as observed for H_2O_2: 3 ± 4 pptv for the clean conditions and 162 ± 112 pptv and 219 ± 169 pptv for the two biomass burning series in average.

NO and NO_2. It is recalled that the reference simulation overestimates the measured NO_x by 40 % (Obs.: 0.372 ppbv, R: 0.518 ppbv). A decrease of anthropogenic and biogenic emissions by 50 % (S1: 0.336 ppbv, S2: 0.337 ppbv) even results into levels below the observations (10 %). That means a drop by 54 % between R, S1 and S2, respectively. Surprisingly, the model reproduces the [NO] to [NO_2] ratio reasonably well. In contrast, the ratio of [H_2O_2] to [HNO_3] – a measure for the removal of HO_x and NO_x – is widely overpredicted: the observations result in 3.64, whereas the simulations increase in the order R (6.14), S1 (11.6) and S2 (12.3). This emphasizes the imbalance of the deposition velocities.

OH and HO_2. The reference simulation overestimates the observed OH (0.04 pptv) by a factor of 3 (R: 0.097 pptv). The decrease of NO_x leads to a drop of 26 % (0.072 pptv). S2 shows an additional insignificant effect of only −3 % (0.07 pptv). These results can be explained by the fact that OH reactants, such as versatile BVOCs were not included in the simulations. As shown in Section 3.2, OH accounts for almost 50 % of the H_2O_2 and about 35 % of the HCHO photochemical loss rates. Consequently, the overprediction has highly likely a deep impact on H_2O_2 and HCHO, whereas those species are still overpredicted. In contrast, the reference simulation underpredicts HO_2 by ca. 35 % (Obs.: average of 32 pptv and median of 20 pptv, R: 13.0 pptv). Lower ambient NO_x results in an insignificant change of −6 % for S1 (12.2 pptv) and a further decrease of 2 % from S1 to S2 (11.9 pptv). Contrary to the [NO] to [NO_2], the [HO_2] to [OH] ratio is not simulated reasonably well. The observations result in ca. 800, whereas the modeled values increase by the order: R (134), S1 (169) and S2 (170). However, as expected, the decrease of NO_x shifts the ratio towards higher values.

Life times of H_2O_2 and HCHO concerning photochemical losses Table 3.19 supports discussing the way the overpredicted H_2O_2 and HCHO manifest in the corresponding mean photochemical life times $\tau_{H_2O_2}$ and τ_{HCHO} during the day. Those are determined by the rate coefficient of the reaction with OH multiplied by its mixing ratio and the photolysis rate, whereas in the case of HCHO both channels – the radical and the molecular – were considered (see table footnotes). Note that the calculation is independent from the H_2O_2 and HCHO mixing ratios, thus the discussion is not correlated to the significant deviations between the model and the measurements. In the case of H_2O_2 the observations show the shortest life time (1.4 d) followed by the reference simulation with 1.8 d, which means a prolongation of 29 %. Since the decrease of the NO_x emissions (S1) have a reducing effect on the OH mixing ratio, $\tau_{H_2O_2}$ increases to 2.2 d (57 % relative to the observations). Then the doubled H_2O_2 deposition velocity (S2) has an insignificant impact on the life time (2.3 d or 64 %). This result reflects the high relevance of the H_2O_2 photolysis rate (j(H_2O_2)) which is underpredicted by ca. 26 % as shown before. Regarding HCHO, the observed life time is about 4.9 h, whereas the reference simulation shows evidence for a prolongation of 18 %. Then S1 and S2 lead to increased values about 6.5 h and 6.6 h due to the significant decreases of OH. As in the case of H_2O_2, this result reflects the high relevance of the HCHO photolysis rate (j(HCHO)): an underprediction by ca. 4.9 % leads to significant life time prolongations.

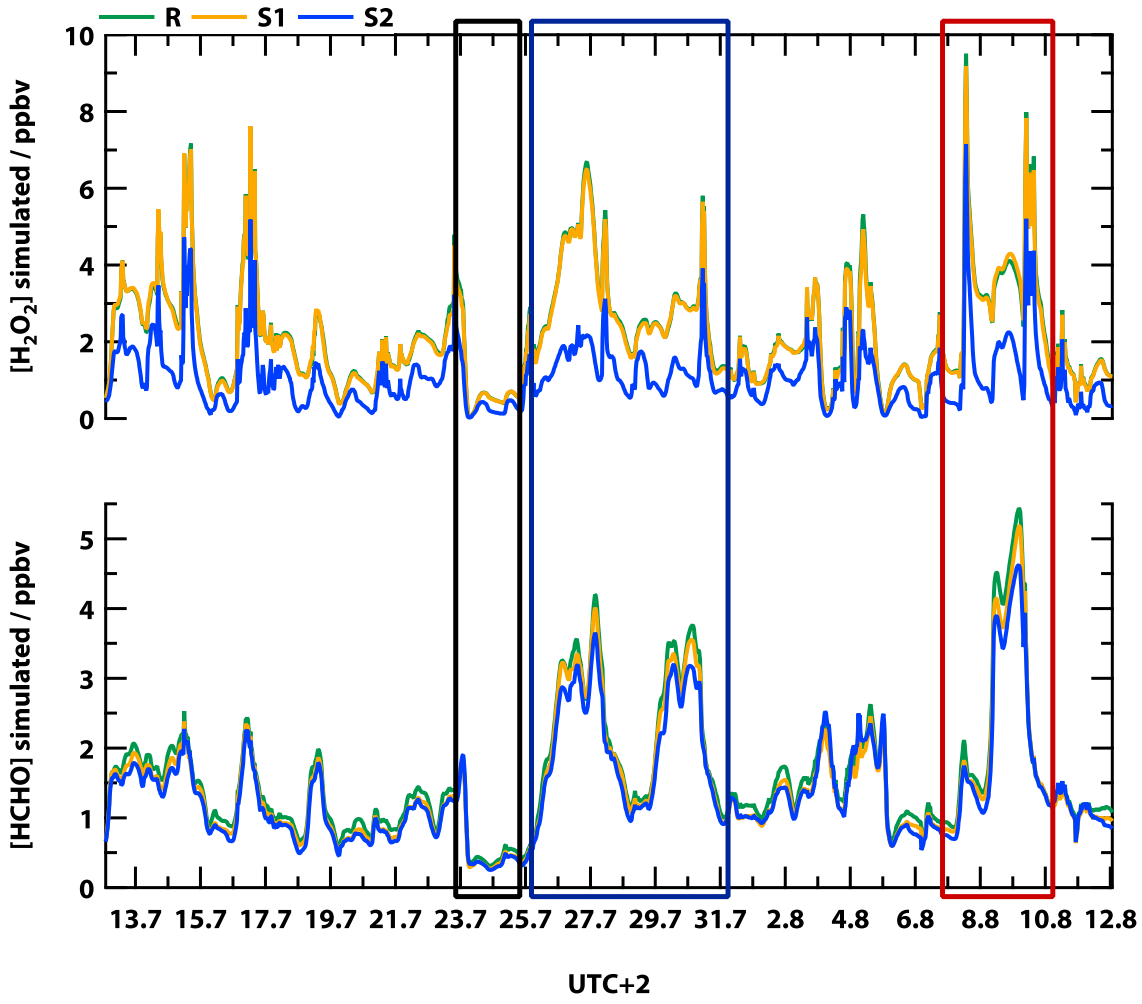

Figure 3.34.: Time series of simulated H_2O_2 and HCHO for R, S1 and S2. Clean conditions are highlighted in black, the two biomass burning series in dark blue and red. Mixing ratios decrease by the order of R, S1 and S2 for both species, whereas the shape remains unchanged. The decrease of ambient NO_x (S1) has a minimal effect on H_2O_2 and HCHO. Doubling the deposition velocities (S2) leads to a significant drop in H_2O_2, which is less pronounced for HCHO.

Table 3.18.: Comparison of mean daytime mixing ratios and deposition parameters for the measurements and the model simulation.

Species	Unit	Measurements	Reference (R)	Simulation (S1)	Simulation (S2)
O_3–NO_x–PAN					
$j(NO_2)$	s^{-1}	0.004 ± 0.003	0.004 ± 0.002	0.004 ± 0.002	0.004 ± 0.002
$[NO_2]$	ppbv	0.331 ± 0.203	0.469 ± 0.257	0.300 ± 0.147	0.301 ± 0.147
[NO]	ppbv	0.0410 ± 0.0340	0.0490 ± 0.0240	0.0360 ± 0.0180	0.0360 ± 0.0180
$[O_3]$	ppbv	43.1 ± 10.8	54.1 ± 12.1	47.20 ± 9.01	47.10 ± 8.93
[PAN]	ppbv	0.241 ± 0.126	0.352 ± 0.159	0.259 ± 0.111	0.257 ± 0.110
Radicals					
[OH]	pptv	0.0400 ± 0.0300	0.0970 ± 0.0730	0.0720 ± 0.0550	0.0700 ± 0.0540
$[HO_2]$	pptv	32 ± 90[a]	13.00 ± 6.56	12.20 ± 6.11	11.90 ± 5.95
Hydroperoxides and Formaldehyde					
$[H_2O_2]$	ppbv	0.639 ± 0.648	2.59 ± 1.48	2.55 ± 1.47	1.440 ± 0.910
[MHP]	ppbv	0.435 ± 0.405[b]	0.409 ± 0.131	0.504 ± 0.177	0.500 ± 0.174
[PAA]	ppbv	0.206 ± 0.230	0.246 ± 0.152	0.347 ± 0.241	0.345 ± 0.239
[HCHO]	ppbv	0.465 ± 0.558	1.580 ± 0.789	1.460 ± 0.761	1.410 ± 0.712
Deposition					
$V_d(H_2O_2)$	cm s^{-1}	5.08 ± 1.87[b]	0.656 ± 0.256	0.638 ± 0.243	1.280 ± 0.486
V_d(HCHO)	cm s^{-1}	24.200 ± 0.940[b]	0.594 ± 0.262	0.573 ± 0.245	1.150 ± 0.490
$[H_2O_2][HNO_3]^{-1}$	—	3.64[c]	6.14 ± 7.65	11.6 ± 15.4	12.3 ± 17.6

[a] In this case, a median value of 20.0 pptv is more reliable (see Section 3.2).

[b] Calculated values according to Section 3.2.

[c] HNO_3 value is of different time resolution (Williams et al., 2011).

Table 3.19.: Mean life time of simulated and measured H_2O_2 and HCHO during the day. The deviation is given by $(\tau_{mod.} - \tau_{obs.})\ \tau_{obs.}^{-1}$.

	$\tau_{H_2O_2}$[a]	Deviation / %	τ_{HCHO}[b]	Deviation / %
Observations	1.4 d	—	4.9 h	—
R	1.8 d	29	5.8 h	18
S1	2.2 d	57	6.5 h	33
S2	2.3 d	64	6.6 h	35

[a] $\tau_{H_2O_2} = \dfrac{1}{k_{H_2O_2+OH}[OH] + j(H_2O_2)}$

[b] $\tau_{HCHO} = \dfrac{1}{k_{HCHO+OH}[OH] + j(HCHO)}$

3.3.5.2. Scatter plots and linear regression parameters for selected trace chemical species.

The previous section suggests that optimizing the modeled NO_x towards observed levels is insufficient to explain the surplus amounts of H_2O_2 and HCHO. On the contrary, a further increase of the deposition velocities might explain these surplus amounts, as the initial values were most likely inaccurate. Figure 3.35 and Table 3.20 shall give a deeper insight into the possible causes by presenting the correlation plots as well as the linear regression parameters. Those include the coefficient of determination (r^2), the intercept a and the slope b. In addition, $a\ (\bar{x}_{\text{mod.}})^{-1}$ is a simple quantification for the offset. Note that Table 3.20 includes only H_2O_2 and HCHO since the decrease of their deposition rates has no significant impact on the related species.

Hydrogen peroxide and formaldehyde. For the reference simulation, H_2O_2 shows a low r^2 (0.19) with a relatively large offset of 69 % (1.78 ppbv) of the modeled daytime average. Note that the observed level is ca. 2.8 times smaller. However, the slope is quite close to unity (0.901). Lower ambient NO_x (S1) leads to insignificant changes ($r^2 = 0.2$, $a = 1.72$ ppbv and $b = 0.928$). Eventually, increasing the deposition velocity (S2) aggravates the coefficient of determination (0.12). However, the offset significantly decreases (1.05 ppbv), whereas the ratio to the daytime average changes minimally (73 %). In addition, S2 has a deep impact on the slope (0.446). In the case of HCHO, R shows a reasonable determination towards the observations (0.64) with a slope very close to unity (1.09). As for H_2O_2, the simulation shows a high offset (1.02 ppbv, 65 % of the modeled daytime average) which is ca. 2.2 times larger in comparison to the observations. The decrease of NO_x (S1) leads to a slightly lower intercept (0.933 ppbv, 64 %) accompanied by insignificant changes of the determination coefficient (0.64) and slope (1.04). Interestingly, the doubled deposition velocity (S2) has almost no impact on the daytime regression parameters ($r^2 = 0.61$, $a = 0.929$ ppbv and $b = 0.955$).

Ozone and nitric oxides. The reference simulation reproduces O_3 reasonably well ($r^2 = 0.41$) with a low offset of 33 % (17.6 ppbv) of the simulated daytime average. The slope is quite high (0.765). Decreasing NO_x emissions (S1) does not effect the coefficient of determination (0.43), whereas the intercept increases to 19.3 ppbv (41 % of the daytime mean). The slope significantly decreases to 0.584. In case of to the simulated NO_x for R, the determination coefficient is rather low ($r^2 = 0.12$) with a relatively high offset value (0.352 ppbv, 68 %) and a slope of 0.628. Reducing the NO_x emissions by half (S1) leads to a significant decrease in the intercept (23.4 pptv or 7 % of the modeled daytime average), whereas the coefficient of determination remains unchanged (0.13). In this case, the slope drops by 50 % to 0.383. In contrast to the simulations of ambient NO_x, the ratio of [NO] to [NO_2] indicates a reasonable cycling of the NO_x. For the reference simulation, the coefficient of determination is rather high ($r^2 = 0.57$) with a relatively low offset (0.0448 or 33 % of the modeled daytime average). The slope is 0.627. Interestingly, the decrease of NO_x emission has no significant impact on the discussed parameters: a determination coefficient of $r^2 = 0.57$, 36 % of relative offset and a slope of 0.658.

Hydroxyl and hydroperoxyl radicals. Noteworthy for the discussion of OH and HO_2 is that the experimental data only covers a few days, whereas the other herein presented species are based on

high instrumental duty cycles (see sections 3.1 and 3.2). This may have an impact on the statistical robustness. Hence, daytime OH shows evidence for a low determination coefficient (r^2 = 0.15) accompanied by a relatively high offset of 0.0477 pptv (49 % of the simulated daytime level) in case of the reference simulation. However, the slope is fairly high (0.890). Lower NO_x (S1) does not affect r^2 (0.14), but definitely the offset (0.0346 pptv, 40 % of the simulated daytime mean) and the slope (0.653). Hydroperoxyl radicals show the lowest coefficient of determination (r^2 = 0.076) and a relatively high intercept of 10.0 pptv (77 %) for R. Due to this fact the regression line is almost tilted (0.0492). The decrease of NO_x (S1) has no significant impact on the parameters: a determination coefficient of r^2 = 0.078, 77 % of relative offset and a slope of 0.0462. In contrast, the [OH] to [HO_2] shows a slightly different trend. For R the determination coefficient of 0.19 is not as low as for HO_2 and the slope is rather high 0.711. Nevertheless the intercept given as a fraction of the simulated daytime average is significant (74 %). The change in NO_x (S1) leads to no striking difference in r^2 (0.15) and the relative offset (76 %), whereas the slope significantly decreases (0.5357).

Table 3.20.: Determination and linear regression coefficients for selected trace gas species of the reference (R) and sensitivity simulations (S1 and S2) versus the observations during daytime. Given are the coefficient of determination (r^2) and intercept a (including the absolute and relative 1σ uncertainty Δa) in the corresponding unit for Figure 3.35.

Species	Unit	r^2	a	$a\ (\bar{x}_{\text{mod.}})^{-1}$ / %	Δa / %	b	Δb / %
Reference Simulation R							
[H_2O_2]	ppbv	0.19	1.78	69	8.2	0.901	14
[HCHO]	ppbv	0.64	1.02	65	3.9	1.09	4.6
[O_3]	ppbv	0.41	17.6	33	12	0.765	5.9
[NO_x]	ppbv	0.12	0.352	68	7.7	0.628	14
[OH]	pptv	0.15	0.0477	49	22	0.890	28
[HO_2]	pptv	0.076	10.0	77	8.9	0.0492	44
$[OH][HO_2]^{-1}$	—	0.19	0.004 80	74	9.8	0.711	27
$[NO][NO_2]^{-1}$	—	0.57	0.0448	33	11	0.627	4.2
Sensitivity Simulation S1							
[H_2O_2]	ppbv	0.20	1.72	68	8.4	0.928	13
[HCHO]	ppbv	0.64	0.933	64	4.1	1.04	4.7
[O_3]	ppbv	0.43	19.3	41	8.3	0.584	5.7
[NO_x]	ppbv	0.13	0.0234	7.0	66	0.383	13
[OH]	pptv	0.14	0.0346	40	23	0.653	29
[HO_2]	pptv	0.078	9.36	77	8.4	0.0462	43
$[OH][HO_2]^{-1}$	—	0.15	0.003 86	76	10	0.537	31
$[NO][NO_2]^{-1}$	—	0.57	0.0534	36	9.4	0.658	4.3
Sensitivity Simulation S2							
[H_2O_2]	ppbv	0.12	1.05	73	9.1	0.446	18
[HCHO]	ppbv	0.61	0.929	66	4.0	0.955	4.9

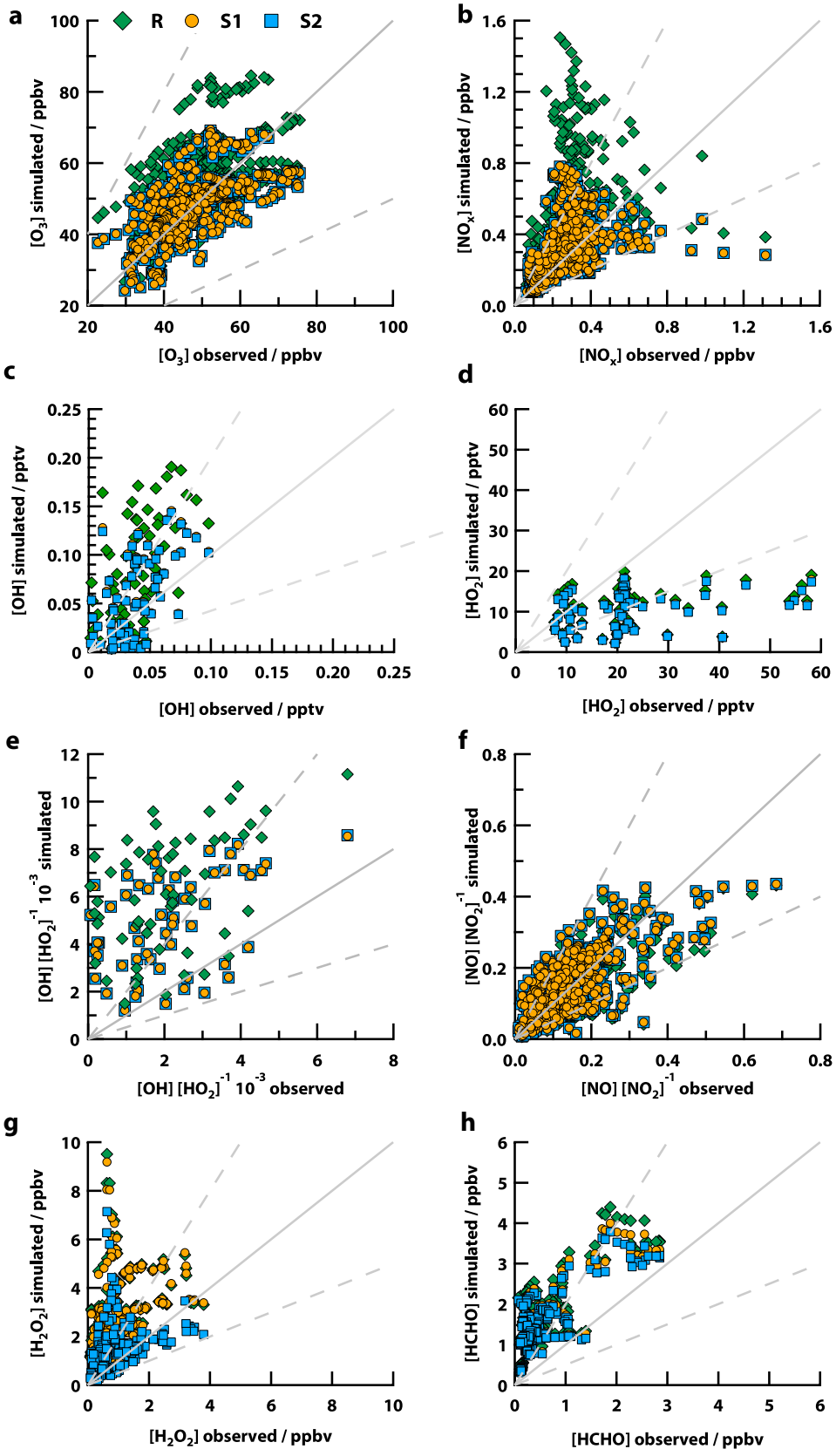

Figure 3.35.: Daytime correlation plots of simulated versus observed O_x, NO_x, H_2O_2 and HCHO for the reference (R) and sensitivity simulations (S1 and S2). Mixing ratios of O_3 ([O_3] in ppbv) (**a**), NO_x ([NO_x] in ppbv) (**b**), OH ([OH] in pptv) (**c**), HO_2 ([HO_2] in pptv) (**d**) as well as the [OH] to [HO_2] (**e**) and [NO] to [NO_2] ratio (**f**) are shown. The bottom part includes H_2O_2 ([H_2O_2] in ppbv) (**g**) and HCHO ([HCHO] in ppbv) (**h**). Grey lines represent unity, whereas dashed depict the 0.5 and 2 slopes, respectively.

3.3.6. Biomass burning events

The combustion of vegetation, in the following biomass burning, is caused by natural (lightning) or human-induced fires (land-clearing) processes. Biomass burning is characterized by significant emissions of particulate matter (aerosols) and gaseous compounds into the troposphere mainly consisting of CO_2, CO, NO_x, CH_4 and partly oxidized volatile organic compounds (oVOCs). Besides, the direct impact on burning areas, emission plumes affect their vicinity (regional impact) and can even have an intercontinental effect (long-range impact) depending on the chemical life time and physical removal of the trace constituents. The impact of biomass burning on the budgets of tropospheric O_3 and other trace chemical species is significant and also human health is affected (Jaffe, 2004; WHO).

The burning process can be divided into three different steps: (i) ignition, (ii) flaming and (iii) smoldering. During the ignition, leaves, needles and twigs are set on fire, whereas the emission potential for VOCs with low vapour pressure is very high. Once the fuel is sufficiently dry, the flaming temperature can range from 600 to 900 K (Chandler, 1983) which sustains the oxidation of cellulose and hemicellulose (50 to 65 %), lignin (16 to 35 %), other extracellular compounds (0.2 to 15 %) and trace minerals. This phase emits the highest amounts of oVOCs such as HCHO and higher aldehydes.

Model studies focusing on the annual European average of tropospheric CO conclude that 16 % (25 ppbv of 155 ppbv) are caused by biomass burning, whereas the fraction is 21 % on a global scale (18 ppbv of 87 ppbv) (Innes et al., 2000). Note that in comparison, the major amount of CO is caused by anthropogenic emissions. The simulated impact on ambient mixing ratios of total NO_x in Europe with and without biomass burning accounts for 2 %, which is insignificant (870 pptv vs. 855 pptv). Once again, emissions due to human activities dominate (Innes et al., 2000). However, biomass burning has a significant impact of 13 % on the global NO_x (170 pptv vs. 150 pptv). The total tropospheric O_3 in Europe increases rather insignificantly by 4 % with and without biomass burning (30.5 ppbv vs. 29.2 ppbv), whereas the global impact accounts for 7 % (20.8 ppbv vs. 19.4 ppbv, Innes et al., 2000). However, the modeled OH concentrations in Europe decrease by 2.2 % including biomass burning (5.79×10^5 cm^{-3} vs. 5.92×10^5 cm^{-3}), whereas the global trend is decreasing by 3 % (7.03×10^5 cm^{-3} vs. 6.82×10^5 cm^{-3}). Finally, SO_2 emissions due to biomass burning are rather insignificant by contributing solely 4 % to the global total (Seinfeld and Pandis, 2006). Do not forget emissions of organic halogen compounds causing global ppt-levels in the troposphere (e. g., CH_3Cl, 500 pptv and CH_3Br, 10 pptv) (Seinfeld and Pandis, 2006). They affect the tropospheric OH.

The correlations of HCHO with CO are excellent, providing strong evidence for the direct production of HCHO from biomass burning. H_2O_2 and CH_3OOH (MHP) moderately correlate with CO (North America) (Lee et al., 1997). The production of HO_2 radicals from H_2O_2 and HCHO oxidation by OH was significant compared to that from CO (Lee et al., 1998a). oVOCs account for the RO_x budget and therefore influence the O_3 production (Yokelson et al., 1999). Biomass burning was also shown to increase H_2O_2, CH_3OOH, and CH_2O mixing ratios up to 1.5, 2, and 1 ppbv, respectively, even after 4–5 days of transit (Snow et al., 2007).

The Russian biomass burning series of the year 2010 from a Finish perspective. The exceptionally warm summer of 2010 is a good proxy for the behaviour with global warming. Two case studies on the impact of polluted air masses from Russian biomass burning plumes on Finland were published (Mielonen et al., 2012; Portin et al., 2012). The first is based on in-situ aerosol and trace gas measurements at the east Finish station Puijo (62°54′ N, 27°39′ E, 306 m a. s. l.; ca. 275 km in the north-east of Hyytiälä) which is located in a semi-urban part of the city of Kuopio (97,000 inhabitants). The second study focuses on remote sensing by employing a state-of-the-art LIDAR technology aiming to determining the entrainment depth of the plumes in Kuopio. Both studies validate the data sets on a spacial and temporal scale by comparison with backtrajectory simulations. The transport from Russia to eastern Finland spread over approximately 1000 km and took 1 to 2 d.

As a result, the pollution series could be clearly identified via in-situ observations and remote sensing for two days: Jul 27 and Aug 8 2010. The aerosol diameter is at least as twice as big compared to background conditions. CO showed significant increases. Unexpectedly, O_3 and NO_x were barely affected. However, the two series show significant differences in the aerosol composition and the entrainment depth: on Jul 27 the plume was located at a height of ca. 2 km, whereas on Aug 8 it formed two layers – one between 1 and 2 km and another between 2.5 and 4 km (Mielonen et al., 2012). Note that the herein presented PBL heights reach maximum values of ca. 2 km.

The performance of the EMAC model for the biomass burning events on Jul 27 and Aug 8. Table 3.21 compares Jul 27 and Aug 8 2010 to the background conditions of the whole campaign. The series were selected by 48 h backtrajectory calculations as well as increases in the mixing ratios of CO. The relative behaviour in the table is defined as $R = 100 \cdot \left([X]_{BB} - [X]_{Backgr.}\right) \cdot [X]^{-1}_{Backgr.}$.

Starting with O_3, the observations show a background level of 40.9 ppbv, whereas the studied days showed 45.6 ppbv (Jul 27) and 48.2 ppbv (Aug 8), respectively, indicating enhanced levels (12 and 18 %). The S1 simulation is comparable with 40.8 ppbv for the background, 48.8 ppbv for Jul 27 and 51.8 ppbv for Aug 8. Those are higher by 20 and 27 %. Interestingly, the NO_x observations are insignificantly affected on the Jul 27 series (0.368 ppbv) compared to the background (0.381 ppbv). In contrast, the plume of Aug 8 shows a significant impact of 27 % (0.485 ppbv). In both cases NO_2 follows that trend. In contrast, NO decreases slightly in both cases (−6.4 %). For the model, NO_x is significantly enhanced during both series: by 8.4 % (0.455 ppbv) on Jul 27 and by 32 % (0.552 ppbv) compared to the unpolluted days (0.420 ppbv). For nitric oxide, the simulation shows background conditions (33.9 pptv) on Jul 27 (35.7 pptv), whereas it is significantly elevated on Aug 8 (47.9 pptv). On both days, the modeled NO_2 levels are elevated (27 and 55 %). As expected, the observed CO mixing ratio shows a significant increase on Jul 27 (146 ppbv, 46 %) compared to the background (99.7 ppbv). On Aug 8, the relative impact is almost double (191 ppbv, 92 %). Oppositely, the biomass burning events have less impact for the model simulation: on Jul 27 the CO level is 30 % (159 ppbv), on Aug 8 it is 44 % (176 ppbv) higher than the background (122 ppbv). Switching to H_2O_2, the observed background conditions show mixing ratios about 0.572 ppbv, which are enhanced by 32 % (0.752 ppbv) on Jul 27. On the other hand, levels of 0.433 ppbv – a value 24 % below the background – are measured for the series of Aug 8. However, the model simulation behaves differently. The average background level of 1.76 ppbv is already significantly higher than the observations as dis-

cussed in previous sections. The plume on Jul 27 leads hereby to a high increase of 72 % (3.0 ppbv), which is more than double the observed relative change. Following the opposite trend, the model even further increases the H_2O_2 levels to 3.96 ppbv (125 % the background) on Aug 7. Note that this disagreement could be explained by clouds and wet deposition in range of the life time for H_2O_2 around the SMEAR II site. Focusing on HCHO, the observed levels are rather small (0.254 ppbv). The plume on Jul 27 has a crucial impact of 325 % on the ambient mixing ratios (1.08 ppbv). In comparison, the plume of Aug 8 shows less pronounced but significant values (0.729 ppbv, 187 % above the background). Similarly to H_2O_2, the model shows an offset for the background leading to values of 1.16 ppbv. For the first biomass burning series (Jul 27) the relative model sensitivity is less pronounced (91 % leading to 2.2 ppbv) than observed. On Aug 8, the impact is even higher (2.75 ppbv or 137 % compared to the background). Note that HCHO may be impacted by cloud formations and wet deposition as previously discussed. For discussing OH and HO_2, note that their levels for the background as well as on Jul 27 are based on the calculations presented in Section 3.2 due to lacking data coverage. However, the first biomass burning event has no significant impact on OH (1.85×10^6 cm^{-3} vs. 1.87 cm^{-3}, 1.1 % above the background). The mixing ratio for HO_2 is more pronounced: on Jul 27 the level (18.1 pptv) is 28 % higher than for background conditions (14.1 pptv). The second plume on Aug 8 shows a more pronounced picture. OH and HO_2 increase to 3.79 cm^{-3} (105 %) and 37.1 pptv (163 %), respectively. The model simulation slightly underestimated the background levels leading to values of 1.73 cm^{-3} for OH and 11.2 pptv for HO_2. The first plume on Jul 27 shows significant relative model responses of 19 % (2.05 cm^{-3}) and 35 % (15.1 pptv), respectively. In contrast to the observations, the trend on Aug 8 is the opposite due to a decrease of 16 % (1.45 cm^{-3}) for OH. Similarly, HO_2 shows less pronounced levels of 13.6 pptv (21 % above the simulated background).

Finally, for putting these results into more context, the 48 h backtrajectories for the series on Jul 27 indicate a complex composition of the air masses originating from the North (unpolluted), Central Europe (anthropogenic pollution) and Russia (biomass burning). On the contrary, air parcels during the event on Aug 8 emerged solely from Central Europe and Russia. Aerosol particles showed were smaller on Jul 27 and located below 2 km in Eastern Finland, whereas the plume on Aug 8 was dominated by "smoky" particulate matter (black carbon) consisting of layers: one between 1 and 2 km and the other between 2.5 and 4 km (Mielonen et al., 2012). The latter indicated a rather complex vertical distribution.

During the series on Jul 27, CO from the biomass burning plumes and Central Europe might have been mixed with Northern air, thus it is uncertain of which origin it came. In contrast, the plume on Aug 8 consists highly likely of CO from anthropogenic and biomass burning emissions. Note that the variation for the simulated CO is less pronounced as expected, since the GFED 3.1 data base delivers solely monthly averages and the extreme conditions of the biomass burning lasted for days and weeks. The observed NO_x shows an insignificant trend during Jul 27 and indicates aged air involving the lower levels of CO. Besides, the increasing O_3 levels are in good agreement with eastern Finish observations (Portin et al., 2012). Trends in observed and simulated O_3 are comparable as well as NO_x. However, the absolute NO mixing ratios show the opposite trend, especially during series on Aug 8. In the case of HCHO, two different trends are shown: the high levels on Jul 27 show evidence for secondary production and fast entrainment of the low air masses. The plume

on Aug 8 is rather "fresh" and shows lower levels, since it is higher located and the air is less aged. The relative increase of H_2O_2 on Jul 27 is in the orders of HO_2 increase, whereas the OH is minor affected. However, the series on Aug 8 shows a decrease in the H_2O_2 levels with an increase in both, HO_2 and OH. Including the high aerosol levels, heterogeneous losses are highly likely. Besides, the OH increases indicating a higher oxidation capacity.

Table 3.21.: Averages of trace gas observations during summer 2010 for Hyytiälä, the EMAC simulation and observations from eastern Finland. The table lists mixing ratios of important trace gases (O_3, NO_x, H_2O_2, HCHO and O_x) for the observations compared to the low NO_x EMAC simulation (S1).

		Hyytiälä (obs.)					Hyytiälä (mod., EMAC S1)				
	Unit	Backgr.	Jul 27	Rel.	Aug 8	Rel.	Backgr.	Jul 27	Rel.	Aug 8	Rel.
O_3	ppbv	40.9	45.6	12	48.2	18	40.8	48.8	20	51.8	27
NO_x	ppbv	0.381	0.368	-3.4	0.485	27	0.420	0.455	8.4	0.552	32
NO	pptv	29.6	27.7	-6.4	27.7	-6.4	33.9	35.7	5.3	47.9	41
NO_2	ppbv	0.351	0.340	-3.2	0.457	30	0.386	0.491	27	0.600	55
CO	ppbv	99.7	146	46	191	92	122	159.0	30	176	44
H_2O_2	ppbv	0.572	0.752	32	0.433	-24	1.76	3.0	72	3.96	125
HCHO	ppbv	0.254	1.08	325	0.729	187	1.16	2.2	91	2.75	137
OH	cm^{-3}	1.85E+06	1.87E+06	1.1	3.79E+06	105	1.73E+06	2.05E+06	19	1.45E+06	-16
HO_2	pptv	14.1	18.1	28	37.1	163	11.2	15.1	35	13.6	21

Event timing and downward transport of secondary HCHO during the biomass burning events. Figure 3.36 depicts the time series of the simulations R, S1 and S2 versus the observed CO and HCHO during the biomass burning series of Jul 27 and Aug 8. Note that CO is basically identical for all three simulations. Further, it is recalled that this work has proven that pure photochemistry is insufficient to explain the observed HCHO levels during the biomass burning series (see Figure 3.22, Section 3.2.7).

To begin with CO, the simulated plume from Jul 26 to 28 shows significantly higher peak levels (236 ppbv) in comparison to the observations (219 ppbv). A notable feature is the steep increase with a similar decrease of the levels in the model, although the absolute durations are in the same order (model: 58 h, observations: 59 h). The second part of the series (from Jul 28 12 a. m. to Jul 30 12 a. m.) shows modeled peak values of 167 ppbv, whereas the observations reached 437 ppbv during one event with a duration of ca. 12 h. However, in this case, the overall duration of the event does not match for the model (50 h) versus the observations (44 h). From Aug 7 to 10, the disagreement is even more significant. The model simulates maximum values of CO (238 ppbv) on Aug 9 with an event duration of 62 h. In contrast, the observed series is "sharper" (48 h) and the peak level is more pronounced (389 ppbv). This shows evidence for the (i) averaging effect of the emission inventory and partly a disagreement of the (ii) injection time and (iii) injection intensity for the simulation.

Switching to HCHO, note that the simulated time series for the reference (R), the low-NO_x (S1) and the increased deposition velocity (S2) simulations are similar as previously discussed. The simulated plume from Jul 26 to 28 shows peak values from 3.65 to 4.14 ppbv above the observations 2.85 ppbv. The observed peak is 14 h earlier, whereas the event duration is the same as for CO. However, the model qualitatively reproduces the main features. The second part of the event is characterized

by an observed HCHO peak level of 3.44 ppbv matching the maximum for CO. In contrast, the simulations only reproduce a plateau ranging from 3.17 to 3.76 ppbv. The absolute event durations also disagree (model: 48 h, observations: 43 h). From Aug 7 to 10, the simulated maximum levels range from 4.62 to 5.42 ppbv, whereas the observed peak value is 2.55 ppbv. Here, the time shift is about 11 h with a delay in the model. Interestingly, the modeled shape of the HCHO time series is comparable but "stretched", with a qualitative reproduction of the main features. Since the HCHO during those events is of secondary production, this indicates a reasonable reproduction of vertical transport within the model.

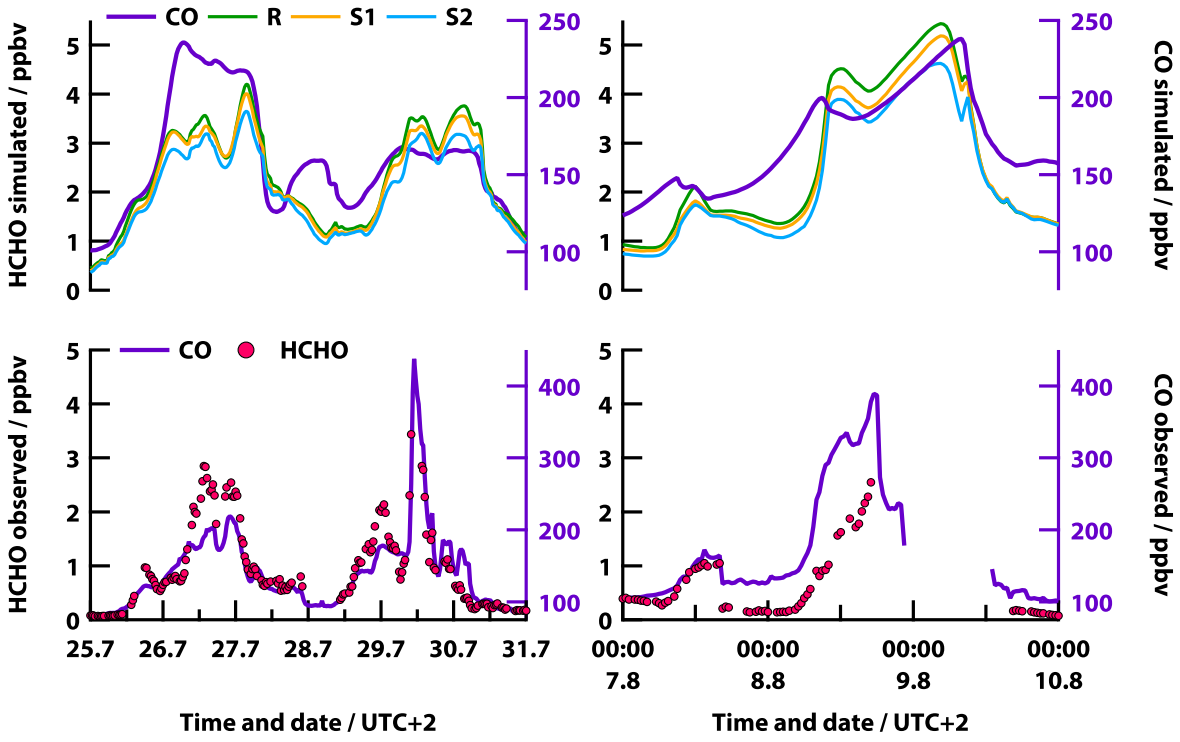

Figure 3.36.: Time series of the simulations versus the observed CO and HCHO on Jul 27 and Aug 8. Simulated data is presented on the two top, observations on the bottom graphs. The left column focuses on Jul 27, whereas the right depicts Aug 8. Please note the different scaling between the top and bottom graphs for CO.

3.3.7. Summary and conclusions

[1] Three model simulations (reference R and two sensitivity studies S1 and S2) were performed with the 3-D model EMAC[8] for the field measurement campaign HUMPPA from Jul 12 to Aug 12, 2010 in boreal Southern Finland (see sections 3.1 and 3.2). VOC chemistry was described by the MIM 1.1 mechanism, which includes basic hydrocarbon and extended isoprene oxidation pathways. Terpene reactions were excluded.

[2] The evaluation of NO_x led to use a vicinal box due to pollutant transport from the town Tampere for this resolution. As a result, the modeled and observed behaviors of NO_x roughly agreed.

[8] ECHAM5 base model with a horizontal resolution of about 1.1 x 1.1° (T106), 31 vertical levels up to 0.01 hPa, nudged meteorology to the ECMWF analysis, EDGAR-CIRCE global anthropogenic emission inventory, GFEDv3.1 biomass burning database

However, this raises the question how the meso-scale transport can be optimized to allow using of the "correct" model box.

[3] The large-scale meteorology and the transport of biomass burning plumes from Russia were reproduced reasonably well. The local meteorology and photolysis rates qualitatively agreed with the observations, whereas high offsets and low coefficients of determination were obtained for the temperature and the relative humidity. Modeled photolysis rates ($j(H_2O_2)$, j(HCHO), $j(NO_2)$ and $j(O^1D)$) fit very well ($r^2 > 0.77$) but underestimated the measured data by 15 % on average. Concerning local vertical transport, the model agreed with the observed downward transport of secondary HCHO from biomass burning plumes in the morning hours. This agrees with the qualitative prediction of downward transport of H_2O_2 from the free troposphere due to an increase in the marine boundary layer height (Fischer et al., 2015). Generally, in this study boundary layer heights were in reasonable orders of magnitude, whereas the daily trends hardly match with the observations. How this affects the vertical transport for O_3, NO_x, H_2O_2 and related species, especially in the morning hours, is an object of future research.

[4] As expected, the reference simulation indicated a good reproduction of long-lived trace chemical species (CO and CH_4) with expected deficits in radical chemistry due to lacking terpene chemistry: OH was overpredicted (by a factor of 2.5), whereas HO_2 was underestimated (by a factor of 2.5) with low correlations compared to the observations (r^2 = 0.15 and 0.076). H_2O_2 and HCHO levels exceeded the measured data by a factor of 4 and 3.4, respectively. The coefficients of determination were low for H_2O_2 (r^2 = 0.19) and high for HCHO (r^2 = 0.64). Finally, the modeled NO_x was still too high (40 %) with a low correlation (r^2 = 0.12). Unexpectedly, the NO_x cycling ([NO] to NO_2 ratio) agreed well (r^2 = 0.57). However, this raises the question whether excessive NO_x levels or underestimated sinks can explain the disagreement for H_2O_2 and HCHO.

[5] Thus two sensitivity simulations S1 (50 % NO_x emissions) and S2 (50 % NO_x emissions and double deposition velocities for H_2O_2 and HCHO) were performed. Both lead to a decrease of 10 % below the observed NO_x levels. The resulting effect was rather insignificant on the trends (coefficients of determination) and mixing ratios of the modeled species including H_2O_2 and HCHO. In contrast, simulation S2 showed a decrease of 44 % in H_2O_2 and 11 % in HCHO compared to R. The determination coefficients remained widely unchanged, whereas that for exceeded S2 the observations (2.2 times for H_2O_2 and 3-fold for HCHO). In contrast, the model underpredicted ambient H_2O_2 for the remote marine boundary layer due to an excessive dry deposition towards the ocean surface (Fischer et al., 2015; Klippel et al., 2011). As discussed earlier, in this study the modeled photolysis rates and deposition velocities are lower than observed. Section 3.2 has demonstrated the high deposition in the boreal forest. Future sensitivity studies using these values can reveal the cause for the high simulated H_2O_2 and HCHO levels. Particularly for HCHO further analysis of the emission inventory can then give a deeper insight on its low sensitivity to NO_x and dry deposition.

A. Appendix – Materials and methods

A.1. Typical time line and performed field measurement campaigns

Ambient mixing ratios of hydrogen peroxide and formaldehyde may be close to the limit of the detection (LOD) of the herein described instruments. In addition, the atmosphere possesses a large amount of versatile trace chemical species with mixing ratios ranging over several orders of magnitude, potentially causing instrumental interferences. This requires a validation under good laboratory practice conditions in the laboratory as well as during field measurement campaigns (e. g., air conditioning) to exclude as many unknown factors as possible. Therefore, every field study started with a preparation period of 2 to 4 weeks including packing and transport, followed by the campaign itself and follow-up tests for assuring the quality of the data (Figure A.1). Transports were always performed as a whole, with instruments already being mounted in the MPI white container. If the instruments were not used for a long time, the tubes were sealed with Parafilm and cleaned after the procedures described in the manuals (AL2; AL4). The usual warm-up time was several hours to 1 d.

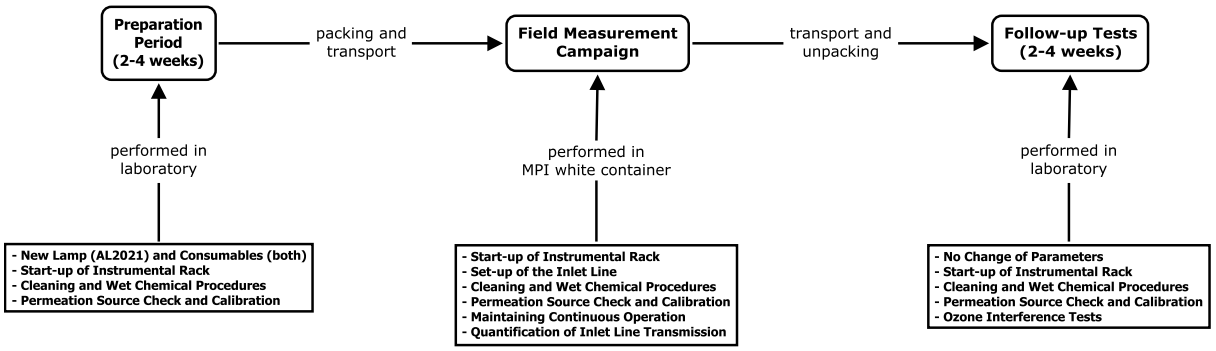

Figure A.1.: Concept map of laboratory and in-field procedures. Field measurement campaigns (**middle**) were accompanied by intense preparation (**left**) and post-processing (**right**) periods. Key activities are listed in the lower boxes. Main activities of the preparation in the laboratory comprise ordering spare parts, starting and cleaning the instruments and validating the gas-phase standards. Main goals during field measurement campaigns were to achieve high instrumental duty cycles accompanied by in-field data validation (in the MPI white container). Next to the field studies, interference tests were performed in the laboratory without changing the instrumental parameters.

For avoiding potential artifacts in the liquid chemistry, new chemicals were ordered and crucial compounds for the gas phase zeroing, such as silica gel and Hopcalite, were regenerated prior to each field measurement campaign. In addition, the instruments were equipped with new consumables, e. g., Ismaprene tubes (IDEX Health & Science GmbH, Wertheim, Germany) for the peristaltic pumps, air filters and (in case of the AL2021) a new Cadmium Pen-Ray® lamp. Besides, all air volume flows (of the instruments and the permeation sources) were weekly measured with a Gilibrator-2® wet bubble calibrator (Sensidyne, St. Petersburg, FL, USA).

A.2. Laboratory and in-field instrumental validation

A.2.1. Reagent and laboratory equipment certification

The reagent quality plays a crucial role for the background signals of the AL2021 and AL4041 (AL2; AL4). Thus, only analytical grade chemicals were used as listed in Table A.1. For excluding artifacts new chemicals were ordered prior to each field measurement campaign. One exception is the acetylacetone for preparing the Hantzsch solution. The background signal highly depends on the purity and even on the supplier of the acetylacetone, which was previously validated by LC-MS (Stickler, 2006), with the supplier VWR® showing the best results.

The same equipment (tubes, fittings and laboratory ware) was used for both, laboratory studies and field measurement campaigns. That stipulates three major requirements: avoidance of artifacts or wall effects, as much as possible, easy transport (e. g., PTFE/PFA instead of glass burettes) and chemical stability towards oxidizing compounds (e. g., H_2SO_4 and $TiCl_4$).

Table A.1.: List of chemicals for laboratory and field campaign use.

Reagent	Grade	Producer/Distributor	Article number	Packaging size
Acetic acid kit for 1 N	p. a.	VWR®/Merck	1.09951.0001	ampoule
Acetylacetone	p. a.	VWR®/Merck	20092.230	250 mL
Ammonium acetate	p. a.	VWR®/Merck	21200.297	1 kg
Boric acid	p. a.	VWR®/Merck	1.00165.0100	100 g
Catalase	Ph. Eur.	Sigma-Aldrich	C100-50MG	2 mL
Chromotropic acid	p. a.	—	—	—
EDTA 99 %	p. a.	Carl Roth	8043.3	100 g
Formaldehyde 37 %	p. a.	Carl Roth	4979.1	1 L
Glacial acetic acid 100 %	p. a.	VWR®/Merck	1.00063.1000	1 L
Hydrochloric acid 1 N	p. a.	VWR®/Merck	1.09057.1000	1 L
Hydrochloric acid, concentrated	—	Fischer Chemical	H/1100/PB15	1 L
Hydrogen peroxide 30 %	p. a.	Carl Roth	8070.2	250 mL
Iodine solution kit for 0.1 N	—	VWR®/Merck	1.09910.0001	ampoule
Peroxidase Type IV	Ph. Eur.	Sigma-Aldrich	P8375-100KU	390.6 mg
p-Hydroxyphenylacetic acid 98 %	—	Acros Organics	121710250	25 g
Potassium hydrogen phthalate 99.8 %	p. a.	Carl Roth	P750.1	500 g
Potassium permanganate kit for 0.002 M	—	VWR®/Merck	1.09930.0001	ampoule
Sodium carbonate	p. a.	Fischer Chemical	S/2920/53	500 g
Sodium hydroxide solution 1 N	p. a.	Fischer Chemical	J/7620/17	2.5 L
Sodium sulfite, anhydrous	p. a.	Fischer Chemical	0316.0250	250 g
Starch, soluble	Ph. Eur.	Acros Organics	424491000	100 g
Sulfuric acid 97 %, glass bottled	p. a.	Sigma-Aldrich	84720-1L-GL	1 L
Titanium tetrachloride	p. a.	Sigma-Aldrich	208566-200G	200 g
Ultrapure water	—	VWR®/Merck	1.16754.9010	10 L

A.2.2. Preparation of solutions and general laboratory procedures

Since the instruments are based on enzyme reactions and liquid organic chemistry the solutions and some chemicals alter with time. Cooling slows down that process and thus the standard stock

solutions and enzymes were always stored between 4 to 8 °C. Reagents for the AL2021 (hydroperoxide measurements) must be precooled for 6 to 12 h, while it is 12 to 24 in case of the AL4021. If not precooled, the background signal was too high or no fluorescence could be measured at all. Those data were neglected for the analysis as described in Chapter 2, Section 2.2.6.7).

Preparation of the AL2021 solutions. More details about the preparation of the solutions are given in AL4; Klippel (2010); Stickler (2006).

Potassium hydrogen phthalate (KHP) stock solution (5 L DURAN® bottle) 4.82 L of ultrapure water (Titripac®) was mixed with 1 M NaOH solution (180 mL). Then, EDTA (100 mg) and 37 % HCHO (1 mL) were added under rigorous stirring.

Fluorescent solution (2 L DURAN® bottle) 2 L of the KHP stock solution was directly transferred into a 2 L DURAN® bottle. POPHA (500 mg) and peroxidase (30 mg) were added under stirring.

Conditioner without catalase Approximately 1.4 L of KHP stock solution was directly transferred into a 2 L DURAN® bottle.

Catalase stock solution (200 mL volumetric flask) 1 mL was mixed with KHP stock solution and agitated.

Conditioner with catalase (1 L DURAN® bottle) 20 mL of catalase stock solution were mixed with KHP stock solution.

Stripping solution (5 L DURAN® bottle) 500 mL of KHP stock solution was diluted with ultrapure water (Titripac®) to 5 L. It was stored without cooling in a light-protected plastic barrel (CurTec Deutschland, Düsseldorf, Germany).

Potassium hydroxide (NaOH) solution (0.05 M, 2 L DURAN® bottle) 1 M NaOH (50 mL) was diluted with ultrapure water (Titripac®) to a volume of 2 L.

Preparation of the AL4021 solutions. More details about the preparation of the solutions are given in (AL4; Klippel, 2010; Stickler, 2006).

Stripping solution (0.05 M H_2SO_4, 5 L DURAN® bottle) Ultrapure water (5 L Titripac®) was mixed with concentrated H_2SO_4 (15 mL). The solution was stored in the refrigerator.

Hantzsch reagent solution (5 L DURAN® bottle) Ammonium acetate (154 g) was dissolved with stirring in ultrapure water (1.8 L Titripac®) and stored in the refrigerator (1). Meanwhile, ultrapure water (200 mL) was mixed with glacial acetic acid (5 mL) in a glass flask and stored as well in the refrigerator (2). Once cold, acetylacetone (4 mL) was added to (2) with stirring or agitation. The unified solutions (1) and (2) were kept cold at least 12 h before use.

B. Appendix – Overview on the observations

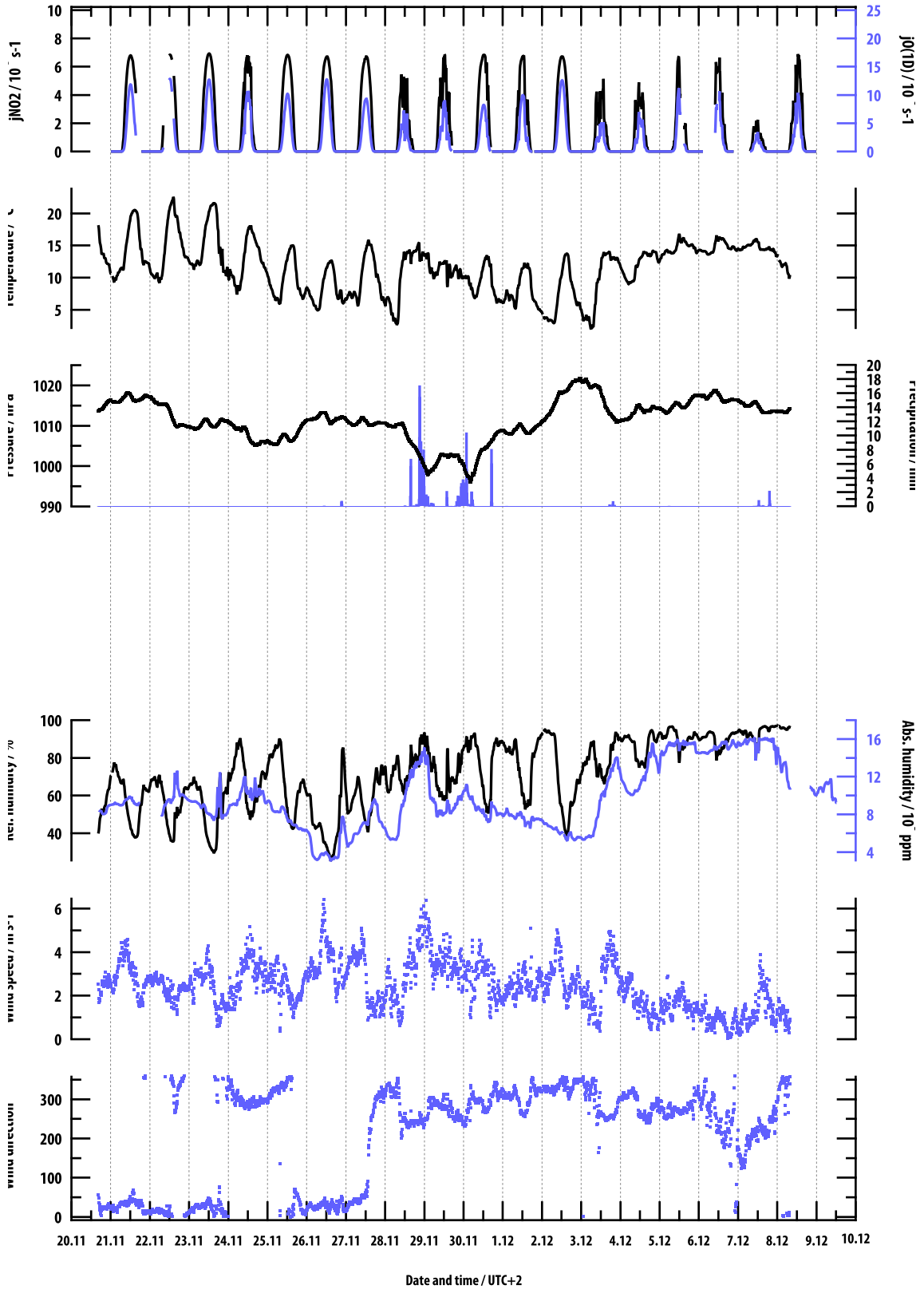

Figure B.1.: Time series of meteorological parameters for DOMINO.

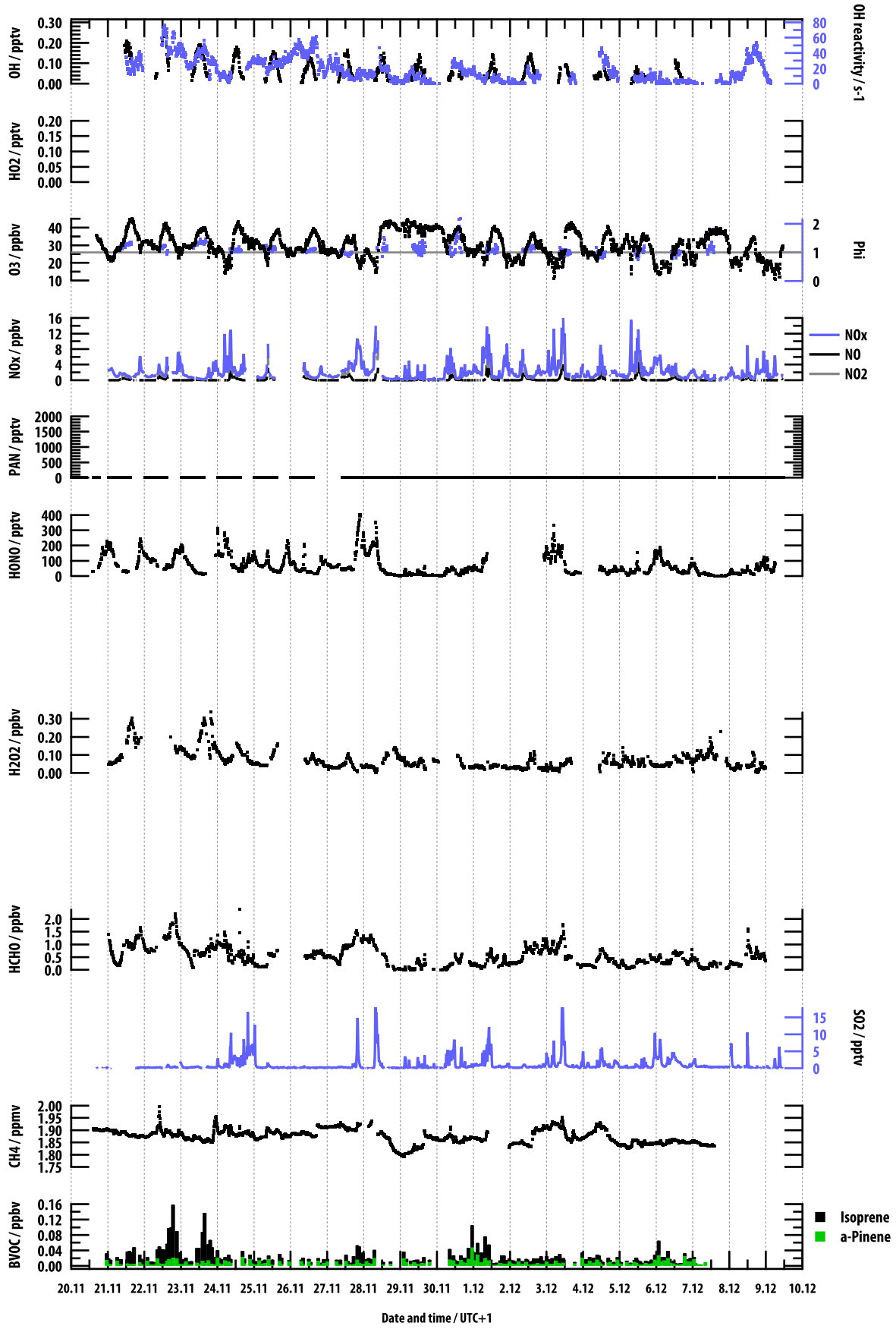

Figure B.2.: Time series of chemical trace gases and related parameters for DOMINO.

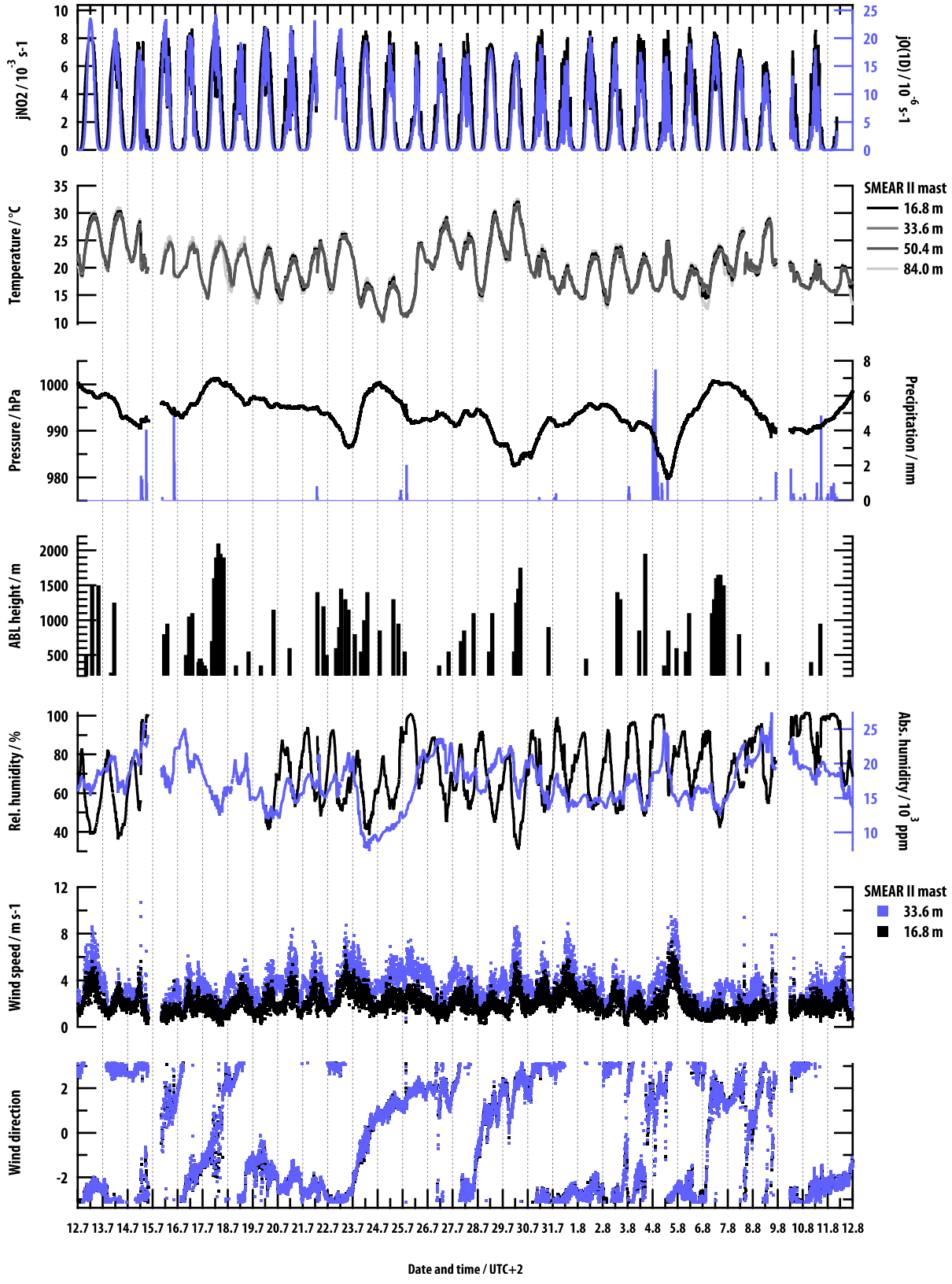

Figure B.3.: Time series of meteorological parameters for HUMPPA.

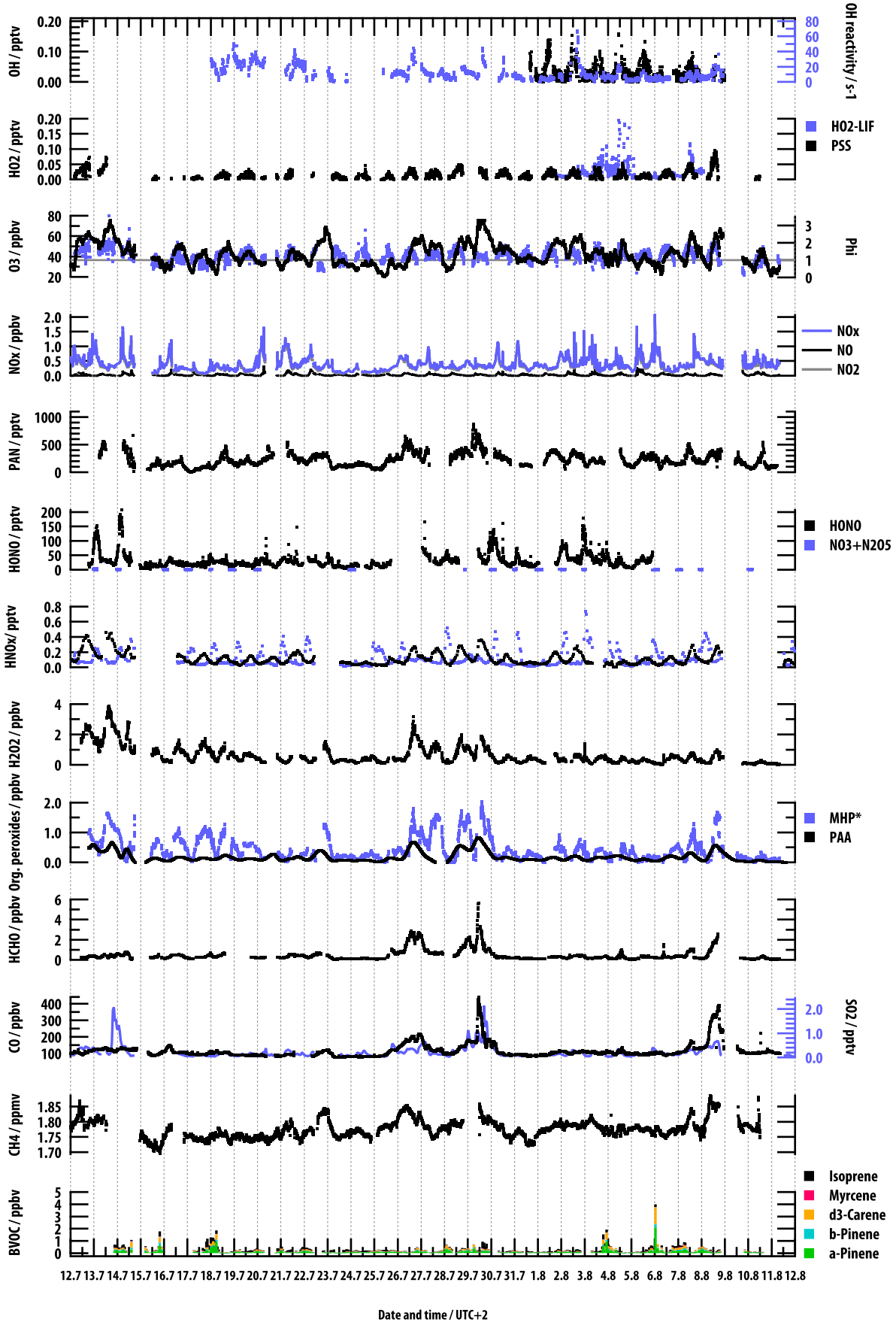

Figure B.4.: Time series of chemical trace gases and related parameters for HUMPPA.

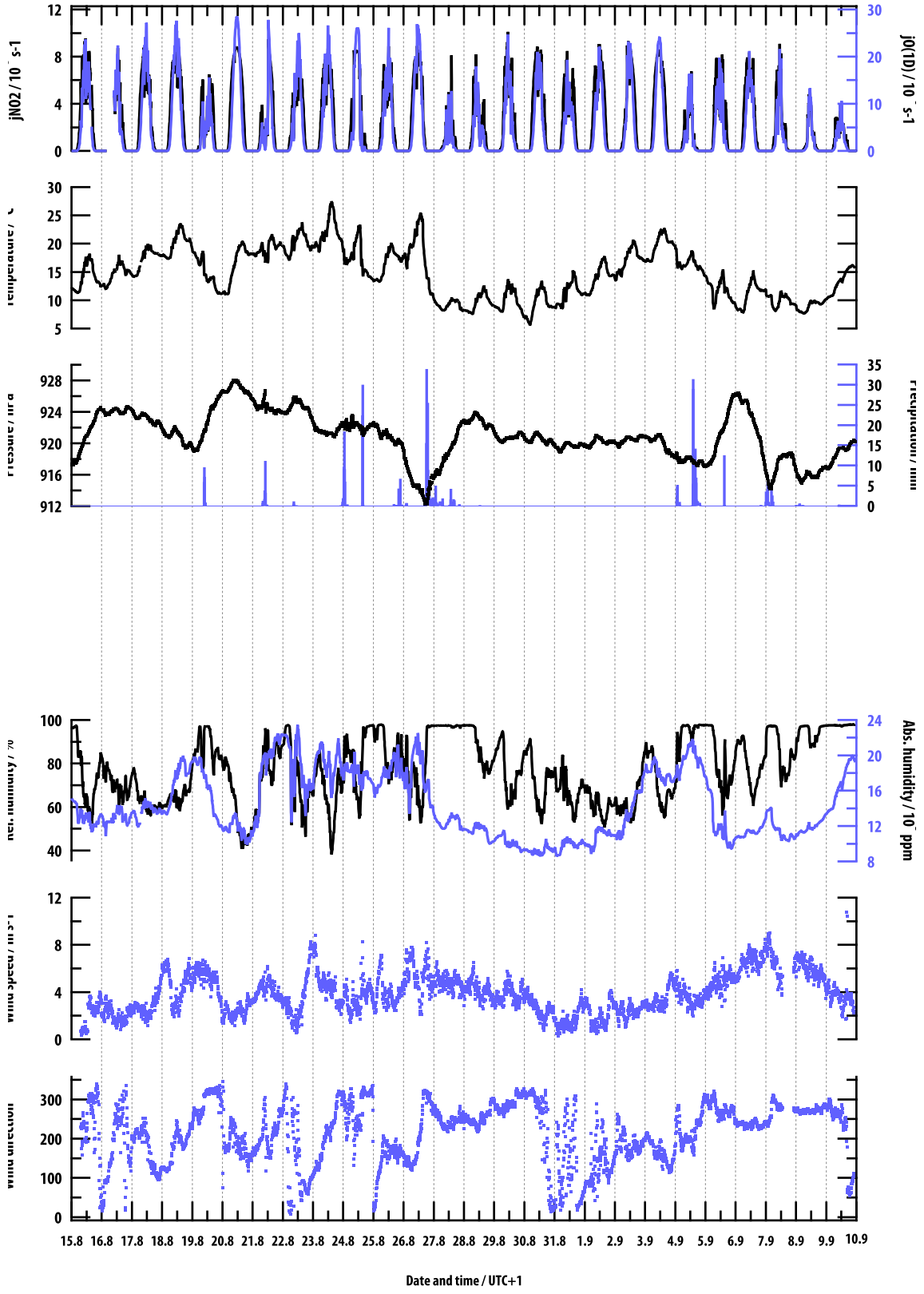

Figure B.5.: Time series of meteorological parameters for PARADE.

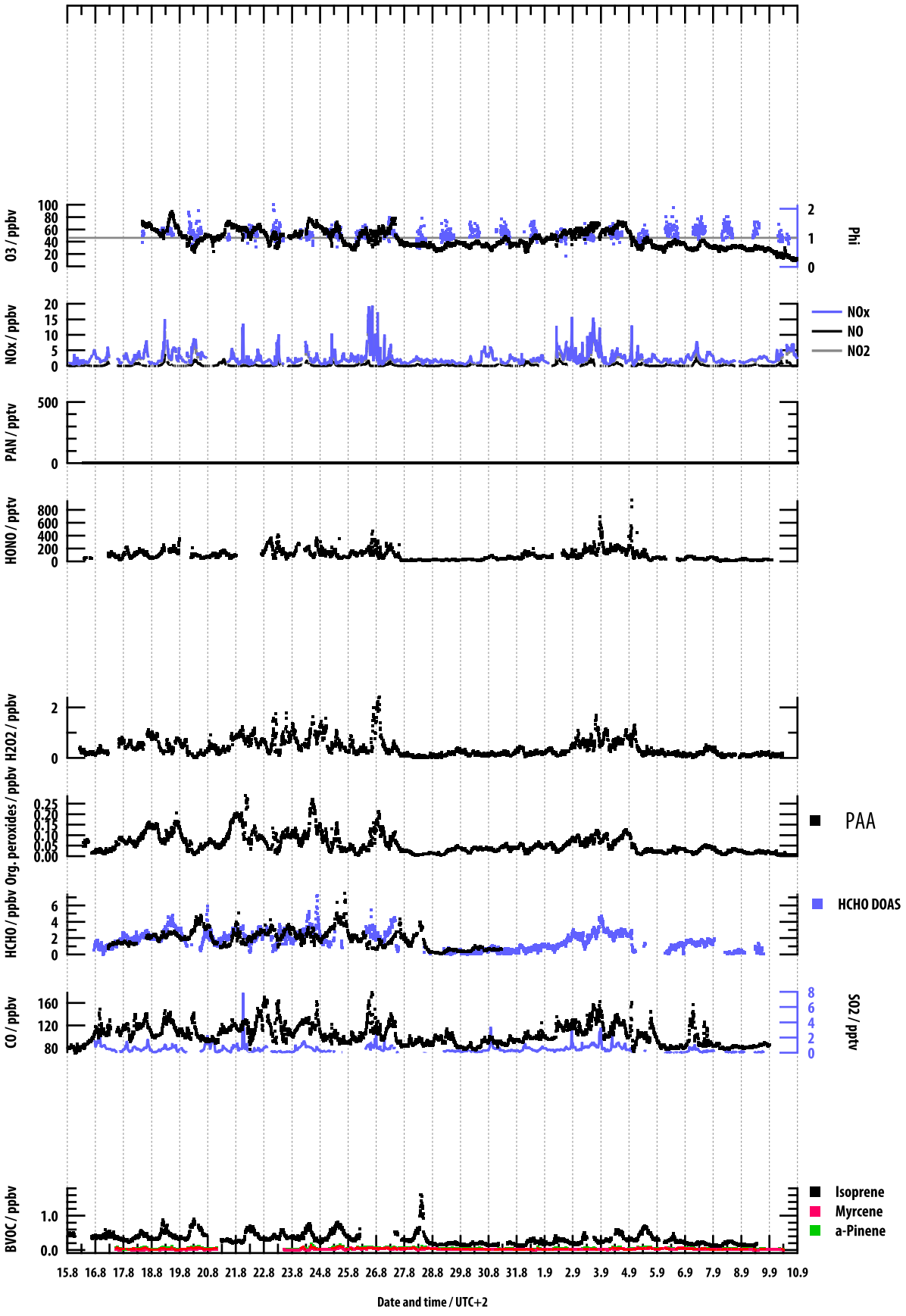

Figure B.6.: Time series of chemical trace gases and related parameters for PARADE.

C. Appendix – Investigation of the photochemical budget of H_2O_2 and HCHO during HUMPPA

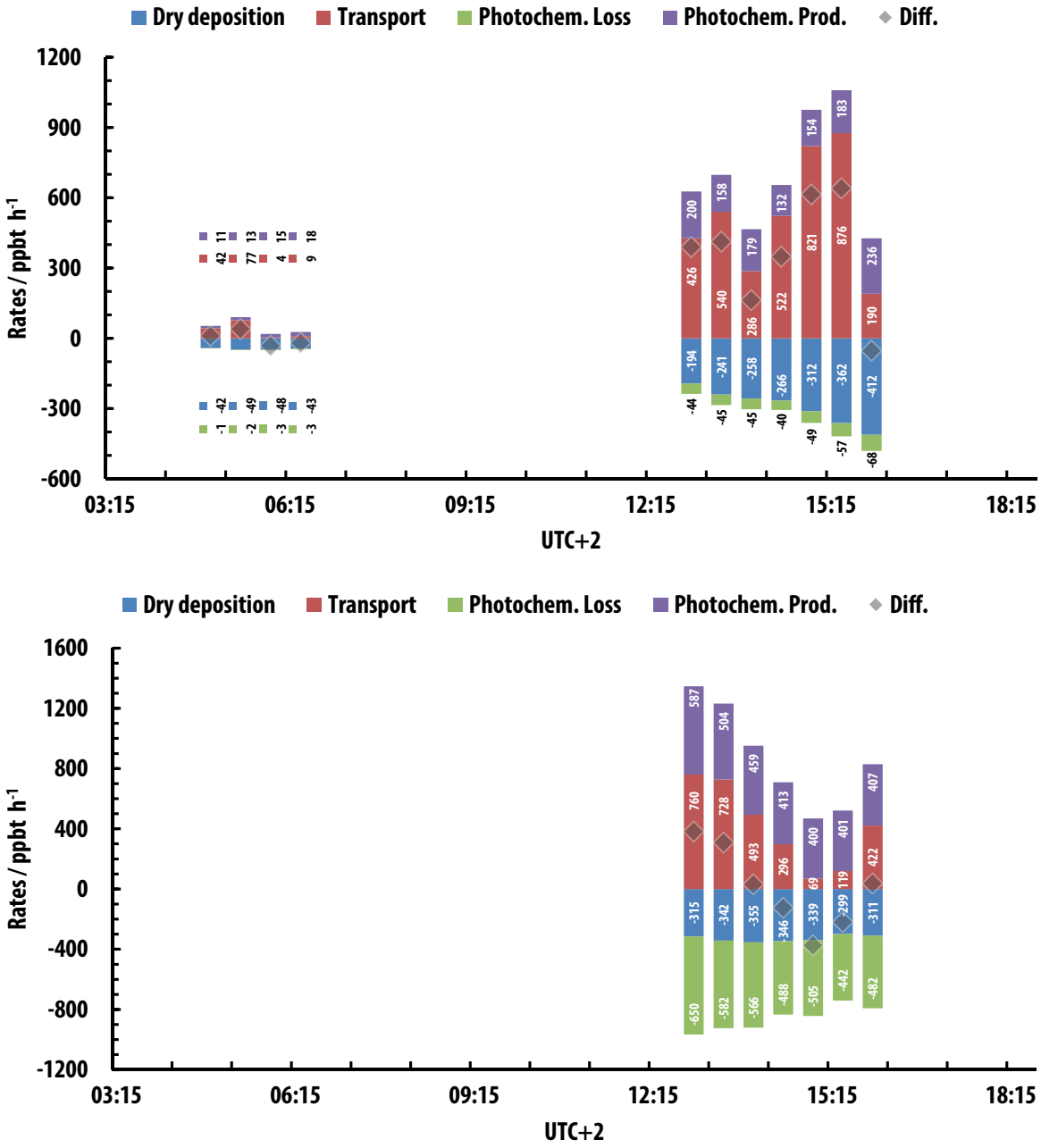

Figure C.1.: Diurnal profiles of the entire budget for H_2O_2 and HCHO as stacked columns for polluted conditions. Mean diurnal profile for Aug 26, 2010 of production and depletion rates (pptv h^{-1}) for H_2O_2 (**top**) and HCHO (**bottom**). Physical processes are broken down to dry deposition and transport (vertical and horizontal), while the photochemical side itemizes production and loss. "Diff." quantifies the observed difference between two time steps. Individual rates are indicated by vertical numbers (pptv h^{-1}).

D. Appendix – Comparison of HUMPPA measurements with the EMAC General Circulation Model

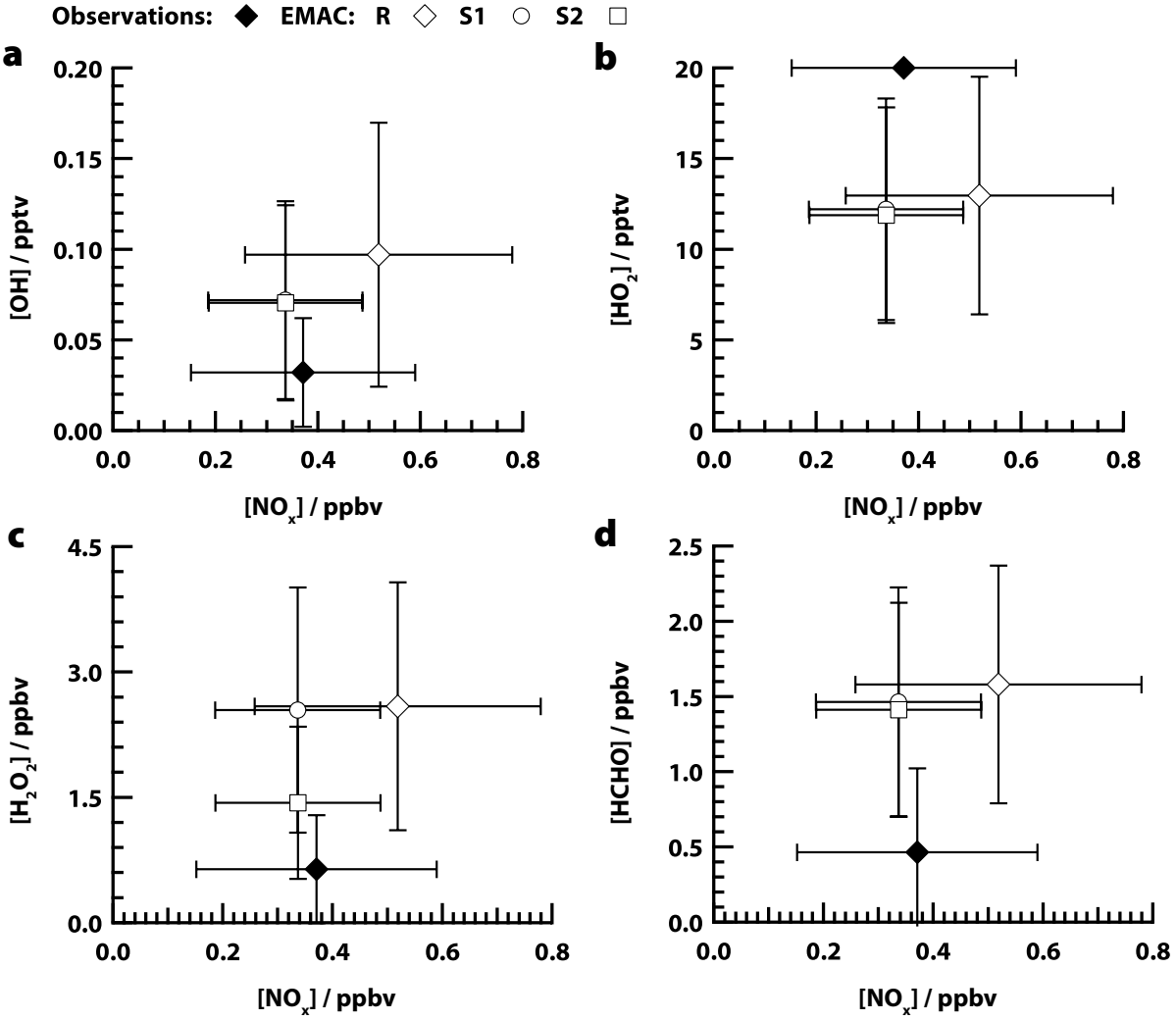

Figure D.1.: Trends in OH, HO_2, H_2O_2 and HCHO depending on NO_x for observations and simulations (R, S1, S2). Mean daytime mixing ratios of OH, HO_2, H_2O_2 and HCHO versus NO_x with the 1σ variability for the entire campaign (**a, b, c, d**). Observed data is included (black diamond), while the simulations are depicted as open markers (R: diamond, S1: circle, S2: square).

E. Appendix – Rate coefficients

Table E.1.: Evaluated second order rate coefficients for gas phase reactions under tropospheric conditions (approximately 200 to 300 K and 0 to 1000 hPa).

Reaction	k_{298} / ($cm^3\ s^{-1}$)	Δk_{298} / ($cm^3\ s^{-1}$)	k_T / ($cm^3\ s^{-1}$)	$\Delta(E/R)$ / (K)	Reference
$O(^1D)$ Reactions					
$O(^1D) + H_2O \longrightarrow 2\,OH$	2.14×10^{-10}	±0.1	2.14×10^{-10}	±100	Atkinson et al. (2004)
HO_x Reactions					
$H + O_2 \xrightarrow{M} HO_2$	$5.5 \times 10^{-32}[N_2]$	±0.1	$5.4 \times 10^{-32}(T/300)^{-1.8}[N_2]$	Δn±0.6	Atkinson et al. (2004)
$OH + O_3 \longrightarrow HO_2 + O_2$	7.3×10^{-14}	±0.15	$1.7 \times 10^{-12}\exp^{-940/T}$	±300	Atkinson et al. (2004)
$OH + HO_2 \longrightarrow H_2O + O_2$	1.1×10^{-10}	±0.1	$4.8 \times 10^{-11}\exp^{250/T}$	±200	Atkinson et al. (2004)
$OH + H_2O_2 \longrightarrow H_2O + HO_2$	1.7×10^{-12}	±0.1	$2.9 \times 10^{-12}\exp^{-160/T}$	±100	Atkinson et al. (2004)
$HO_2 + O_3 \longrightarrow OH + 2\,O_2$	2.0×10^{-15}	±0.2	$2.03 \times 10^{-16}(T/300)^{4.57}\exp^{693/T}$	±100	Atkinson et al. (2004)
$HO_2 + HO_2 \xrightarrow{H_2O} H_2O_2 + O_2$[a]	1.6×10^{-12}	±0.15	$2.2 \times 10^{-13}\exp^{600/T}$	±200	Atkinson et al. (2004)
NO_x Reactions					
$HO_2 + NO \longrightarrow NO_2 + OH$	8.5×10^{-12}	±0.1	$3.45 \times 10^{-12}\exp^{270/T}$	±100	Atkinson et al. (2004)
$NO + O_3 \longrightarrow NO_2 + O_2$	1.8×10^{-14}	±0.08	$1.4 \times 10^{-12}\exp^{-1310/T}$	±200	Atkinson et al. (2004)
Reactions of Organic Compounds					
$OH + CO \longrightarrow H + CO_2$					
$OH + CO \xrightarrow{M} HOCO$					
Overall Reaction		±0.05	$1.44 \times 10^{-13}\left(1 + \frac{[N_2]}{4.2 \times 10^{19}\ cm^{-3}}\right)$		Atkinson et al. (2006)
$OH + CH_4 \longrightarrow CH_3 + H_2O$	6.4×10^{-15}	±0.08	$1.85 \times 10^{-12}\exp^{-1690/T}$	±100	Atkinson et al. (2006)
$OH + HCHO \longrightarrow H_2O + HCO$	8.5×10^{-12}	±0.08	$5.4 \times 10^{-12}\exp^{135/T}$	±100	Atkinson et al. (2006)
$OH + CH_3OH \longrightarrow H_2O + CH_2OH$					
$OH + CH_3OH \longrightarrow H_2O + CH_3O$					
Overall Reaction	9.0×10^{-13}	±0.08	$2.85 \times 10^{-12}\exp^{-345/T}$	±150	Atkinson et al. (2006)
$OH + CH_3OOH \longrightarrow H_2O + CH_2OOH$					
$OH + CH_3OOH \longrightarrow H_2O + CH_3O_2$					
Overall Reaction	1.0×10^{-11}	±0.3	$5.3 \times 10^{-12}\exp^{190/T}$	±200	Atkinson et al. (2006)
$OH + \alpha$ – Pinene $\longrightarrow$ products	5.3×10^{-11}	±0.15	$1.2 \times 10^{-11}\exp^{440/T}$	±200	Atkinson et al. (2006)
$OH + CH_2 = C(CH_3)CH = CH_2$ $\longrightarrow 0.6$ HCHO + …	1.0×10^{-10}	±0.06	$2.7 \times 10^{-11}\exp^{390/T}$	±200	Atkinson et al. (2006)
$O_3 + \alpha$ – Pinene $\longrightarrow 0.16\ H_2O_2 + 0.15$ HCHO	9.0×10^{-17}	±0.2	$6.3 \times 10^{-16}\exp^{-580/T}$	±300	Atkinson and Arey (2003b), Atkinson et al. (2006)
$O_3 + \Delta^3$ – Carene $\longrightarrow 0.6\ H_2O_2 + 0.16$ HCHO	3.8×10^{-17}				Becker et al. (1993), Atkinson and Arey (2003a)
$O_3 + CH_2 = C(CH_3)CH = CH_2$ $\longrightarrow 0.9$ HCHO + …	1.27×10^{-17}	±0.08	$1.03 \times 10^{-14}\exp^{-1995/T}$	±200	Atkinson et al. (2006)
$HO_2 + CH_3O_2 \longrightarrow CH_3OOH + O_2$	5.2×10^{-12}	±0.2	$3.8 \times 10^{-13}\exp^{780/T}$	±200	Atkinson et al. (2006)
$CH_3 + O_2 \xrightarrow{M} CH_3O_2$	9.5×10^{-13}	±0.2	$7 \times 10^{-31}(T/300)^{-3.0}[N_2]$	Δn±1	Atkinson et al. (2006)
$CH_3O + O_2 \longrightarrow HCHO + HO_2$	1.9×10^{-15}	±0.2	$7.2 \times 10^{-14}\exp^{-1080/T}$	±500	Atkinson et al. (2006)
$CH_3O_2 + CH_3O_2$ $\longrightarrow$ HCHO + …	3.5×10^{-13}	±0.12	$1.03 \times 10^{-13}\exp^{365/T}$	±200	Atkinson et al. (2006)
$CH_3O_2 + NO \longrightarrow CH_3O + NO_2$	7.7×10^{-12}	±0.05	$2.3 \times 10^{-12}\exp^{360/T}$	±100	Atkinson et al. (2006)
Photolysis Reactions					
$O_3 + h\nu \longrightarrow O_2 + O(^1D)$					
$NO_2 + h\nu \longrightarrow NO + O(^3P)$					
$H_2O_2 + h\nu \longrightarrow 2\,OH$					
$HCHO + h\nu \longrightarrow HCO + H$					
$HCHO + h\nu \longrightarrow H_2 + CO$					
$CH_3OOH + h\nu \longrightarrow OH + CH_3O$					

[a] In the presence of water, the rate coefficient k_T is multiplied by $\left\{1 + 1.4 \times 10^{-21}[H_2O]\exp(2200/T)\right\}$.

Table E.2.: Evaluated kinetic data for the oxidation of terpenes via O_3.

Terpene	$k_{298}/(\mathrm{cm^3\ s^{-1}})$	HCHO yield	H_2O_2 yield
Isoprene	1.27×10^{-17} [a]	0.9 [b]	0.1 [c]
Δ^3-Carene	3.7×10^{-17} [a]	0.16 [d]	0.6 [c]
Myrcene	4.7×10^{-16} [a]	0.26 [d]	0.3 [e]
α-Pinene	8.7×10^{-17} [f]	0.15 [d]	0.5 [c]
β-Pinene	1.5×10^{-17} [a]	0.84 [g]	0.35 [g]
		0.70 [d]	0.15 [c]
		0.42 [b]	

[a] Atkinson (1997)

[b] Grosjean et al. (1993)

[c] Becker et al. (1990)

[d] Ruppert et al. (1999)

[e] Estimated value, average of the yields from the other monoterpenes.

[f] Atkinson et al. (2006)

[g] Winterhalter et al. (2000)

Table E.3.: Evaluated kinetic data for the oxidation of alkenes with OH.

Terpene	$k_{298}/(\mathrm{cm^3\ s^{-1}})$	HCHO yield
Isoprene	1.0×10^{-10} [a]	0.63 [b]
Δ^3-Carene	8.8×10^{-11} [c]	0.21 [d]
Myrcene	3.4×10^{-10} [e]	0.30 [d]
α-Pinene	5.4×10^{-11} [f]	0.23 [g]
β-Pinene	7.9×10^{-11} [a]	0.54 [h]

[a] Atkinson (1997)

[b] Tuazon and Atkinson (1990)

[c] Atkinson et al. (1990)

[d] Orlando et al. (2000)

[e] Hites and Turner (2009)

[f] Atkinson et al. (2006)

[g] Nozière et al. (1999)

[h] Hatakeyama et al. (1991)

List of Figures

List of Tables

References

AL2021 User Manual, Aero-Laser GmbH, Garmisch-Partenkirchen.

AL4021 User Manual, Aero-Laser GmbH, Garmisch-Partenkirchen.

Arlander, D. W., Brüning, D., Schmidt, U., and Ehhalt, D. H.: The tropospheric distribution of formaldehyde during TROPOZ II, Journal of Atmospheric Chemistry, 22, 251–269, 1995.

Atkinson, R.: Gas-Phase Tropospheric Chemistry of Volatile Organic Compounds: 1. Alkanes and Alkenes, Journal of Physical and Chemical Reference Data, 26, 215, 1997.

Atkinson, R. and Arey, J.: Atmospheric Degradation of Volatile Organic Compounds, Chemical Reviews, 103, 4605–4638, 2003a.

Atkinson, R. and Arey, J.: Gas-phase tropospheric chemistry of biogenic volatile organic compounds: a review, Atmospheric Environment, 37, 197–219, 2003b.

Atkinson, R., Hasegawa, D., and Aschmann, S. M.: Rate constants for the gas-phase reactions of O_3 with a series of monoterpenes and related compounds at 296 ± 2 K, International Journal of Chemical Kinetics, 22, 871–887, 1990.

Atkinson, R., Baulch, D. L., Cox, R. A., Crowley, J. N., Hampson, R. F., Hynes, R. G., Jenkin, M. E., Rossi, M. J., and Troe, J.: Evaluated kinetic and photochemical data for atmospheric chemistry: Volume I - gas phase reactions of O_x, HO_x, NO_x and SO_x species, Atmospheric Chemistry and Physics, 4, 1461–1738, 2004.

Atkinson, R., Baulch, D. L., Cox, R. A., Crowley, J. N., Hampson, R. F., Hynes, R. G., Jenkin, M. E., Rossi, M. J., Troe, J., and IUPAC Subcommittee: Evaluated kinetic and photochemical data for atmospheric chemistry: Volume II - gas phase reactions of organic species, Atmospheric Chemistry and Physics, 6, 3625–4055, 2006.

Ayers, G. P., Penkett, S. A., Gillett, R. W., Bancy, B., Galbally, I. E., and Meyer, C. P.: Evidence for photochemical control of ozone concentrations in unpolluted marine air, Nature, 360, 446–449, 1992.

Ayers, G. P., Penkett, S. A., Gillett, R. W., Bandy, B. J., Galbally, I. E., Meyer, C. P., Elsworth, C. M., Bentley, S. T., and Forgan, B. W.: The annual cycle of peroxides and ozone in marine air at Cape Grim, Tasmania, Journal of Atmospheric Chemistry, 23, 221–252, 1996.

Ayers, G. P., Granek, H., and Boers, R.: Ozone in the marine boundary layer at Cape Grim: Model simulation, Journal of Atmospheric Chemistry, 27, 179–195, 1997.

Baer, M. and Nester, K.: Parametrization of trace gas dry deposition velocities for a regional mesoscale diffusion-model, Annales Geophysicae - Atmospheres, Hydrospheres and Space Sciences, 10, 912–923, 1992.

Balasubramanian, R. and Husain, L.: Observations of gas-phase hydrogen peroxide at an elevated rural site in New York, Journal of Geophysical Research, 102, 21 209–21 220, 1997.

Becker, K. H., Brockmann, K. J., and Bechara, J.: Production of hydrogen peroxide in forest air by reaction of ozone with terpenes, Nature, 346, 256–258, 1990.

Becker, K. H., Bechara, J., and Brockmann, K.: Studies on the formation of H_2O_2 in the ozonolysis of alkenes, Atmospheric Environment Part A-General Topics, 27, 57–61, 1993.

Bielski, B. H. J., Cabelli, D. E., Arudi, R. L., and Ross, A. B.: Reactivity of HO_2 / O_2^- Radicals in Aqueous Solution, Journal of Physical and Chemical Reference Data, 14, 1041, 1985.

Bricker, C. E. and Johnson, H. R.: Spectrophotometric Method for Determining Formaldehyde, Industrial & Engineering Chemistry Analytical Edition, 17, 400–402, 1945.

Campos, T. L. and Kok, G. L.: Evaluation of Horibe traps for cryogenic collection of hydrogen peroxide and methyl hydroperoxide, Atmospheric Environment, 30, 2575–2582, 1996.

Cantrell, C. A., Shetter, R. E., Calvert, J. G., Parrish, D. D., Fehsenfeld, F. C., Goldan, P. D., Kuster, W. C., Williams, E. J., Westberg, H. H., Allwine, G., and Martin, R.: Peroxy radicals as measured in ROSE and estimated from photostationary state deviations, Journal of Geophysical Research, 98, 18 355, 1993.

Cantrell, C. A., Shetter, R. E., Gilpin, T. M., Calvert, J. G., Eisele, F. L., and Tanner, D. J.: Peroxy radical concentrations measured and calculated from trace gas measurements in the Mauna Loa Observatory Photochemistry Experiment 2, Journal of Geophysical Research, 101, 14 653, 1996.

Cantrell, C. A., Shetter, R. E., Calvert, J. G., Eisele, F. L., Williams, E., Baumann, K., Brune, W. H., Stevens, P. S., and Mather, J. H.: Peroxy radicals from photostationary state deviations and steady state calculations during the Tropospheric OH Photochemistry Experiment at Idaho Hill, Colorado, 1993, Journal of Geophysical Research, 102, 6369, 1997.

Cantrell, C. A., Mauldin, L., Zondlo, M., Eisele, F., Kosciuch, E., Shetter, R., Lefer, B. L., Hall, S., Campos, T., Ridley, B., Walega, J., Fried, A., Wert, B., Flocke, F., Weinheimer, A. J., Hannigan, J., Coffey, M., Atlas, E., Stephens, S., Heikes, B. G., Snow, J., Blake, D., Blake, N., Katzenstein, A., Lopez, J., Browell, E. V., Dibb, J., Scheuer, E., Seid, G., and Talbot, R.: Steady state free radical budgets and ozone photochemistry during TOPSE, Journal of Geophysical Research, 108, 8361 ff, 2003.

Carlier, P., Hannachi, H., and Mouvier, G.: The chemistry of carbonyl compounds in the atmosphere - A review, Atmospheric Environment (1967), 20, 2079–2099, 1986.

Carlier, P., Freshnet, P., Lescoat, V., Pashalidis, S., and Mouvier, G.: Daily Profil Study of the Atmospheric Formaldehyde Concentrations at the "Pointe de Penmarch" under Pure Marine Conditions, in: Physico-Chemical Behaviour of Atmospheric Pollutants, edited by Restelli, G. and Angeletti, G., pp. 582–587, Springer Netherlands, Dordrecht, 1990.

Carpenter, L. J., Monks, P. S., Bandy, B. J., Penkett, S. A., Galbally, I. E., and Meyer, C. P.: A study of peroxy radicals and ozone photochemistry at coastal sites in the northern and southern hemispheres, Journal of Geophysical Research, 102, 25 417–25 427, 1997.

Choi, W., Faloona, I. C., Bouvier-Brown, N. C., McKay, M., Goldstein, A. H., Mao, J., Brune, W. H., LaFranchi, B. W., Cohen, R. C., Wolfe, G. M., Thornton, J. A., Sonnenfroh, D. M., and Millet, D. B.: Observations of elevated formaldehyde over a forest canopy suggest missing sources from rapid oxidation of arboreal hydrocarbons, Atmospheric Chemistry and Physics, 10, 8761–8781, 2010.

Claiborn, C. S. and Aneja, V. P.: Measurements of Atmospheric Hydrogen Peroxide in the Gas Phase and in Cloud Water at Mt. Mitchell, North Carolina, Journal of Geophysical Research, 96, 18 771–18 787, 1991.

Cofer, W. R. and Edahl, R. A.: A new technique for collection, concentration and determination of gaseous tropospheric formaldehyde, Atmospheric Environment (1967), 20, 979–984, 1986.

Cofer, W. R., Collins, V. G., and Talbot, R. W.: Improved aqueous scrubber for collection of soluble atmospheric trace gases, Environmental Science & Technology, 19, 557–560, 1985.

Corrigan, A. L., Russell, L. M., Takahama, S., Äijälä, M., Ehn, M., Junninen, H., Rinne, J., Petäjä, T., Kulmala, M., Vogel, A. L., Hoffmann, T., Ebben, C. J., Geiger, F. M., Chhabra, P., Seinfeld, J. H., Worsnop, D. R., Song, W., Auld, J., and Williams, J.: Biogenic and biomass burning organic aerosol in a boreal forest at Hyytiälä, Finland, during HUMPPA-COPEC 2010, Atmospheric Chemistry and Physics, 13, 12 233–12 256, 2013.

Crounse, J. D., McKinney, K. A., Kwan, A. J., and Wennberg, P. O.: Measurement of Gas-Phase Hydroperoxides by Chemical Ionization Mass Spectrometry, Analytical Chemistry, 78, 6726–6732, 2006.

Dasgupta, P. K., Dong, S., and Hwang, H.: Diffusion Scrubber-Based Field Measurements of Atmospheric Formaldehyde and Hydrogen Peroxide, Aerosol Science and Technology, 12, 98–104, 1990.

Diesch, J.-M., Drewnick, F., Zorn, S. R., Weiden-Reinmüller, S.-L. v. d., Martinez, M., and Borrmann, S.: Variability of aerosol, gaseous pollutants and meteorological characteristics associated with changes in air mass origin at the SW Atlantic coast of Iberia, Atmospheric Chemistry and Physics, 12, 3761–3782, 2012.

Dong, S. and Dasgupta, P. K.: Fast fluorometric flow injection analysis of formaldehyde in atmospheric water, Environmental Science & Technology, 21, 581–588, 1987.

Draxler, R. and Rolph, G.: HYSPLIT (HYbrid Single-Particle Lagrangian Integrated Trajectory), URL `http://ready.arl.noaa.gov/HYSPLIT.php`, 2012.

Fagnani, E.: Chromotropic acid–formaldehyde reaction in strongly acidic media. The role of dissolved oxygen and replacement of concentrated sulphuric acid, Talanta, 60, 171–176, 2003.

Fels, M. and Junkermann, W.: The occurrence of organic peroxides in air at a mountain site, Geophysical Research Letters, 21, 341, 1994.

Finlayson-Pitts, B. J. and Pitts, J. N.: Atmospheric Chemistry: Fundamentals; Experimental Techniques, John Wiley & Sons New York, 1986.

Fischer, H., Kormann, R., Klüpfel, T., Gurk, C., Königstedt, R., Parchatka, U., Mühle, J., Rhee, T. S., Brenninkmeijer, C. A. M., Bonasoni, P., and Stohl, A.: Ozone production and trace gas correlations during the June 2000 MINATROC intensive measurement campaign at Mt. Cimone, Atmospheric Chemistry and Physics, 3, 725–738, 2003.

Fischer, H., Pozzer, A., Schmitt, T., Jöckel, P., Klippel, T., Taraborrelli, D., and Lelieveld, J.: Hydrogen peroxide in the marine boundary layer over the South Atlantic during the OOMPH cruise in March 2007, Atmospheric Chemistry and Physics, 15, 6971–6980, 2015.

Fried, A.: Airborne tunable diode laser measurements of formaldehyde during TRACE-P: Distributions and box model comparisons, Journal of Geophysical Research, 108, 2003.

Fried, A., Walega, J. G., Olson, J. R., Crawford, J. H., Chen, G., Weibring, P., Richter, D., Roller, C., Tittel, F. K., Heikes, B. G., Snow, J. A., Shen, H., O'Sullivan, D. W., Porter, M., Fuelberg, H., Halland, J., and Millet, D. B.: Formaldehyde over North America and the North Atlantic during the summer 2004 INTEX campaign: Methods, observed distributions, and measurement-model comparisons, Journal of Geophysical Research, 113, 2008.

Fuchs, H., Bohn, B., Hofzumahaus, A., Holland, F., Lu, K. D., Nehr, S., Rohrer, F., and Wahner, A.: Detection of HO_2 by laser-induced fluorescence: calibration and interferences from RO_2 radicals, Atmospheric Measurement Techniques, 4, 1209–1225, 2011.

Giese, M., Bauer-Doranth, U., Langebartels, C., and Sandermann Jr, H.: Detoxification of Formaldehyde by the Spider Plant (Chlorophytum comosum L.) and by Soybean (Glycine max L.) Cell-Suspension Cultures, Plant Physiology, 104, 1301–1309, 1994.

Gnauk, T., W. Rolle, and G. Spindler: Diurnal variations of atmospheric hydrogen peroxide concentrations in Saxony (Germany), Journal of Atmospheric Chemistry, 27, 79–103, 1997.

Grosjean, D., Williams, E. L., and Grosjean, E.: Atmospheric chemistry of isoprene and of its carbonyl products, Environmental Science & Technology, 27, 830–840, 1993.

Grossmann, D.: Hydrogen peroxide, organic peroxides, carbonyl compounds, and organic acids measured at Pabstthum during BERLIOZ, Journal of Geophysical Research, 108, 2003.

Gunz, D. and Hoffmann, M.: Atmospheric chemistry of peroxides: a review, Atmospheric Environment Part A-General Topics, 24, 1601–1633, 1990.

Hafermann, S.: Messungen von Wasserstoffperoxid in der Troposphäre, Diploma thesis, Johannes-Gutenberg Universität, Mainz, 2011.

Hafermann, S. and Reiffs, A.: personal communication, 2013.

Hak, C., Pundt, I., Kern, C., Platt, U., Dommen, J., Ordóñez, C., Prévôt, A. S. H., Junkermann, W., Astorga-Lloréns, C., Larsen, B. R., Mellqvist, J., Strandberg, A., Yu, Y., Galle, B., Kleffmann, J., Lörzer, J. C., Braathen, G. O., and Volkamer, R.: Intercomparison of four different in-situ techniques for ambient formaldehyde measurements in urban air, Atmospheric Chemistry and Physics Discussions, 5, 2897–2945, 2005.

Hakola, H., Tarvainen, V., Laurila, T., Hiltunen, V., Hellén, H., and Keronen, P.: Seasonal variation of VOC concentrations above a boreal coniferous forest, Atmospheric Environment, 37, 1623–1634, 2003.

Hakola, H., Hellén, H., Hemmilä, M., Rinne, J., and Kulmala, M.: In situ measurements of volatile organic compounds in a boreal forest, Atmospheric Chemistry and Physics, 12, 11 665–11 678, 2012.

Hall, B. D. and Claiborn, C. S.: Measurements of the dry deposition of peroxides to a Canadian boreal forest, Journal of Geophysical Research, 102, 29 343–29 353, 1997.

Hall, B. D., Baldocchi, D., Hall, B., and Claiborn, C. S.: Measurement and modeling of the dry deposition of peroxides, Atmospheric Environment, 33, 577–589, 1999.

Hallquist, M., Wenger, J. C., Baltensperger, U., Rudich, Y., Simpson, D., Claeys, M., Dommen, J., Donahue, N. M., George, C., Goldstein, A. H., Hamilton, J. F., Herrmann, H., Hoffmann, T., Iinuma, Y., Jang, M., Jenkin, M. E., Jimenez, J. L., Kiendler-Scharr, A., Maenhaut, W., McFiggans, G., Mentel, T. F., MONOD, A., Prévôt, A. S. H., Seinfeld, J. H., Surratt, J. D., Szmigielski, R., and Wildt, J.: The formation, properties and impact of secondary organic aerosol: current and emerging issues, Atmospheric Chemistry and Physics, 9, 5155–5236, 2009.

Hard, T. M., O'Brien, R. J., Chan, C. Y., and Mehrabzadeh, A. A.: Tropospheric free radical determination by fluorescence assay with gas expansion, Environmental Science & Technology, 18, 768–777, 1984.

Harder, J. W., Fried, A., Sewell, S., and Bruce, H.: Comparison of tunable diode laser and long-path ultraviolet/visible spectroscopic measurements of ambient formaldehyde concentrations during the 1993 OH Photochemistry Experiment, Journal of Geophysical Research, 102, 6267–6282, 1997.

Harris, G. W., Klemp, D., Zenker, T., Burrows, J. P., and Mathieu, B.: Tunable diode laser measurements of trace gases during the 1988 Polarstern cruise and intercomparisons with other methods, Journal of Atmospheric Chemistry, 15, 315–326, 1992.

Hatakeyama, S., Izumi, K., Fukuyama, T., Akimoto, H., and Washida, N.: Reactions of OH with α-pinene and β-pinene in air: Estimate of global CO production from the atmospheric oxidation of terpenes, Journal of Geophysical Research, 96, 947, 1991.

Hauglustaine, D. A., Madronich, S., Ridley, B. A., Walega, J. G., Cantrell, C. A., Shetter, R. E., and Hübler, G.: Observed and model-calculated photostationary state at Mauna Loa Observatory during MLOPEX 2, Journal of Geophysical Research, 101, 14 681, 1996.

Hauglustaine, D. A., Madronich, S., Ridley, B. A., Flocke, S. J., Cantrell, C. A., Eisele, F. L., Shetter, R. E., Tanner, D. J., Ginoux, P., and Atlas, E. L.: Photochemistry and budget of ozone during the Mauna Loa Observatory Photochemistry Experiment (MLOPEX 2), Journal of Geophysical Research, 104, 30 275, 1999.

Heard, D. E. and Pilling, M. J.: Measurement of OH and HO_2 in the Troposphere, Chemical Reviews, 103, 5163–5198, 2003.

Heikes, B. G.: Aqueous H_2O_2 production from O_3 in glass impingers, Atmospheric Environment, 18, 1433–1455, 1984.

Heikes, B. G.: Formaldehyde and Hydroperoxides at Mauna Loa Observatory, Journal of Geophysical Research, 97, 18 001, 1992.

Heikes, B. G., Kok, G. L., Walega, J. G., and Lazrus, A. L.: H_2O_2, O_3 and SO_2 Measurements in the Lower Troposphere Over the Eastern United States During Fall, Journal of Geophysical Research, 92, 915–931, 1987.

Heikes, B. G., Snow, J. A., Egli, P., O'Sullivan, D. W., Crawford, J. H., Olson, J., Chen, G., Davis, D. D., Blake, N. J., and Blake, D. R.: Formaldehyde over the central Pacific during PEM-Tropics B, Journal of Geophysical Research, 106, 32 717–32 731, 2001.

Heland, J., Kleffmann, J., Kurtenbach, R., and Wiesen, P.: A New Instrument To Measure Gaseous Nitrous Acid (HONO) in the Atmosphere, Environmental Science & Technology, 35, 3207–3212, 2001.

Hellpointner, E. and Gäb, S.: Detection of methyl, hydroxymethyl and hydroxyethyl hydroperoxides in air and precipitation, Nature, 337, 631–634, 1989.

Hellén, H., Hakola, H., Reissell, A., and Ruuskanen, T. M.: Carbonyl compounds in boreal coniferous forest air in Hyytiälä, Southern Finland, Atmospheric Chemistry and Physics, 4, 1771–1780, 2004.

Hewitt, C. N. and Kok, G. L.: Formation and occurrence of organic hydroperoxides in the troposphere: Laboratory and field observations, Journal of Atmospheric Chemistry, 12, 181–194, 1991.

Hites, R. A. and Turner, A. M.: Rate constants for the gas-phase β-myrcene + OH and isoprene + OH reactions as a function of temperature, International Journal of Chemical Kinetics, 41, 407–413, 2009.

Hofzumahaus, A., Rohrer, F., Lu, K., Bohn, B., Brauers, T., Chang, C.-C., Fuchs, H., Holland, F., Kita, K., Kondo, Y., Li, X., Lou, S., Shao, M., Zeng, L., Wahner, A., and Zhang, Y.: Amplified Trace Gas Removal in the Troposphere, Science, 324, 1702–1704, 2009.

Holland, F.: Measurements of OH and HO_2 radical concentrations and photolysis frequencies during BERLIOZ, Journal of Geophysical Research, 108, 2003.

Holland, F., Hessling, M., and Hofzumahaus, A.: In Situ Measurement of Tropospheric OH Radicals by Laser-Induced Fluorescence—A Description of the KFA Instrument, Journal of the Atmospheric Sciences, 52, 3393–3401, 1995.

Hosaynali-Beygi, Z.: Oxidation photochemistry in the remote marine boundary layer, Ph.D. thesis, Johannes-Gutenberg Universität, Mainz, 2010.

Hosaynali-Beygi, Z., Fischer, H., Harder, H. D., Martinez, M., Sander, R., Williams, J., Brookes, D. M., Monks, P. S., and Lelieveld, J.: Oxidation photochemistry in the Southern Atlantic boundary layer: unexpected deviations of photochemical steady state, Atmospheric Chemistry and Physics, 11, 8497–8513, 2011.

Hua, W., Chen, Z. M., Jie, C. Y., Kondo, Y., Hofzumahaus, A., Takegawa, N., Chang, C.-C., Lu, K. D., Miyazaki, Y., Kita, K., Wang, H. L., Zhang, Y. H., and Hu, M.: Atmospheric hydrogen peroxide and organic hydroperoxides during PRIDE-PRD'06, China: their concentration, formation mechanism and contribution to secondary aerosols, Atmospheric Chemistry and Physics, 8, 6755–6773, 2008a.

Hua, W., Chen, Z. M., Jie, C. Y., Kondo, Y., Hofzumahaus, A., Takegawa, N., Lu, K. D., Miyazaki, Y., Kita, K., Wang, H. L., Zhang, Y., and Hu, M.: Atmospheric hydrogen peroxide and organic hydroperoxides during PRIDE-PRD'06, China: their concentration, formation mechanism and contribution to secondary aerosols, Atmospheric Chemistry and Physics Discussions, 8, 10 481–10 530, 2008b.

Innes, J. L., Beniston, M., and Verstraete, M. M.: Biomass burning and its inter-relationships with the climate system, Kluwer Academic Publishers, Dordrecht and and Boston, 2000.

Ischiropoulos, H., Nelson, J., Duran, D., and Al-Mehdi, A.: Reactions of nitric oxide and peroxynitrite with organic molecules and ferrihorseradish peroxidase: Interference with the determination of hydrogen peroxide, Free Radical Biology & Medicine, 20, 373–381, 1996.

Jackson, A. V. and Hewitt, C. N.: Hydrogen peroxide and organic hydroperoxide concentrations in air in a eucalyptus forest in central Portugal, Atmospheric Environment, 30, 819–830, 1996.

Jackson, A. V. and Hewitt, C. N.: Atmosphere Hydrogen Peroxide and Organic Hydroperoxides: A Review, Critical Reviews in Environmental Science and Technology, 29, 175–228, 1999.

Jacob, D. J.: Heterogeneous chemistry and tropospheric ozone, Atmospheric Environment, 34, 2131–2159, 2000.

Jacob, P. and Klockow, D.: Hydrogen peroxide measurements in the marine atmosphere, Journal of Atmospheric Chemistry, 15, 353–360, 1992.

Jacob, P., Neftel, A., and Klockow, D.: Die Peroxyoxalat-Chemilumineszenz und ihre Anwendung zur Bestimmung von Wasserstoffperoxid in der Außenluft und ihren Niederschlägen, VDI Ber, 608, 377–399, 1987.

Jacob, P., Tavares, T. M., Rocha, V. C., and Klockow, D.: Atmospheric H_2O_2 field measurements in a tropical environment: Bahia, Brazil, Atmospheric Environment Part A-General Topics, 24, 377–382, 1990.

Jacobson, M. Z.: Fundamentals of Atmospheric Modeling, Cambridge Univ. Press, Cambridge, 2005.

Jeuken, A. B. M., Siegmund, P. C., Heijboer, L. C., Feichter, J., and Bengtsson, L.: On the potential of assimilating meteorological analyses in a global climate model for the purpose of model validation, Journal of Geophysical Research, 101, 16 939–16 950, 1996.

Junkermann, W. and Stockwell, W. R.: On the budget of photooxidants in the marine boundary layer of the tropical South Atlantic, Journal of Geophysical Research, 104, 8039–8046, 1999.

Junkermann, W., Platt, U., and Volz-Thomas, A.: A photoelectric detector for the measurement of photolysis frequencies of ozone and other atmospheric molecules, Journal of Atmospheric Chemistry, 8, 203–227, 1989.

Jöckel, P., Sander, R., Kerkweg, A., Tost, H., and Lelieveld, J.: Technical Note: The Modular Earth Submodel System (MESSy) - a new approach towards Earth System Modeling, Atmospheric Chemistry and Physics, 5, 433–444, 2005.

Jöckel, P., Tost, H., Pozzer, A., Brühl, C., Buchholz, J., Ganzeveld, L. N., Hoor, P., Kerkweg, A., Lawrence, M. G., G., Sander, R., Steil, B., Stiller, G., Tanarhte, M., Taraborrelli, D., van Aardenne, J. A., and Lelieveld, J.: The atmospheric chemistry general circulation model ECHAM5/MESSy1: consistent simulation of ozone from the surface to the mesosphere, Atmospheric Chemistry and Physics, 6, 5067–5104, 2006.

Kelly, T. J. and Fortune, C. R.: Continuous Monitoring of Gaseous Formaldehyde Using an Improved Fluorescence Approach, International Journal of Environmental Analytical Chemistry, 54, 249–263, 1994a.

Kelly, T. J. and Fortune, C. R.: Continuous monitoring of gaseous formaldehyde using an improved fluorescence approach, International Journal of Environmental Analytical Chemistry, 54, 249–263, 1994b.

Kerkweg, A., Buchholz, J., Ganzeveld, L. N., Pozzer, A., Tost, H., and Jöckel, P.: Technical Note: An implementation of the dry removal processes DRY DEPosition and SEDImentation in the Modular Earth Submodel System (MESSy), Atmospheric Chemistry and Physics, 6, 4617–4632, 2006a.

Kerkweg, A., Sander, R., Tost, H., and Jöckel, P.: Technical note: Implementation of prescribed (OFFLEM), calculated (ONLEM), and pseudo-emissions (TNUDGE) of chemical species in the Modular Earth Submodel System (MESSy), Atmospheric Chemistry and Physics, 6, 3603–3609, 2006b.

Kesselmeier, J., Bode, K., Hofmann, U., Müller, H., Schäfer, L., Wolf, A., Ciccioli, P., Brancaleoni, E., Cecinato, A., Frattoni, M., Foster, P., Ferrari, C., Jacob, V., Fugit, J. L., Dutaur, L., Simon, V., and Torres, L.: Emission of short chained organic acids, aldehydes and monoterpenes from Quercus Ilex L. and Pinus Pinea L. in relation to physiological activites, carbon budget and emission algorithms, Atmospheric Environment, 31, 119–133, 1997.

Kimmerer, T. W. and Kozlowski, T. T.: Ethylene, Ethane, Acetaldehyde, and Ethanol Production By Plants under Stress, Plant Physiology, 69, 840–847, 1982.

Kimmerer, T. W. and MacDonald, R. C.: Acetaldehyde and Ethanol Biosynthesis in Leaves of Plants, Plant Physiology, 84, 1204–1209, 1987.

Klemm, O., Held, A., Forkel, R., Gasche, R., Kanter, H.-J., Rappenglück, B., Steinbrecher, R., Müller, K., Plewka, A., Cojocariu, C., Kreuzwieser, J., Valverde-Canossa, J., Schuster, G., Moortgat, G. K., Graus, M., and Hansel, A.: Experiments on forest/atmosphere exchange: Climatology and fluxes during two summer campaigns in NE Bavaria, Atmospheric Environment, 40, 3–20, 2006.

Klippel, T.: Hydroperoxide und Formaldehyd in der Troposphäre über Europa, Ph.D. thesis, Ruprecht-Karls-Universität, Heidelberg, 2010.

Klippel, T., Fischer, H., Bozem, H., Lawrence, M. G., Butler, T. M., Jöckel, P., Tost, H., Martinez, M., Harder, H. D., Regelin, E., Sander, R., Schiller, C. L., Stickler, A., and Lelieveld, J.: Distribution of hydrogen peroxide and formaldehyde over Central Europe during the HOOVER project, Atmospheric Chemistry and Physics, 11, 4391–4410, 2011.

Kok, G. L., Darnall, K. R., Winer, A. M., Pitts, J. N., and Gay, B. W.: Ambient air measurements of hydrogen peroxide in the California South Coast Air Basin, Environmental Science & Technology, 12, 1077–1080, 1978a.

Kok, G. L., Holler, T. P., Lopez, M. B., Nachtrieb, H. A., and Yuan, M.: Chemiluminescent method for determination of hydrogen peroxide in the ambient atmosphere, Environmental Science & Technology, 12, 1072–1076, 1978b.

Kormann, R., Fischer, H., Reus, M. d., Lawrence, M. G., Brühl, C., Kuhlmann, R., Holzinger, R., Williams, J., Lelieveld, J., Warneke, C., Gouw, J. A. d., Heland, J., Ziereis, H., and Schlager, H.: Formaldehyde over the eastern Mediterranean during MINOS: Comparison of airborne in-situ measurements with 3D-model results, Atmospheric Chemistry and Physics, 3, 851–861, 2003.

Kovacs, T. A. and Brune, W. H.: Total OH Loss Rate Measurement, Journal of Atmospheric Chemistry, 39, 105–122, 2001.

Krinke, S. M. W.: Experimentelle Bestimmung der Depositionsgeschwindigkeit von Formaldehyd und Ozon über einem Laubwaldbestand, Ph.D. thesis, Universität Stuttgart, Stuttgart, 1999.

Kroll, J. H. and Seinfeld, J. H.: Chemistry of secondary organic aerosol: Formation and evolution of low-volatility organics in the atmosphere, Atmospheric Environment, 42, 3593–3624, 2008.

Kuhlmann, R.: A model for studies of tropospheric ozone and nonmethane hydrocarbons: Model evaluation of ozone-related species, Journal of Geophysical Research, 108, 2003.

LaFranchi, B. W., Wolfe, G. M., Thornton, J. A., Harrold, S. A., Browne, E. C., Min, K. E., Wooldridge, P. J., Gilman, J. B., Kuster, W. C., Goldan, P. D., Gouw, J. A. d., McKay, M., Goldstein, A. H., Ren, X., Mao, J., and Cohen, R. C.: Closing the peroxy acetyl nitrate budget: observations of acyl peroxy nitrates (PAN, PPN, and MPAN) during BEARPEX 2007, Atmospheric Chemistry and Physics, 9, 7623–7641, 2009.

Lazrus, A. L., Kok, G. L., Gitlin, S. N., Lind, J. A., and McLaren, S. E.: Automated fluorimetric method for hydrogen peroxide in atmospheric precipitation, Analytical Chemistry, 57, 917–922, 1985.

Lazrus, A. L., Kok, G. L., Lind, J. A., Gitlin, S. N., Heikes, B. G., and Shetter, R. E.: Automated fluorometric method for hydrogen peroxide in air, Analytical Chemistry, 58, 594–597, 1986.

Lee, J. H., Tang, I. N., and Weinstein-Lloyd, J. B.: A non-enzymatic method for the determination of hydrogen peroxide in atmospheric samples, Analytical Chemistry, 62, 2381–2384, 1990.

Lee, J. H., Chen, Y., and Tang, I. N.: Heterogeneous loss of gaseous hydrogen peroxide in an atmospheric air sampling system, Environmental Science & Technology, 25, 339–342, 1991.

Lee, M., Noone, B. C., O'Sullivan, D. W., and Heikes, B. G.: Method for the Collection and HPLC Analysis of Hydrogen Peroxide and C_1 and C_2 Hydroperoxides in the Atmosphere, Journal of Atmospheric and Oceanic Technology, 12, 1060–1070, 1995.

Lee, M., Heikes, B. G., Jacob, D. J., Sachse, G. W., and Anderson, B. E.: Hydrogen peroxide, organic hydroperoxide, and formaldehyde as primary pollutants from biomass burning, Journal of Geophysical Research, 102, 1301–1309, 1997.

Lee, M., Heikes, B. G., and Jacob, D. J.: Enhancements of hydroperoxides and formaldehyde in biomass burning impacted air and their effect on atmospheric oxidant cycles, Journal of Geophysical Research, 103, 13 201–13 212, 1998a.

Lee, M., Heikes, B. G., and O'Sullivan, D. W.: Hydrogen peroxide and organic hydroperoxide in the troposphere: a review, Atmospheric Environment, 34, 3475–3494, 2000.

Lee, Y.-N., Zhou, X., Kleinman, L. I., Nunnermacker, L. J., Springston, S. R., Daum, P. H., Newman, L., Keigley, W. G., Holdren, M. W., Spicer, C. W., Young, V., Fu, B., Parrish, D. D., Holloway, J., Williams, J., Roberts, J. M., Ryerson, T. B., and Fehsenfeld, F. C.: Atmospheric chemistry and distribution of formaldehyde and several multioxygenated carbonyl compounds during the 1995 Nashville/Middle Tennessee Ozone Study, Journal of Geophysical Research, 103, 22 449–22 462, 1998b.

Leighton, P. A.: Photochemistry of air pollution, Physical Chemistry, Academic Press, 1961.

Lelieveld, J.: Stability of tropospheric hydroxyl chemistry, Journal of Geophysical Research, 107, 2002.

Lelieveld, J., Dentener, F. J., Peters, W., and Krol, M. C.: On the role of hydroxyl radicals in the self-cleansing capacity of the troposphere, Atmospheric Chemistry and Physics, 4, 2337–2344, 2004.

Levy, H.: Normal atmosphere: large radical and formaldehyde concentrations predicted, Science, 173, 141–143, 1971.

Li, J. and Dasgupta, P. K.: Selective Measurement of Gaseous Hydrogen Peroxide with Light Emitting Diode-Based Liquid-Core Waveguide Absorbance Detector, Analytical Sciences, 19, 517–523, 2003.

Lightfoot, P., Cox, R. A., Crowley, J. N., Destriau, M., Hayman, G., Jenkin, M. E., Moortgat, G. K., and Zabel, F.: Organic peroxy radicals: Kinetics, spectroscopy and tropospheric chemistry, Atmospheric Environment Part A-General Topics, 26, 1805–1961, 1992.

Lind, J. A. and Kok, G. L.: Correction to "Henry's law determinations for aqueous solutions of hydrogen peroxide, methylhydroperoxide, and peroxyacetic acid" by John A. Lind and Gregory L. Kok, Journal of Geophysical Research, 99, 21 119, 1994.

Lindinger, W. and Jordan, A.: Proton-transfer-reaction mass spectrometry (PTR–MS): on-line monitoring of volatile organic compounds at pptv levels, Chemical Society Reviews, 27, 347, 1998.

Logan, J. A., Prather, M. J., Wofsy, S. C., and McElroy, M. B.: Tropospheric Chemistry: A Global Perspective, Journal of Geophysical Research, 86, 7210–7254, 1981.

Lutgens, F. K., Tarbuck, E. J., and Tasa, D.: The atmosphere: An introduction to meteorology, Pearson, Boston, 12 edn., 2013.

Mannschreck, K., Gilge, S., Plass-Dülmer, C., Fricke, W., and Berresheim, H.: Assessment of the applicability of NO-NO_2-O_3 photostationary state to long-term measurements at the Hohenpeissenberg GAW Station, Germany, Atmospheric Chemistry and Physics, 4, 1265–1277, 2004.

Mielonen, T., Portin, H., Komppula, M., Leskinen, A., Tamminen, J., Ialongo, I., Hakkarainen, J., Lehtinen, K., and Arola, A.: Biomass burning aerosols observed in Eastern Finland during the Russian wildfires in summer 2010 – Part 2: Remote sensing, Atmospheric Environment, 47, 279–287, 2012.

Mihelcic, D.: Peroxy radicals during BERLIOZ at Pabstthum: Measurements, radical budgets and ozone production, Journal of Geophysical Research, 108, 2003.

Monks, P. S.: Gas-phase radical chemistry in the troposphere, Chemical Society Reviews, 34, 376, 2005.

Müller, K., Haferkorn, S., Grabmer, W., Wisthaler, A., Hansel, A., Kreuzwieser, J., Cojocariu, C., Rennenberg, H., and Herrmann, H.: Biogenic carbonyl compounds within and above a coniferous forest in Germany, Atmospheric Environment, 40, 81–91, 2006.

Niki, H., Maker, P. D., Savage, C. M., Breitenbach, L. P., and Hurley, M. D.: FTIR spectroscopic study of the mechanism for the gas-phase reaction between ozone and tetramethylethylene, The Journal of Physical Chemistry, 91, 941–946, 1987.

Nondek, L., Rodler, D., and Birks, J. W.: Measurement of Sub-ppbv Concentrations of Aldehydes in a Forest Atmosphere Using a New HPLC Technique, Environmental Science & Technology, 26, 1174–1178, 1992.

Notario, A., Bravo, I., Adame, J. A., Díaz-de Mera, Y., Aranda, A., Rodríguez, A., and Rodríguez, D.: Partitioning, sources and variability of regional and local oxidant ($OX = O_3 + NO_2$) in a coastal rural area in the southwest of Iberian Peninsula, Environmental Science and Pollution Research, 2013.

Nozière, B., Barnes, I., and Becker, K.-H.: Product study and mechanisms of the reactions of α-pinene and of pinonaldehyde with OH radicals, Journal of Geophysical Research, 104, 23 645, 1999.

Nölscher, A., Bourtsoukidis, E., Bonn, B., Kesselmeier, J., Lelieveld, J., and Williams, J.: Seasonal measurements of total OH reactivity fluxes, total ozone loss rates and missing emissions from Norway spruce in 2011, Biogeosciences Discussions, 9, 13 497–13 536, 2012a.

Nölscher, A. C., Williams, J., Sinha, V., Custer, T., Song, W., Johnson, A. M., Axinte, R., Bozem, H., Fischer, H., Pouvesle, N., Phillips, G., Crowley, J. N., Rantala, P., Rinne, J., Kulmala, M., Gonzales, D., Valverde-Canossa, J., Vogel, A., Hoffmann, T., Ouwersloot, H. G., Vilà-Guerau Arellano, J. d., and Lelieveld, J.: Summertime total OH reactivity measurements from boreal forest during HUMPPA-COPEC 2010, Atmospheric Chemistry and Physics, 12, 8257–8270, 2012b.

Nölscher, A. C., Bourtsoukidis, E., Bonn, B., Kesselmeier, J., Lelieveld, J., and Williams, J.: Seasonal measurements of total OH reactivity emission rates from Norway spruce in 2011, Biogeosciences, 10, 4241–4257, 2013.

Orlando, J. J., Nozière, B., Tyndall, G. S., Orzechowska, G. E., Paulson, S. E., and Rudich, Y.: Product studies of the OH- and ozone-initiated oxidation of some monoterpenes, Journal of Geophysical Research, 105, 11 561, 2000.

O'Sullivan, D. W.: Long-term and seasonal variations in the levels of hydrogen peroxide, methylhydroperoxide, and selected compounds over the Pacific Ocean, Journal of Geophysical Research, 109, 2004.

O'Sullivan, D. W., Lee, M., Noone, B. C., and Heikes, B. G.: Henry's Law Constant Determinations for Hydrogen Peroxide, Methyl Hydroperoxide, Hydroxymethyl Hydroperoxide, Ethyl Hydroperoxide, and Peroxyacetic Acid, The Journal of Physical Chemistry, 100, 3241–3247, 1996.

O'Sullivan, D. W., Heikes, B. G., Lee, M., Chang, W. L., Gregory, G. L., Blake, D. R., and Sachse, G. W.: Distribution of hydrogen peroxide and methylhydroperoxide over the Pacific and South Atlantic Oceans, Journal of Geophysical Research, 104, 5635–5646, 1999.

Ouwersloot, H. G., Vilà-Guerau Arellano, J. d., Nölscher, A. C., Krol, M. C., Ganzeveld, L. N., Breitenberger, C., Mammarella, I., Williams, J., and Lelieveld, J.: Characterization of a boreal convective boundary layer and its impact on atmospheric chemistry during HUMPPA-COPEC-2010, Atmospheric Chemistry and Physics, 12, 9335–9353, 2012.

Parrish, D. D., Trainer, M., Williams, E. J., Fahey, D. W., Hübler, G., Eubank, C. S., Liu, S. C., Murphy, P. C., Albritton, D. L., and Fehsenfeld, F. C.: Measurements of the NO_x-O_3 photostationary state at Niwot Ridge, Colorado, Journal of Geophysical Research, 91, 5361, 1986.

Paulson, S. E., Flagan, R. C., and Seinfeld, J. H.: Atmospheric photooxidation of isoprene part I: The hydroxyl radical and ground state atomic oxygen reactions, International Journal of Chemical Kinetics, 24, 79–101, 1992.

Penkett, S. A., Jones, B., Brich, K., and Eggleton, A.: The importance of atmospheric ozone and hydrogen peroxide in oxidising sulphur dioxide in cloud and rainwater, Atmospheric Environment (1967), 13, 123–137, 1979.

Penkett, S. A., Monks, P. S., Carpenter, L. J., Clemitshaw, K. C., Ayers, G. P., Gillett, R. W., Galbally, I. E., and Meyer, C. P.: Relationships between ozone photolysis rates and peroxy radical concentrations in clean marine air over the Southern Ocean, Journal of Geophysical Research, 102, 12 805–12 817, 1997.

Phillips, G. J., Pouvesle, N., Thieser, J., Schuster, G., Axinte, R., Fischer, H., Williams, J., Lelieveld, J., and Crowley, J. N.: Peroxyacetyl nitrate (PAN) and peroxyacetic acid (PAA) measurements by iodide chemical ionisation mass spectrometry: first analysis of results in the boreal forest and implications for the measurement of PAN fluxes, Atmospheric Chemistry and Physics, 13, 1129–1139, 2013.

Pilz, W. and Johann, I.: Die Bestimmung Kleinster Mengen von Wasserstoffperoxyd in Luft, International Journal of Environmental Analytical Chemistry, 3, 257–270, 1974.

Platt, U. and D. Perner: Direct measurements of atmospheric CH_2O, HNO_2, O_3, NO_2 and SO_2 by Differential Optical Absorption in the near u.v., Journal of Geophysical Research, 85, 7453–7458, 1980.

Portin, H., Mielonen, T., Leskinen, A., Arola, A., Pärjälä, E., Romakkaniemi, S., Laaksonen, A., Lehtinen, K., and Komppula, M.: Biomass burning aerosols observed in Eastern Finland during the Russian wildfires in summer 2010 – Part 1: In-situ aerosol characterization, Atmospheric Environment, 47, 269–278, 2012.

Pozzer, A., Jöckel, P., Tost, H., Sander, R., Ganzeveld, L. N., Kerkweg, A., and Lelieveld, J.: Simulating organic species with the global atmospheric chemistry general circulation model ECHAM5/MESSy1: a comparison of model results with observations, Atmospheric Chemistry and Physics, 7, 2527–2550, 2007.

Pozzer, A., Meij, A. d., Pringle, K. J., Tost, H., Doering, U. M., van Aardenne, J. A., and Lelieveld, J.: Distributions and regional budgets of aerosols and their precursors simulated with the EMAC chemistry-climate model, Atmospheric Chemistry and Physics, 12, 961–987, 2012.

Pringle, K. J., Tost, H., Message, S., Steil, B., Giannadaki, D., Nenes, A., Fountoukis, C., Stier, P., Vignati, E., and Lelieveld, J.: Description and evaluation of GMXe: a new aerosol submodel for global simulations (v1), Geoscientific Model Development, 3, 391–412, 2010a.

Pringle, K. J., Tost, H., Pozzer, A., Pöschl, U., and Lelieveld, J.: Global distribution of the effective aerosol hygroscopicity parameter for CCN activation, Atmospheric Chemistry and Physics, 10, 5241–5255, 2010b.

Prinn, R. G.: The Cleansing Capacity of the Atmosphere, Annual Review of Environment and Resources, 28, 29–57, 2003.

Pöschl, U., Kuhlmann, R., Poisson, N., and Crutzen, P. J.: Development and Intercomparison of Condensed Isoprene Oxidation Mechanisms for Global Atmospheric Modeling, Journal of Atmospheric Chemistry, 37, 29–52, 2000.

Reeves, C. E. and Penkett, S. A.: Measurements of Peroxides and What They Tell Us, Chemical Reviews, 103, 5199–5218, 2003.

Regelin, E.: Räumliche und jahreszeitliche Verteilung von OH- und HO_2-Radikalen in der Troposphäre über Europa, Ph.D. thesis, Johannes-Gutenberg Universität, Mainz, 2011.

Reiffs, A.: Untersuchung des RO_2-Mischungsverhältnisses auf Grundlage des photochemischen NO-NO_2-O_3 Gleichgewichts im Rahmen der PARADE 11 Feldmesskampagne, Diploma thesis, Johannes-Gutenberg Universität, Mainz, 2012.

Ren, X., Brune, W. H., Mao, J., Mitchell, M. J., Lesher, R. L., Simpas, J. B., Metcalf, A. R., Schwab, J. J., Cai, C., and Li, Y.: Behavior of OH and HO_2 in the winter atmosphere in New York City, Atmospheric Environment, 40, 252–263, 2006.

Ridley, B. A., Madronich, S., Chatfield, R. B., Walega, J. G., Shetter, R. E., Carroll, M. A., and Montzka, D. D.: Measurements and model simulations of the photostationary state during the Mauna Loa Observatory Photochemistry Experiment: Implications for radical concentrations and ozone production and loss rates, Journal of Geophysical Research, 97, 10 375, 1992.

Riedel, K.: Untersuchung der Photooxidantien Wasserstoffperoxid, Methylhydroperoxid und Formaldehyd in der Troposphäre der Antarktis, Ph.D. thesis, Universität Bremen, Bremen, 2001.

Roeckner, E., Brokopf, R., Esch, M., Giorgetta, M., Hagemann, S., Kornblueh, L., Manzini, E., Schlese, U., and Schulzweida, U.: Sensitivity of Simulated Climate to Horizontal and Vertical Resolution in the ECHAM5 Atmosphere Model, Journal of Climate, 19, 3771–3791, 2006.

Rohrer, F., Brüning, D., Grobler, E. S., Weber, M., Ehhalt, D. H., Neubert, R., Schüßler, W., and Levin, I.: Mixing ratios and photostationary state of NO and NO_2 observed during the POPCORN field campaign at a rural site in Germany, Journal of Atmospheric Chemistry, 31, 119–137, 1998.

Ross, H. B., Johansson, C., Serves, C. d., and Lind, J.: Summertime diurnal variations of atmospheric peroxides and formaldehyde in Sweden, Journal of Atmospheric Chemistry, 14, 411–423, 1992.

Ruppert, L., Becker, K. H., Noziere, B., and Spittler, M.: Development of Monoterpene Oxidation Mechanisms: Results from Laboratory and Smog Chamber Studies, Transactions on Ecology and the Environment, 1999.

Sadanaga, Y., Yoshino, A., Watanabe, K., Yoshioka, A., Wakazono, Y., Kanaya, Y., and Kajii, Y.: Development of a measurement system of OH reactivity in the atmosphere by using a laser-induced pump and probe technique, Review of Scientific Instruments, 75, 2648–2655, 2004.

Sakugawa, H. and Kaplan, I. R.: Atmospheric H_2O_2 measurement: Comparison of cold trap method with impinger bubbling method, Atmospheric Environment (1967), 21, 1791–1798, 1987.

Sakugawa, H., Kaplan, I. R., Tsai, W., and Cohen, Y.: Atmospheric hydrogen peroxide, Environmental Science & Technology, 24, 1452–1462, 1990.

Salthammer, T., Mentese, S., and Marutzky, R.: Formaldehyde in the Indoor Environment, Chemical Reviews, 110, 2536–2572, 2010.

Sander, R.: Compilation of Henry's Law Constants for Inorganic and Organic Species of Potential Importance in Environmental Chemistry (Version 3), URL `http://www.henrys-law.org`, 1999.

Sander, R., Kerkweg, A., Jöckel, P., and Lelieveld, J.: Technical note: The new comprehensive atmospheric chemistry module MECCA, Atmospheric Chemistry and Physics, 5, 445–450, 2005.

Sauer, F.: Measurements of hydrogen peroxide and individual organic peroxides in the marine troposphere, Atmospheric Environment, 31, 1173–1184, 1997.

Sauer, F.: Hydrogen peroxide, organic peroxides and organic acids in a forested area during FIELDVOC'94, Chemosphere - Global Change Science, 3, 309–326, 2001.

Sawicki, E., Hauser, T. R., and McPherson, S.: Spectrophotometric Determination of Formaldehyde and Formaldehyde-Releasing Compounds with Chromotropic Acid, 6-Amino-1-naphthol-3-sulfonic Acid (J Acid), and 6-Anilino-1-napthol-3-sulfonic Acid (Phenyl J Acid), Analytical Chemistry, 34, 1460–1464, 1962.

Seinfeld, J. H. and Pandis, S. N.: Atmospheric chemistry and physics: From air pollution to climate change, J. Wiley, Hoboken and N.J, 2 edn., 2006.

Serves, C. d.: Gas phase formaldehyde and peroxide measurements in the Arctic atmosphere, Journal of Geophysical Research, 99, 25 391–25 398, 1994.

Sillman, S.: The relation between ozone, NO_x and hydrocarbons in urban and polluted rural environments, Atmospheric Environment, 33, 1821–1845, 1999.

Singh, H. B., O'Hara, D., HERLTH, D., Bradshaw, J. D., Sandholm, S. T., Gregory, G. L., Sachse, G. W., Blake, D. R., Crutzen, P. J., and Kanakidou, M. A.: Atmospheric measurements of peroxyacetyl nitrate and other organic nitrates at high latitudes: Possible sources and sinks, Journal of Geophysical Research: Atmospheres, 97, 16 511–16 522, 1992.

Sinha, V., Williams, J., Crowley, J. N., and Lelieveld, J.: The Comparative Reactivity Method - a new tool to measure total OH Reactivity in ambient air, Atmospheric Chemistry and Physics, 8, 2213–2227, 2008.

Sinha, V., Williams, J., Diesch, J.-M., Drewnick, F., Martinez, M., Harder, H. D., Regelin, E., Kubistin, D., Bozem, H., Hosaynali-Beygi, Z., Fischer, H., Andrés-Hernández, M. D., Kartal, D., Adame, J. A., and Lelieveld, J.: Constraints on instantaneous ozone production rates and regimes during DOMINO derived using in-situ OH reactivity measurements, Atmospheric Chemistry and Physics, 12, 7269–7283, 2012.

Slemr, F., Harris, G. W., Hastie, D. R., Mackay, G. I., and Schiff, H. I.: Measurement of Gas Phase Hydrogen Peroxide in Air by Tunable Diode Laser Absorption Spectroscopy, Journal of Geophysical Research, 91, 5371–5378, 1986.

Snow, J. A., Heikes, B. G., Shen, H., O'Sullivan, D. W., Fried, A., and Walega, J.: Hydrogen peroxide, methyl hydroperoxide, and formaldehyde over North America and the North Atlantic, Journal of Geophysical Research, 112, 2007.

Soergel, M., Regelin, E., Bozem, H., Diesch, J.-M., Drewnick, F., Fischer, H., Harder, H. D., Held, A., Hosaynali-Beygi, Z., Martinez, M., and Zetzsch, C.: Quantification of the unknown HONO daytime source and its relation to NO_2, Atmospheric Chemistry and Physics, 11, 10 433–10 447, 2011.

Solberg, S., Dye, C., Schmidbauer, N., Herzog, A., and Gehrig, R.: Carbonyls and nonmethane hydrocarbons at rural European sites from the mediterranean to the arctic, Journal of Atmospheric Chemistry, 25, 33–66, 1996.

Song, W., Williams, J., Yassaa, N., Martinez, M., Carnero, J. A. A., Hidalgo, P. J., Bozem, H., and Lelieveld, J.: Winter and summer characterization of biogenic enantiomeric monoterpenes and anthropogenic BTEX compounds at a Mediterranean Stone Pine forest site, Journal of Atmospheric Chemistry, 2012.

Staffelbach, T. A., Kok, G. L., Heikes, B. G., McCully, B., Mackay, G. I., Karecki, D. R., and Schiff, H. I.: Comparison of hydroperoxide measurements made during the Mauna Loa Observatory Photochemistry Experiment 2, Journal of Geophysical Research, 101, 14 729–14 739, 1996.

Stevens, P. S., Mather, J. H., Brune, W. H., Eisele, F., Tanner, D., Jefferson, A., Cantrell, C. A., Shetter, R. E., Sewall, S., Fried, A., Henry, B., Williams, E., Baumann, K., Goldan, P., and Kuster, W. C.: HO_2 / OH and RO_2 / HO_2 ratios during the Tropospheric OH Photochemistry Experiment: Measurement and theory, Journal of Geophysical Research, 102, 6379, 1997.

Stickler, A.: HCHO, H_2O_2 und CH_3OOH in der Troposphäre, Ph.D. thesis, Johannes-Gutenberg Universität, Mainz, 2006.

Stickler, A., Fischer, H., Williams, J., Reus, M. d., Sander, R., Lawrence, M. G., Crowley, J. N., and Lelieveld, J.: Influence of summertime deep convection on formaldehyde in the middle and upper troposphere over Europe, Journal of Geophysical Research, 111, 2006.

Stocker, T. F., Dahe, Q., and Plattner, G.-K.: Climate Change 2013: The Physical Science Basis, Working Group I Contribution to the Fifth Assessment Report of the Intergovernmental Panel on Climate Change. Summary for Policymakers (IPCC, 2013), 2013.

Stotzky, G. and Schenck, S.: Observations on Organic Volatiles from Germinating Seeds and Seedlings, American Journal of Botany, 63, 798, 1976.

Stull, R. B.: An Introduction to Boundary Layer Meteorology, Atmospheric and Oceanographic Sciences Library, Springer Netherlands, 1988.

Sumner, A. L., Shepson, P. B., Couch, T. L., Thornberry, T., Carroll, M. A., Sillman, S., Pippin, M., Bertman, S. B., Tan, D., Faloona, I. C., Brune, W. H., Young, V., Cooper, O. R., Moody, J., and Stockwell, W. R.: A study of formaldehyde chemistry above a forest canopy, Journal of Geophysical Research, 106, 24 387–24 405, 2001.

Tan, D., Faloona, I. C., Simpas, J. B., Brune, W. H., Shepson, P. B., Couch, T. L., Sumner, A. L., Carroll, M. A., Thornberry, T., Apel, E. C., Riemer, D., and Stockwell, W. R.: HO_x budgets in a deciduous forest: Results from the PROPHET summer 1998 campaign, Journal of Geophysical Research, 106, 24 407–24 427, 2001.

Tanner, R. L. and Meng, Z.: Seasonal variations in ambient atmospheric levels of formaldehyde and acetaldehyde, Environmental Science & Technology, 18, 723–726, 1984.

Tanner, R. L. and Shen, J.: Measurement of Hydrogen Peroxide in Ambient Air by Impinger and Diffusion Scrubber, Aerosol Science and Technology, 12, 86–97, 1990.

Tanner, R. L., Markovits, G. Y., Ferreri, E. M., and Kelly, T. J.: Sampling and determination of gas-phase hydrogen peroxide following removal of ozone by gas-phase reaction with nitric oxide, Analytical Chemistry, 58, 1857–1865, 1986.

Thompson, A. M.: The Oxidizing Capacity of the Earth's Atmosphere: Probable Past and Future Changes, Science, 256, 1157–1165, 1992.

Thornton, J. A.: Ozone production rates as a function of NO_x abundances and HO_x production rates in the Nashville urban plume, Journal of Geophysical Research, 107, 2002.

Tost, H., Jöckel, P., Kerkweg, A., Sander, R., and Lelieveld, J.: Technical note: A new comprehensive SCAVenging submodel for global atmospheric chemistry modelling, Atmospheric Chemistry and Physics, 6, 565–574, 2006.

Tuazon, E. C. and Atkinson, R.: A product study of the gas-phase reaction of Isoprene with the OH radical in the presence of NO_x, International Journal of Chemical Kinetics, 22, 1221–1236, 1990.

Vairavamurthy, A., Roberts, J. M., and Newman, L.: Methods for determination of low molecular weight carbonyl compounds in the atmosphere: A review, Atmospheric Environment Part A-General Topics, 26, 1965–1993, 1992.

van Aalst, M. K., van den Broek, M. M. P., Bregman, A., Brühl, C., Steil, B., Toon, G. C., Garcelon, S., Hansford, G. M., Jones, R. L., Gardiner, T. D., Roelofs, G. J., Lelieveld, J., and Crutzen, P. J.: Trace gas transport in the 1999/2000 Arctic winter: comparison of nudged GCM runs with observations, Atmospheric Chemistry and Physics, 4, 81–93, 2004.

van der Werf, G. R., Randerson, J. T., Giglio, L., Collatz, G. J., Mu, M., Kasibhatla, P. S., Morton, D. C., DeFries, R. S., Jin, Y., and van Leeuwen, T. T.: Global fire emissions and the contribution of deforestation, savanna, forest, agricultural, and peat fires (1997–2009), Atmospheric Chemistry and Physics, 10, 11 707–11 735, 2010.

van Valin, C. C., Ray, J. D., Boatman, J. F., and Gunter, R. L.: Hydrogen peroxide in air during winter over the south-central United States, Geophysical Research Letters, 14, 1146, 1987.

Viskari, E.: Seasonal and diurnal variation in formaldehyde and acetaldehyde concentrations along a highway in Eastern Finland, Atmospheric Environment, 34, 917–923, 2000.

Volz-Thomas, A.: Introduction to Special Section: Photochemistry Experiment in BERLIOZ, Journal of Geophysical Research, 108, 2003a.

Volz-Thomas, A.: Inorganic trace gases and peroxy radicals during BERLIOZ at Pabstthum: An investigation of the photostationary state of NO_x and O_3, Journal of Geophysical Research, 108, 2003b.

Wagner, V.: Formaldehyd in der maritimen Grenzschicht über dem Indischen Ozean: Feldmessungen und Modellierung, Wiss.-Verl. Maraun, Frankfurt/M, 1 edn., 2000.

Wagner, V.: Are CH_2O measurements in the marine boundary layer suitable for testing the current understanding of CH_4 photooxidation?: A model study, Journal of Geophysical Research, 107, 2002.

Wagner, V., Schiller, C., and Fischer, H.: Formaldehyde measurements in the marine boundary layer of the Indian Ocean during the 1999 INDOEX cruise of the R/V Ronald H. Brown, Journal of Geophysical Research, 106, 28 529–28 538, 2001.

Warneck, P.: OH production rates in the troposphere, Planetary and Space Science, 23, 1507–1518, 1975.

Watanabe, K., Nagao, I., and Tanaka, H.: Atmospheric hydrogen peroxide concentration measured at Ogasawara Hahajima Island in the sub-tropical Pacific Ocean, Journal of Meteorological Society of Japan, 74, 393–398, 1996.

Watkins, B. A., Parrish, D. D., Buhr, S., Norton, R. B., Trainer, M., Yee, J. E., and Fehsenfeld, F. C.: Factors influencing the concentration of gas phase hydrogen peroxide during the summer at Kinterbish, Alabama, Journal of Geophysical Research, 100, 22 841–22 851, 1995a.

Watkins, B. A., Parrish, D. D., Trainer, M., Norton, R. B., Yee, J. E., Fehsenfeld, F. C., and Heikes, B. G.: Factors influencing the concentration of gas phase hydrogen peroxide during the summer at Niwot Ridge, Colorado, Journal of Geophysical Research, 100, 22 831–22 840, 1995b.

Weller, R., Schrems, O., Boddenberg, A., Gäb, S., and Gautrois, M.: Meridional distribution of hydroperoxides and formaldehyde in the marine boundary layer of the Atlantic (48 °N-35 °S) measured during the Albatross campaign, Journal of Geophysical Research, 105, 14 401–14 412, 2000.

Wesely, M. L. and Hicks, B. B.: A review of the current status of knowledge on dry deposition, Atmospheric Environment, 34, 2261–2282, 2000.

West, P. W. and Sen, B.: Spectrophotometric determination of traces of formaldehyde, Fresenius' Zeitschrift für Analytische Chemie, 153, 177–183, 1956.

Whitaker, J. S., Hamill, T. M., Wei, X., Song, Y., and Toth, Z.: Ensemble Data Assimilation with the NCEP Global Forecast System, Monthly Weather Review, 136, 463–482, 2008.

Wiesufer, S., Boddenberg, A., Ligon, A. P., Dallmann, G., Turner, W. V., and Gäb, S.: An automated instrument for determining atmospheric H_2O_2 and organic hydroperoxides by stripping and HPLC, Environmental Science and Pollution Research, pp. 41–47, 2002.

Williams, J., Crowley, J. N., Fischer, H., Harder, H. D., Martinez, M., Petaja, T., Rinne, J., Bäck, J., Boy, M., Dal Maso, M., Hakala, J., Kajos, M., Keronen, P., Rantala, P., Aalto, J., Aaltonen, H., Paatero, J., VESALA, T., Hakola, H., Levula, J., Pohja, T., Herrmann, F., Auld, J., Mesarchaki, E., Song, W., Yassaa, N., Noelscher, A., Johnson, A. M., Custer, T., Sinha, V., Thieser, J., Pouvesle, N., Taraborrelli, D., Tang, M. J., Bozem, H., Hosaynali-Beygi, Z., Axinte, R., Oswald, R., Novelli, A., Kubistin, D., Hens, K., Javed, U., Trawny, K., Breitenberger, C., Hidalgo, P. J., Ebben, C. J., Geiger, F. M., Corrigan, A. L., Russell, L. M., Ouwersloot, H. G., Arellano, J. V.-G. d., Ganzeveld, L. N., Vogel, A., Beck, M., Bayerle, A., Kampf, C. J., Bertelmann, M., Koellner, F., Hoffmann, T., Valverde, J., Gonzalez, D., Riekkola, M.-L., Kulmala, M., and Lelieveld, J.: The summertime Boreal forest field measurement intensive (HUMPPA-COPEC-2010): an overview of meteorological and chemical influences, Atmospheric Chemistry and Physics, 11, 10 599–10 618, 2011.

Winterhalter, R., Neeb, P., Grossmann, D., Kolloff, A., Horie, O., and Moortgat, G. K.: Products and Mechanism of the Gas Phase Reaction of Ozone with β-Pinene, Journal of Atmospheric Chemistry, 35, 165–197, 2000.

Wolverton, B. C., Mcdonald, R. C., and Watkins, E. A.: Foliage plants for removing indoor air pollutants from energy-efficient homes, Economic Botany, 38, 224–228, 1984.

Yassaa, N., Song, W., Lelieveld, J., Vanhatalo, A., Bäck, J., and Williams, J.: Diel cycles of isoprenoids in the emissions of Norway spruce, four Scots pine chemotypes, and in Boreal forest ambient air during HUMPPA-COPEC-2010, Atmospheric Chemistry and Physics, 12, 7215–7229, 2012.

Yokelson, R. J., Goode, J. G., Ward, D. E., Susott, R. A., Babbitt, R. E., Wade, D. D., Bertschi, I., Griffith, D. W. T., and Hao, W. M.: Emissions of formaldehyde, acetic acid, methanol, and other trace gases from biomass fires in North Carolina measured by airborne Fourier transform infrared spectroscopy, Journal of Geophysical Research, 104, 30 109–30 125, 1999.

Yokouchi, Y., Fujii, T., Ambe, Y., and Fuwa, K.: Gas chromatographic-mass spectrometric analysis of formaldehyde in ambient air using a sampling tube, Journal of Chromatography A, 180, 133–138, 1979.

Zhang, X., Chen, Z., Wang, H., He, S., and Huang, D.: An important pathway for ozonolysis of alpha-pinene and beta-pinene in aqueous phase and its atmospheric implications, Atmospheric Environment, 43, 4465–4471, 2009.

Zhou, X., Lee, Y.-N., Newman, L., Chen, X., and Mopper, K.: Tropospheric formaldehyde concentration at the Mauna Loa Observatory during the Mauna Loa Observatory Photochemistry Experiment 2, Journal of Geophysical Research, 101, 14 711–14 719, 1996.

Zöllner, M.: Untersuchungen zur troposphärischen Photochemie am GAW-Observatorium Izana, Ph.D. thesis, Johannes-Gutenberg Universität, Mainz, 2008.

Acknowledgements

[redacted]